

IntechOpen

Magnetic Materials

Edited by Khan Maaz



MAGNETIC MATERIALS

Edited by **Khan Maaz**

Magnetic Materials

<http://dx.doi.org/10.5772/61497>

Edited by Khan Maaz

Contributors

Igor Bychkov, Dmitry Kuzmin, Vladimir Shavrov, Krzysztof Zdzislaw Sokalski, Barbara Slusarek, Jan Szczyglowski, Andrzej Stupakiewicz, Mihai Dimian, Aurelian Rotaru, Leszek Mariusz Malkinski, Rahmatollah Eskandari, Fanny Béron, Peterson Grandini De Carvalho, Luis Carlos Costa Arzuza, Karoline Moura, Marcos Vincius Puydinger Dos Santos, Kleber Roberto Pirota, Sheng Yun Wu, Jhong-Yi Ji, Iman Roqan, Zulia Caamaño, Katsuhisa Taguchi, Roberto Zivieri

© The Editor(s) and the Author(s) 2016

The moral rights of the and the author(s) have been asserted.

All rights to the book as a whole are reserved by INTECH. The book as a whole (compilation) cannot be reproduced, distributed or used for commercial or non-commercial purposes WITHOUT INTECH's written permission.

Enquiries concerning the use of the book should be directed to INTECH rights and permissions department (permissions@intechopen.com).

Violations are liable to prosecution under the governing Copyright Law.



Individual chapters of this publication are distributed under the terms of the Creative Commons Attribution 3.0 Unported License which permits commercial use, distribution and reproduction of the individual chapters, provided the original author(s) and source publication are appropriately acknowledged. If so indicated, certain images may not be included under the Creative Commons license. In such cases users will need to obtain permission from the license holder to reproduce the material. More details and guidelines concerning content reuse and adaptation can be found at <http://www.intechopen.com/copyright-policy.html>.

Notice

Statements and opinions expressed in the chapters are those of the individual contributors and not necessarily those of the editors or publisher. No responsibility is accepted for the accuracy of information contained in the published chapters. The publisher assumes no responsibility for any damage or injury to persons or property arising out of the use of any materials, instructions, methods or ideas contained in the book.

First published in Croatia, 2016 by INTECH d.o.o.

eBook (PDF) Published by IN TECH d.o.o.

Place and year of publication of eBook (PDF): Rijeka, 2019.

IntechOpen is the global imprint of IN TECH d.o.o.

Printed in Croatia

Legal deposit, Croatia: National and University Library in Zagreb

Additional hard and PDF copies can be obtained from orders@intechopen.com

Magnetic Materials

Edited by Khan Maaz

p. cm.

Print ISBN 978-953-51-2427-6

Online ISBN 978-953-51-2428-3

eBook (PDF) ISBN 978-953-51-6670-2

We are IntechOpen, the world's leading publisher of Open Access books Built by scientists, for scientists

3,800+

Open access books available

116,000+

International authors and editors

120M+

Downloads

151

Countries delivered to

Our authors are among the
Top 1%

most cited scientists

12.2%

Contributors from top 500 universities



WEB OF SCIENCE™

Selection of our books indexed in the Book Citation Index
in Web of Science™ Core Collection (BKCI)

Interested in publishing with us?
Contact book.department@intechopen.com

Numbers displayed above are based on latest data collected.
For more information visit www.intechopen.com



Meet the editor



Dr. Maaz Khan is working as Principal Scientist in the Pakistan Institute of Nuclear Science and Technology (PINSTECH), Islamabad. He received his PhD degree from the Quaid-i-Azam University and completed his postdoctorates in South Korea and China. He is working on fabrication and structural, magnetic, optical, and electrical characterization of nanomaterials. He has published more than 55 articles and 1 book. Dr. Khan is serving as Executive Editor of the International Journal of Nano Studies and Technology (IJNST) and is part of the editorial board of the World Journal of Condensed Matter Physics, Advances in Alloys and Compounds, International Journal of Materials Science and Applications, American Journal of Nano Research and Applications, and Frontiers in Physics. Dr. Khan has also edited two books, with few others in progress.

Contents

Preface XI

- Chapter 1 **Scaling in Magnetic Materials 1**
Krzysztof Z. Sokalski, Barbara Ślusarek and Jan Szczygłowski
- Chapter 2 **How to Characterize Cylindrical Magnetic Nanowires 41**
Fanny Béron, Marcos V. Puydinger dos Santos, Peterson G. de Carvalho, Karoline O. Moura, Luis C.C. Arzuza and Kleber R. Pirota
- Chapter 3 **Magnetization Dynamics–Induced Charge and Spin Transport on the Surface of a Topological Insulator Subjected to Magnetism 71**
Katsuhisa Taguchi
- Chapter 4 **Metamaterial Properties of 2D Ferromagnetic Nanostructures: From Continuous Ferromagnetic Films to Magnonic Crystals 93**
Roberto Zivieri
- Chapter 5 **Molecular Magnetism Modeling with Applications in Spin Crossover Compounds 117**
Mihai Dimian and Aurelian Rotaru
- Chapter 6 **Proteresis of Core-Shell Nanocrystals: Investigation through Theoretical Simulation and Experimental Analysis 147**
Jhong-Yi Ji and Sheng Yun Wu
- Chapter 7 **Radiation and Propagation of Waves in Magnetic Materials with Helicoidal Magnetic Structure 161**
Igor V. Bychkov, Dmitry A. Kuzmin and Vladimir G. Shavrov

- Chapter 8 **Giant Magnetoimpedance Effect and AC Magnetic Susceptibility in Amorphous Alloys System of FeCoNbBSiCu 181**
Zulia Isabel Caamaño De Ávila, Amilkar José Orozco Galán and Andrés Rosales-Rivera
- Chapter 9 **Magnetization Statics and Ultrafast Photoinduced Dynamics in Co/garnet Heterostructures 195**
Andrzej Stupakiewicz
- Chapter 10 **Magnetic Micro-Origami 223**
Leszek Malkinski and Rahmatollah Eskandari
- Chapter 11 **Magnetic Properties of Gadolinium-Doped ZnO Films and Nanostructures 249**
Iman S. Roqan, S. Assa Aravindh and Singaravelu Venkatesh

Preface

This book provides up-to-date information on recent trends and developments in material technology, characterization techniques, and theory and applications of magnetic materials with novel contributions from the renowned scientists in the field of material science and magnetism. The book addresses diverse groups of readers, including students, engineers, and researchers, from different fields—physics, chemistry, engineering, electronics, and materials science—who wish to enhance their knowledge and research capabilities in magnetism and magnetic materials.

The book contains eleven chapters discussing scaling in magnetic materials, characterization of cylindrical magnetic nanowires, magnetic dynamics–induced charge and spin transport on the surface of topological insulator with magnetism, metamaterial properties of 2D ferromagnetic nanostructures, molecular magnetism modeling with their application in spin-crossover compounds, proteresis of core-shell nanocrystals, radiation and propagation of waves in magnetic materials with helicoidal magnetic structure, giant magneto-impedance effect and AC magnetic susceptibility in amorphous alloys systems, magnetization statics and ultrafast photo-induced dynamics in Co/garnet heterostructures, magnetic micro-origami, and magnetic properties of rare earth and transition metals. The topics in the book are brought to an appropriate level covering a wide range of magnetic materials. At the end of each chapter, proper references are included, which can lead the readers to the best sources in the literature and help them to go into more depth in the field of magnetism.

I am grateful to the InTech’s publishing team for making this project possible and to all the authors who have contributed to this book. I am also thankful to the Publishing Process Manager Ms. Romina Rován for her cooperative attitude during the reviewing and publishing processes. I hope that this book will help the readers to learn more about magnetic materials and will provide an opportunity to strengthen their knowledge in the field of magnetism and magnetic materials.

Dr. Maaz Khan
Physics Division
PINSTECH, Islamabad
Pakistan

Scaling in Magnetic Materials

Krzysztof Z. Sokalski, Barbara Ślusarek and
Jan Szczygłowski

Additional information is available at the end of the chapter

<http://dx.doi.org/10.5772/63285>

Abstract

The chapter presents applications of the scaling in several problems of magnetic materials. Soft magnetic materials (SMMs) and soft magnetic composites (SMCs) are considered. Application of scaling in investigations of problems, such as power losses, losses separation, data collapse of the losses characteristics and modelling of the magnetic hysteresis, is presented. The symmetry group generated by scaling and gauge transformations enables us to introduce the classification of the hysteresis loops with respect to the equivalence classes. SMC materials require special treatment in the production process. Therefore, algorithms for optimization of the power losses are created. The algorithm for optimization processes is based on the scaling and the notion of the pseudo-equation of state. The scaling makes modelling and calculations easy; however, the data must obey the scaling. Checking procedure of statistical data to this respect is presented.

Keywords: magnetic materials, hysteresis loop, power losses, losses separation, scaling, gauge

1. Introduction

The notion of scaling describes invariance of various phenomena and their mathematical models with respect to a change of scale. Let us take into account the simplest mathematical model revealing such behaviour:

$$y = Ax^\alpha. \quad (1)$$

where α and A are the constants of model. Such functions appear in mathematical modelling in physics, mathematics, biology, economics and engineering. In this section, we consider data of classical gas. By simple calculation, we will prove that these data are self-similar. Let us change the scale of the both variables x and y with respect to $\lambda > 0$ multiplier.

$$x' = \lambda^\beta x, y' = \lambda^\gamma y. \quad (2)$$

Substituting (2)–(1) we obtain:

$$y' = A'x'^\alpha, \quad (3)$$

where β and γ are scaling exponents and $A' = \lambda^{\gamma-\alpha\beta} A$ is the model constant in new scale. (1)–(3) reveal that the phenomenon described by the model (1) is self-similar. This means that the phenomenon reproduces itself on different scales. In achieving the property of self-similarity, an important role plays dimensional analysis. Its idea is very simple: physical laws cannot depend on an arbitrary choice of basic units of measurement [1]. Set of all transformations (2) and multiplication constitutes $\mathcal{G}_\lambda = (\mathbb{R}_+, \cdot)$ group. In the next section, we will consider self-similar model of hysteresis loop. Extension of (2) to the two parameters group is necessary to this respect. Let us extend (1) to non-homogenous form:

$$y = Ax^\alpha + c, \quad (4)$$

The full symmetry of (4) consists of the two transformations, λ scaling and χ gauge transformation:

$$y' = A(\lambda x)^\alpha + c + \chi. \quad (5)$$

where χ is additive gauge operation which constitutes additive group $\mathcal{G}_\chi = (\mathbb{R}, +)$. Therefore, the full symmetry of (5) consists of the following direct product: $\mathcal{G}_{\lambda,\chi} = \mathcal{G}_\lambda \times \mathcal{G}_\chi$ [2]. However, the symmetry of the hysteresis loop will occur to be semi-direct product.

In this chapter, we will consider more advanced function and then the models (1) and (4). Therefore, we will need definition of homogenous function in general sense [3] which has played crucial role in the all achievements presented in this chapter. Let $f(x_1, x_2, \dots, x_n)$ be a function of n variables. If $\exists (\alpha_0, \alpha_1, \alpha_2, \dots, \alpha_n) \in \mathbb{R}^{n+1}$ such that $\forall \lambda \in \mathbb{R}_+$, the following relation holds:

$$\lambda^{\alpha_0} f(x_1, x_2, \dots, x_n) = f(\lambda^{\alpha_1} x_1, \lambda^{\alpha_2} x_2, \dots, \lambda^{\alpha_n} x_n). \quad (6)$$

Then, $f(x_1, x_2, \dots, x_n)$ is homogenous function in general sense. Based on the measurement data of classical gas presented in **Table 1**, we present simple application of this notion. We assume that the phenomena are represented by measurement data which satisfy certain relation called law. Let us assume that searched on phenomenon have a form of the homogenous function in general sense:

$$\lambda^a \rho(T, p) = \rho(\lambda^b T, \lambda^g p). \quad (7)$$

$\rho[\text{mol}\cdot\text{m}^{-3}]$	$T[\text{K}]$	$p[\text{Pa}]$
0.096	500	400
0.090	515	385
0.084	530	370
0.078	545	355
0.073	560	340
0.068	575	325
0.063	590	310
0.059	605	295
0.054	620	280
0.050	635	265
0.046	650	250

Table 1. Measurement data of classical gas.

where ρ , T and p are gas density, temperature and pressure, respectively. Coefficients a , b and c are the scaling exponents. Since (7) holds for each value of λ , we are free to substitute the following expression $\lambda = T^{-1/b}$ and get the following relation:

$$T^{-a/b} \rho(T, p) = \rho(1, T^{-g/b} p). \quad (8)$$

Introducing new symbols for the scaling exponents: $\alpha = \frac{a}{b}$, $\gamma = \frac{g}{b}$ we derive the following equation of state:

$$T^{-\alpha} \rho = AT^{-\gamma} p. \quad (9)$$

where the right-hand side of (8) was approximated by linear function, A is an expansion's coefficient. In the next sections of this chapter, we will use the Maclaurin expansion beyond

the linear term as a way for creation of scaling function. Equation (9) depends on the one effective exponent $\delta = \gamma - \alpha$:

$$\rho(T, p) = A \frac{p}{T^\delta}. \quad (10)$$

where the model constants A and δ have to be determined from the experimental data of **Table 1**. Using formula (10) and **Table 1** we have created error function Chi^2 which was minimized by the SOLVER program of the Excel package. The obtained results are as follows: $A = 0.121$ (mol K J⁻¹) and $\delta = 1.002$ (-). Note that $A^{-1} = 8.22$ (mol⁻¹ K⁻¹J) reveals an approximation of the gas constant. Mentioned and illustrated above methodology for applications of the scaling and the gauge transformations will be applied to the following problems: self-similarity of hysteresis, self-similarity of total loss in SMM, multi-scaling of core losses in SMM, optimization of total loss in SMC and scaling conception of losses separation.

2. Self-similar model of hysteresis loop

The goal of the present section is to describe the self-similar mathematical model of hysteresis loop which enables us to express its self-similarity by the homogeneous function in general sense. Derivation of the model based on the well-known properties of $\tanh(\cdot)$ suits for model of initial magnetization function [4]. It describes properly the saturation for both asymptotic values of the magnetic field $H \rightarrow \pm\infty$, as well as and the behaviour of magnetization in the neighbourhood of origin. However, this is too rigid for scaling. We make $\tanh(\cdot)$ to be a softer by making the base of the natural logarithm free parameters [5]:

$$\tanh(x) \rightarrow \tan H(a, b, c, d; x) = \frac{a^x - b^{-x}}{c^x + d^{-x}}. \quad (11)$$

where the bases have to satisfy the following conditions: $a > 1, b > 1, c > 1, d > 1$. These conditions guarantee correctness of the model; however, a little deviations from the mentioned constrains are possible.

First, we write down the model expression for initial magnetization curve:

$$M_p(X, \varepsilon) = M_0 P(X, \varepsilon); X \in [0, X_{max}]. \quad (12)$$

where M_0 is magnetization corresponding to saturation expressed in tesla: [T], $X = \frac{H}{h}$, where H is magnetic field, and h is a parameter of the magnetic field dimension (A m⁻¹) to be determined. Function $P(X, \varepsilon)$ is of the following form:

$$P(X, \varepsilon) = \frac{a^{X-\varepsilon} - b^{-X+\varepsilon}}{c^{X-\varepsilon} - d^{-X+\varepsilon}} \quad (13)$$

where ε is modelling parameter related to θ , where $\varepsilon \in [-\frac{\theta}{2}, +\frac{\theta}{2}]$. Let the upper and the lower branches of the hysteresis loop are of the following forms:

$$M_F(X, \theta) = M_0 F(X, \theta); \quad M_G(X, \theta) = M_0 G(X, \theta). \quad (14)$$

where

$$F(X, \theta) = \frac{a^{X+\theta} - b^{-X-\theta}}{c^{X+\theta} - d^{-X-\theta}} \quad G(X, \theta) = \frac{a^{X-\theta} - b^{-X+\theta}}{c^{X-\theta} - d^{-X+\theta}}. \quad (15)$$

Let us consider for illustration the following symmetric example: $a = b = c = d = 4$ and $\theta = 1.3$, $\varepsilon = 0$, $M_0 = 1$ (See **Figure 1**).

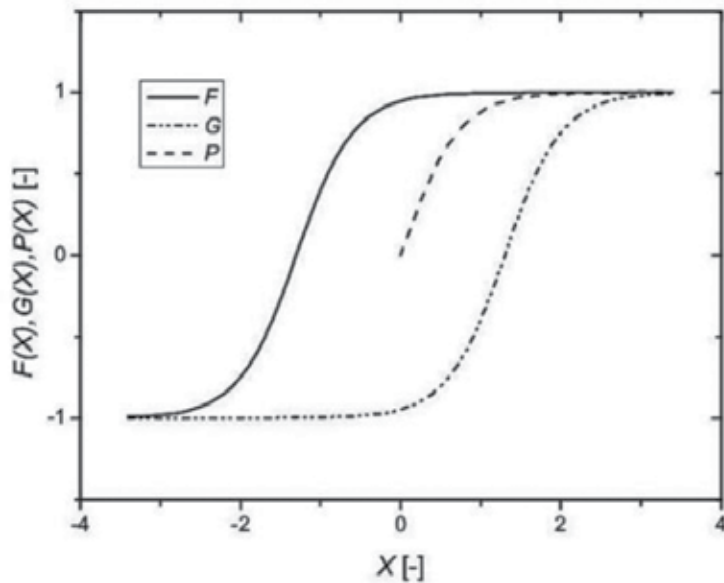


Figure 1. A model of nucleation-type hysteresis constructed with functions F , P and G according to (12)–(15).

Due to the asymptotic properties of magnetization, the functions $F(X, \theta)$ and $G(X, \theta)$ have to possess the same asymptotic properties. As we have mentioned, these components get equal values for $H \rightarrow \pm\infty$. However, due to the uncertainty of measured magnitudes, it is possible to accept the saturation points at $X = X_{min}$ and $X = X_{max}$ being the end points of the hysteresis loop.

Therefore, the modelling process has to ensure that the initial function satisfies the following constrain:

$$|F(X_{max}, \theta) - G(X_{max}, \theta)| \leq |\psi|. \quad (16)$$

where $|\psi| = su p_X \frac{|M_F(X, \theta) - M_G(X, \theta)|}{M_0}$ is dimensionless measure of uncertainty corresponding to $|M_F(X) - M_G(X)|$.

The scaling in space of loops is performed by scaling each loop's component (13), (14), (15) and (16). For simplicity of further investigations, we consider simplified symmetric model, where all the bases of $\tan H()$ are equal:

$$\frac{M_F(X, \theta)}{M_0} = \frac{(a)^{X+\theta} - (a)^{-X-\theta}}{(a)^{X+\theta} + (a)^{-X-\theta}} \quad (17)$$

$$\frac{M_G(X, \theta)}{M_0} = \frac{(a)^{X-\theta} - (a)^{-X+\theta}}{(a)^{X-\theta} + (a)^{-X+\theta}} \quad (18)$$

$$\frac{M_P(X, \varepsilon)}{M_0} = \frac{(a)^{X+\varepsilon} - (a)^{-X-\varepsilon}}{(a)^{X+\varepsilon} + (a)^{-X-\varepsilon}} \quad (19)$$

Let us perform scaling on (17) and (18). Since exponents are dimensionless, the scaling on this level cannot be supported by dimension analysis. However, we are able to scale the following magnitudes a , $M_F(X, \theta)$, $M_G(X, \theta)$, $M_P(X, \theta)$, and to prove the following theorem:

For the symmetric model (17)–(19), the hysteresis loop is invariant with respect to scaling and gauge transformation [5]. Following definition of the homogeneous function in general sense (6), we write down the scaled form of the hysteresis loop:

$$\frac{M_F(X, \theta)}{M_0} \lambda^v = \frac{(\lambda^\alpha a)^{X+\theta} a^\chi - (\lambda^\alpha a)^{-X-\theta} a^{-\chi}}{(\lambda^\alpha a)^{X+\theta} a^\chi + (\lambda^\alpha a)^{-X-\theta} a^{-\chi}}, \quad (20)$$

$$\frac{M_G(X, \theta)}{M_0} \lambda^v = \frac{(\lambda^\alpha a)^{X-\theta} a^\chi - (\lambda^\alpha a)^{-X+\theta} a^{-\chi}}{(\lambda^\alpha a)^{X-\theta} a^\chi + (\lambda^\alpha a)^{-X+\theta} a^{-\chi}}, \quad (21)$$

where exponentials a^x and a^{-x} represent action of the gauge transformation. This formal trick guarantees proper order of actions: the first has to be performed scaling than after that gauge

transformation. According to the assumption just above (6), we are free to make the following substitution:

$$\lambda^\alpha = a^{p-1}, \tag{22}$$

where $p \in \mathbb{R} \setminus 0$. Substituting (22) leads to the following forms of (20) and (21):

$$\frac{M_F(X, \theta)}{M_0} a^n = \frac{(a)^{p(X+\theta)+\chi} - (a)^{p(-X-\theta)-\chi}}{(a)^{p(X+\theta)+\chi} + (a)^{p(-X-\theta)-\chi}} \tag{23}$$

$$\frac{M_G(X, \theta)}{M_0} a^n = \frac{(a)^{p(X-\theta)+\chi} - (a)^{p(-X+\theta)-\chi}}{(a)^{p(X-\theta)+\chi} + (a)^{p(-X+\theta)-\chi}}. \tag{24}$$

where for abbreviation, we introduce $n = \frac{\nu}{\alpha}(p-1)$. Introducing the following new variables:

$$M'_0 = a^{-n} M_0, X' = pX + \chi, \theta' = p\theta, \tag{25}$$

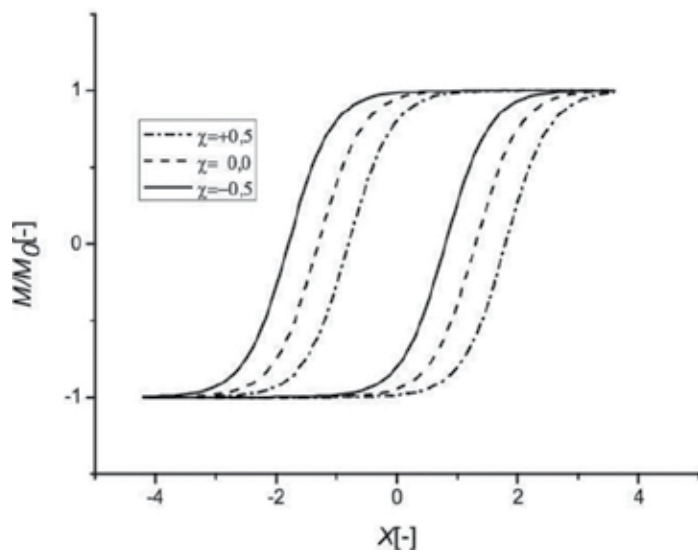


Figure 2. Magnetic hysteresis family for $a=4$, $p=1$, $n=1$, $\theta=1.3$, $\frac{\nu}{\alpha}=1$.

we derive (17) and (18), which proves the considered thesis. The initial magnetization curve (19) is invariant with respect to scaling and gauge transformation as well. The proof goes the same way as for (17) and (18). Therefore, we can formulate conclusion that the presented model

of hysteresis loop is self-similar. Below in **Figures 2–4**, we present some examples of the hysteresis loops which may suggest how to apply the scaling and gauge transformation for modelling of hysteresis phenomena.

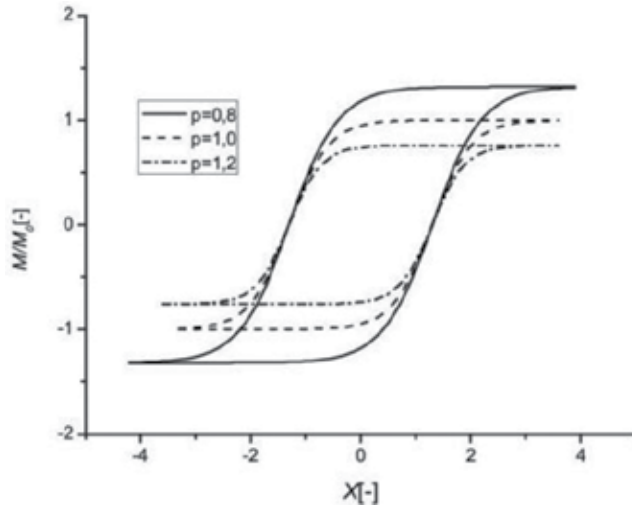


Figure 3. Magnetic hysteresis family for $a=4$, $\chi=0$, $n=1$, $\theta=1.3$, $\frac{v}{\alpha}=1$.

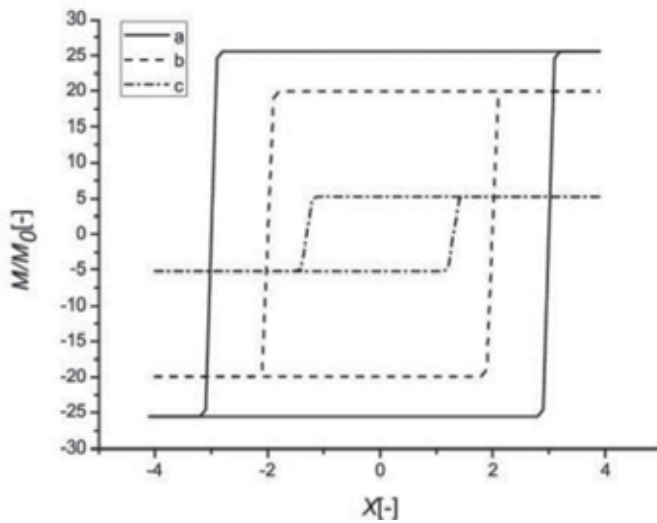


Figure 4. Magnetic hysteresis family for the following values of the model and scaling parameters: (a) $a=4$, $\theta=3$, $p=14$, $\frac{v}{\alpha}=-0.18$, $\chi=0$, (b) $a=4$, $\theta=2$, $p=13$, $\frac{v}{\alpha}=-0.18$, $\chi=0$, (c) $a=4$, $\theta=1.3$, $\chi=0$, (b) $\theta=2$, $p=13$, $\frac{v}{\alpha}=-0.18$, $\chi=0$.

Figure 2 presents how the pure gauge transformations generate a displacement of transformed loops along the horizontal axis. **Figure 3** presents compression of loops along the vertical axis under the scaling. Finally, **Figure 4** presents the loop's family for large value of the scaling parameter p . Each element of this set resembles the Preisach hysteron [6, 7].

Multi-scaling of hysteresis loop. The derived above mathematical model of the hysteresis loop is not full. There is need to extend considered model with respect to frequency, pick of induction and temperature. As we have shown the loop's model is self-similar with respect to scaling of the following magnitudes X , M_0 and θ , these are as follows: dimensionless magnetic field, amplitude of magnetization and loop's closing parameter, respectively. By introducing new independent variables, we introduce new scales and corresponding new scaling parameters [8]. We have shown in [8, 9] that it is always possible to introduce a new characteristic scale; however, one must investigate whether the considered system possesses corresponding symmetry. This can be known only from investigations of the measurement data. In the considered model, there are two places where the new variables can be implemented. These are base of the tanH() function and the loop's closing parameter θ . There are many possible combinations for configurations of the new variables in presented model which can be applied:

$$(i) \left[B_m^{\beta'} a \left(\frac{f}{B_m^{\alpha'}}, \frac{T}{B_m^{\gamma'}} \right); B_m^{\beta'} \theta \left(\frac{f}{B_m^{\alpha'}}, \frac{T}{B_m^{\gamma'}} \right) \right]; (ii) \left[B_m^{\beta} a \left(\frac{f}{B_m^{\alpha'}}, \frac{T}{B_m^{\gamma'}} \right); B_m^{\beta} \theta(-) \right]; (iii) \left[B_m^{\beta'} a \left(\frac{f}{B_m^{\alpha'}} \right); \theta(-) \right]. \quad (25a)$$

The list (25a) is not closed and can be extended as needed. We assume that $a(f, B_m, T)$ and $\theta(f, B_m, T)$ are homogenous functions in general sense. To simplify considerations, we chose for illustration the temperature less model (iii), where $\theta(-)$ is a constant. For the model of the function $a\left(\frac{f}{B_m^{\alpha'}}\right)$, we chose the square polynomial:

$$a = B_m^{\beta'} \left(\Gamma_1' \frac{f}{B_m^{\alpha'}} + \Gamma_2' \left(\frac{f}{B_m^{\alpha'}} \right)^2 \right) \quad (25b)$$

where $\alpha', \beta', \Gamma_1', \Gamma_2'$ are model constants to be calculated from the measurement data, whereas the B_m pick of induction is correlated with X_{min} and X_{max} . Formulae (25b), (14) and (15) constitute frequency- and pick of induction-dependent loop model.

Equivalence classes and partitioning [10]. Transformation formulae (25) enable us to investigate algebraic structure of all the transformations which are composed of scaling and gauge transformation. Therefore, the whole set of p and the multiplication constitute $\mathcal{G}_p = \{\mathbb{R} \setminus \{0\}, \cdot\}$ group. Moreover, $\forall a > 0$ and $\forall \frac{v}{\alpha} \neq 0$, the following expression $a^{(1-p)\frac{v}{\alpha}}$ represents an infinite number of groups being isomorphic to \mathcal{G}_p . Gauge transformations $\chi \in \mathbb{R}$ and the addition constitute $\mathcal{G}_\chi = \{\mathbb{R}, +\}$ group. Each of revealed group possesses the own representation space. \mathcal{G}_p group operates in the spaces generated by X , θ and M_0 and \mathcal{G}_χ group operates in the space

spanned by X variable. The considered model of loop reveals a combination of \mathcal{G}_p and \mathcal{G}_χ which operates in space generated by (X, θ) pair. Therefore, total symmetry of the considered model can be presented in the following matrix representation (26):

$$\begin{bmatrix} p & 0 & 0 \\ 0 & a^{(1-p)\frac{v}{\alpha}} & 0 \\ 0 & 0 & p \end{bmatrix} \begin{bmatrix} X \\ M_0 \\ \theta \end{bmatrix} + \begin{bmatrix} \chi \\ 0 \\ 0 \end{bmatrix} = \begin{bmatrix} X' \\ M'_0 \\ \theta' \end{bmatrix}. \quad (26)$$

Therefore, the total symmetry of the considered group has got the structure of the following semi-direct product $\mathcal{G}_G = (\mathcal{G}_p \times \mathcal{G}_{p'} \times \mathcal{G}_p) \ltimes \mathcal{G}_{\chi,0,0}$, where $p' = a^{(1-p)\frac{v}{\alpha}}$ represents isomorphic mapping $\mathcal{G}_p \rightarrow \mathcal{G}_{p'}$. Let V_h be space of the all hysteresis' models represented by (14) and (15). Group element $g_{p,p',p,\chi} \in \mathcal{G}_G$ is automorphism in V_h if $\forall v \in V_h$ yields $g_{p,p',p,\chi} v \in V_h$. Set of the all automorphisms \mathbf{G}_A

constitutes automorphism group, where $\mathcal{G}_A \subset \mathcal{G}_G$. Let us distinguish the loop $v_1 = \begin{bmatrix} X_1 \\ M_{01} \\ \theta_1 \end{bmatrix} \in V_h$, and

relate v_1 with v_2 :

$$v_1 \mathcal{R} v_2, \quad (26a)$$

where \mathcal{R} means the binary relation given by (26).

Definition:

Equivalence binary relation on a set $V(h)$ is a relation, which is reflexive, symmetric and transitive [11]. Due to the group structure of \mathcal{G}_G , (26a) satisfies these conditions and \mathcal{R} is equivalence relation.

Let \mathcal{R} be an equivalence relation on V_h , then $E_{v_1} \subset V_h$ containing all elements $v_2 \in V_h$ satisfying (26a) is called the equivalence class of v_1 . The sets E_{v_i} are pairwise disjoint, that is $E_{v_i} \cap E_{v_j} = \emptyset$ if $v_i \neq v_j$. Union of the all equivalence classes is the V_h space: $\cup_{v_i} E_{v_i} = V_h$. What practical use one may have from equivalence relations and partitioning. Let us assume the following $v_1 \mathcal{R} v_2$ relation, and then there exists a group element which relates both loops means that they are equivalent. However, in the opposite case, the two loops do not belong to a common class and then they are relevantly different from the algebra point of view.

3. Losses scaling in soft magnetic materials

Density of the total power losses in magnetic materials under variable magnetic field is due to eddy currents generated in the material. These may be generated for various scales of dimen-

sions: currents caused by Barkhausen jumps, what leads to a dependence $P_{hys} \propto (B^{1.6} f)$ [11], currents around moving domain walls $P_{exc} \propto (Bf)^{\frac{3}{2}}$ [12] and currents in the whole material volume $P_{clas} \propto (Bf)^2$ [11]. All of the aforementioned dependencies obey a power law, however, with a diverse value of exponents [13]. Therefore, one cannot talk about universality of the presented above formulae. However, certain universality of the power losses data of soft magnetic materials has been derived by applying the scaling. The proposed approach has been based on assumption that the density of the total power loss in soft magnetic materials was self-similar like intermittency of fully developed turbulent flow [1]. Moreover, using simple model of hysteresis loop (14), (15) and assuming semi-static conditions, we derive the following formula for the total power loss [14]:

$$P_{tot} = f\mu_0 M_0 h a^{-n} \ln\left(\frac{(a^{2(p\theta+pX_{max}+\chi)+1})}{(a^{2(pX_{max}+\chi)+2p\theta})}\right) \cdot \frac{(a^{2(pX_{min}+\chi)+a^{2p\theta}})}{(a^{2(p\theta+pX_{min}+\chi)+1})} (p \cdot \ln(a))^{-1}. \quad (26b)$$

In case of the symmetric extrema of magnetic field $X_{min} = -X_{max}$, (26b) gets the following form:

$$P_{tot} = 4\theta f \mu_0 M_0 h a^{-n}. \quad (26c)$$

where a , $n = \frac{\nu}{\alpha}(p-1)$, $h = \frac{H}{X}$, θ and M_0 are the hysteresis loop parameters and μ_0 is the permeability of free space.

According to (26c), the formula for P_{tot} is monomial which is always self-similar mathematical expression. This theoretical result confirms experimental observations concerning homogeneity of P_{tot} in soft magnetic materials.

Let us assume that the density of the total power losses is homogenous function in general sense (6). Let $P_{tot}(f, B_m)$ be density of the total power losses, where f and B_m are frequency and the pick of magnetic induction of flux waveform. Applying (6) for the two independent variables, we derive the most general form for P_{tot} :

$$P_{tot}(f, B_m) = B_m^\beta F(B_m^{-\alpha} f), \quad (27)$$

where α and β are scaling exponents and $F(\cdot)$ is an arbitrary function. These three unknown magnitudes have to be determined from experimental data. As the simplest approach to estimation of $F(\cdot)$, we have applied the Maclaurin expansion of (27):

$$P_{tot}(f, B_m) = B_m^\beta (\Gamma^{(1)}(B_m^{-\alpha} f) + \Gamma^{(2)}(B_m^{-\alpha} f)^2). \quad (28)$$

where $\Gamma^{(k)} = \frac{1}{k!} \Gamma^{(k)}(0)$. Since the total losses vanish for $f = 0$ or for $B_m = 0$, the constant term of expansion (28) equals zero.

3.1. Measurement data

The measurement of density of total power losses was carried out following the IEC Standards (60404-2, 60404-6). During measurements, the shape factor of secondary voltage was equal to $1.111 \pm$ per cent. Extended uncertainty of obtained measurements was equal to about 0.5%. The measurements covered the three following classes of soft magnetic materials:

- Crystalline materials;
- Amorphous alloys, Co-based and Fe-based; and
- Nanocrystalline alloy.

Density of total power losses was measured as a function of the maximum induction $B_m \in [0.1 (T), 1.8(T)]$ at fixed values of $f \leq 400 (Hz)$. Samples of conventional crystalline materials were strips, whereas the remaining ones had the shape of cylinder.

3.2. Estimation of expansion parameters (28) from measurement data

Magnetic materials	$\alpha(-)$	$\beta(-)$	$\Gamma^{(1)}(m^2 T^{(\alpha-\beta)} / s^2)$	$\Gamma^{(2)}(m^2 T^{(2\alpha-\beta)} / s)$
GO-3% Si-Fe	-2.16	-1.19	12.78×10^{-3}	37.68×10^{-6}
$Co_{71.5}Fe_{2.5}Mn_2Mo_1Si_9B_{14}$	-1.55	-0.35	2.88×10^{-3}	1.90×10^{-6}
$Fe_{73.5}Cu_1Nb_3Si_{13.5}B_9$	-1.81	-0.70	0.17×10^{-3}	0.71×10^{-6}

Table 2. Values of scaling exponents α , β and values of amplitudes $\Gamma^{(k)}$.

Firstly, the initial values of exponents α , β and amplitudes $\Gamma^{(k)}$ were assumed and differences between all measurement values of density of total power losses and values of density of total power losses obtained from expansion (28) were calculated. Next, the Chi^2 function was optimized. Constraint of normal distribution of error was applied. Results of optimization for exponents α , β and amplitudes $\Gamma^{(k)}$ for chosen magnetic materials are given in **Table 2**.

The results, that is scaled values of the measurement data and the values obtained from the mathematical model, for the chosen magnetic materials, are shown in **Figures 5–7**, in the $\frac{P_{tot}}{B_m^\beta} / \frac{f}{B_m^\alpha}$ coordinates system. Based on the all results concerning the density of total power losses, the universal relationship between the scaling exponents α and β was stated. This relation is of the following form [15]:

$$\beta = 1.35\alpha + 1.75, \quad (29)$$

See also **Figure 8**. The origin of the relationship in (29) will be subject of further relations.

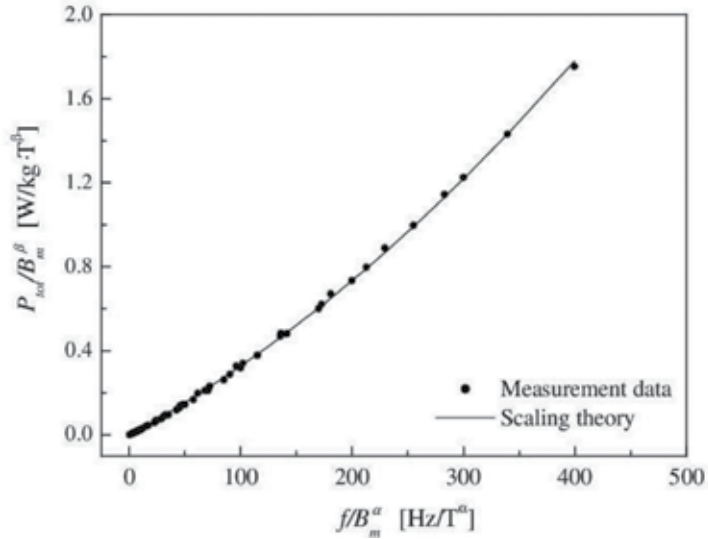


Figure 5. A comparison of measurement data of total density of power losses P_{tot} (markers) and values obtained from the scaling theory (solid line) for Co-based amorphous alloy $C_{0.71.5}Fe_{2.5}Mn_2Mo_1Si_9B_{14}$.

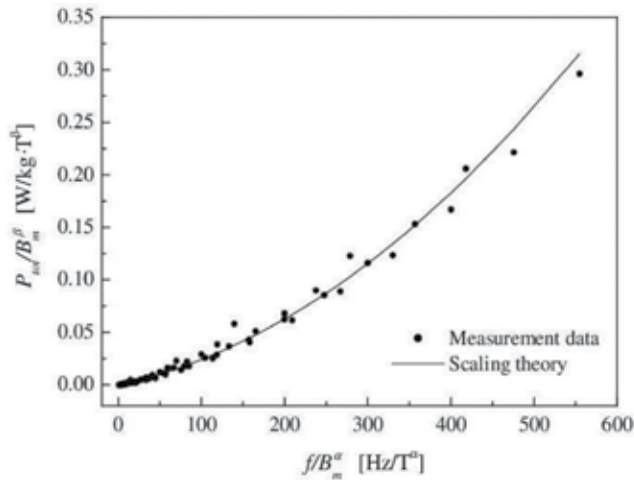


Figure 6. A comparison of measurement data of total density of power losses P_{tot} (markers) and values obtained from the scaling theory (solid line) for nanocrystalline alloy $Fe_{73.5}Cu_1Nb_3Si_{13.5}B_9$.

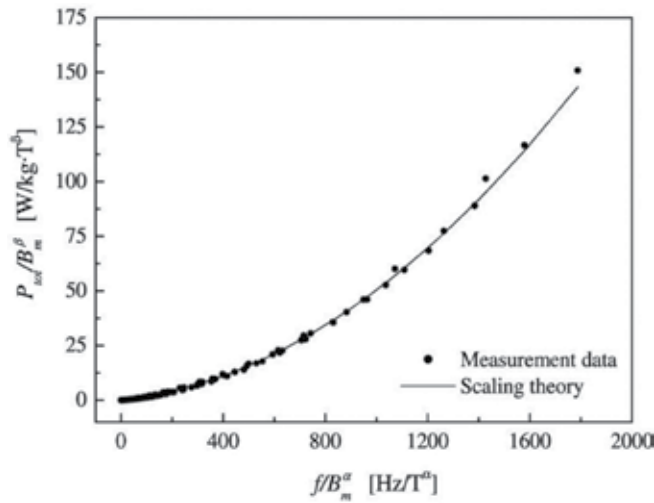


Figure 7. A comparison of measurement data for total density of power losses P_{tot} (markers) and values obtained from the scaling theory (solid line) for grain-oriented silicon steel 3% Si-Fe.

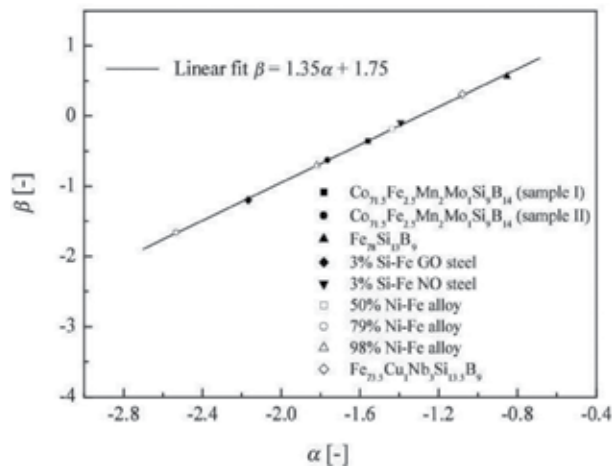


Figure 8. The universal relationship of the scaling exponents α and β . Markers correspond to estimations from experimental data, and continuous line corresponds to (29).

The three achievements resulting from scaling should be emphasized. The first one is a satisfactory agreement between the measurement data and the theoretical description. The second one is relation (29), which establishes the universal linear relationship between the scaling exponents and decreases the number of free parameters. The third achievement consists in revealing the data collapse. **Figures 5–7** are drawn in $\frac{P_{tot}}{B_m^\beta} / \frac{f}{B_m^\alpha}$ coordinates system and present the continuous sets of the losses characteristics of different values of B_m collapsed

just to a single curve. This effect is called “a single-sample data collapse” Reversible procedure $(\frac{P_{tot}}{B_m^\beta}, \frac{f}{B_m^\alpha}) \rightarrow (P_{tot}, f)$ splits the collapsed curves to separate curves for different values of B_m . This effect will be demonstrated for more complicated case (see **Figure 14**). Therefore, the scaling can be also applied as method for a compression of data. All examples in **Figures 5–7** present the single-sample data collapses. Having data for different materials and introducing for each of them are the following dimensionless magnitudes:

$$\tilde{P}_{tot} = \frac{\Gamma^{(2)}}{\Gamma^{(1)^2}} \frac{P_{tot}}{B_m^\beta}, \quad \tilde{f} = \frac{\Gamma^{(2)}}{\Gamma^{(1)}} \frac{f}{B_m^\alpha}, \quad (30)$$

We obtain the multi-sample data collapse (see **Figure 9**). These results confirm the assumption of density of total power losses scaling. Applying these transformations to (28), we derive the dimensionless low for the density of power losses in soft magnetic materials:

$$\tilde{P}_{tot} = \tilde{f} + \tilde{f}^2. \quad (31)$$

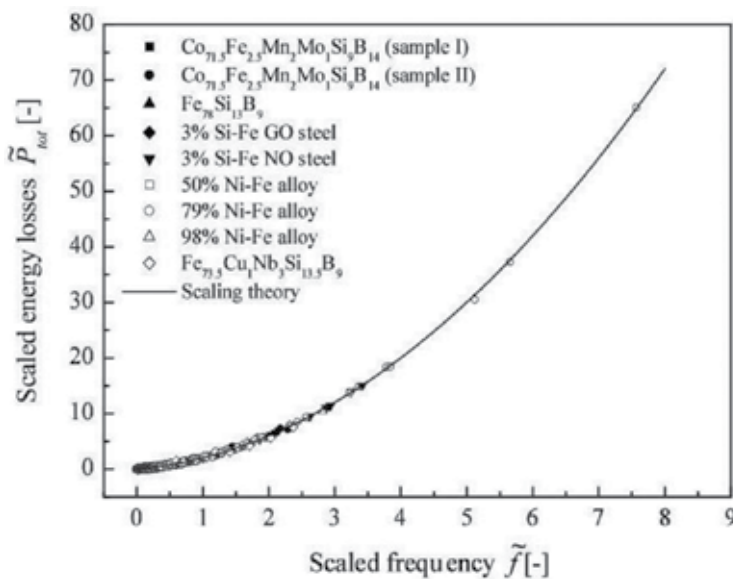


Figure 9. The multi-sample data collapse for total density of power losses \tilde{P}_{tot} (markers) and values obtained from the scaling theory (solid line).

3.3. An application of the multi-sample data collapse

Mostly, the data collapse is applying as a tool for the detection of self-similarity. Here, we present a new application which solves problem of comparison measurements taken in

different laboratories [16]. In 1995, the leading European Laboratories busy with measurements of the electrical steel magnetic properties were trying to compare the measurement results of the power loss in electrical sheet steel under the conditions of rotating and alternating flux [17]. Taking from [17] the idea of the inter-comparison of measurement data of the energy losses in soft magnetic materials, we perform such an inter-comparison with data taken in two laboratories [16, 18], however, under the conditions of axial and alternating flux. Self-similarity of the density power losses enables us to scale off the interference of the sample's geometry and the material type from the dependence of power losses versus the pick of induction and magnetizing frequencies. This property of SMM allows comparing different measurement sets. Successively, this fact allows introducing an absolute measure of uncertainty characterizing the given measurement set. Therefore, the way for assessing the uncertainty contributions would not interfere with the abovementioned data comparison. Formula (30) suits very well to the mentioned above phenomena and constitute background for solution of the presented problem.

For inter-comparison, we have selected two sets of power losses data. The first one belongs to Yuan [18] and consists of the following three sets of data: $S_1 = Fe_{76}Mo_2Si_2P_{10}C_{7.5}B_{2.5}$, $S_2 = Fe_{79.8}Mo_{2.1}Si_{2.1}P_8C_6B_2$, $S_3 = Fe_{80}Mo_1Si_2P_8C_6B_3$. The samples were thin ribbons wound into toroids. For details concerning measurement methods, we refer readers to [18]. On the basis of measured data, the parameters' values of (28) have been estimated (see **Table 3**, after [18]).

Sample	$\alpha(-)$	$\beta(-)$	$\Gamma^{(1)}(\text{m}^2\text{T}^{(\alpha-\beta)\text{s}^{-2}})$	$\Gamma^{(2)}(\text{m}^2\text{T}^{(2\alpha-\beta)\text{s}^{-1}})$
S_1	-1.533	-0.319	6.744×10^{-3}	1.322×10^{-6}
S_2	-0.364	1.259	1.412×10^{-2}	1.917×10^{-6}
S_3	-0.504	1.069	9.11×10^{-3}	3.389×10^{-6}
P_1	-2.945	-1.776	2.90×10^{-3}	4.60×10^{-6}
P_2	-1.519	-0.375	2.53×10^{-3}	6.79×10^{-6}
P_3	-3.231	-1.365	3.22×10^{-4}	1.95×10^{-7}

*The data for S_1 , S_2 and S_3 have been kindly supplied by the authors of Yuan et al. [18].

Table 3. Scaling exponents and coefficients of (28).

The second set contains some of our results [15, 19] for the power losses in the following alloys: amorphous ribbon $P_1 = Fe_{7.8}Si_{13}B_9$, Co-based amorphous alloy $P_2 = Co_{71.5}Fe_{2.5}Mn_{12}Mo_1Si_9B_{14}$ and nanocrystalline alloy $P_3 = Fe_{73.5}Cu_1Nb_3Si_{15.5}B_7$. The corresponding scaling exponents α , β and the scaling coefficients $\Gamma^{(1)}$, $\Gamma^{(2)}$ are presented in **Table 3**.

Plotting \tilde{P}_{tot} versus \tilde{f} for the all considered samples (**Figure 10**), we confirm that the data collapse takes place for the selected samples.

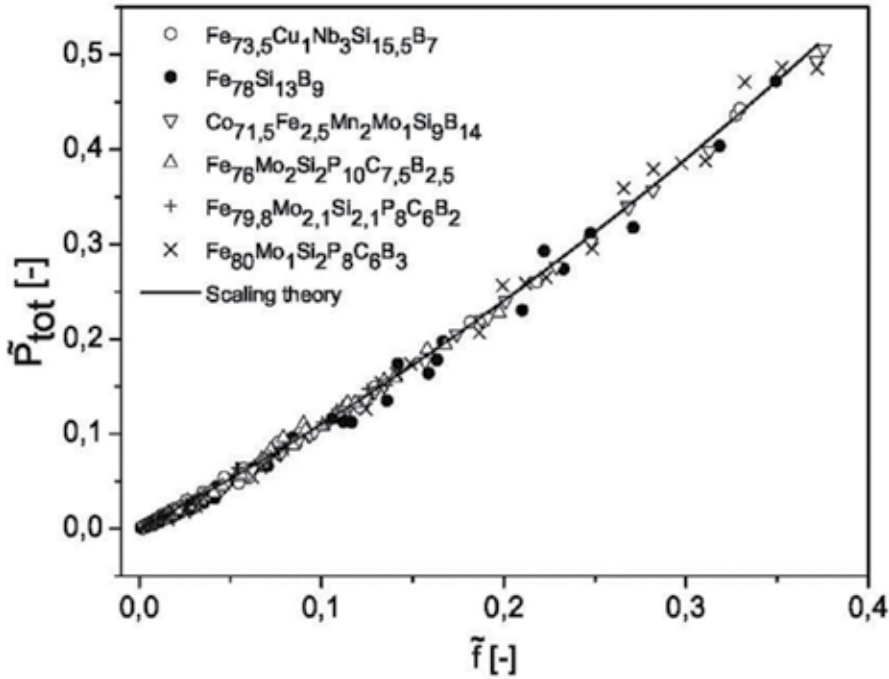


Figure 10. The data collapse for total power losses of compared materials.

Since all the magnitudes in (31) are dimensionless and the formula for \tilde{P}_{tot} is sample independent, we propose to introduce a measure of uncertainty characterizing the measurement set by the total distance of all empirical points from the scaling curve (31):

$$D = \sqrt{\frac{1}{N} \sum_{i=1}^N \left(\tilde{P}_{tot}^{exp}(\tilde{f}_i) - \tilde{P}_{tot}^{th}(\tilde{f}_i) \right)^2}, \quad (32)$$

where \tilde{P}_{tot}^{exp} , \tilde{P}_{tot}^{th} are the power losses, measured and calculated from formula (31), \tilde{f}_i is dimensionless frequency, where index i is running through the whole series of experimental data and N denotes length of the measured series. We consider the two sets of experimental data S and \mathbb{P} corresponding to different LABs. Each set consists of the three series which correspond to different samples. To create effective measure of uncertainty characterizing measurement set of the given LAB, we calculate average measure D_{av} for the three samples belonging to either of two selected sets:

$$D_{av}^2 = \sum_{i=1}^3 \frac{N_i}{N_1 + N_2 + N_3} D_i^2. \quad (33)$$

Comparisons of uncertainty measures are presented in **Table 4**.

Sample	N_i	$D_i^2(-)$	$\sqrt{D_{av}^2}(-)$
S_1	48	1.64×10^{-5}	8.11×10^{-3}
S_2	40	7.42×10^{-3}	
S_3	32	1.29×10^{-4}	
P_1	48	9.23×10^{-5}	6.53×10^{-3}
P_2	47	2.05×10^{-5}	
P_3	49	1.53×10^{-5}	

Table 4. Comparisons of uncertainty measures.

Progress in modern technologies depends on the comprehensive knowledge of material properties under standard and non-standard conditions. However, an agreed standardized method does not exist, and the reproducibility of the different methods used in different laboratories is unknown. We are of the opinion that the reason of such situation is lacking of statistical method enabling the appropriate data's inter-comparison. In this section, we have proposed a solution of this problem. As we have shown, the data collapse supplies method that enables us to introduce universal measure of uncertainty, which compares different experimental sets even based on different measurement methods. Therefore, the introduced method also can serve as a tool to compare measurement data obtained in different laboratories. The measure (33) expresses the total uncertainty characterizing the data set for the chosen range of dimensionless frequency \tilde{f} . There are four contributions to D_{av} resulting from the following: (1) uncertainty characterizing the measurement method and construction of the measurement set, (2) uncertainty of measurements of elementary magnitudes, (3) errors resulting from the approximation (28) and uncertainty of estimations of α , β , $\Gamma^{(1)}$ and $\Gamma^{(2)}$. The derived method is universal and can be applied to investigations of any phenomenon satisfying the self-similarity conditions.

4. Multi-scaling of core losses in soft magnetic materials

The application of soft magnetic materials in electronic devices requires knowledge of the losses under different excitation conditions: sinusoidal and non-sinusoidal flux waveforms of different shapes, with and without DC bias. Scaling theory allows the total power losses density to be derived in the form of a general homogeneous function, which depends on the peak to peak of the magnetic inductance ΔB , frequency f , DC bias H_{DC} and temperature T :

$$P_{tot} = F(f, \Delta B, H_{DC}, T). \quad (34)$$

The form of this function has been generated through the Maclaurin expansion with respect to scaled frequency. The parameters of the model consist of expansion coefficients, scaling exponents, parameters of DC bias mapping, parameters of temperature factor and tuning exponents. Values of these model parameters were estimated on the basis of measured data of total power density losses. However, influence of the DC bias on the self-similarity of measurement data was very relevant. In order to apply scaling to (34), the right-hand side has to be a homogeneous function in a general sense. This assumption has to be satisfied both by the experimental data and by the mathematical model. However, according to the results given in [20], Eq. (34) and measurement data are not uniform in the required sense when there is a DC bias. This problem has been solved by using the method invented by Van den Bossche and Valchev [21]. Their method consists in mapping of magnetic field into a pseudo-magnetization by using $\tanh(\cdot)$:

$$P_{tot} = F(f, \Delta B, \tanh(H_{DC} \cdot c_0), T). \quad (35)$$

Following Bossche and Valchev, we have applied series of the mappings as expansion coefficients for modelling $F(\cdot, \cdot, \cdot, \cdot)$ function of (35):

$$H_{DC} \rightarrow [M_0, M_1, M_2, M_3]. \quad (36)$$

where $M_i = \tanh(H_{DC} c_i)$, where c_i are expansion coefficients, to be determined from measurement data. Therefore, applying definition for the homogeneous function in general sense, we have formulated the following scaling hypothesis: $\exists \{a, b, c, d, g\} \in \mathbb{R}^5 : \forall \lambda \in \mathbb{R}_+$ yields: $P_{tot}(\lambda^a f, \lambda^b(\Delta B), \lambda^c [M_0, M_1, M_2, M_3], \lambda^d T) = \lambda^g P_{tot}(f, \Delta B, [M_0, M_1, M_2, M_3], T)$. Substituting the following $\lambda = (\Delta B)^{-1/b}$, we derive the most general form for P_{tot} which satisfies above hypothesis:

$$P_{tot} = (\Delta B)^\beta F\left(\frac{f}{(\Delta B)^\alpha}, \frac{[M_0, M_1, M_2, M_3]}{(\Delta B)^\gamma}, \frac{T}{(\Delta B)^\delta}\right). \quad (37)$$

where $\alpha = \frac{a}{b}$, $\beta = \frac{g}{b}$, $\gamma = \frac{c}{b}$, $\delta = \frac{d}{b}$ are effective scaling exponents. $F(\cdot, \cdot, \cdot)$ is an arbitrary function of the three variables. Both the effective exponents and the F function have to be determined.

General formula (37) enables us to construct mathematical model which maps the four-dimensional space spanned by f , ΔB , DC bias and T into the one-dimensional P_{tot} space. In the first step, we separate the temperature factor $\Theta(\cdot)$:

$$F\left(\frac{f}{(\Delta B)^\alpha}, \frac{[M_0, M_1, M_2, M_3]}{(\Delta B)^\gamma}, \frac{T}{(\Delta B)^\delta}\right) = \Phi\left(\frac{f}{(\Delta B)^\alpha}, \frac{[M_0, M_1, M_2, M_3]}{(\Delta B)^\gamma}\right) \Theta\left(\frac{T}{(\Delta B)^\delta}\right). \quad (38)$$

Let us assume that $\Phi(\cdot, \cdot)$ consists of two terms which need not be independent. However, the second one is H_{DC} dependent in contrary to the first one. For both of them, we assume the Maclaurin expansions with respect to scaled frequency $f/(\Delta B)^\alpha$, which is very much suited for the Bertotti decomposition. Moreover, the first term should describe losses for $H_{DC} \rightarrow 0$, whereas the second term must vanish for this condition. The resulting expression takes the following form:

$$\Phi\left(\frac{f}{(\Delta B)^\alpha}, H_{DC}\right) = \sum_{i=1}^4 \Gamma_i \left(\frac{f}{(\Delta B)^\alpha}\right)^i + \sum_{i=0}^3 \Gamma_{i+5} \left(\frac{f}{(\Delta B)^\alpha}\right)^i \frac{\tanh(H_{DC} \cdot c_i)}{(\Delta B)^\gamma}. \quad (39)$$

Since (39) has been created by the Maclaurin expansion, all series exponents are integers. However, it may be so that the best error's minimum is obtained for fractional values of exponents. For this purposes, we introduce tuning exponents x and y :

$$\Phi\left(\frac{f}{(\Delta B)^\alpha}, H_{DC}\right) = \sum_{i=1}^4 \Gamma_i \left(\frac{f}{(\Delta B)^\alpha}\right)^{i(1-x)} + \sum_{i=0}^3 \Gamma_{i+5} \left(\frac{f}{(\Delta B)^\alpha}\right)^{(i+y)(1-x)} \frac{\tanh(H_{DC} \cdot c_i)}{(\Delta B)^\gamma}. \quad (40)$$

On the basis of some numerical test simulations, we have selected the following Padé approximant for $\Theta(\cdot)$:

$$\Theta = \left(\frac{\psi_0 + \theta(\psi_1 + \theta\psi_2)}{1 + \theta(\psi_3 + \theta\psi_4)} \right)^{1-z} \quad (41)$$

where $\theta = \frac{T + \tau}{\Delta B^\delta}$ is gauged and scaled temperature, T is measured temperature in $^\circ\text{C}$, z is tuning parameter, and ψ_i are Padé approximant coefficients. After all improvements of $F(\cdot, \cdot, \cdot)$, the final form is still homogenous function in general sense (6).

In order to perform core loss measurements, the B - H loop measurement has been evaluated as the most suitable. This technique enables rapid measurement while retaining a good accuracy. The measurement set works in the following way: two windings are placed around the core under test. Taking into account the number of secondary winding turns and the effective core cross section, the secondary winding voltage V is integrated into the core flux density B . Next taking into account the number of primary winding turns and the effective magnetic path length of the core under test, the magnetic field strength H is calculated.

Then, the total power losses per unit volume is the enclosed area of the $B-H$ loop multiplied by the frequency f . The test system consists of a power stage, a power supply, an oscilloscope and a heating chamber. It is controlled by a MATLAB program running on a PC computer under Microsoft Windows. The power stage is capable of a maximum input voltage of 450 V, output current of 25 A and a switching frequency of up to 200 kHz. The $B-H$ loop measurements have been performed for SIFERRIT. The rectangular voltage shape across the core and DC bias has been applied, while the duty cycle was 50%.

The tested core data were as follows:

- Material name: EPCOS N87
- Core shape: toroid R42
- Number of primary windings: 10
- Number of secondary windings: 5
- Magnetic path length [mm]: 354
- Cross section [mm²]: 840

The following factors influence the accuracy of measurements:

- Phase shift error of voltage and current <4%
- Equipment accuracy <5.6%
- Capacitive couplings negligible (capacitive currents are relatively lower compared to inductive currents)
- Temperature <4%.

A	β	δ	Γ_1	Γ_2	Γ_3	Γ_4	Γ_5
-11.63	-8.64	-0.179	-1.408	739.5	1253.4	4238.5	0.123
Γ_6	Γ_7	Γ_8	c_0	c_1	c_2	c_3	γ
-30.97	-51.87	-4201.4	-0.488	-2.44E-02	-0.181	0.165	0.00
T	ψ_1	ψ_2	ψ_3	ψ_4	ψ_5	x	y
7.77E-02	-0.899	2.397	14.45	-1.27E-01	0.283	0.526	0.289
z							
4.84E-02							

Table 5. The set of estimated model's parameters of (37)–(41).

T	ΔB	f	H _{DC}	P _{tot}	T	ΔB	f	H _{DC}	P _{tot}
[°C]	[T]	[kHz]	[A/m]	[Wm ⁻³]	[°C]	[T]	[kHz]	[A/m]	[Wm ⁻³]
28.1	0.395	1	8.634	4064.3	28.1	0.391	1	20.146	4469.0
28.1	0.374	1	60.634	6332.4	28.3	0.351	1	86.651	6463.6
17.7	0.398	2	7.801	9452.1	17.8	0.398	2	20.555	10663.8
18.9	0.396	2	35.583	12745.8	18.5	0.377	2	89.240	16015.6
26.2	0.400	5	6.570	21131.3	26.4	0.4	5	17.820	23110.0
26.5	0.398	5	33.230	28057.3	27.1	0.386	5	89.400	35209.8
28.4	0.401	10	5.892	41549.0	28.6	0.401	10	17.477	45257.9
28.8	0.400	10	31.820	54650.9	29.7	0.393	10	73.960	63821.6
30.8	0.386	10	105.000	64632.1	28.4	0.49	1	11.694	6611.0
28.4	0.488	1	24.299	7196.0	28.4	0.451	1	78.390	8771.6
19.1	0.497	2	10.120	15234.1	19.2	0.496	2	23.718	16781.0
19.3	0.485	2	54.630	19235.9	19.8	0.475	2	76.860	20100.2
27.7	0.502	5	8.920	34634.8	27.4	0.503	5	15.020	36195.2
27.7	0.501	5	21.500	37496.6	28.6	0.496	5	47.500	41259.7
31.7	0.499	10	20.520	71226.8	32.2	0.494	10	45.040	76876.5
32.6	0.487	10	67.140	80858.2	28.5	0.588	1	14.420	10042.9
28.7	0.561	1	57.970	11239.6	28.7	0.541	1	78.080	11255.7
29.1	0.580	2	12.820	19689.9	28.7	0.576	2	54.360	22043.0
30.1	0.592	5	42.400	52126.7	31.1	0.599	10	10.290	92648.6
31.3	0.595	10	31.230	96446.4	28.9	0.684	1	22.050	14150.5
28.1	0.389	1	33.507	5358.8	28.4	0.346	1	91.066	6376.4
18.2	0.386	2	68.034	15049.1	18.7	0.367	2	110.590	16027.7
26.8	0.394	5	58.800	32614.3	27.5	0.386	5	97.779	35945.6
29.2	0.396	10	61.172	62814.4	30.2	0.387	10	99.190	64410.1
28.3	0.473	1	54.300	8296.5	28.5	0.443	1	85.100	8702.4
19.7	0.480	2	68.360	20073.3	20.2	0.469	2	87.440	20547.5
28.1	0.500	5	31.420	39530.2	31.5	0.499	10	7.570	65879.7
27.3	0.501	5	15.030	36194.3	28.5	0.58	1	36.010	10790.0
28.7	0.586	2	33.490	21002.2	30.2	0.616	5	36.050	54344.9
34.7	0.586	10	61.250	96583.3	29.0	0.669	1	41.330	14417.5

Table 6. Selected 60 records of the measurement data of SIFERRIT N87.

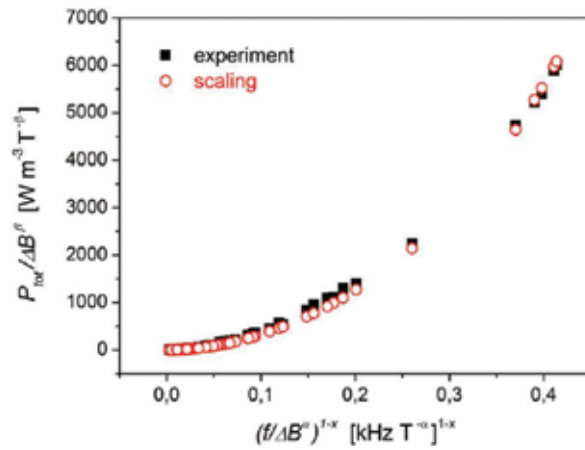


Figure 11. Projection of the measurement points and the scaling theory points (38)–(41) in $((\frac{f}{\Delta B^\alpha})^{(1-x)}, P_{tot} / \Delta B^\beta)$ plane.

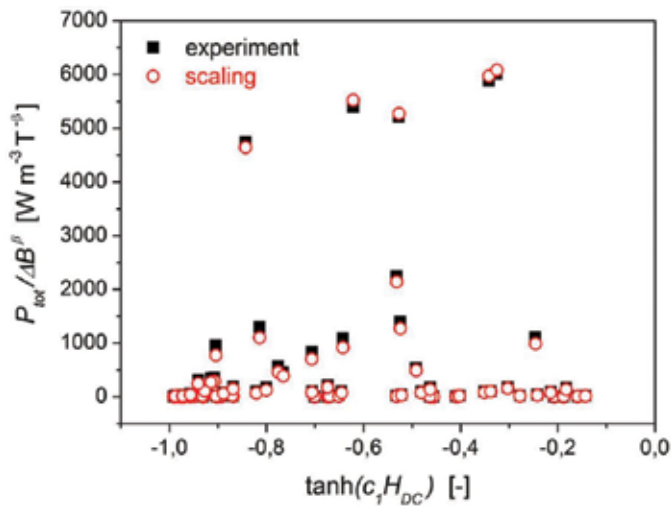


Figure 12. Projection of the measurement points and the scaling theory points (38)–(41) in $(\tanh(c_1 H_{DC}), P_{tot} / \Delta B^\beta)$ plane.

Some comments concerning temperature change/stabilization have to be done. For details of the applied measurement method and the errors of the relevant factors, we refer to [22, 24]. The parameter values of (37)–(41) have been estimated by minimizing χ^2 of our experimental data and using the simplex method of Nelder and Mead [23]. The measurement series consists of 60 points (see **Table 5**). The standard deviation per point is equal to 15 Wm^{-3} . Applying the formulae (37)–(41) and the estimated parameter values (**Table 6**), we have drawn the three scatter plots given in **Figures 11–13**, which compare estimated points those obtained through

experimentation in the three projections, respectively. Note that in order to ensure numerical stability during the estimation process, the unit of frequency was set at 1 kHz, while other magnitudes were expressed in the SI unit system.

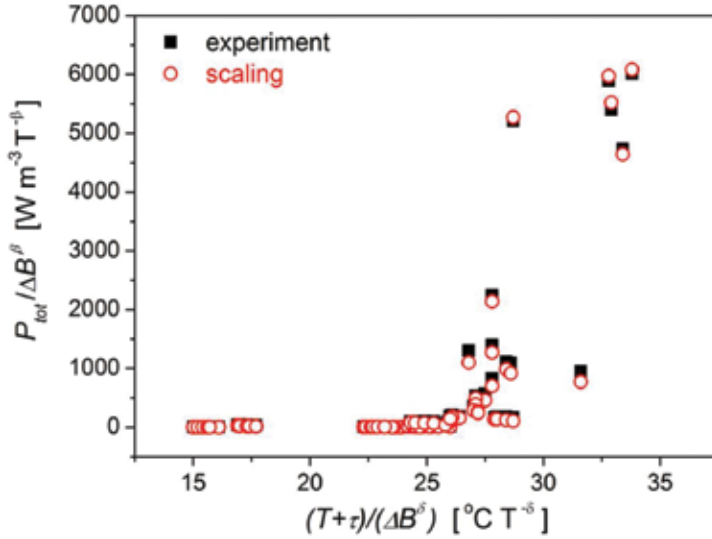


Figure 13. Projection of the measurement points and the scaling theory points (38)–(41) in $((T + \tau) / \Delta B^\delta, P_{tot} / \Delta B^\beta)$ plane.

Scaled variables $P_{tot} / (\Delta B)^\beta$ and $f / (\Delta B)^\alpha$ are very convenient for the model parameter estimations. By using these variables, the number of independent variables is reduced. Also the collapsed form of power losses characteristic is very compact and easy to implement. However, for the purpose of designing of magnetic circuits, it is necessary to have the split characteristics which describe the physical magnitude P_{tot} versus the physical ones: T , f , H_{DC} and ΔB . Note that formula (37) is suitable just for this task. Let us assume the characteristics family for the following values of the independent variables: T , f , H_{DC} and $T = 30^\circ\text{C}$, $H_{DC} = 7 \frac{\text{A}}{\text{m}}$, $\Delta B = \in \{0.4 - 0.7\}T$, and $f = \in \{0.0 - 10.0\}\text{kHz}$. Using (37) and applying (38)–(41) as well as **Table 6**, we derive the characteristics presented in **Figure 14**.

The efficiency of scaling in solving problems concerning power losses in soft magnetic material has already been confirmed in recent papers [15, 25]. However, this paper is the first one which presents an application of scaling in modelling the temperature dependence of the core losses. The presented method is universal, which means that it works for a wide spectrum of excitations and different soft magnetic materials. Moreover, the presented model formulae (37)–(41) are not closed and can be adapted for a current problem by fitting the forms of both factors Φ and Θ . Ultimately, one must say that the degree of success achieved when applying the scaling depends on the property of the data. The data must obey the scaling.

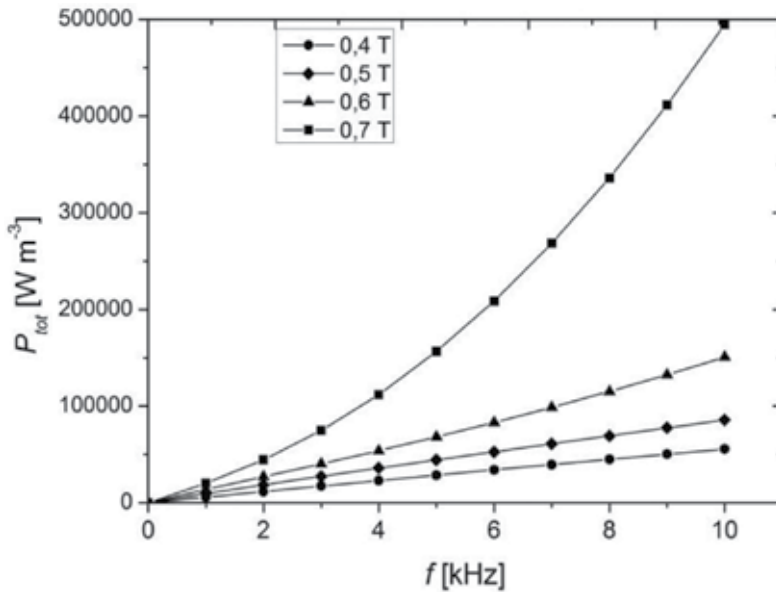


Figure 14. Family of the power losses characteristics P_{tot} versus frequency f derived for SIFERRIT N87 material for $T = 30^\circ\text{C}$, $H_{DC} = 7 \frac{\text{A}}{\text{m}}$.

5. Optimization of power losses in soft magnetic composites

Recently, novel concept of technological parameters' optimization has been applied in soft magnetic composites (SMCs) by Ślusarek et al. [26]. This concept is based on the assumption that power losses in SMC obey the scaling law. The efficiency of this approach has been confirmed in [9]. The scaling is very useful tool due of the three reasons:

- It reduces number of independent variables f and B_m to the effective one f / B_m^α ,
- Determines general form of losses of power characteristic in a form of homogenous function in general sense, and
- Determines general form of losses of power characteristics in a form of different dimensions.

Therefore, applying concept of the homogenous function in general sense, we apply the following expansion:

$$\frac{P_{tot}}{B_m^\beta} = \left(f / B_m^\alpha \right) \cdot \left(\Gamma_1 + f / B_m^\alpha \cdot \left(\Gamma_2 + f / B_m^\alpha \cdot \left(\Gamma_3 + f / B_m^\alpha \cdot \Gamma_4 \right) \right) \right). \quad (42)$$

Γ_n , α and β parameters have been estimated for different values of pressure and temperature [9]. For the purpose of this paper, we take into account only one family of power losses

characteristics which are presented in **Figures 15** and **16**. The corresponding estimated values of the model parameters are presented in **Table 7**. For all other details concerning SMC material and measurement data, we refer to [9]. Now we are ready to formulate the goals of this section. Main goal is to describe minimization of the power losses in SMC by using model density of power losses (42) and corresponding values of the model parameters. From the first row of **Table 7**, we can see that dimensions of the Γ_n coefficients depend on the values of α and β exponents. Therefore, the power losses characteristics presented in **Figures 15** and 16 are different dimensions. So, we have to answer the following question: Are we able to relate them in the optimization process which has been described in [9, 26]?

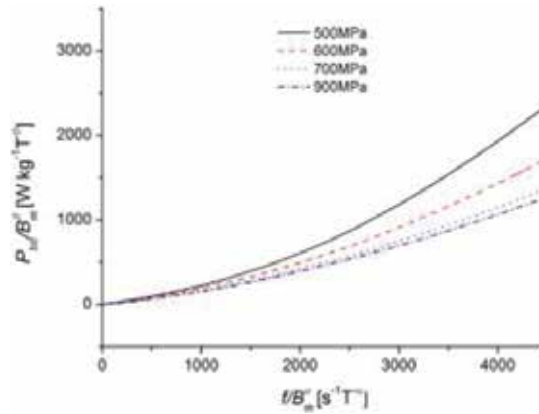


Figure 15. Selection of the power losses characteristics $P_{tot}/(B_m)^\alpha$ versus $f/(B_m)^\beta$ calculated according to (42) and **Table 1** for Somaloy 500 [26], $T = 500^\circ\text{C}$.

In this section, we show that if the considered characteristics obey the scaling, then the binary relation between them is invariant with respect to this transformation and comparison of two magnitudes of different dimensions has mathematical meaning. Reach measurement data of power losses in Somaloy 500 have been transformed into parameters of (42) versus hardening temperature and compaction pressure (**Table 7**) in [26]. Information contained in this table enables us to infer about topological structure of set of the power losses characteristics and finally to construct pseudo-state equation for SMC and derive new algorithm for the best values of technological parameters.

Scaling of binary relations. Let the power losses characteristic has the form determined by the scaling (27). It is important to remain that α and β are defined by initial exponents a , b and c (see after formula (27)):

$$\alpha = \frac{a}{b}; \beta = \frac{c}{b}. \quad (43)$$

Let us concentrate our attention at the point on the $\frac{f}{B_m^\beta}$ axis of **Figures 15** or **16**:

$$\frac{f}{B_m^\alpha} = \frac{f_1}{B_{m1}^{\alpha_1}} = \frac{f_2}{B_{m2}^{\alpha_2}} = \frac{f_3}{B_{m3}^{\alpha_3}} = \frac{f_4}{B_{m4}^{\alpha_4}} \quad (44)$$

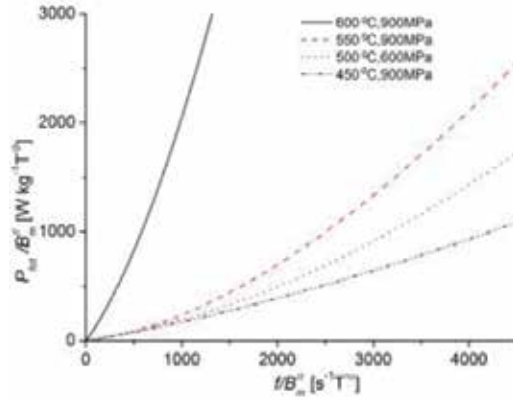


Figure 16. Selection of the power losses characteristics $P_{tot}/(B_m)^\alpha$ versus $f/(B_m)^\alpha$ calculated according to (42) and Table 1 for Somaloy 500 [26].

Let us take into account the two characteristics and let us assume that

$$\frac{P_{tot1}}{B_{m1}^{\beta_1}} > \frac{P_{tot2}}{B_{m2}^{\beta_2}} \quad (45)$$

T	p	α	β	Γ_1	Γ_2	Γ_3	Γ_4
[°C]	[MPa]	[-]	[-]	[m ² s ⁻² T ^{$\alpha-\beta$}]	[m ² s ⁻¹ T ^{$2\alpha-\beta$}]	[m ² T ^{$3\alpha-\beta$}]	[m ² s T ^{$4\alpha-\beta$}]
500	500	-1.312	-0.011	0.171	3.606×10^{-5}	1.953×10^{-8}	-2.255×10^{-12}
500	600	-1.383	-0.125	0.153	3.328×10^{-5}	9.254×10^{-8}	-1.177×10^{-12}
500	700	-1.735	-0.517	0.156	2.393×10^{-5}	2.309×10^{-8}	-8.075×10^{-14}
500	900	-1.395	-0.082	0.101	6.065×10^{-5}	-8.031×10^{-8}	7.877×10^{-13}
400	800	-1.473	-0.28	0.183	1.347×10^{-5}	3.689×10^{-9}	1.185×10^{-13}
450	800	-1.596	-0.123	0.145	2.482×10^{-5}	-1.218×10^{-9}	6.120×10^{-14}
550	800	-2.034	-1.326	0.106	1.407×10^{-4}	-1.066×10^{-8}	4.541×10^{-13}
600	800	-1.608	-0.232	1.220	8.941×10^{-4}	-5.302×10^{-8}	1.664×10^{-11}

Values of scaling exponents and coefficients of (42) versus compaction pressure and hardening temperature, a selection from [26].

Table 7. Somaloy 500.

Therefore, the considered binary relation is the strong inequality and corresponds to natural order presented in **Figures 15** and **16**. The most important question of this research is whether (45) is invariant with respect to scaling:

$$\frac{P'_{tot1}}{B_{m1}^{\beta_1}} > \frac{P'_{tot2}}{B_{m2}^{\beta_2}}. \quad (46)$$

Let $\lambda > 0$ be an arbitrary positive real number. Then, the scaling of (46) goes according to the following algorithm:

- Let us perform the scaling with respect to λ of all independent magnitudes and the dependent one:

$$f'_i = \lambda^{a_i} f_i; B'_{mi} = \lambda^b B_{mi}; P'_{tot} = \lambda^{c_i} P_{tot}, \quad (47)$$

where $i = 1, 2 \dots 4$ labels the considered characteristics.

- Substituting appropriate relations of (47) to (48), we derive:

$$\frac{P'_{tot1}}{B_{m1}^{\beta_1}} \lambda^{c_1 - b_1 \beta_1} > \frac{P'_{tot2}}{B_{m2}^{\beta_2}} \lambda^{c_2 - b_2 \beta_2}. \quad (48)$$

- Collecting all powers of λ on the left-hand side of (48) and taking into account (43) we derive that the resulting power has to be equal zero:

$$\lambda^{c_1 - b_1 \beta_1 - c_2 + b_2 \beta_2} = 1. \quad (49)$$

Therefore, (45) is invariant with respect to scaling. This binary relation has mathematical meaning and constitutes the total order in the set of characteristics.

Binary equivalence relations. The result derived in subsection **Scaling of binary relations** can be supplemented with the following binary equivalence relation. Let

$$X_{i,j} = \left(\frac{f_{i,j}}{B_{mi,j}^{\alpha_i}}, \frac{P_{toti,j}}{B_{mi,j}^{\beta_i}} \right) \quad (50)$$

be the j th point of the i th characteristic. Two points, j and k , are related if they belong to the same i th characteristic:

$$X_{i,j} \mathbf{R} X_{i,k}. \quad (51)$$

Theorem: \mathbf{R} is equivalence relation. (The proof is trivial and can be done by checking out that the considered relation is reflexive, symmetric and transitive.) Therefore, \mathbf{R} constitutes division of the positive-positive quarter of plane spanned by (50). The characteristics do not intersect each other except in the origin point which is excluded from the space. The result of this section implies that the power losses characteristics (27) and (42) are invariant with respect to scaling. Structure of derived here the set of all characteristics of which some examples are presented in **Figures 15** and **16** enable us to derive a formal pseudo-state equation of SMC. This equation constitutes a relation of the hardening temperature, the compaction pressure and a parameter characterizing the power losses characteristics corresponding to the values of these technological parameters. Finally, the pseudo-state equation will improve the algorithm for designing the best values of technological parameters.

Pseudo-equation of state for SMC. Let C is set of all possible power losses characteristics in considered SMC. Each characteristic is smooth curve in $[f/(B_m)^\alpha, P_{tot}/(B_m)^\beta]$ plane which corresponds to a point in $[T, p]$ plane. In order to derive the pseudo-state equation, we transform each power losses characteristic into a number V corresponding to (T, p) point. By this way, we obtain a function of two variables:

$$(T, p) \rightarrow V. \tag{52}$$

This function must satisfy the following condition. Let us concentrate our attention at the two following points:

$$\frac{f_1}{B_{m1}^{\alpha_1}} = \frac{f}{B_m^\alpha}, \frac{f_2}{B_{m2}^{\alpha_2}} = \frac{f}{B_m^\alpha}. \tag{53}$$

Let us consider the two characteristics $P_{tot1}/(B_{m1})^{\beta_1}$ and $P_{tot2}/(B_{m2})^{\beta_2}$ of the two samples composed in T_1, p_1 and T_2, p_2 temperatures and pressures, respectively, while the other technological parameters such as powder compositions and volume fraction are constant. Let us assume that for (53), the following relation holds:

$$\frac{P_{tot1}}{B_{m1}^{\beta_1}} > \frac{P_{tot2}}{B_{m2}^{\beta_2}} \tag{54}$$

It results from the derived structure of that (54) holds for each value of (53). Therefore, we have to assume the following condition of sought $V(T, p)$. If the relation (54) holds for given values of temperature and pressure T_1, p_1, T_2, p_2 , then the following relation for $V(T, p)$ has to be satisfied:

$$V(T_1, p_1) > V(T_2, p_2). \tag{55}$$

Moreover, $V(T, p)$ has to indicate place of corresponding characteristic in the ordered set. The simplest choice satisfying these requirements is the following average:

$$V(T, p) = \frac{1}{\varphi_{\max} - \varphi_{\min}} \int_{\varphi_{\min}}^{\varphi_{\max}} \frac{P_{\text{tot}} \left(\frac{f}{B_m^\alpha} \right)}{B_m^\beta} d \left(\frac{f}{B_m^\alpha} \right), \quad (56)$$

The integration domain is common for all characteristics. We have selected the following common domain for the data presented in **Figures 15** and **16** $\varphi_{\min} = 0$, $\varphi_{\max} = 4000$ ($\text{s}^{-1} \text{T}^{-\alpha}$).

Using (42), we transform (56) to the working formula for the V we measure:

$$V(T, p) = \frac{1}{\varphi_{\max} - \varphi_{\min}} \int_{\varphi_{\min}}^{\varphi_{\max}} x \left(\Gamma_1 + x(\Gamma_2 + x(\Gamma_3 + x\Gamma_4)) \right) dx. \quad (57)$$

T	p	V
[K]	[MPa]	[W kg ⁻¹ T ^{-β}]
723.15	800	40.60
773.15	900	43.75
773.15	700	47.25
673.15	800	50.30
773.15	600	57.12
823.15	800	81.50
773.15	500	89.28
742.15	764	492.3
753.15	780	509.2
804.15	764	528.5
711.15	764	547.0
873.15	800	720.0

Table 8. V measure versus hardening temperature and compaction pressure.

where $x = \frac{f}{B_m^\alpha}$ and Γ_i are coefficients dependent on T and p (see **Table 7**). The values of $V(T, p)$ are tabulated in **Table 8**. **Table 8** enables us to draw pseudo-isotherm. It is presented in **Figure 17**. However, in order to derive the complete pseudo-state equation, we must create a mathematical model. On the basis of **Figure 17**, we start from the classical gas state equation as an initial approximation:

$$\frac{p \cdot V}{k_B \cdot T} = 1. \quad (58)$$

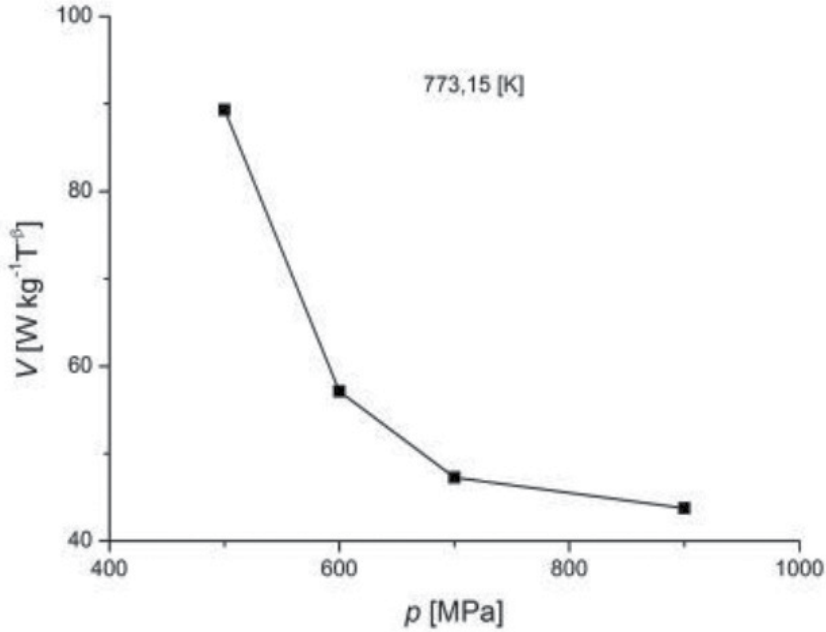


Figure 17. Pseudo-isotherm $T = 500^\circ\text{C}$ of the low-losses phase, according to data of **Table 8**, for Somaloy 500 [1].

where k_B is the pseudo-Boltzmann constant.

In order to extend (58) to a realistic equation, we apply again the scaling hypothesis (27):

$$V\left(\frac{T}{T_c}, \frac{p}{p_c}\right) = \left(\frac{p}{p_c}\right)^\gamma \Phi\left(\frac{\frac{T}{T_c}}{\left(\frac{p}{p_c}\right)^\delta}\right). \quad (59)$$

where $\Phi(\bullet)$ is an arbitrary function to be determined. Parameters γ , δ and T_c , p_c are scaling exponents and scaling parameters, respectively, to be determined. For our conveniences, we introduce the following variables:

$$\tau = \left(\frac{T}{T_c} \right); \quad \pi = \frac{p}{p_c}; \quad X = \frac{\frac{T}{T_c}}{\left(\frac{p}{p_c} \right)^\delta} = \frac{\tau}{\pi^\delta}. \quad (60)$$

In order to extend (58) to a full-state equation, we apply the Padé approximant by analogy to virial expansion derived by [27]:

$$V(\tau, \pi) = \pi^\gamma \frac{G_0 + X(G_1 + X(G_2 + X(G_3 + XG_4)))}{1 + X(D_1 + X(D_2 + X(D_3 + XD_4)))}, \quad (61)$$

where $G_0, \dots, G_4, D_1, \dots, D_4$ are coefficients of the Padé approximant. All parameters have to be determined from the data presented in **Table 8**.

Estimation of parameters for pseudo-equation of state. At the beginning, we have to notice that the data collected in **Table 8** reveal sudden change of V between two points: [773, 15; 500, 0] and [742, 15; 764, 0]. This suggests existence of a crossover between two phases: low-losses phase and high-losses phase. We take this effect into account and we divide the data of **Table 8** into two subsets corresponding to these two phases, respectively. Since the crossover consists in changing of characteristic exponents for the given universality class, it is necessary to perform estimations of the model parameters for each phase separately. Minimizations of χ^2 for both phases have been performed by using MICROSOFT EXCEL 2010, where

$$\chi^2 = \sum_{i=1}^N \left(V(\tau_i, \pi_i) - \pi_i^\gamma \frac{G_0 + X_i(G_1 + X_i(G_2 + X_i(G_3 + X_i G_4)))}{1 + X_i(D_1 + X_i(D_2 + X_i(D_3 + X_i D_4)))} \right)^2. \quad (62)$$

γ	δ	T_c	p_c	G_0	G_1	G_2
1.2812	0.1715	21.622	37.729	370315315	-47752251	1734952
G_3	G_4	D_1	D_2	D_3	D_4	-
-1.3764	-678.26	170.80	6243.8	386.96	-28.699	-

Values of pseudo-state equation's parameters and the Padé approximant's coefficients of (61)

Table 9. Somaloy 500, low-losses phase.

γ	δ	T_c	p_c	G_0	G_1	G_2
1.5550	0.1810	22.949	30.197	365210688	-47714207	1762773
G_3	G_4	D_1	D_2	D_3	D_4	-
-1.3763	-683.38	170.77	5739.9	387.81	-22.514	-

Values of pseudo-state equation's parameters and the Padé approximant's coefficients of (61)

Table 10. Somaloy 500, high-losses phase.

where $N = 7$ and $N = 5$ for the low-losses and high-losses phases, respectively. **Tables 9 and 10** present estimated values of the model parameters for the low-losses and high-losses phases, respectively.

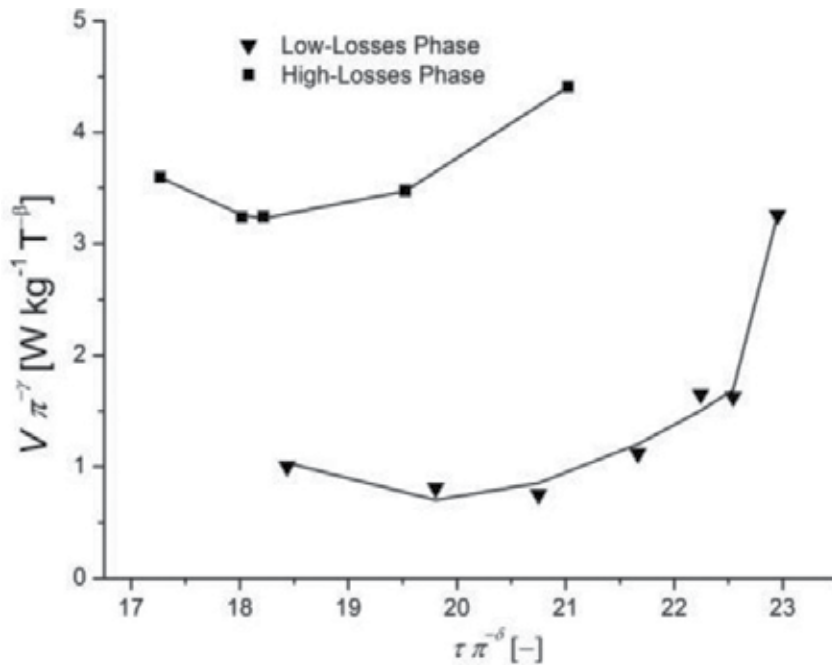


Figure 18. Phase diagram for Somaloy 500.

Optimization of technological parameters. Function $V(T, p)$ serves a power loss measure versus the hardening temperature and compaction pressure. In order to explain how to optimize the technological parameters with the pseudo-state Eq. (61), we plot the phase diagram of considered SMC **Figure 17**. Note that all losses' characteristics collapsed to a one curve for the each phase. Taking into account the low-losses phase, we determine the lowest losses at $\tau \cdot \pi^{-\delta} = 19, 75$ (see **Figure 18**). This gives the following continuous subspace of the optimal points:

$$\frac{T}{T_c} \left(\frac{p}{p_c} \right)^\delta = 19,75. \quad (63)$$

Formula (63) represents the minimal iso-power loss curve. All points satisfying (63) are solutions of the optimization problem for technical parameters of SMC. By introducing the binary relations, we have revealed twofold. The power losses characteristics do not cross each other which makes the topology's set of these curves very useful and effectively that we can perform all calculations in the one-dimensional space spanned by the scaled frequency or here in the case of pseudo-state equation in the scaled temperature. For general knowledge concerning such a topology, we refer to the paper [28]. The obtained result is the continuous set of points satisfying (63). All solutions of these equations are equivalent for the optimization of the power losses. Therefore, the remaining degree of freedom can be used for optimizing the magnetic properties of the considered SMC.

6. Scaling conception of losses separation

In this section, we show how to expand losses into polynomial series. The distinction between different eddy current scales, that is a macroscale, covering the whole bulk material and a microscale covering the area of moving domain walls, introduced by Bertotti's theory, has led to the following relationship of the three terms:

$$P_{tot} = c_1 f B_m^\beta + c_2 \sigma f^2 B_m^2 + 8\sqrt{(\sigma G S V_0)} f^{1.5} B_m^{1.5}, \quad (64)$$

where σ is conductivity, G is the constant equal to 0.1356; S is sample cross section, whereas V_0 is a parameter dependent on flux density. In general case, (64) is not homogenous expression; therefore, this can describe the self-similarity property only for $\beta=1$. However, the Bertotti interpretation of each term is correct

$$P_{tot} = P_{hys} + P_{clas} + P_{exc}. \quad (65)$$

where the presented in (65) components are hysteresis, classical and excess losses, respectively.

In this chapter, we have shown how the two-component formula for losses (28) can be transformed to dimensionless expression (30) and (31). This expression helps us to consider the data collapse. However, in the case of expansion of (27) over the square term, (31) does not apply.

Then, one can consider partial data collapses in the expansions up to necessary degree. Let us consider, for example, (42):

$$\frac{P_{tot}}{B_m^\beta} = (\Gamma_1 \cdot (f/B_m^\alpha) + \Gamma_2 \cdot (f/B_m^\alpha)^2 + \Gamma_3 \cdot (f/B_m^\alpha)^3 + \Gamma_4 \cdot (f/B_m^\alpha)^4),$$

Formula (42) is the fourth-degree polynomial of the (f/B_m^α) scaled frequency. Let us span all possible binomial subspaces:

$$\Sigma = \{S_{12}, S_{13}, S_{14}, S_{23}, S_{24}, S_{34}\},$$

where $S_{i_j} = \{(f/(B_m^\alpha))^i, (f/(B_m^\alpha))^j\}$. To consider partial data collapse in S_{12} , we perform the following transformations:

$$P_{tot1,2} = \frac{\Gamma_2 P_{tot}}{\Gamma_1^2 B_m^\beta}, f_{1,2} = \frac{\Gamma_2 f}{\Gamma_1 B_m^\alpha}. \tag{66}$$

Substituting (66) to (42), we get

$$P_{tot1,2}(f_{1,2}) = f_{1,2}(1 + f_{1,2}) + f_{1,2}^3 \frac{\Gamma_1}{\Gamma_2^2} (\Gamma_3 + f_{1,2} \frac{\Gamma_1 \Gamma_4}{\Gamma_2}). \tag{67}$$

Note that (67) is dimensionless full formula for the scaled loss. Moreover, expression $f_{12}(1 + f_{12})$ is sample independent. The linear and square terms describe the hysteresis and the classical losses, respectively. The cubic and the fourth-order terms correspond to the excess losses. Moreover, the square and linear terms describe the partial data collapse in S_{12} [29]. Using (67), one can compare losses data of different measurements projected on S_{12} subspace. The analogical equations for the S_{34} subspace read:

$$P_{tot3,4} = \frac{\Gamma_4^3 P_{tot}}{\Gamma_3^4 B_m^\beta}, f_{3,4} = \frac{\Gamma_4 f}{\Gamma_3 B_m^\alpha}, \tag{68}$$

$$P_{tot3,4}(f_{3,4}) = f_{3,4}^3 (1 + f_{3,4}) + f_{3,4} \frac{\Gamma_2^2}{\Gamma_3^4} (\Gamma_1 + f_{3,4} \frac{\Gamma_2 \Gamma_3}{\Gamma_4}). \tag{69}$$

Sample	α	β	Γ_1	Γ_2	Γ_3	Γ_4
P1	-2.347	-1.407	2.25E-03	7.96E-06	-5.19E-09	1.76E-12
P2	-1.519	-0.375	2.53E-03	6.79E-06	-6.48E-09	2.78E-12
P4	-2.372	-1.295	1.80E-02	2.04E-05	7.68E-09	-1.37E-12
P7	-2.437	-1.401	2.28E-03	1.05E-05	3.08E-07	-8.38E-10

Table 11. Scaling exponents and expansion coefficients.

Applying (68) and (69), one can complete the data comparison by considering partial data collapse using $f_{3,4}^3(1 + f_{3,4})$ polynomial which is also sample independent. In the case of expansion (42), the comparisons performed in S_{12}, S_{34} spaces are completed. To test the presented comparison formalism, we present the following measurement data: P1—amorphous alloy $Fe_{78}Si_{13}B_9$, P2—amorphous alloy $Co_{71.5}Fe_{2.5}Mn_2Mo_1Si_9B_{14}$, P4—crystalline material-oriented electrotechnical steel shits 3% Si-Fe and P7—iron-nickel-alloy 79%Ni-Fe. Processed measurement data in the form of scaling exponents and expansion coefficients are presented in **Table 11**:

Figures 19 and **20** present the completed partial collapses for the considered problem:

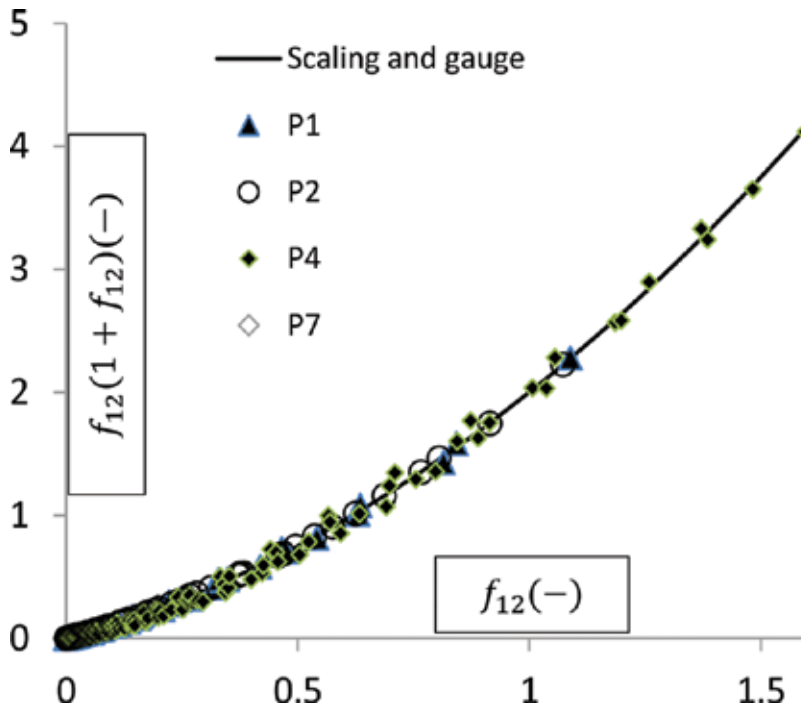


Figure 19. Partial data collapse in S_{12} space.

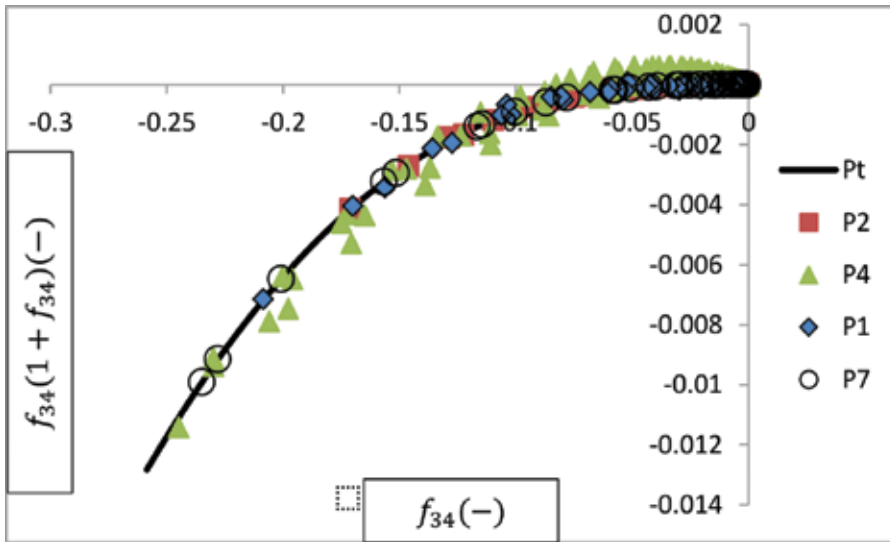


Figure 20. Partial data collapse in S_{34} space.

In order to make a numerical comparison of the measurement qualities taken from different samples, one can introduce analogically to (32) the measures of uncertainty for the both spaces S_{12} and S_{34} . The comparisons must be done and interpreted independently for S_{12} and S_{34} . Qualitative analysis on the basis of Figures 19 and 20 shows that the uncertainty measure of S_{34} for the sample P_4 is significantly high.

7. Summary

We have presented many examples of the measurements of power losses in soft magnetic materials, including composites. Moreover, working conditions were determined by multidimensional parameter space: frequency, pick of induction, DC bias and temperature. On the basis of obtained results of experimental and theoretical considerations, we confirm that the total power loss in soft magnetic materials is self-similar. This is very important for practices, since the fundamental parameter used by technologists in the processes aimed at tailoring properties of magnetic materials as well as in design and work analysis of magnetic circuits is loss density. However, there is one important detail which has to be discussed at the end. In order to determine $F(\cdot)$ in (27), the Maclaurin expansion has been applied up to the second-order term. Note that each two-term formula can be reduced to dimensionless form (28). Therefore, one could conclude that the data collapse is trivial. However, this is not so because relevance of the data collapse depends on measurement data. If data transformed by (30) get place on (31), then these data satisfy the axioms of homogeneity, they are invariant with respect to scaling as well as they are self-similar. What to do if the two-term expansion (28) is not sufficient? Then, one should extend (28) up to sufficient polynomial order. For an example,

see (42). In general case, reduction of losses characteristic to dimensionless form is not possible. However, for comparison of different measurement data, it is possible always to perform transformation of data to dimensionless magnitudes partially in the two-dimensional subspaces (67), (69) and obtain full comparison by collecting the all independent comparisons in S_{ij} subspaces.

Author details

Krzysztof Z. Sokalski^{1*}, Barbara Ślusarek² and Jan Szczygłowski¹

*Address all correspondence to: ksokalski76@gmail.com

1 Czestochowa University of Technology, Czestochowa, Poland

2 Tele and Radio Research Institute, Warszawa, Poland

References

- [1] Barenblatt G.I. *Scaling*. Cambridge Texts in Applied Mathematics. Cambridge: Cambridge University Press; 2003. 52 p.
- [2] Hamermesh M. *Group Theory and Its Application to Physical Problems*. London: Pergamon Press; 1962. 1–30 pp.
- [3] Stanley H.E. *Introduction to Phase Transitions and Critical Phenomena*. Oxford: Clarendon Press; 1971. 78 p.
- [4] Takać J. A phenomenological mathematical model of hysteresis. *COMPEL: Int. J. Comput. Math. Electr. Electron. Eng.* 2001;20:1014–1022. doi:10.1108/EUM0000000005771
- [5] Sokalski K.Z. An approach to modeling and scaling of hysteresis in magnetic materials. Magnetization curve. *Acta Phys. Pol. A.* 2015;127:850–853. doi:10.12692/APhysPolA.127.850
- [6] Preisach F. On the magnetization phenomenon. *Z. Phys.* 1935;94:277. doi:10.1007/BF01349418
- [7] Mayergoyz I.D. *Mathematical Models of Hysteresis*. New York: Springer-Verlag; 1991
- [8] Sokalski K.Z. Modeling and Scaling of Hysteresis in Magnetic Materials. Frequency, Pick of Induction and Temperature Dependence, arXiv:1510.06635v1 [physics.gen-ph]. doi:10.13140/RG.2.1.3909.44802015-10-19T17:34:48UTC
- [9] Sokalski K.Z., Jankowski B., Ślusarek B. Binary relations between magnitudes of different dimensions used in material science optimization problems. Pseudo-state

- equation of soft magnetic composites. *Mater. Sci. Appl.* 2014;5:1040–1047. doi:10.4236/msa.2014.514107
- [10] Folders S. *Fundamental Structures of Algebra and Discrete Mathematics*. New York: John Wiley & SONS, Inc.; 1994.
- [11] Bozorth R.M. *Ferromagnetism*. New York: IEEE Magnetic Society; 1993.
- [12] Bertotti G. A general statistical approach to the problem of Eddy current losses. *J. Magn. Magn. Mater.* 1984;41:253–260. doi:10.1016/0304-8853(84)90192-6
- [13] Szczygłowski J., Kopciuszewski P., Wilczyński W., Roman A. Energy losses in Fe-based and Co-based amorphous materials. *Mater. Sci. Eng. B* 2000;75:13–16. doi:10.1016/S0921-5107(00)00376-7
- [14] Sokalski K.Z. Integral and differential dependence between losses and hysteresis in magnetic materials. 2016 (submitted to *Acta Physica Polonica a*)
- [15] Sokalski K., Szczygłowski J., Najgebauer M., Wilczyński W. Losses scaling in soft magnetic materials. *COMPEL: Int. J. Comput. Math. Electr. Electron. Eng.* 2007;26:640–649. doi:10.1108/03321640710751118
- [16] Sokalski K., Szczygłowski J. Data collapse of energy loss in soft magnetic materials as a way for testing measurement set. *Acta Phys. Pol. Ser. A* 2010;117:497–499.
- [17] Sievert J., Ahlers H., Birkfeld M., Cornut B., Fiorillo F., Hempel K.A, Kochmann T., Kedous-Lebouc A., Meydan T., Moses A., Rietto AM. European inter-comparison of measurements of rotational power loss in electrical sheet steel. *J. Magn. Magn. Mater.* 1996;160:115–118. doi:10.1016/0304-8853(96)00129-1
- [18] Yuan W.J., Liu F.J., Pang S.J., Song Y.J., Zhang T. Core loss characteristics of Fe-based amorphous alloys. *Intermetallic*. 2009;17:278–280. doi:10.1016/j.intermet.2008.07.016
- [19] Sokalski K., Szczygłowski J. Formula for energy loss in soft magnetic materials and scaling. *Acta Phys. Pol. A* 2009;115:920–924.
- [20] Sokalski K., Szczygłowski J. Core losses under DC bias condition based on scaling. 2011. PLCRC/50002437/02/1725/2011 REPORT, ABB CRACOW.
- [21] Van den Bossche A., Valchev V. Modeling ferrite core losses in power electronics. *Int. Rev. Electr. Eng.* 2006;1:14–22.
- [22] Mühlethaler J., Biela J., Kolar J.W., Ecklebe A. Improved core-loss calculation for magnetic components employed in power electronic systems. *IEEE Trans. Power Electron.* 2012;27:964–973. doi:10.1109/TPEL.2011.2162252
- [23] Nedler J.A., Mead R. A simplex method for a function minimization. *Comput. J.* 1965;7:308–313. doi:10.1093/comjnl/7.4.308

- [24] Mühlethaler J., Biela J., Kolar J.W., Ecklebe A. Core losses under the DC bias condition based on Steinmetz parameters. *IEEE Trans. Power Electron.* 2012;27:953–963. doi:10.1109/TPEL.2011.2160971
- [25] Ruszczyk A., Sokalski K.Z. Unified model of temperature dependence of core losses in soft magnetic materials exposed to non-sinusoidal flux waveforms and DC bias condition. *COMPEL: Int. J. Comput. Math. Electr. Electron. Eng.* 2001;20:1014–1023. doi:10.1108/COMPEL-11-2013-0407
- [26] Ślusarek B., Jankowski B., Sokalski K., Szczygłowski J. Characteristics of power loss in SMC a Kay for designing the best values of technological parameters. *J. Alloys. Comp.* 2013;581:699–704. doi:10.1016/j.jallcom.2013.07.084
- [27] Ree F.H, Hoover W.G. Fifth and sixth virial coefficients for hard spheres and hard disks. *J. Chem. Phys.* 1964;40:939–950. doi:10.1063/1.1725286
- [28] Egenhofer M.J. A formal definition of binary topological relationships. In: *Proceedings of the Third International Conference on Foundations of Data Organization and Algorithms (FODO)*; Paris, France. *Lecture Notes in Computer Science*, 367, (Springer-Verlag, New York, June 1989) pp. 457–472.
- [29] Sokalski K., Szczygłowski J., Wilczyński W. Scaling conception of energy loss' separation in soft magnetic materials. *Int. J. Condens. Matter Adv. Mater. Supercond. Res.* 2014;12(4):1–16. See also arXiv:1111.0939v1. doi:10.13140/2.1.2394.8489

How to Characterize Cylindrical Magnetic Nanowires

Fanny Béron, Marcos V. Puydinger dos Santos,
Peterson G. de Carvalho, Karoline O. Moura,
Luis C.C. Arzuza and Kleber R. Pirola

Additional information is available at the end of the chapter

<http://dx.doi.org/10.5772/63482>

Abstract

Cylindrical magnetic nanowires made through the help of nanoporous alumina templates are being fabricated and characterized since the beginning of 2000. They are still actively investigated nowadays, mainly due to their various promising applications, ranging from high-density magnetic recording to high-frequency devices, passing by sensors, and biomedical applications. They also represent suitable systems in order to study the dimensionality effects on a given material. With time, the development in fabrication techniques allowed to increase the obtained nanowire complexity (controlled crystallinity, modulated composition and/or geometry, range of materials, etc.), while the improvements in nanomanipulation permitted to fabricate system based either on arrays or on single nanowires. On the other side, their increased complexity requires specific physical characterization methods, due to their particular features such as high anisotropy, small magnetic volume, dipolar interaction field between them, and interesting electronic properties. The aim of this chapter was to offer an ample overview of the magnetic, electric, and physical characterization techniques that are suitable for cylindrical magnetic nanowire investigation, of what is the specific care that one needs to take into account and which information will be extracted, with typical and varied examples.

Keywords: magnetic materials, nanotechnology, cylindrical magnetic nanowires, nanoporous alumina templates, characterization techniques

1. Introduction

The continuing progress in fabrication techniques nowadays lead scientists to succeed in producing nanosystems that are always smaller, more complex, and/or fabricated with more control. This achievement is highly interesting for both fundamental studies and technological improvements, since it provides novel systems permitting to test phenomena at mankind frontiers of knowledge. However, the counterpart is that these new nanosystems also require improvements in the characterization technique field, to yield more efficient, more sensible, and sometimes up to revolutionary, characterization methods. Without the ability to adequately probe the fabricated system characteristics, they remain useless and their promised advances need to wait until the development of suitable characterization techniques.

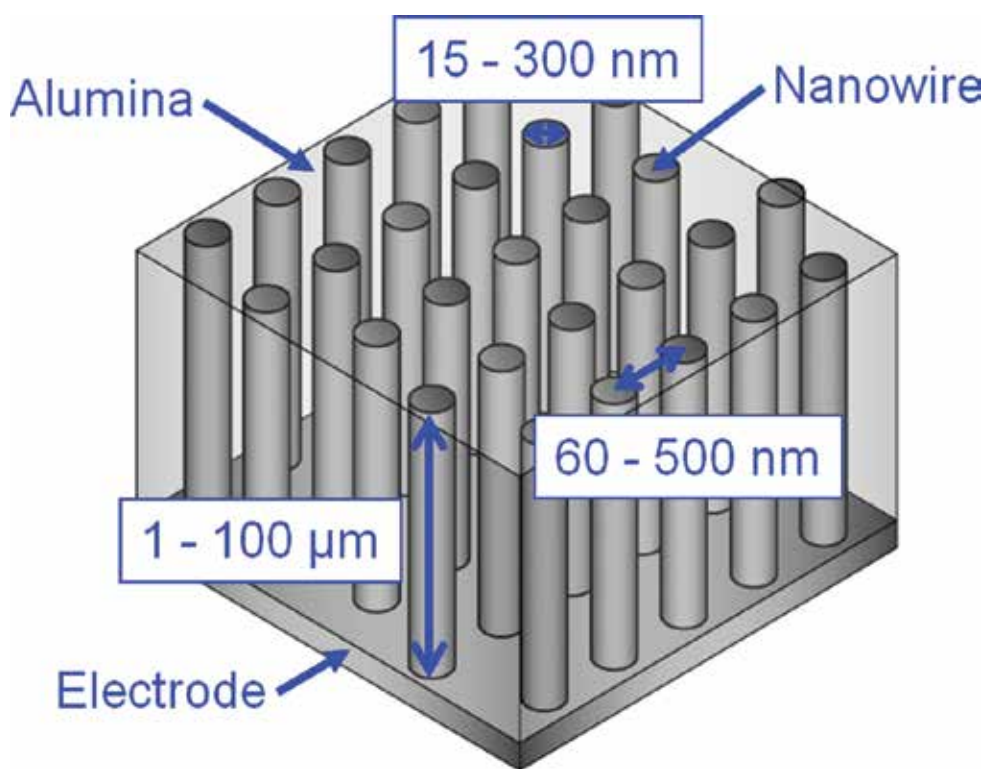


Figure 1. Representation of nanowire arrays embedded in a nanoporous alumina template. Reprinted with permission from [11]. Copyright 2010 by InTech.

Cylindrical magnetic nanowires represent a good example of the kind of nanosystems that become enabled due to a new fabrication technique. After the finding regarding how to obtain controlled nanoporous alumina templates by Masuda et al. in 1995 [1], the ordered, parallel, and with high-aspect ratio pores were quickly identified as perfect mold for electrodeposited metallic nanowires (**Figure 1**) [2–4]. Using magnetic materials, those nanowires are still actively

investigated nowadays, mainly due to their various promising applications, ranging from high-density magnetic recording [5] to high-frequency devices [6], passing by sensors [7], and biomedical applications [8]. They also represent suitable systems in order to study the dimensionality effects on a given material [9, 10]. With time, the development in fabrication techniques permitted to increase the obtained nanowire complexity (controlled crystallinity, modulated composition and/or geometry, range of materials, etc.), while the improvements in nanomanipulation permitted to fabricate systems based either on arrays or on single nanowires.

However, characterizing cylindrical magnetic nanowires presents specific challenges, due to their particular features. Among them, the small volume of a nanowire, and therefore its low magnetic signal, complicates both the manipulation of individual nanowires for their subsequent characterization and most of the single nanowire magnetic probing. It also limits the electrical current that a nanowire can support without melting, making them highly sensible to electrical discharge. Furthermore, nanowires present, by definition, a high-length/diameter ratio, typically larger than 50. This peculiar shape induces a mechanical fragility along the nanowire, thereby making its manipulation difficult and facilitating the apparition of longitudinal mechanical stress, which may interfere with their properties. From a magnetic point of view, this high-aspect ratio yields a large magnetic shape anisotropy that typically governs its magnetic behavior. Another important component influencing it is the large dipolar interaction field among nanowires when in array conformation, due to the small interdistance between them. However, this interaction field also needs to be taken into account when nanowires are free, like in solution. Finally, a last particular feature is the large nanowire surface (in comparison to its volume). It makes nanowires highly sensible to their environment, which may be an advantage, as in sensors, but can also be an issue while characterizing them (e.g., favoring the surface oxidation).

As previously stated, the magnetic nanowires' increased complexity requires specific characterizations, in order to efficiently understand their properties and behavior and take advantage of their novelty. The understanding of a magnetic system, such as magnetic nanowires, requires studying not only its magnetic behavior but also its electrical and physical properties. The emphasis on one or another aspect depends on the specific objective of the study or application. Therefore, the aim of this chapter is to offer an ample overview of the physical, electrical, and magnetic characterization techniques that are suitable for cylindrical magnetic nanowire investigation. For each method, the specific care that one needs to take into account and which information can be extracted are discussed, with typical and varied examples.

2. Physical characterization

Since magnetic properties are intrinsically linked to the system morphology, composition, and crystalline structure, they represent fundamental information while investigating magnetic nanowires. A common first step is to verify the obtained nanowire geometry by microscopy, either scanning electron microscopy (SEM) or transmission electron microscopy (TEM). Coupled to these microscopes, other spectroscopy techniques allow knowing the nanowire

composition, such as energy-dispersive X-ray spectroscopy (EDS) and electron energy loss spectroscopy (EELS). Radiation diffraction techniques yield information about the crystalline or magnetic structure and can be performed on the complete array, through X-ray, neutron, or electron diffraction, or locally on a nanowire section, with the help of a high-resolution TEM (HRTEM). Finally, phase transitions are well probed through specific heat measurements.

2.1. Geometry/morphology

As any nanostructure, nanowire fabrication often requires a visual inspection of the obtained product, before pursuing further characterization. Even if nanowires are basically long cylinders, their exact geometry (diameter, length, and interdistance in the array) directly influences their magnetic behavior. For example, their coercivity is highly sensible to their diameter, much more than to their length, while their interdistance controls the interaction field strength in the array, among others. Due to the fabrication technique used, nanowires grown in nanoporous alumina templates always exhibit a distribution, even very narrow, of their geometric parameter values. Furthermore, since nanowires are not restricted to homogeneous cylinders, their morphology also needs to be probed.

Such information can be obtained by electron microscopy techniques, due to the length scale required (less than 5-nm resolution at minimum). Scanning electron microscopy (SEM) and transmission electron microscopy (TEM) are the two best equipments for nanowire imaging. While the resolution of the first is lower, it is compensated by the facts that it is a cheaper, more widespread and easier to operate microscope.

2.1.1. Scanning electron microscopy (SEM)

SEM is a technique that enables the inspection of nanostructures by means of an electron beam guided through magnetic and electrostatic lenses. The wealth of different information that can be obtained by SEM method is caused by the multitude of signals that arise when an electron interacts with the specimen. The different types of electron scattering (backscattered, secondary, and Auger electrons) are the basis of most electron microscopy methods [12]. The widespread use of SEM became possible after 1958, when researchers from Cambridge (UK) built the first commercial prototype [13]. The typical primary electron beam used in a SEM is of 1–30 kV, with a beam current of 1 pA to 20 nA that can be focused in about 2–100-nm spot size, depending on the emitter source [14, 15]. A detailed description of the SEM operation can be found in [16].

This technique is highly adequate for proper measurements of the nanowire (and array) dimensions. Array cross-sectional view (easily obtained by simply breaking the fragile alumina template) facilitates the evaluation of geometrical parameter distribution (**Figure 2a**). Free nanowires can also be investigated, after selectively dissolving the alumina template and dispersing them on a substrate, generally Si (**Figure 2b**). Despite the relatively low resolution of SEM, it commonly allows zooming on some specific nanowire regions, such as the dendritic region at the bottom, if voltage reduction protocol described in [17] is used to thin the alumina barrier layer and allows the pores filling by electrodeposition (**Figure 2c**). Finally, the evalua-

tion of the pores-filling ratio can be completed by the top view of the array (**Figure 2d**). Additionally, as a non-destructive technique, one can inspect the nanowires along with electrical measurements, thermal annealing, or chemical reactions inside the SEM chamber [18]. However, electron beam exposure can induce hydrocarbon molecule deposition (from the vacuum chamber) on the scanned nanowire surface, leading to some contamination [19]. This can be avoided by reducing the beam current and exposure time over the surface [15].

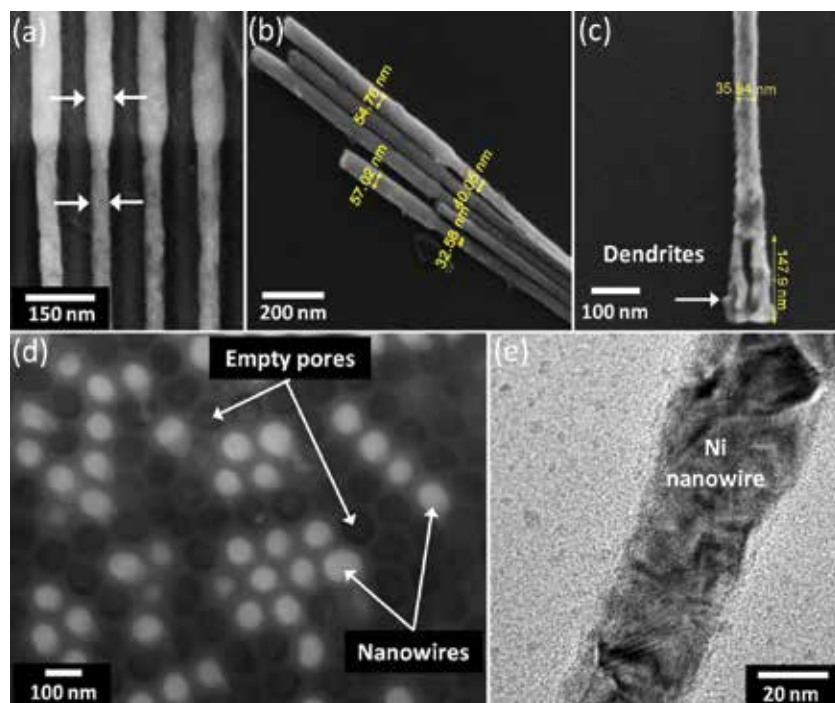


Figure 2. (a–d) SEM images of Ni nanowires with modulated diameter fabricated through the three-step anodization technique [20]. (a) Cross-sectional view, showing the diameter modification region; (b) zoom on free nanowires upper segment; (c) zoom on the dendritic region, at the nanowire base; (d) array-top view, where the filled pores appear clearer; and (e) TEM image of a Ni nanowire region. Reprinted with permission from [21]. Copyright 2015 by IEEE.

2.1.2. Transmission electron microscopy (TEM)

In order to observe the nanowires' geometrical aspects in more detail, higher resolution images can be obtained by using TEM. In a conventional TEM, a thin specimen is irradiated with an electron beam with uniform current density. Typically, the acceleration voltage is at least 100–200 kV, while medium voltage instruments work at 200–500 kV to provide better transmission, and some equipments can reach up to 3 MV. The use of such a high voltage allows to produce a very small electron beam spot (typically <5 nm and, at best, <0.1 nm in diameter). On the other hand, strong electron/atom interactions through elastic and inelastic scattering can lead to some damages to the sample. This technique therefore requires a very thin specimen,

typically of the order of 5–100 nm for 100-keV electrons, depending on the sample material [22, 23].

Fortunately, most nanowires are thin enough in order to be directly investigated by TEM, without further preparation than dispersing free nanowires on a carbon TEM grid. Interesting morphological information that can be obtained includes surface roughness, layer interface sharpness, or even atomic plane directions, to name a few, besides more precise geometrical characterization than with a SEM (**Figure 2e**). Generally, TEM nanowire characterization is not limited to geometry and morphology but specialized in local investigation. It usually takes advantage of the high-energy electron beam to perform local spectroscopy (Section 2.2). Moreover, given the small beam diameter, large electron diffraction occurs on the sample, which reveals useful crystallographic information that will be described more in detail in Section 2.3.2. Finally, even local magnetic information can be obtained, as will be discussed in Section 4.3.2. As expected, its operation presents much more difficulties compared to SEM.

A common challenge concerning the inspection by electron microscope of nanoporous alumina membrane is the charging effects from the electron beam on the scanned area (mainly insulating). This effect can be avoided by depositing a very thin layer (<50 nm) of carbon or metal on the top surface [12, 24], whereas the dimensions of the inspected structures are larger than the metal layer thickness. However, the SEM contrast of nonconductive specimens varies widely depending on the coating metal and thickness, which influences the measurement's accuracy on the scanned structures [25]. For TEM analysis, if the charge dissipation is insufficient, as is the case for insulating materials, the sample becomes unstable under the beam and the analysis becomes impossible.

2.2. Chemical composition

Since chemical composition is not necessarily totally controlled during the nanowire fabrication, either by electrodeposition or other alumina template-filling methods, probing their chemical composition is essential. This is especially important for alloyed or multi-element nanowires, as well as for multilayered ones. In the last case, a direct visualization of the chemical composition configuration is highly helpful. This is also true for local investigation, such as for surface oxidation, for example.

Therefore, it is highly advantageous to use some features of the electron microscopes described above to simultaneously perform a composition characterization of the nanowires. Mainly, both SEM and TEM possess a high-energy electron beam, which allows high sensibility, while their scanning possibilities permit to map the chemical composition, usually superimposed to their morphology image. The typical techniques used for nanowires are the energy-dispersive X-ray spectroscopy (EDS) and the electron energy loss spectroscopy (EELS). Generally speaking, while the first determines the presence or not of an element, the second can probe their chemical environment. Both techniques can lead to a mapping of local chemical properties with high spatial resolution when coupled to a TEM, whereas EDS can also be performed in a SEM chamber.

2.2.1. Energy dispersive X-ray spectroscopy (EDS)

EDS measures the energy and intensity distribution of the X-rays generated by the impact of the high-energy electron beam on the surface of the sample (**Figure 3a**). The principle is based on the inner-shell electrons that may be excited by the incident beam, thus leaving holes in the atom's electronic shells. When these holes are filled by higher energy electrons, the energy level difference creates a released X-ray. Since its energy depends on the electronic structure of the atom, the elemental composition within the probed area can be determined to a high degree of precision. More information about the EDS technique is available in [26].

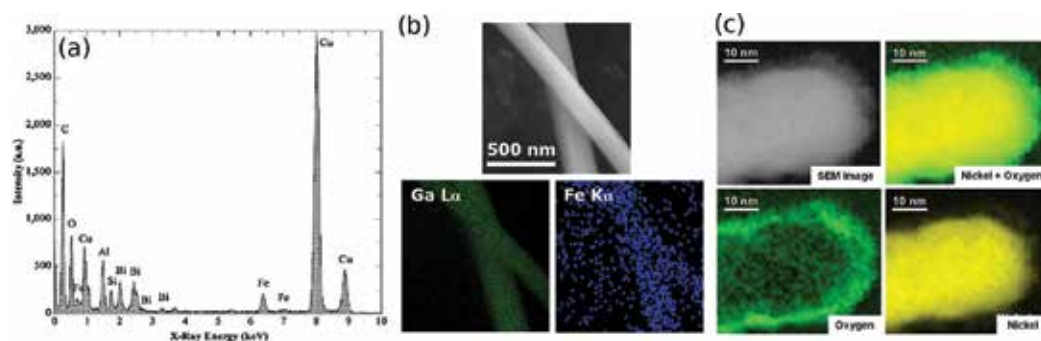


Figure 3. (a) EDS spectrum of BiFeO₃ nanowires made by sol-gel preparation into alumina template. Reprinted with permission from [10]. Copyright 2013 by Elsevier Ltd, (b) EDS composition mapping of Fe₃Ga₄ nanowires fabricated through the metallic-flux nanonucleation method. Reprinted with permission from [9]. Copyright 2016 by Nature Publishing Group, and (c) EELS analysis for the composition mapping of Ni nanowire after dissolving the alumina template. Reprinted with permission from [28]. Copyright 2013 by Brazilian Microelectronics Society.

Specifically in nanowire characterization case, EDS is particularly useful to determine their chemical composition [27], their stoichiometry, and their impurity content. As mentioned before, since EDS is a local probe, it allows focusing on the nanowires, being either free or still in the alumina array (viewed in cross section). On counterpart, EDS data from nanowires require to be analyzed keeping in mind the low material thickness. Especially for light elements, the incident electron beam may not sufficiently interact with the atoms while passing through the nanowire diameter, thus preventing the emission of the characteristic X-ray spectrum of the material. In these cases, elemental percentage cannot be determined with precision, and EDS results are limited to probe the presence or not of the elements (in concentration above the detection limit). Care should also be taken about the EDS mapping spatial resolution (**Figure 3b**). Since it depends on the size of the interaction volume, which in turn is controlled by the accelerating voltage and the mean atomic number of the sample, the spatial resolution is better while performing EDS mapping in a TEM than in a SEM, on the order of 0.5 and 10 nm, respectively.

2.2.2. Electron energy loss spectroscopy (EELS)

In order to overcome the EDS disadvantages and obtain more precise information about the material chemical composition, one can use EELS technique instead. It allows obtaining

chemical information with a better energy resolution, passing from tens of eV for EDS to around 1 eV for EELS. Moreover, the EELS spatial resolution is generally higher than the corresponding EDS experiment because the EDS data are affected by beam broadening, unless the sample is very thin [29]. However, as a main drawback, EELS represents a more difficult technique to operate.

During an EELS measurement, some incident electrons of known energy will be scattered through inelastic interactions. The detection of the energy and momentum of the scattered electrons provides information on the excitations in the sample. As in EDS, inner-shell ionizations allow to determine the material atomic composition. However, a careful analysis of the spectrum also gives access to data about the chemical environment, such as the chemical bonding and the valence-/conduction-band electronic properties, among others [30, 31]. Since EELS is based on energy losses, the spectrum identification is facilitated for sharp and well-defined excitation edges, such as exhibited by low atomic number elements. The reader interested by more information about EELS as surface analysis technique is referenced to [32].

Therefore, in addition to determine the atomic composition for nanowires including light elements, EELS nanowire characterization is commonly used to investigate their oxidation state. In this case, the EELS- and TEM-coupled results can show the nanowire surface oxidation after being released from the alumina template (**Figure 3c**), which is critical for good electrical contact, as will be explained in Section 3.2. Another EELS capacity especially useful for nanowires is the ability to locally determine the valence state of a given element in the nanowire.

2.3. Structural characterization

Nanowires are by definition highly anisotropic, due to their elongated shape. However, in addition to the induced large axial shape anisotropy, one may need to also consider the magnetocrystalline contribution to the effective anisotropy. Therefore, the crystalline texture is especially important to resolve for nanowires made of materials with non-negligible magnetocrystalline anisotropy, like Co in hexagonal-close package (hcp). In this case, the uniaxial magnetocrystalline anisotropy constant being of the same order of magnitude than the shape anisotropy of an infinite cylinder, it makes the effective anisotropy very sensitive to the nanowire texture.

Crystalline structure being, by definition, a repetitive pattern of a unit cell of atoms, the characterization techniques are based on the diffraction principle. X-ray diffraction (XRD) is the most common one and can be applied to nanowires. However, due to their small volume, the measurements require to be performed on several nanowires together, preventing to resolve local modifications of the crystalline structure along the nanowires. Substituting the incident beam from X-rays to high-energy electrons, precise local crystalline structure can be probed. Therefore, TEM chamber, through techniques such as selected area electron diffraction (SAED) and high-resolution TEM, represents an ideal environment for nanowire crystalline structure investigation.

2.3.1. X-ray diffraction (XRD)

As mentioned above, monochromatic X-rays are used in XRD technique as incident beam that will be scattered through elastic interactions with the atom electrons. For some specific scattering angles that depend on the crystalline structure, a constructive interference is obtained and detected. Careful analysis of the diffraction pattern yields the identification of the crystal symmetry and unit cell, as well as allowing characterization of more subtle aspects, such as stress and disorder in the unit cell.

X-ray diffraction is commonly used to determine the basic composition, crystalline phase, and texture of electrodeposited nanowires. Due to geometry restrictions, the XRD experiment is usually performed in the θ - 2θ mode with the scattering vector parallel to the nanowires inside the porous template, but it is also possible to remove the nanowires from the template and dispose them on a surface (such as a silicon wafer or glass) to set the scattering vector perpendicular to the nanowires. In the first geometry, only the crystalline planes perpendicular to the scattering vector contribute to the diffractogram peaks (**Figure 4a**). This particular situation yields that, besides the usual element and phase determination through their position, their relative intensity gives information about the crystalline texture, that is, the preferential grain orientation in the nanowires [33]. The XRD rocking curve technique, where the detector angle is fixed and the sample slightly tilted around a given angle, is a more powerful tool for the nanowire crystalline texture determination [34] (**Figure 4a** inset). However, due to the small volume of the electrodeposited nanowires and because they often do not completely fill the pore length, the diffractogram count can be very low and additional diffraction peaks arising from the template/substrate complicate the data analysis. Therefore, synchrotron radiation is preferred, since it leads to a higher signal coming from the nanowires.

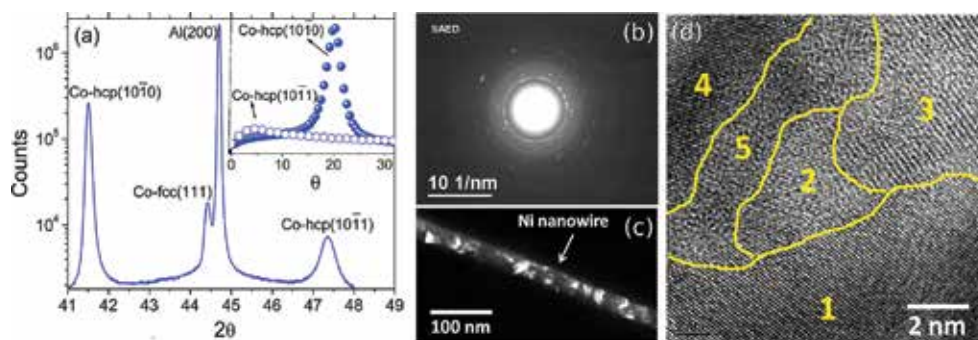


Figure 4. (a) XRD pattern of hcp/fcc bi-crystalline Co nanowires. Inset: rocking curves for two different hcp peaks. Reprinted with permission from [34]. Copyright 2015 by AIP Publishing LLC. (b–d) Structural characterization through electron diffraction of a polycrystalline Ni nanowire. Reprinted with permission from [21]. Copyright 2015 by IEEE, (b) SAED diffraction pattern, (c) dark-field TEM images, showing size distribution of planes under the same diffraction condition, and (d) HRTEM showing the crystallographic planes.

2.3.2. Electron diffraction

Another way to improve the nanowire diffraction signal is to again take advantage of the incident high-energy electron beam present in a TEM. The diffraction principle remains similar as in XRD, with the difference that it is electrons that are elastically scattered, allowing a higher resolution. Also, the diffraction is probed in transmission, instead as in reflection, yielding a pattern of bright spots indicating the constructive interference conditions. Several probing techniques are available in a TEM chamber, but due to their morphology (thin but long) and nanoscale dimensions, nanowires represent an ideal system for those.

One can perform a selected area electron diffraction (SAED) in a region as small as of a few hundreds of nanometers, which can be a specific region along a nanowire. Indexing the obtained diffraction pattern is a powerful tool to study its crystalline structure (**Figure 4b**). The very short electron wavelength (of the pm order, but with relatively low energy when compared with X-rays) gives access to a precise description of the atom's position. Additionally, one can also select a diffraction spot of SAED and enhance the contrast of the volume that contributes to that spot (**Figure 4c**). This imaging technique, called dark-field TEM, is useful to investigate planar defects, stacking faults, and grain size along individual nanowires, quickly allowing identifying repetitive crystalline pattern. Additionally, direct atomic observation is possible through a high-resolution TEM (HRTEM), to image the crystalline planes (**Figure 4d**). Therefore, by directly measuring the interplanar distances, one can determine the phase and orientation of the grains, and also estimate their size. For a brief review of SAED and HRTEM applied to nanowires, one can refer to [35].

Finally, it is noteworthy to mention that specific heat, a technique which will be explained in the next section, can also be used to indirectly investigate nanowire crystalline structure [9]. The measurement does not require removing the nanowires from the template, which can represent a great advantage. On the counterpart, one requires a bulk sample of the same material, in a crystalline structure thought as similar as in the nanowires. Specific heat measurement yields the system Debye temperature, which is related to the phonon spectrum. By comparing the Debye temperatures, it is possible to see if both phonon spectra, and therefore crystalline structures, are similar or not.

2.4. Phase transition

In certain systems, it is advantageous to explore their physical properties by means of specific heat measurements. The specific heat of a material is one of the most important thermodynamic properties denoting its heat retention or loss of capacity. Therefore, its variation with temperature or magnetic field may indicate crystalline and/or magnetic phase transitions [36]. The specific heat acquisition can be performed in a small-mass calorimeter. In one of the various measurement protocols, it is placed into the sample chamber which controls the heat added to/removed from a sample while monitoring the resulting change in temperature. During a measurement, a given quantity of heat is first applied at constant power for a fixed time, before allowing the sample to cool down during an equivalent time. Unlike other techniques that monitor magnetic transition phase, such as magnetometry, specific heat measurements can

provide important additional information on the electronic structure and crystal lattice. However, care to the extent and in the analysis of the results need to be made more cautiously.

Like bulk systems, nanowires can undergo phase transitions. Interestingly, the transition temperature and nature may be modified for nanowires, as consequences of their lower dimensionality [9, 37] (**Figure 5**). However, performing specific heat measurements on nanowires represents a challenging task, due to the requirements to remove the contributions to the signal arising from everything else than the nanowires with precision. For nanowire arrays, this means to also measure, in the same conditions, a similar (in mass and geometry) empty alumina template. Accuracy in results depends on the correct mass determination of each component, which needs to be estimated for the nanowires.

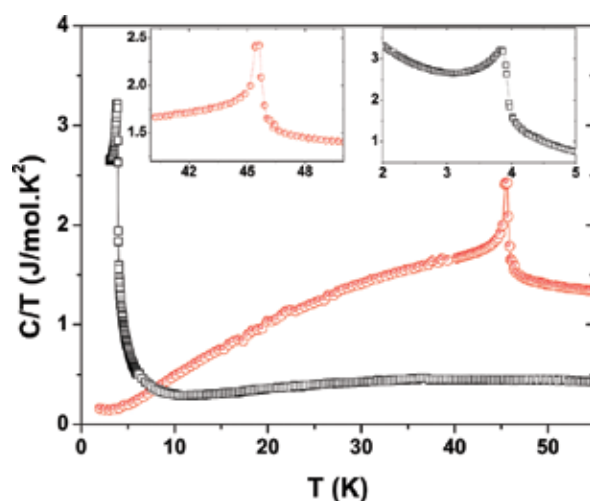


Figure 5. Specific heat divided by temperature as a function of temperature of GdIn_3 nanowires (black curve) and its bulk correspondent (red curve), fabricated through the metallic-flux nanonucleation method. The sharp peaks show an antiferromagnetic transition, zoomed in the respective inset. Reprinted with permission from [37]. Copyright 2014 by Elsevier Ltd.

3. Electrical characterization

The growing interest in magnetic nanowires is connected to the possibility of employing them for advanced applications in wide technological fields. For example, nanowires represent ideal candidates for sensor devices, since they present high sensitivity to their environment [38, 39]. Moreover, they are presently intensively investigated for a large range of spintronic devices, due to the nanowire dimensions comparable or smaller than scaling lengths in magnetism and spin-polarized transport. Transport and magnetic properties, such as anisotropic magnetoresistance, field-induced magnetization reversal in single nanowires, domain-wall magnetoresistance, quantized spin transport in nanoconstrictions, among others

[40–43], represent essential characterization for nanowires intended to play a major role in tomorrow's high technology.

In this chapter, we focus on direct current (DC) electrical characterization. The reader interested in radio-frequency (RF) nanowire measurements is referred to [6]. The main difficulty to perform electrical measurements on nanowires is to succeed in obtaining a good electrical contact. In this sense, several techniques have been implemented [38–40]. Here, we will restrain ourselves to the description of electrical characterization performed on single or few cylindrical nanowires. First, we describe a technique where the connected nanowires remain inside the nanowire array, thereby feeling the interaction field from their neighbors. In the second part, a method to measure free single nanowires is presented.

3.1. Nanowires embedded in array

Electrical characterization of nanowire arrays still embedded in porous alumina is an interesting technique because of their spatial ordering. In this case, the idea is to electrically connect nanowires both extremity, which is facilitated by the electrode already present at the nanowires' bottom, used for their electrodeposition. Even if the barrier layer thinning method can be used to obtain an electrical contact [44], removing completely the barrier layer and closing the pores with a thick conductive film (usually Au) is preferred to lower the resistance. The top contact may be fabricated by filling the remaining pores length by a metallic material, like Cu [41, 43], or by mechanically polishing the top of the template before depositing an electrode by sputtering [40, 42].

Using lithography techniques, one can limit the template region electrically connected, measuring current transport over thousands of nanowires at the same time. The main advantage of this technique is to improve signal-to-noise ratio. In counterpart, the electrical characteristic in response to an electrical excitation is averaged [41], which prevents spin-transfer experiments.

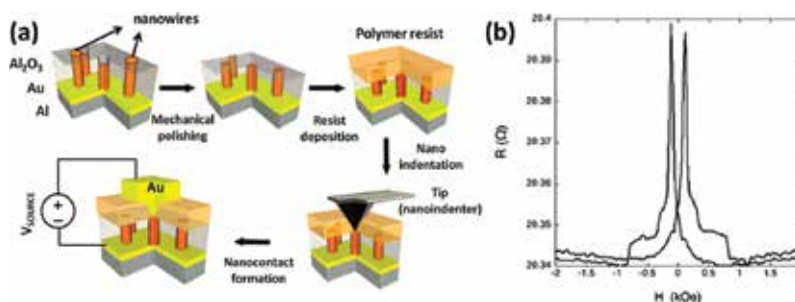


Figure 6. (a) Schematic illustration of the single nanowire contacting process on an array of nanowires electrodeposited in supported nanoporous alumina template and (b) magnetoresistance curve for Py/Cu/Py spin-valve nanowire with 80 nm of diameter and external magnetic field in-plane with the membrane. Reprinted with permission from [40]. Copyright 2007 by American Chemical Society.

However, one can also define electrical nanocontacts on a single electrodeposited nanowire inside the porous membrane. This can be done by the indentation of an ultrathin-insulating photoresist layer deposited on the top face of the thinned alumina template after the electrodeposition. A modified atomic force microscope designed for local resistance measurement is used as a nanoindenter, allowing an easy access point onto individual nanowires at the surface of the template [40, 42], as shown in **Figure 6a**. As a consequence, magnetic properties, such as magnetoresistance signal, can be extracted from one individual nanowire (**Figure 6b**).

Despite the presence of the interaction field on the measured nanowire, this technique presents several advantages. First, the template size and shape yield a convenient sample-handling method [41]. Second, since the probed nanowire remains inside the alumina template, it does not suffer surface oxidation due to the contact with alumina-etching solution and ambient atmosphere. The major drawback of this oxidation is that it increases the nanowire resistance. As a consequence, it makes spin-transfer experiments more difficult, leading to a small giant magnetoresistance signal. Moreover, it favors the apparition of heating problem due to Joule effect, limiting the current density that one can inject in the nanowire before melting it.

3.2. Free nanowires

To avoid magnetic interactions between closer nanowires inside the porous membrane, which can influence the electrical and magnetic measurements of a single nanowire, one can release them from the membrane using a convenient etching solution. Two options exist to establish an electrical contact on a single nanowire, both involving the design of proper electrodes by optical or e-beam lithography. The first one consists of patterning the electrodes after dispersing the nanowires on a substrate [45]. While this method does not require nanowire manipulation, the critical step is the careful electrode alignment with the lying nanowire. Here, we will focus on the opposite technique, where the electrodes are first patterned and the free nanowires are placed afterwards between them. Depending on the nanowire manipulation technique, this method can reach large outflow.

For metallic nanowires, dielectrophoresis (DEP) technique allows to adequately position the nanowires to electrically connect them with the electrodes to further transport measurements. After chemically etching the alumina membrane, the nanowires must then be dispersed in dimethylformamide (DMF), a dielectric medium, in order to avoid nanowire cluster formation [21, 38, 41, 43]. Then, the metallic nanowires suspended in the DMF can be directly manipulated through alternating electric fields produced by a pair of electrodes separated by a gap region, as reported in [38] (**Figure 7a**). For optimized DEP parameters, one can trap one single nanowire to carry out electrical/magnetic measurements [38, 39, 41, 43] (**Figure 7b**).

As shown, DEP is an adequate tool to insert nanowire between electrodes for electrical transport measurements [38]. As already mentioned above, compared to the in-template electrical measurement, this technique removes the effects from the dipolar field from neighboring nanowires. Moreover, it permits to use a four-point resistance measurement method, since the electrode geometry is more versatile. Therefore, it makes possible to pattern a series of electrodes on a single nanowire in order to follow a domain-wall propagation. However, when the nanowire touches the electrodes, a large contact resistance is sometimes

present due to native oxide or organic residues, leading to a Schottky-like behavior (nonlinear). Several options are available to reduce the contact resistance, such as depositing a thin metallic layer on the nanowire extremities by focused ion beam-induced deposition (FIBID) (**Figure 7c**) [38]. Another option consists of improving the contact resistance by passing a low current into the nanowire, allowing subsequent temperature-dependent electrical resistivity and magnetoresistance measurements (**Figure 7d**) [28].

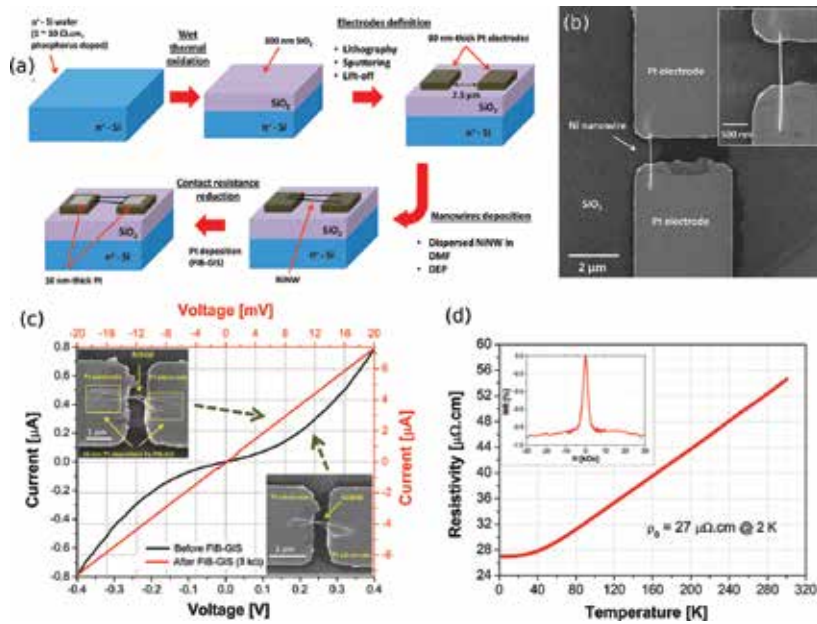


Figure 7. Electrical characterization of free Ni nanowires manipulated through DEP technique, as presented in [38]. (a) Schematic illustration of the sample preparation, (b) SEM image of one single nanowire deposited on electrodes, (c) current versus voltage curves before (black, left, and down axes) and after (red, right, and up axes) 10-nm-thick Pt layer deposition by FIBID (a and c reprinted with permission from [38]. Copyright 2015 by American Vacuum Society), and (d) resistivity evolution with temperature of one single nanowire, showing metallic behavior. Inset: magnetoresistance measurement with the current flowing perpendicular to the applied field at 300 K. Reprinted with permission from [28]. Copyright 2013 by Brazilian Microelectronics Society.

Whatever the techniques used to connect a single nanowire, its electrical characterization is subjected to a special care about the current that can flow through it. Above a certain limit, it begins to damage the nanowire due to heat dissipation. Therefore, in addition to control the current during the electrical measurements, one needs to also prevent electrical discharge when preparing the sample.

4. Magnetic characterization

Obviously, the investigation of magnetic nanowires cannot be complete without probing their magnetic properties. Magnetometry, which is the magnetization measurement, yields the basic

magnetic behavior, typically through the acquisition of a major hysteresis curve. For an array, it can be performed on a vibrating sample magnetometer (VSM) or a superconducting quantum interference device (SQUID), while micro-SQUID and magneto-optical Kerr effect (MOKE) are suitable for single nanowire. All these magnetization measurement techniques can also be used to perform specific field routine, such as first-order reversal curves (FORCs), which give the statistical distribution of hysteresis operators, or the angular dependence, to probe the magnetization-reversal processes. On the other hand, useful magnetic characterization is not limited to the magnetization value acquisition. Nanowire array magnetization reversal can be probed by means of magnetic force microscopy (MFM), while imaging the domain walls and/or magnetic structure along a single nanowire is enabled by MFM and electron holography, for example. For its part, ferromagnetic resonance (FMR) is an adequate tool to probe the material anisotropy.

4.1. Magnetometry techniques

While typical nanowire arrays exhibit a magnetic signal relatively easy to measure with conventional equipment, due to the high nanowire density, single nanowires require more sensible technique. Furthermore, the sample manipulation does not present specific challenge for measuring an array, apart from the magnetic field orientation with respect to the nanowire axis. However, the first problem to overcome before measuring single nanowire magnetization is their proper positioning. These differences naturally divide the magnetometry techniques between the array and single nanowire-oriented ones.

4.1.1. Array magnetometry

Most of conventional magnetometers coupled with magnets able to apply field of at least 1 T are sufficient to measure the magnetization arising from a nanowire array. Due to the high density of nanowires, its magnetic signal typically yields several memu, which is higher than the sensibility of standard magnetometer for bulk systems. The two main equipment used for nanowire magnetic characterization are the vibrating sample magnetometer (VSM) and the superconducting quantum interference device (SQUID) magnetometer. Both are based on Faraday's law principle, which states that a variation in the magnetic flux density passing through a conductive coil induces a current in this coil to compensate the variation. The sample is therefore magnetized by an external magnetic field and its position with respect to the detecting coils is changed, thus inducing a measured voltage that is subsequently converted in magnetic moment.

The VSM detection system [46] is simpler than the one in a SQUID. The sensing coils are usually copper coils located around the sample. A relatively good sensitivity is gained by mechanically vibrating the sample at a given frequency (typically less than 100 Hz) and using a lock-in amplifier to filter the signal induced. In counterpart, the SQUID benefits of a higher sensitivity. Here, the detector is a superconducting loop, which imposes a quantization of the magnetic flux. This loop contains two Josephson junctions that break the flowing current symmetry in the presence of a magnetic flux variation. For more information about SQUID operation, the reader is referred to the study of Ramasamy et al. [47].

Apart from the proper sample centering, nanowire array magnetization acquisition is relatively straightforward. The only experimental aspect to take care is the applied magnetic field direction relative to the nanowire axis, due to the anisotropy of the system (**Figure 8a**). Since the measurement is performed on a whole array, one needs to remember that it exhibits the array magnetic properties, which may differ from the individual nanowire ones (see Section 4.2.1). For example, the coercivity obtained represents when half of the array magnetic volume reversed its magnetization, while the susceptibility is related to the interaction field between the nanowires.

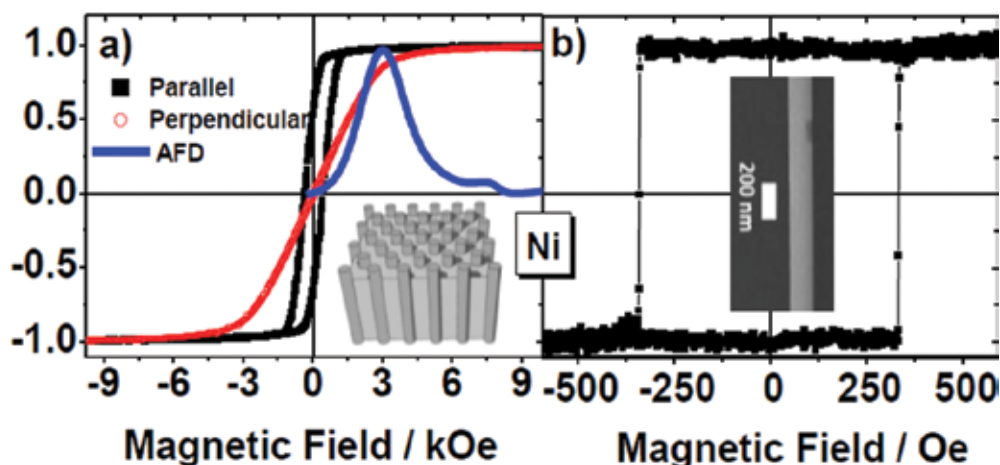


Figure 8. Typical normalized magnetization curves for Ni nanowires (130 nm of diameter, $\approx 20\text{-}\mu\text{m}$ long). (a) Nanowire array measured both parallel (black) and perpendicular (red) to the nanowire axis on a commercial VSM. It evidences the axial easy axis of the array. In blue, the anisotropy field distribution calculated according to [48] and (b) single nanowire measured axially on a MOKE setup. The squared hysteresis loop denotes a clear axial easy axis. Reprinted with permission from [49]. Copyright 2012 by IOP Publishing Ltd.

4.1.2. Single nanowire magnetometry

To overcome this discrepancy, the direct magnetic measurement of one nanowire should deliver the individual properties. However, in addition to the difficulties created by the necessity to adequately position the individual nanowire with respect to the sensing element, the low magnetic signal arising from a single nanowire represents a complex challenge. Two different solutions have essentially been implemented.

The first one consists of fabricating a micro-SQUID detector around a free nanowire lying on a substrate [50]. The nanowire proximity with the superconducting loop, coupled to its high-detection sensibility, allows performing magnetization measurement. However, this technique has several drawbacks that explain why it is not largely widespread. Mainly, the micro-SQUID detector fabrication, made by complex lithography, is restrained to a unique nanowire, thus severely limiting the number of single nanowires that can be characterized in a reasonable period of time.

On the other side, the magneto-optical Kerr effect (MOKE) is normally used as a superficial magnetic characterization technique due to its small penetration length. Nevertheless, its penetration length of the order of the tens of nanometer is enough to probe the magnetic signal from single nanowires, while actually removing unwanted background signal, as from the substrate. Compared to the micro-SQUID, the MOKE technique is advantaged by the facts that it can be performed on a conventional MOKE setup and allows to quickly measure several nanowires, making distribution properties possible to evaluate. It consists of shining an incident polarized light on the magnetic sample and measuring the rotation of the reflected light [51]. This rotation depends on the relative orientation of the incident polarization with the sample magnetization. Therefore, there exist three different configurations (longitudinal, transversal, and polar) that allow detecting magnetization in the parallel, perpendicular, and out-of-plane directions, respectively.

In order to succeed in measuring the magnetic properties of isolated nanowires by MOKE, it is important to carefully perform the measurement. Good focus of the laser spot on the sample and cautious alignment of the lens system are primordial to avoid signal loss. Additionally, the low magnetic signal requires that the hysteresis loops must be averaged several times (up to thousands) to improve the signal-to-noise ratio. As already stated, the magnetic characterization of single nanowires yields fundamental properties such as the individual switching field and squareness of nanowires [49] (**Figure 8b**). This information is essential to study the magnetization-reversal mechanisms in nanowires.

4.2. Magnetometry routines

Even if major magnetization hysteresis curves, from an array or a single nanowire, give a valuable characterization, the knowledge directly extracted from them remains limited: saturation magnetization, susceptibility, coercivity, squareness, and so on. However, different magnetic behaviors can be easily probed, still using the same setups as for the major curve acquisition. The idea consists of modifying the measurement routine in order to select a specific kind of behavior to follow and investigate. For example, instead of sweeping the magnetic field between saturation values, but performing reversal curves, which begin in the hysteresis area, one is able to get access to the switching of individual nanowires while measuring the whole array. This technique, called first-order reversal curve (FORC), is very powerful when applied to nanowire systems. Another possibility is to change the angle during the measurement, since nanowire magnetic behavior depends on their anisotropy. This technique represents an effective way to achieve to experimentally study the magnetization-reversal mechanisms occurring in the nanowires. Both procedures are easily implemented in any magnetometer and can be applied to both nanowire array and single nanowire. Therefore, they should be considered as part as basic nanowire characterization, along with major hysteresis curves, due to the richness of information obtained.

4.2.1. First-order reversal curve (FORC) technique

Major hysteresis curves yield the magnetic properties of whole nanowire arrays. However, the magnetization of the array can be viewed as the average of the nanowire magnetization. The

objective of the FORC technique is to extract the individual magnetic entities characteristics while performing a measurement on the whole system. A complete description of the implementation of the FORC method for nanowire arrays is available in [11]. It is based on the classical Preisach model, where magnetic entities are modeled as squared hysteresis operators called mathematical hysterons. In order to obtain the statistical distribution of these operators, only described by their width and field shift, Mayergoyz developed a specific field-sweeping routine [52]. It consists of minor curves beginning at a reversal field (inside the hysteretic area) and returning to the saturation (**Figure 9a**). The FORC result is calculated from these data through a second-order mixed derivative and represented as a contour plot (**Figure 9b**). If the measured system meets the required conditions for the classical Preisach model, it can be considered as the hysterons statistical distribution.

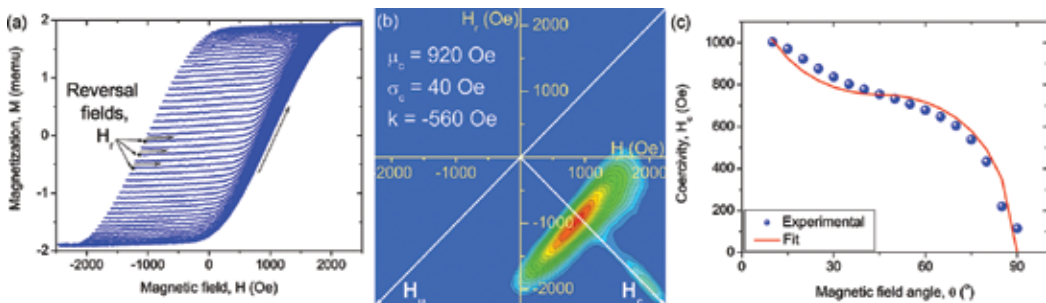


Figure 9. Different magnetization measurement procedure results applied to an Ni nanowire array (35-nm diameter, 3.5- μm long). (a) First-order reversal curves measurement along the nanowire axis, (b) respective FORC result. Color scale ranging from blue (null value) to red (maximum value), and (c) angular evolution of the array coercivity along with the analytic fit for a transverse domain-wall nucleation. The effective anisotropy constant was evaluated at $3.612 \times 10^5 \text{ erg/cm}^3$.

Several nanowires, due to their large shape anisotropy, exhibit a squared hysteresis curves when measured axially. Therefore, the hysterons could be associated with the individual nanowire magnetic behavior, leading to a clever way to get access to the single nanowire properties without requiring to remove them from the template. This explains why the FORC technique is highly suitable to investigate nanowires. However, like most of real systems, nanowire arrays do not meet the criteria for the classical Preisach model, due to their interaction field. The FORC result analysis thus necessitates to be performed carefully. The physical analysis model, based on simulated behavior of physically meaningful hysterons, has been developed in this sense [53]. It allowed obtaining a quantitative parametrization of the FORC result in order to extract the mean and distribution width coercivity and the interaction field at saturation, among other values [54]. Even if the method is based on hysteretic operators, information about the system reversibility can also be extracted [55].

Typical axial FORC result for nanowire appears as a distribution narrow along the coercivity, while elongated along the interaction field axis (**Figure 9b**). It may be interpreted as nanowires with similar coercivity, and therefore geometrical dimensions, submitted to a large and almost uniform interaction field dependent on the magnetization. In general, a ridge may appear

along the coercivity axis and is attributed to the nonuniformity of this interaction field, the measurement being carried on a finite array [56]. In addition to the homogeneous nanowires, the FORC method remains suitable for more complex systems, such as multilayer nanowires, when coupled to the physical analysis model for the result analysis.

4.2.2. Angular-dependent magnetization curves

From a general point of view, all anisotropic system behavior is highly dependent on the applied magnetic field direction. From the other side, varying the field angle allows obtaining data from which additional information may be extracted. On most of magnetometers working with an electromagnet, which produces a horizontal applied field, modifying the measurement angle is easy and generally implemented in the control software. It is more challenging for superconducting coil, since the magnetic field is vertical in this case. Manual angle variation is usually required, thus increasing the total measurement time.

For nanowires, the classical case is to perform hysteresis curves along the axial and transverse directions, to determine the easy axis direction (e.g., see **Figure 8a**). In the last years, angle-dependent magnetization curves turned out to be richer in information, after it proved its ability to be interpreted as a signature of the magnetization-reversal processes. Nanowires with diameter up to few hundreds of nanometers usually reverse their magnetization through the domain-wall nucleation/propagation mechanism. Depending on their properties, the domain wall nucleated may be either transverse or vortex. Assuming that a transverse domain-wall nucleation can be modeled as the coherent rotation of a volume equivalent to the domain wall [57], the angular nanowire coercivity can be calculated in this case [58] (**Figure 9c**). Deviations from this model can be interpreted as the occurrence of other mechanisms (curling, fanning, coherent rotation, etc.) or domain-wall types (mainly vortex), while fitting yields quantitative values of the anisotropy constants. A special care with the precision of the field direction angle should be taken during the measurement, but can be easily overcome while performing the analytical fit.

4.3. Magnetization imaging

For nanowires, the interest in obtaining a direct or an indirect visualization of their magnetic structure depends on the resolution and area observed. High-resolution imaging allows probing a particular region of the nanowire and observes details of the magnetic domains and domain walls, which is probably the best way to understand and to control them. Since the domain-wall dynamics is very sensitive to their morphology [59, 60], it is fundamental to know their geometry for all applications involving domain-wall propagation. The domain pattern of a whole nanowire, for its part, gives valuable information about its magnetization-reversal mechanism. Finally, investigations of the nanowire array complex magnetization reversal and interaction field are helped by large-scale imaging of several nanowires, usually performed on the template top surface.

The two last cases are well resolved by using the magnetic force microscopy (MFM) technique, where a magnetized atomic force microscopy tip maps the stray field. For further local

magnetic information, several methods have been developed. They are usually more complicated to operate than MFM and not always suitable for cylindrical nanowires, due to their geometry. Here, we focus on a powerful characterization that can be performed in a TEM chamber and that can yield highly valuable local information: electron holography.

The main problem concerning magnetization imaging of nanowires and nanowire arrays is that both systems are tridimensional, instead of planar. Therefore, one needs to keep in mind that the observation made is not complete and that some additional features of the internal magnetization structure may be hidden from the observer. By example, assumptions about the nanowire magnetic structure are required when imaging nanowire array top extremity. Also, the nanowires' cylindrical shape makes the domain-wall internal structure very difficult to be seen, like the core of a vortex domain wall, since it lays parallel to the nanowire axis and near its center.

4.3.1. Magnetic force microscopy (MFM)

Among several techniques, the MFM is probably one of the most used magnetic imaging tools. Here, we give a brief description of the technique, but a most complete, although compact description, can be found in [61]. As mentioned above, the MFM is an atomic force microscope

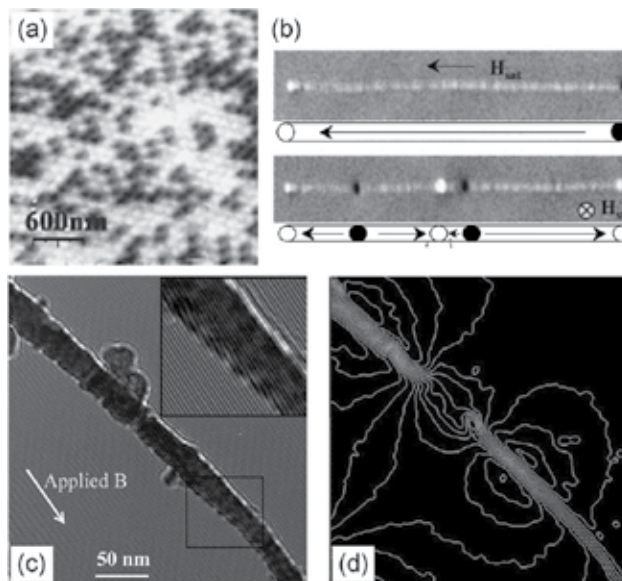


Figure 10. (a and b) MFM images in the remanent state. The clear and dark spots denoted outgoing and ingoing stray field, respectively. (a) Top surface of Ni nanowire arrays. The clear and dark circles represent the nanowires magnetized upward and downward. Reprinted with permission from [65]. Copyright 2004 by EDP Sciences, (b) individual 35-nm Co nanowire after saturation in a field parallel (top) and perpendicular (bottom) to the nanowire axis. A sketch of the possible domain pattern is underneath. Reprinted with permission from [64]. Copyright 2000 by American Physical Society, and (c and d) electron holography results of a multilayer Cu/CoFeB nanowire (80/230 nm) for an axial-applied magnetic field. Reprinted with permission from [66]. Copyright 2014 by AIP Publishing LLC. (c) Hologram. (d) Associated map of perpendicular magnetic field, with 0.1-T contour spacing.

with a magnetic tip, usually a thin (<50 nm) coated film with high coercivity of Ni, Co, or CoCr, among others, for the tip magnetization to be fixed during the scan. The tip lies on one end of a cantilever that raster scans the sample. The scanned area can be as large as 200 μm^2 and the typical resolution is 30 nm. In alternating current (AC) mode, which provides a better resolution, the cantilever tip is put to oscillate near its resonance frequency by piezoelectric crystals, while the tip-sample interaction changes the amplitude, frequency, and phase of the oscillating cantilever. All these changes are measurable (by a laser reflected from the cantilever) and can be used to calculate the force exerted at the tip by the sample. To consider only the magnetostatic interaction between the tip and the stray field generated by the sample, the lift-height technique is usually employed. In this mode, the tip is brought very close to the sample and a first scan is performed. The tip is then lifted and a second scan is done, thus eliminating the topographic contribution. A lift height of 50 nm is usually sufficient to image nanowires. Due to the complicated and not necessarily fixed magnetization tip and the unsolvable problem of the reconstruction of the magnetization sample by the sensed sample stray field, MFM is usually considered as a qualitative technique. Despite this, it is very useful, especially if combined with other techniques such as magnetometry, magnetoresistance measurements, and micromagnetic simulations.

Since the samples do not require any special preparations, only to lay on a plane surface, MFM is used to image both the top of nanowire arrays and free nanowires. Due to the large axial shape anisotropy, nanowires are usually taken to remain monodomain under axial-applied magnetic field. Therefore, investigations about individual nanowire-switching field and complex magnetostatic interaction between nanowires take advantages of the large template area that MFM can scan [62, 63] (**Figure 10a**). Actually, this monodomain state can be directly observed by performing MFM imaging of free nanowires. It allows visualizing the magnetic domains along the nanowire, and thus the presence of domain walls [64] (**Figure 10b**). However, in cylindrical nanowires, the domain-wall length is typically of a few nanometers, for Co, Ni, Fe, and alloys. Therefore, the MFM resolution does not normally provide much information about the domain-wall geometry, especially if it is a vortex or a helical, that have a small stray field compared with transverse domain wall.

4.3.2. *Electron holography*

Electron holography, performed in a TEM chamber, allows obtaining higher resolution imaging of the magnetic structure. The principle is to get access to the phase shift of the electron wave that traveled through the sample, not only to its amplitude, as in conventional TEM imaging techniques. By creating two paths for the electron beam, one passing through the sample while the other remaining undisturbed, the interference pattern creates an electron hologram, which depends on the phase shift. Therefore, the sample local magnetic properties influence the electron wave when passing through it and can be directly observed afterwards. More information about this powerful technique can be found in [67, 68], the second being specifically dedicated to magnetic material investigations.

Being performed using the high-energy electron beam from a TEM, typical electron holography resolution is of 5 nm and results are usually associated with micromagnetic simulations.

Due to the technique complexity, the best use of electron holography for nanowires is to probe the fine magnetic structure that is out of range for MFM equipment. More specifically, it allows to obtain a clear image of nanowire domain walls [69], as well as the detailed domain pattern created by multilayers [66] (Figure 10c and d).

4.4. Anisotropy probing

Finally, as was mentioned several times, nanowire magnetic behavior is intrinsically related to their anisotropy, both global and local variations. Even if magnetometry can be used to indirectly probe the system anisotropy properties, ferromagnetic resonance (FMR) is a powerful technique to obtain more accurate data. The FMR phenomenon is based on the resonance arising when the frequency of an applied transverse AC magnetic field is equal to the material Larmor frequency, which is the frequency of magnetization precession around the effective magnetic field. Since the anisotropy energy modifies the effective magnetic field, even the anisotropy constant distribution is accessible through FMR. A complete description of the phenomenon and the various ways to measure it is reviewed in [70].

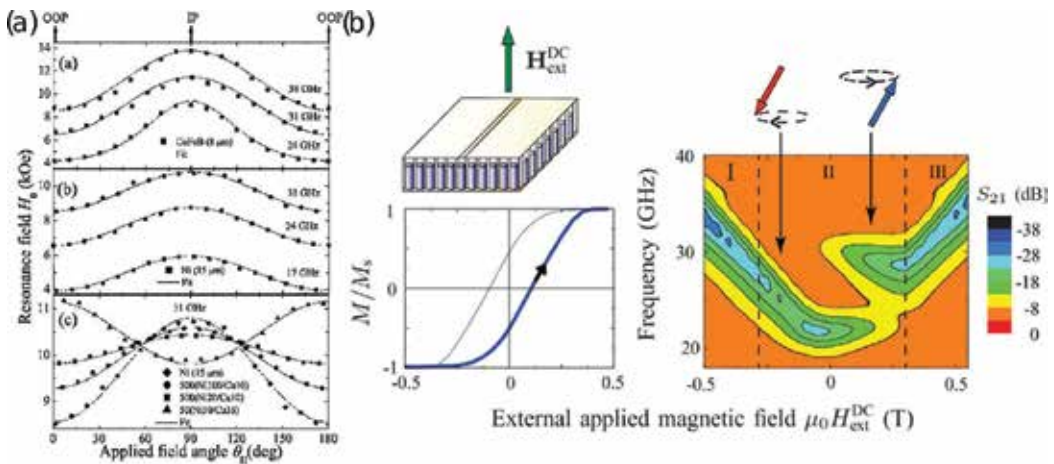


Figure 11. (a) Resonance field evolution with the magnetic field angle for CoFeB, Ni, and Ni/Cu nanowires. Reprinted with permission from [74]. Copyright 2007 by AIP Publishing LLC and (b) illustration of the double-resonance phenomenon occurring in a CoFeB nanowire array (40-nm diameter, 200- μ m long). Left: schematic of the microstrip line and major hysteresis curve branch used to measure FMR. Right: resulting contour plot. Reprinted with permission from [72]. Copyright 2009 by AIP Publishing LLC.

In the specific case of monodomain nanowires, both the anisotropy intensity and direction distributions are highly important since electrodeposited nanowires generally present homogeneities, which could greatly affect their magnetic behavior. On the other side, electromagnetic wave propagation directly depends on the medium effective anisotropy, leading to a crucial information for all nanowire applications related with high-frequency devices (Figure 11a) [71]. Finally, the array magnetization reversal may lead to the interesting phenomenon of

double resonance (**Figure 11b**) [72]. Several setups have been developed to measure FMR in nanowires and nanowire arrays. The reader interested to push further his knowledge in the area is referenced to the following book chapter [73].

5. Conclusion

In summary, the adequate use of the different characterization techniques available is essential for any researcher that is investigating magnetic nanowires, since the cost in time and money is high. Moreover, improper data analysis can lead to incorrect conclusions, while the unknown existence of a characterization technique can severely delay the advancement of a research project. This chapter is meant to serve as a reference guide for the specific system that constitutes magnetic nanowires.

Author details

Fanny Béron*, Marcos V. Puydinger dos Santos, Peterson G. de Carvalho, Karoline O. Moura, Luis C.C. Arzuza and Kleber R. Pirota

*Address all correspondence to: fberon@ifi.unicamp.br

Gleb Wataghin Physics Institute, State University of Campinas, Campinas, Brazil

References

- [1] Masuda H, Fukuda K. Ordered metal nanohole arrays made by a two-step replication of honeycomb structures of anodic alumina. *Science*. 1995;268:1466–1468. DOI: 10.1126/science.268.5216.1466
- [2] Nielsch K, Muller F, Li AP, Gösele U. Uniform nickel deposition into ordered alumina pores by pulsed electrodeposition. *Advanced Materials*. 2000;12:582–586. DOI: 10.1002/(SICI)1521-4095(200004)12:8<582::AID-ADMA582>3.0.CO;2-3
- [3] Pirota KR, Navas D, Hernández-Vélez D, Nielsch K, Vázquez M. Novel magnetic materials prepared by electrodeposition techniques: arrays of nanowires and multi-layered microwires. *Journal of Applied Physics*. 2004;369:18–26. DOI: 10.1016/j.jallcom.2003.09.040
- [4] Lupu N, editor. *Electrodeposited Nanowires and their Applications*. 1st ed. Vukovar: INTECH; 2000. 236 p. DOI: 10.5772/2799

- [5] Irshad MI, Ahmad F, Mohamed NM. A Review on Nanowires as an Alternative High Density Magnetic Storage Media . In: AIP Conference Proceedings; 12–14 June 2012; Malaysia. Melville: AIP; 2012. p. 625.
- [6] Frake JC, Kano S, Ciccarelli C, Griffiths J, Sakamoto M, Teranishi T, Majima Y, Smith CG, Buitelaar MR. Radio-frequency capacitance spectroscopy of metallic nanoparticles. *Scientific Reports*. 2015;5:1–6. DOI: 10.1038/srep10858
- [7] Chena X, Wonga CKY, Yuan CA, Zhanga G. Nanowire-based gas sensors. *Sensors and Actuators B: Chemical*. 2013;177:178–195. DOI: 10.1016/j.snb.2012.10.134
- [8] Patolsky F, Zheng G, Lieber CM. Nanowire sensors for medicine and the life sciences. *Nanomedicine*. 2006;1:51–65. DOI: 10.2217/17435889.1.1.51
- [9] Moura KO, de Oliveira LAS, Rosa PFS, Béron F, Pagliuso PG, Pirola KR. Effect of dimensionality on the magnetic properties of Fe_3Ga_4 crystals. *Scientific Reports*. In press.
- [10] de Oliveira LAS, Pirola KR. Synthesis, structural and magnetic characterization of highly ordered single crystalline BiFeO_3 nanotubes. *Materials Research Bulletin*. 2013;48:1593–1597. DOI: 10.1016/j.materresbull.2012.12.066
- [11] Béron F, Carignan L-P, Ménard D, Yelon A. Extracting Individual Properties from Global Behaviour: First-order Reversal Curve Method Applied to Magnetic Nanowire Arrays. In: Lupu N, editor. *Electrodeposited Nanowires and their Applications*. Vukovar: INTECH; 2010. p. 167–188. DOI: 10.5772/39475
- [12] Reimer L. *Scanning Electron Microscopy: Physics of Image Formation and Microanalysis*. 2nd ed. New York: Springer; 1998. 502 p. DOI: 10.1007/978-3-540-38967-5
- [13] Oatley CW. The early history of the scanning electron microscope. *Journal of Applied Physics*. 2002;53:R1–R13. DOI: 10.1063/1.331666
- [14] Babin S, Gaeovski M, Joy D, Machin M, Martynov A. Technique to automatically measure electron-beam diameter and astigmatism: BEAMETR. *Journal of Vacuum Science & Technology B*. 2006;24:2956–2959. DOI: 10.1116/1.2387158.
- [15] Utke I, Hoffmann P, Melngailis J. Gas-assisted focused electron beam and ion beam processing and fabrication. *Journal of Vacuum Science and Technology B*. 2008;26:1197–1276. DOI: 10.1116/1.2955728
- [16] Mehta R. Interactions, Imaging and Spectra in SEM. In: Kazmiruk V, editor. *Scanning Electron Microscopy*. Vukovar: INTECH; 2012. p. 17–30. DOI: 10.5772/35586
- [17] Cheng W, Steinhart M, Gosele U, Wehrspohn RB. Tree-like alumina nanopores generated in a non-steady-state anodization. *Journal of Materials Chemistry*. 2007;17:3493–3495. DOI: 10.1039/B709618F

- [18] Chen Q, Wang S, Peng LM. Establishing ohmic contacts for in situ current–voltage characteristic measurements on a carbon nanotube inside the scanning electron microscope. *Nanotechnology*. 2006;17:1087–1098. DOI: 10.1088/0957-4484/17/4/041
- [19] Hirsch P, Kässens M, Püttmann M, Reimer L. Contamination in a scanning electron microscope and the influence of specimen cooling. *Scanning*. 1994;16:101–110. DOI: 10.1002/sca.4950160207
- [20] Arzuza LCC, López-Ruiz R, Salazar-Aravena D, Knobel M, Béron F, Pirota KR. Domain wall propagation tuning in magnetic nanowires through geometric modulation. *Physical Review B*. Forthcoming.
- [21] Puydinger dos Santos MV, Lima LPB, Mayer RA, Bettini J, Béron F, Pirota K, Diniz JA. Electrical Characterization of Electrodeposited Ni Nanowires for MagFET Application. In: 30th Symposium on Microelectronics Technology and Devices (SBMicro); 31 August–4 September 2015; Salvador. New York: IEEE; 2015. p. 4. DOI: 10.1109/SBMicro.2015.7298149
- [22] Williams DB, Carter CB. *Transmission Electron Microscopy – A Textbook for Materials Science*. 2nd ed. New York: Springer; 2009. 757 p. DOI: 10.1007/978-0-387-76501-3
- [23] Reimer L, Kohl H. *Transmission Electron Microscopy*. 5th ed. New York: Springer; 2008. 590 p. DOI: 10.1007/978-0-387-40093-8
- [24] Ayache J, Beaunier L, Boumendil J, Ehret G, Laub D. *Sample Preparation Handbook for Transmission Electron Microscopy: Methodology*. 1st ed. New York: Springer; 2010. 250 p. DOI: 10.1007/978-0-387-98182-6
- [25] Kim, KH, Akase Z, Suzuki T, Shindo D. Charging effects on SEM/SIM contrast of metal/insulator system in various metallic coating conditions. *Materials Transactions*. 2010;51:1080–1083. DOI: 10.2320/matertrans.M2010034
- [26] Ii, S. Nanoscale Chemical Analysis in Various Interfaces with Energy Dispersive X-ray Spectroscopy and Transmission Electron Microscopy. In: Sharma SK, editor. *X-ray Spectroscopy*. Vukovar: INTECH; 2012. p. 265–280. DOI: 10.5772/31645
- [27] Zhang J, Ma H, Zhang S, Zhang H, Deng X, Lan Q, Xue D, Bai F, Mellorsc NJ, Peng Y. Nanoscale characterisation and magnetic properties of $\text{Co}_{81}\text{Cu}_{19}/\text{Cu}$ multilayer nanowires. *Journal of Materials Chemistry C*. 2015;3:85–93. DOI: 10.1039/c4tc01510j
- [28] Puydinger dos Santos MV, Velo M, Domingos RD, Bettini J, Diniz JA, Béron F, Pirota KR. Electrodeposited nickel nanowires for magnetic-field effect transistor (MagFET). *Journal of Integrated Circuits and Systems*. In press.
- [29] Rivière JC, Myhra S, editors. *Handbook of Surface and Interface Analysis Methods for Problems-solving*. 2nd ed. New York: CRC Press; 2009. 671 p.
- [30] Egerton RF. *Electron Energy-loss Spectroscopy in the Electron Microscope*. 3rd ed. New York: Springer; 2011. 491 p. DOI: 10.1007/978-1-4419-9583-4

- [31] Brydson R. *Electron Energy Loss Spectroscopy*. 1st ed. New York: Garland Science; 2001. 152 p.
- [32] Tinkov V. Non-destructive Surface Analysis by Low Energy Electron Loss Spectroscopy. In: Farrukh MA, editor. *Advanced Aspects of Spectroscopy*. Vukovar: INTECH; 2012. p. 195–220. DOI: 10.5772/48090
- [33] Maaz K, Karim S, Usman M, Mumtaz A, Liu J, Duan JL, Maqbool M. Effect of crystallographic texture on magnetic characteristics of cobalt nanowires. *Nanoscale Research Letters*. 2010;5:1111–1117. DOI: 10.1007/s11671-010-9610-5
- [34] Pirota KR, Béron F, Zanchet D, Rocha TCR, Navas D, Torrejón J, Vazquez M, Knobel M. Magnetic and structural properties fcc/hcp bi-crystalline multilayer Co nanowires array prepared by controlled electroplating. *Journal of Applied Physics*. 2011;109:083919-1–083919-6. DOI: 10.1063/1.3553865
- [35] Romeu D, Gomez A, Reyes-Gasga J. Electron Diffraction and HRTEM Structure Analysis of Nanowires. In: Hashim A, editor. *Nanowires – Fundamental Research*. Vukovar: INTECH; 2011. p. 461–484. DOI: 10.5772/18915
- [36] Chaplot SL, Mittal R, Choudhury N, editors. *Thermodynamic Properties of Solids: Experiments and Modeling*. Chichester: Wiley; 2010. 342 p. DOI: 10.1002/9783527630417.ch1
- [37] Rosa PFS, Oliveira LAS, Jesus CBR, Moura KO, Adriano C, Iwamoto W, Garitezi TM, Granado E, Saleta ME, Pirota KR, Pagliuso PG. Exploring the effects of dimensionality on the magnetic properties of intermetallic nanowires. *Solid State Communications*. 2014;191:14–18. DOI:10.1016/j.ssc.2014.04.013
- [38] Puydinger dos Santos MV, Lima LPB, Mayer RA, Béron F, Pirota K, Diniz JA. Dielectrophoretic manipulation of individual nickel nanowires for electrical transport measurements. *Journal of Vacuum Science and Technology B*. 2015;33:031804. DOI: 10.1116/1.4918732
- [39] Wu J, Yin B, Wu F, Myung Y, Banerjee P. Charge transport in single CuO nanowires. *Applied Physics Letters*. 2014;105:183506. DOI: 10.1063/1.4900966
- [40] Piroux L, Renand K, Guillemet, Mátéfi-Tempfli S, Mátéfi-Tempfli M, Antohe VA, Fusil S, Bouzouane K, Cros V. Template-grown NiFW/Cu/NiFe nanowires for spin transfer devices. *Nano Letters*. 2007; 7:2563. DOI: 10.1021/nl070263s
- [41] Leitão DC, Sousa CT, Ventura J, Amaral JS, Carpinteiro F, Pirota KR, Vazquez M, Sousa JB, Araujo JP. Characterization of electrodeposited Ni and Ni₈₀Fe₂₀ nanowires. *Journal of Non-Crystalline Solids*. 2008;354:5241. DOI: 10.1016/j.jnoncrysol.2008.05.088
- [42] Fusil S, Piroux L, Mátéfi-Tempfli S, Mátéfi-Tempfli M, Michotte S, Saul C K, Pereira LG, Bouzouane K, Cros V, Deranlot C. Nanolithography based contacting method for electrical measurements on single template synthesized nanowires. *Nanotechnology*. 2005;16:2936. DOI: 10.1088/0957-4484/16/12/036

- [43] Pirola KR, Navas D, Hernández-Vélez M, Nielsch K, Vázquez M. Novel magnetic materials prepared by electrodeposition techniques: arrays of nanowires and multi-layered microwires. *Journal of Alloys and Compounds*. 2004;369:18. DOI: 10.1016/j.jallcom.2003.09.040
- [44] Ohgai T. Magnetoresistance of Nanowires Electrodeposited into Anodized Aluminum Oxide Nanochannels. In: Peng X, editor. *Nanotechnology and Nanomaterials*. Vukovar: INTECH; 2012. p. 101–125. DOI: 10.5772/52606
- [45] Vila L, Piroux L, George JM, Fert A, Faini G. Multiprobe magnetoresistance measurements on isolated magnetic nanowires. *Applied Physics Letters*. 2002;80:3805–3807. DOI: 10.1063/1.1478783
- [46] Foner S. Versatile and sensitive vibrating-sample magnetometer. *Review of Scientific Instruments*. 1959;30:548–557. DOI: 10.1063/1.1716679
- [47] Ramasamy N, Janawadkar M. SQUID Based Nondestructive Evaluation. In: Omar M, editor. *Nondestructive Testing Methods and New Applications*. Vukovar: INTECH; 2012. p. 25–52. DOI: 10.5772/36406
- [48] De La Torre Medina J, Darques M, Piroux L, Encinas A. Application of the anisotropy field distribution method to arrays of magnetic nanowires. *Journal of Applied Physics*. 2009;105:023909. DOI: 10.1063/1.3067773
- [49] Vega V, Böhnert T, Martens S, Waleczek M, Montero-Moreno JM, Görlitz D, Prida VM, Nielsch K. Tuning the magnetic anisotropy of Co-Ni nanowires: comparison between single nanowires and nanowire arrays in hard-anodic aluminum oxide membranes. *Nanotechnology*. 2012;23:465709. DOI: 10.1088/0957-4484/23/46/465709
- [50] Doudin B, Mailly D, Hasselbach K, Benoit A, Meier J, Ansermet J-P, Barbara B, Wernsdorfer W. Nucleation of magnetization reversal in individual nanosized nickel wires. *Physical Review Letters*. 1996;77:1873. DOI: 10.1103/PhysRevLett.77.1873
- [51] Tiwari U, Ghosh R, Sen P. Theory of magneto-optic Kerr effects. *Physical Review B*. 1994;49:2159. DOI: 10.1103/PhysRevB.49.2159
- [52] Mayergoyz ID. Mathematical models of hysteresis. *Physical Review Letters*. 1986;56:1518. DOI:10.1103/PhysRevLett.56.1518
- [53] Béron F, Ménard D, Yelon A. First-order reversal curve diagrams of magnetic entities with mean interaction field: a physical analysis perspective. *Journal of Applied Physics*. 2008;103:07D908. DOI: 10.1063/1.2830955
- [54] Béron F, Clime L, Ciureanu M, Ménard D, Cochrane RW, Yelon A. Magnetostatic interactions and coercivities of ferromagnetic soft nanowires in uniform length arrays. *Journal of Nanoscience and Nanotechnology*. 2008;8:2944–2954. DOI: 10.1166/jnn.2008.159

- [55] Béron F, Clime L, Ciureanu M, Ménard D, Cochrane RW, Yelon A. Reversible and quasireversible information in first-order reversal curve diagrams. *Journal of Applied Physics*. 2007;101:09J107. DOI: 10.1063/1.2712172
- [56] Dobrotă CU, Stancu A. Tracking the individual magnetic wires' switchings in ferromagnetic nanowire arrays using the first-order reversal curves (FORC) diagram method. *Physica B: Condensed Matter*. 2015;457:280–286. DOI: 10.1016/j.physb.2014.10.006
- [57] Escrig J, Lavín R, Palma JL, Denardin JC, Altbir D, Cortés A, Gómez H. Geometry dependence of coercivity in Ni nanowire arrays. *Nanotechnology*. 2008;19:07513. DOI: 10.1088/0957-4484/19/7/075713
- [58] Vivas LG, Escrig J, Trabada DG, Badini-Confalonieri GA, Vázquez M. Magnetic anisotropy in ordered textured Co nanowires. *Applied Physics Letters*. 2012;100:252405. DOI: 10.1063/1.4729782
- [59] Wieser R, Vedmedenko EY, Weinberger P, Wiesendanger R. Current-driven domain wall motion in cylindrical nanowires. *Physical Review B*. 2010;82:144430. DOI: 10.1103/PhysRevB.82.144430
- [60] Yan M, Kákay A, Gliga S, Hertel R. Beating the walker limit with massless domain walls in cylindrical nanowires. *Physical Review Letters*. 2010;104:057201. DOI: 10.1103/PhysRevLett.104.057201
- [61] Ferri FA, Pereira da Silva MA, Marega Jr E. Magnetic Force Microscopy: Basic Principles and Applications. In: Bellitto V, editor. *Atomic Force Microscopy – Imaging, Measuring and Manipulating Surfaces at the Atomic Scale*. Vukovar: INTECH; 2012. p. 39–56. DOI: 10.5772/34833
- [62] Tabasum MR, Zighem F, De La Torre Medina J, Piraux L, Nysten B. Intrinsic switching field distribution of arrays of Ni₈₀Fe₂₀ nanowires probed by in situ magnetic force microscopy. *Journal of Superconductivity and Novel Magnetism*. 2013;26:1375–1379. DOI: 10.1007/s10948-012-1975-5
- [63] Yuana J, Peia W, Hasagawaa T, Washiyaa T, Saitoa H, Ishioa S, Oshimac H, Itoh K. Study on magnetization reversal of cobalt nanowire arrays by magnetic force microscopy. *Journal of Magnetism and Magnetic Materials*. 2008;320:736–741. DOI: 10.1016/j.jmmm.2007.08.023
- [64] Ebels U, Radulescu A, Henry Y, Piraux L, Ounadjela K. Spin Accumulation and domain wall magnetoresistance in 35 nm Co wires. *Physical Review Letters*. 2000;84:983–986. DOI: 10.1103/PhysRevLett.84.983
- [65] Vázquez M, Hernández-Vélez M, Pirota K, Asenjo A, Navas D, Velázquez J, Vargas P, Ramos C. Arrays of Ni nanowires in alumina membranes: magnetic properties and spatial ordering. *The European Physical Journal B*. 2004;40:489–497. DOI: 10.1140/epjb/e2004-00163-4

- [66] Akhtari-Zavareh A, Carignan LP, Yelon A, Ménard D, Kasama T, Herring R, Dunin-Borkowski RE, McCartney MR, Kavanagh KL. Off-axis electron holography of ferromagnetic multilayer nanowires. *Journal of Applied Physics*. 2014;116:023902. DOI: 10.1063/1.4887488
- [67] Tonomura A. Fundamentals and Applications of Electron Holography. In: Rosen J, editor. *Holography, Research and Technologies*. Vukovar: INTECH; 2011. p. 441–452. DOI: 10.5772/14280
- [68] Kasama T, Dunin-Borkowski RE, Beleggia M. Electron Holography of Magnetic Materials. In: Monroy Ramirez FA, editor. *Holography – Different Fields of Application*. Vukovar: INTECH; 2011. p. 53–80. DOI: 10.5772/22366
- [69] Biziere N, Gatel C, Lassalle-Balier R, Clochard MC, Wegrowe JE, Snoeck E. Imaging the fine structure of a magnetic domain wall in a Ni nanocylinder. *Nano Letters*. 2013;13:2053–2057. DOI: 10.1021/nl400317j
- [70] Yalcin O. Ferromagnetic Resonance. In: Yalcin O, editor. *Ferromagnetic Resonance – Theory and Applications*. Vukovar: INTECH; 2013. p. 1–46. DOI: 10.5772/56134
- [71] Carignan LP, Yelon A, Ménard D, Caloz C. Ferromagnetic Nanowire Metamaterials: Theory and Applications. *IEEE Transactions on Microwave Theory and Technique*. 2011;59:2568–2586. DOI:10.1109/TMTT.2011.2163202
- [72] Carignan LP, Boucher V, Kodera T, Caloz C, Yelon A, Ménard D. Double ferromagnetic resonance in nanowire arrays. *Applied Physics Letters*. 2009;95:062504. DOI: 10.1063/1.3194296
- [73] Sharma M, Pathak S, Monika Sharma M. FMR Measurements of Magnetic Nanostructures. In: Yalcin O, editor. *Ferromagnetic Resonance – Theory and Applications*. Vukovar: INTECH; 2013. p. 93–110. DOI: 10.5772/56615
- [74] Carignan LP, Lacroix C, Ouimet A, Ciureanu M, Yelon A, Ménard D. Magnetic anisotropy in arrays of Ni, CoFeB, and Ni/Cu nanowires. *Journal of Applied Physics*. 2007;102:023905. DOI: 10.1063/1.2756522

Magnetization Dynamics–Induced Charge and Spin Transport on the Surface of a Topological Insulator Subjected to Magnetism

Katsuhisa Taguchi

Additional information is available at the end of the chapter

<http://dx.doi.org/10.5772/62531>

Abstract

We theoretically show spin and charge transport on the disordered surface of a three-dimensional topological insulator with a magnetic insulator when localized spin of the magnetic insulator depends on time and space. To ascertain the transports, we use a low-energy effective Hamiltonian on the surface of a topological insulator using the exchange interaction and calculate analytically using Green's function techniques within the linear response to the exchange interaction. As a result, the time-dependent localized spin induces the charge and spin current. These currents are detected from change in the half-width value of the ferromagnetic resonance of the localized spin when the magnetic resonance of the localized spin is realized in the attached magnetic insulator. We also show spin and charge current generation in a three-dimensional Weyl–Dirac semimetal, which has massless Dirac fermions with helicity degrees of freedoms. The time-dependent localized spin drives the charge and spin current in the system. The charge current as well as the spin current in the Weyl–Dirac system are slightly different from those on the surface of the topological insulator.

Keywords: Spin pumping, Spin–momentum locking, Surface of topological insulator, Weyl–Dirac semimetal, Massless Dirac fermions

1. Introduction

A crucial issue in spintronics is the generation and manipulation of a charge and spin current by magnetism, since these mechanisms can be applicable to magnetic devices. One way to generate charge and spin flow is called “spin pumping,” which pumps from the angular

momentum of a magnetization's localized spin into that of electrons through the dynamics of magnetization as well as spin-orbit interactions [1, 2]. No other way of doing this has so far been discussed in the field of metallic spintronics.

Ever since the discovery of a topological insulator (TI) [3–6], spintronics using topology has been studied. A TI has a gapless surface, its bulk is insulating, but its surface is metallic as a result of two-dimensional massless Dirac fermions on the surface [4–6]. Because of spin-orbit interactions on the surface the spin and momentum of Dirac fermions are perfectly linked to each other. The relation between a TI's spin and momentum is dubbed “spin-momentum locking,” and the direction in which they travel is perpendicular to each other. Because of spin-momentum locking, unconventional spin-related phenomena—such as magnetoresistance [7–15], the magnetoelectric effect [16–21], diffusive charge-spin transport [22–25], and the spin pumping effect [26–31]—have so far been the only phenomena theoretically and experimentally studied.

Of the unconventional phenomena on the surface of a TI, spin pumping is one of the most interesting when it comes to spintronics. Here spin pumping on the surface is different from that in metals. As a result of spin-momentum locking on the surface the localized spin plays the role of a vector potential, whereas time-differential localized spin effectively plays the role of an electric field acting on electrons on the surface of the TI [16–19]. As a result, even in the absence of an applied electric field, the charge current is generated by time-dependent localized spin as shown in **Figure 1**. The induced charge current flows along $\mathbf{z} \times \partial_t \mathbf{S}$ [28–31]. Actually, this spin pumping effect on the surface has been experimentally demonstrated in the junction of the TI by attaching magnetic materials [29–31] by changing the half-width value when ferromagnetic resonance is realized in the attached magnetic material [32, 33].

Recently, it has been reported that localized spin on the surface of a TI subject to magnetism depends on space and its spin texture seems to be a magnetic domain wall [34]. It is predicted that in the presence of a spatial-dependent spin structure the charge current, which reflects the spin structure, is induced [28]. Moreover, the spin current as well as the charge density are induced when an inhomogeneous spin structure exists on the surface. Detailed results are shown in Section 2. This study may help the study of spin pumping on the surface of a TI with inhomogeneous spin textures [35, 36].

Recently, the next generation of spintronics has been theoretically and experimentally studied in Weyl-Dirac semimetals. A Weyl-Dirac semimetal possessing three-dimensional massless Dirac fermions has attracted much attention in condensed matter physics [37–39]. Such a semimetal has been experimentally demonstrated [40–45]. In addition, Weyl-Dirac semimetals have been theoretically predicted in a superlattice heterostructure based on the TI. Such a heterostructure has been realized in the GeTe/Sb₂Te₃ superlattice [46].

Spin-momentum locking occurs in a Weyl-Dirac semimetal, but the locking is slightly different from that on the surface of the TI. As a result of spin-momentum locking, the spin polarization (charge density) and the charge current (spin current) are linked to each other. Moreover, Dirac fermions have helicity degrees of freedom, which are decomposed into left- and right-handed fermions. Note that the total charge flow of Dirac fermions of left- and right-handed Weyl

fermions is preserved. In a Weyl–Dirac semimetal the anomaly-related effect, which is discussed in the field of relativistic high-energy physics, has also been discussed in condensed matter physics. Studies up to the moment have asserted that the charge current is generated by magnetic properties with helicity degrees of freedoms [47–54]. Our goal is to introduce the helicity-dependent spin pumping effect, one of the characteristic properties of Dirac fermions (as shown in Section 3).

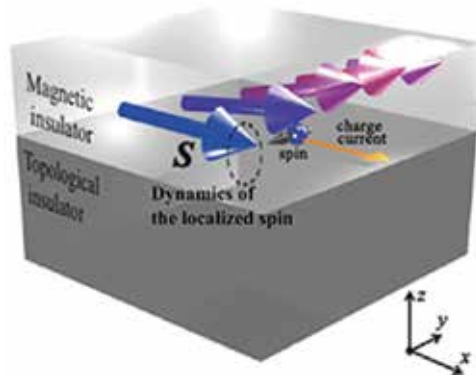


Figure 1. Schematic of spin pumping on the surface of a topological insulator with localized spins of the attached magnetic insulator. Here, the localized spin depends on positions on the surface. The dynamics of the localized spin (dashed line) drives the charge current (orange arrow) on the surface. Then, the charge current is also polarized because of spin–momentum locking on the surface.

2. Spin and charge transport due to spin pumping on the surface of a topological insulator

2.1. Model

We will calculate the charge and spin current due to spin pumping on the surface of a TI with an attached magnetic insulator (MI) (as illustrated in **Figure 1**). To do so, we consider the following low-energy effective Hamiltonian, which describes the surface of the TI with localized spin of the MI [4]:

$$H = H_{\text{TI-surface}} + H_{\text{ex}} + H_{\text{imp}}, \quad (1)$$

where $H_{\text{TI-surface}}$, H_{ex} , and H_{imp} are the low-energy effective Hamiltonian on the surface of the TI, the spin–exchange interaction between the localized spin of the attached MI and the spin of conduction electrons, and the nonmagnetic impurity scattering on the surface of the TI, respectively. $H_{\text{TI-surface}}$ is given by

$$\sum_{\vec{k}} \psi_{\vec{k}}^{\dagger} [-\hbar v_{F,B} (\vec{k} \times \vec{\sigma})_z - E_F] \psi_{\vec{k}} \quad (2)$$

where $v_{F,B}$, E_F , \vec{k} , and $\vec{\sigma}$ are the velocity of bare electrons, the Fermi energy, momentum on the surface of the TI, and the Pauli matrix in the spin space, respectively; and $\Psi_{\vec{k}} = (\Psi_{\uparrow}, \Psi_{\downarrow})$ and Ψ^{\dagger} are the annihilation and creation operators of the electrons with up-spin and down-spin index (\uparrow, \downarrow). H_{ex} is represented by

$$H_{\text{ex}} = -J_{\text{ex}} \int dx^2 \psi^{\dagger} (\vec{S} \cdot \vec{\sigma}) \psi, \quad (3)$$

where J_{ex} is the coefficient of the exchange interaction; and \vec{S} is the localized spin of the MI on the surface. Here, we take into account the space- and time-dependence of \vec{S} . H_{imp} is given by

$$H_{\text{imp}} = \int dx^2 \psi^{\dagger} u_{\text{imp}} \psi \quad (4)$$

Nonmagnetic impurity scattering is taken into account for a delta function type [19, 21–24] and is considered within the Born approximation. Because of impurity scattering the Fermi velocity of bare Dirac fermions in Eq. (2) is modified by $v_{F,B} \rightarrow v_F$ [23, 24, 28]. We use v_F in what follows.

2.2. Charge and spin current due to localized spin dynamics

We will calculate the charge and spin current as well as the charge and spin density due to magnetization dynamics on the surface of the TI. They are given using the Keldysh–Green function and the lesser component of Green's function [48] as

$$\begin{aligned} \langle j^i(x, t) \rangle &= ev_F \langle \psi^{\dagger}(x, t) \sigma^i \psi(x, t) \rangle = -i \frac{\hbar}{2\pi} ev_F \text{tr}[\sigma^i G^<(x, t; x, t)] = \frac{ev_F}{2} \langle s^i \rangle, \\ \langle j_{s,\alpha}^i(x, t) \rangle &= \frac{1}{2} v_F \varepsilon^{z\alpha i} \langle \psi^{\dagger}(x, t) \psi(x, t) \rangle = -\frac{i\hbar}{h} v_F \varepsilon^{z\alpha i} \text{tr}[G^<(x, t; x, t)] = \frac{v_F}{2e} \varepsilon^{z\alpha i} \langle \rho \rangle. \end{aligned} \quad (5)$$

As a result of spin–momentum locking the charge current $\langle j^i \rangle$ and spin current $\langle j_{s,\alpha}^i \rangle$ are proportional to the spin density $\langle s^i \rangle$ and charge density $\langle \rho \rangle$, respectively, where $\langle \rangle =$ denotes the expectation value in H and $e (<0)$ is the charge of Dirac fermions. These relations are derived from the Heisenberg equation. The superscript and subscripts in $\langle j_{s,\alpha}^i \rangle$ show the direction of flow and spin of the spin current, respectively. In what follows the charge and spin current are considered within the linear response to H_{ex} . This assumption can be a good approximation because the energy scale of the exchange interaction is smaller than that of the bandwidth of the low-energy effective Hamiltonian on the surface of the TI [28, 31]. We also assume the TI has a metallic surface of and that a finite Fermi surface exists on the surface; that is, $\hbar/(E_F \tau) \ll 1$ where \hbar is the Planck constant and τ is the relaxation time of nonmagnetic impurity scatterings on the surface.

The charge and spin current are represented by

$$\begin{aligned}
 j^i(x, t) &= \frac{ie\hbar v_F J_{\text{ex}}}{L^2} \sum_{q, \Omega} e^{i(\Omega t - q \cdot x)} \text{tr}[\sigma^i \Pi^j(q, \Omega)] S r_{q, \Omega}^j, \\
 j_{s, \alpha}^i(x, t) &= \frac{i\hbar v_F J_{\text{ex}}}{2L^2} \varepsilon^{z\alpha i} \sum_{q, \Omega} e^{i(\Omega t - q \cdot x)} \text{tr}[\Pi^j(q, \Omega)] S r_{q, \Omega}^j,
 \end{aligned}
 \tag{6}$$

where q and Ω are the momentum and frequency of the localized spin $S_{q, \Omega}^j$, respectively; L^2 is the area of the surface; and Π^j is the response function. These currents are obtained from Π^j :

$$\Pi^j(\vec{q}, \Omega) = \sum_{\omega, \vec{k}} (f_{\omega+\Omega/2} - f_{\omega-\Omega/2}) g_{\omega-\Omega/2, \vec{k}-\vec{q}/2}^R \Lambda^j(\vec{q}, \Omega) g_{\omega+\Omega/2, \vec{k}+\vec{q}/2}^A \tag{7}$$

where f_{ω} , $g_{\omega, \vec{k}}^R = ([g_{\omega, \vec{k}}^A]^\dagger) = [h\omega/(2\pi) + E_F - \hbar v_F/(2\pi)(\mathbf{k} \times \boldsymbol{\sigma})_z + i\hbar/(4\pi\tau)]^{-1}$, and Λ^j are the Fermi distribution function, the retarded (advanced) Green function, and the vertex correction of the ladder diagram, respectively. The above functions are estimated in the regime $\Omega\tau \ll 1$ and $qv_F\tau \ll 1$, which are satisfied when the dynamics of the localized spin is lower than the terahertz regime and the spatial gradient of the localized spin is slow compared with the electron mean free path. Then, by expanding Ω and q within $\Omega\tau \ll 1$ and $qv_F\tau \ll 1$, the vertex function Λ^j is represented by $\Lambda^j = [\Gamma + \Gamma^2 + \Gamma^3 + \dots]^j \sigma^n = [(1 - \Gamma)^{-1}]^j \sigma^n$ with

$$\Gamma^j \equiv n_c u_i^2 \sum_{\omega, \vec{k}} g_{\omega-\Omega/2, \vec{k}-\vec{q}/2}^R \sigma^j g_{\omega+\Omega/2, \vec{k}+\vec{q}/2}^A = \Gamma^j \sigma^n \tag{8}$$

where Γ^j ($|\Gamma^j| < 1$) is the 3×3 matrix ($j, n = 0, x, y$). As a result, Π^j is given by

$$\begin{pmatrix} \Pi^0 \\ \Pi^x \\ \Pi^y \end{pmatrix} = -\frac{\Omega}{2\pi} \begin{pmatrix} \frac{l}{q^2 |^2 + i\Omega\tau} & \frac{i|q_y}{q^2 |^2 + i\Omega\tau} & \frac{-i|q_x}{q^2 |^2 + i\Omega\tau} \\ \frac{ilq_y}{q^2 |^2 + i\Omega\tau} & l - \frac{q^2 |^2}{2(q^2 |^2 + i\Omega\tau)} & \frac{q_x q_y |^2}{q^2 |^2 + i\Omega\tau} \\ \frac{-i|q_x}{q^2 |^2 + i\Omega\tau} & \frac{q_x q_y |^2}{q^2 |^2 + i\Omega\tau} & l - \frac{q^2 |^2}{2(q^2 |^2 + i\Omega\tau)} \end{pmatrix} \begin{pmatrix} \sigma^0 \\ \sigma^x \\ \sigma^y \end{pmatrix} \tag{9}$$

where σ^0 is the identity matrix; and l is the mean free path on the surface. From Eqs. (5–9) the spin and charge current are given by

$$\begin{aligned}\langle j^i \rangle &= -2ev_e^{\text{TI}} J_{\text{ex}} v_F \tau \left((\bar{z} \times \partial_t \bar{S}^{\parallel})^i - \ell^2 [\bar{z} \times (\bar{z} \times \bar{\nabla})] [\bar{\nabla} \times \partial_t \langle \bar{S}^{\parallel} \rangle_{\text{D}}] \right)_z, \\ \langle j_{s,\alpha}^i \rangle &= \varepsilon^{z\alpha i} v_e^{\text{TI}} J_{\text{ex}} v_F \ell^2 [\bar{\nabla} \times \partial_t \langle \bar{S}^{\parallel} \rangle_{\text{D}}]_z,\end{aligned}\quad (10)$$

where v_e^{TI} is the density of state on the surface of the TI; $\langle S^{\parallel} \rangle_{\text{D}}$ is the convolution between S^{\parallel} and the diffusion propagator D on the surface; and S^{\parallel} is the in-plane localized spin $S^{\parallel} = S - S^z z$ as

$$\begin{aligned}\langle \bar{S}^{\parallel} \rangle_{\text{D}} &\equiv \frac{1}{\tau} \int_{-\infty}^{\infty} dt' \int dx' D(x - x', t - t') \bar{S}^{\parallel}(x', t'), \\ D(x - x', t - t') &= \frac{1}{L^2} \sum_{\bar{q}, \Omega} \frac{1}{q^2 v_F \tau + i\Omega} e^{i(\Omega t - \bar{q} \cdot \bar{x})}.\end{aligned}\quad (11)$$

Eq. (10) shows that time-dependent localized spin induces the charge and spin current and that they can be decomposed into local and nonlocal contributions. The first term in Eq. (10) is the charge current due to spin dynamics at that position on the surface; its direction is along the $z \times \partial_t S^{\parallel}$ direction [28–31]. On the other hand, the second term in Eq. (10) is the charge current due to both time- and spatial-dependent localized spin; its direction is along the $[z \times (\bar{z} \times \partial)] [\partial \times \partial_t \langle S^{\parallel} \rangle_{\text{D}}]_z$ direction, where $\langle S^{\parallel} \rangle_{\text{D}}$ indicates the nonlocal contribution from the localized spin. Moreover, this term is zero when the spin texture is spatially uniform. Therefore, this charge current is caused by diffusion with the dynamics of the spatial inhomogeneous spin texture. It is noted that this second term is also described by the spatial gradient of the charge density.

Because of spin–momentum locking on the surface of the TI, spin polarization is given by $\langle j \rangle = 2ev_F(z \times \langle s \rangle)$. Thus, the properties of spin polarization are similar to those of the charge current.

Eq. (11) shows that the spin current is induced by the time- and spatial-dependent S^{\parallel} . Then, the charge density is also generated because of spin–momentum locking. In addition, the second term of the charge current $\langle j \rangle_{\text{nonlocal}} = 2ev_F v_e^{\text{TI}} J_{\text{ex}} \tau \ell^2 [z \times (\bar{z} \times \partial)] [\partial \times (\partial_t \langle S^{\parallel} \rangle_{\text{D}})]_z$ is given by the spatial gradient of the charge density, whereas $\langle j \rangle_{\text{nonlocal}}$ is proportional to the spatial gradient of the spin current [28] as

$$\langle j^i \rangle_{\text{nonlocal}} = -e \ell \varepsilon^{z\alpha n} \nabla^i \langle j_{s,\alpha}^n \rangle. \quad (12)$$

This result shows that the relation between the charge and spin current is different from that in the metallic spintronics system [2]. The spin current is proportional to the charge current and spin current flow is perpendicular to the charge flow and its spin polarization.

Note that no out-of-plane localized spin $S^z z$ contributes in a dominant way to charge and spin current generation. The reason is σ^z does not couple with momentum p in Eq. (2). Therefore,

we believe a warping effect [1–4] on the surface of the TI is likely. Spin polarization along the z -direction is also generated by spin dynamics.

2.3. Spin torque

Based on these results, we look at localized spin dynamics after generation of the charge current and spin polarization on the surface [24]. We assume there is an external static and AC magnetic field on the surface—as shown in **Figure 2(a)**. The static magnetic field arranges the localized spin texture and the AC magnetic field triggers its spin dynamics. The propagation direction of the microwave is parallel to the static magnetic field, which is along the y -axis. The texture is called the “longitudinal conical spin order” [56].

After applying the microwave the dynamics of the localized spin of the MI is induced by the in-plane AC magnetic field of the microwave. The dynamics of the spin induces the charge and spin current. Then, from $\langle j \rangle = 2ev_F(z \times \langle s \rangle)$, Eq. (10), and spin–momentum locking, spin polarization is also generated. Note that spin polarization induced in this way acts on the localized spin as an effective exchange field for localized spin. This contribution is given from the Landau–Lifshitz–Gilbert (LLG) equation of motion [32, 33] on the surface of the TI:

$$\partial_t \vec{M} \equiv -\gamma\mu(\vec{M} \times \vec{H}) + \frac{\alpha_G}{M}(\vec{M} \times \partial_t \vec{M}) + \vec{T}_e \quad (13)$$

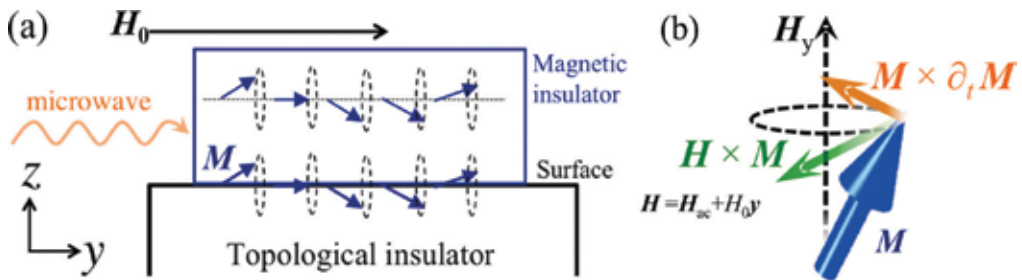


Figure 2. (a) Schematic of the setup used to detect spin and charge current generation. The texture of the magnetization M depends on space. Such magnetization is along the applied static magnetic field H_0 , and the magnetization dynamics is induced by the applied magnetic field of the microwave. (b) Schematic of the spin torque acting on M .

where $M = -M(S/S)$ is magnetization of the MI; γ is the gyromagnetic ratio; μ is permeability; α_G is a Gilbert damping constant; $H = H_0 + H_{AC}$ are the applied magnetic fields on the surface; and H_0 and H_{ac} denote the static and AC magnetic fields, respectively. The first term of Eq. (13) denotes the field-like torque that drives the dynamics of M . The second term is the damping torque that prevents its dynamics—these terms are schematically illustrated in **Figure 2(b)**.

The third term T_e is the spin torque due to spin polarization of Dirac fermions on the surface of the TI ($\langle s \rangle$). It is given by $T_e = 2J_{\text{ex}}a^2 (\mathbf{M} \times \langle s \rangle)$, where a is the lattice constant on the surface.

Since T_e is proportional to $\langle s \rangle$, this torque is decomposed into local (T_e^{L}) and nonlocal spin torque (T_e^{D}) terms as

$$\begin{aligned}\bar{T}_e^{\text{L}} &= \frac{\kappa}{M^{\parallel}} \bar{\mathbf{M}} \times \partial_t \bar{\mathbf{M}}^{\parallel}, \\ \bar{T}_e^{\text{D}} &= \frac{\kappa}{M^{\parallel}} \ell^2 \bar{\mathbf{M}} \times (z \times \bar{\nabla})(\bar{\nabla} \times \partial_t \langle \bar{\mathbf{M}}^{\parallel} \rangle_{\text{D}})_z,\end{aligned}\quad (14)$$

where $M^{\parallel} = -M(S^{\parallel}/S)$ is in-plane magnetization; and κ is the dimensionless coefficient.

As a result of spin-momentum locking the torque is $T_e \sim \mathbf{M} \times \langle \mathbf{j} \rangle$. This relation is useful as a way of detecting nonzero $\langle \mathbf{j} \rangle$ [29–31]. Moreover, nonlocal spin torque can be described by $T_e^{\text{D}} \sim \mathbf{M} \times \langle \mathbf{j} \rangle_{\text{nonlocal}}$. Eq. (12) shows this torque may well be affected by spin current contribution, whereas the relation between spin torque and spin current can be used as a way to detecting $\langle j_{s,\alpha}^i \rangle$ on the surface:

$$\bar{T}_e^{\text{D}} = \frac{J_{\text{ex}} \tau a^2}{\hbar} \varepsilon^{zai} \bar{\mathbf{M}} \times [(z \times \bar{\nabla})(\bar{\nabla} \times \langle j_{s,i}^a \rangle)]. \quad (15)$$

We now consider magnetization when it is given by $\mathbf{M} = (M_x, M_y, M_z) = [m \cos(\mathbf{q} \cdot \mathbf{x} - \Omega t), M_y, m \sin(\mathbf{q} \cdot \mathbf{x} - \Omega t)]$ with $\mathbf{q} = (q_x, q_y)$, $m^2 \ll M_y$, $M_y \sim M$, and $\partial_t M_y \sim 0$. Such a time-dependent magnetic structure is assumed to be realized when the magnitude of the static magnetic field is larger than that of the AC magnetic field $H_{\text{AC}} = (h_x, 0, h_z)$; that is, $h_x, h_z \ll H_0$. Then, substituting this \mathbf{M} into Eqs. (13) and (14), the LLG equation becomes a linear approximation:

$$\begin{aligned}\partial_t m_x &= \omega_H m_z - \omega_M h_z + \alpha_G \partial_t m_z, \\ \partial_t m_z &= -\omega_H m_x + \omega_M h_x - (\alpha_G + \kappa) \partial_t m_z + \kappa q_y^2 \partial_t \langle M^{\parallel,x} \rangle_{\text{D}},\end{aligned}\quad (16)$$

where $\omega_H = \gamma \mu H$ and $\omega_M = \gamma \mu M$ are the angular frequencies of H_0 and M , respectively; and $\kappa q_y^2 \partial_t \langle M^{\parallel,x} \rangle_{\text{D}}$ indicates the contribution from T_e^{D} . Substituting $\langle M^{\parallel,x} \rangle_{\text{D}}$ into Eq. (13), we obtain magnetic permeability around the surface:

$$\begin{pmatrix} m_x \\ m_z \end{pmatrix} = \begin{pmatrix} \chi_{xx} & \chi_{xz} \\ \chi_{zx} & \chi_{zz} \end{pmatrix} \begin{pmatrix} h_x \\ h_z \end{pmatrix} \quad (17)$$

where χ_{xx} and χ_{zx} denote the longitudinal and transverse magnetic permeability as

$$\begin{aligned} \chi_{xx}(q, \Omega) &= \frac{(\omega_H + i\alpha\Omega)\omega_M}{[\omega_H + i\alpha\Omega][\omega_H + i(\alpha\tilde{k}_{q,\Omega})\Omega] - \zeta_{q,\Omega}\Omega^2}, \\ \chi_{zz}(q, \Omega) &= \frac{\omega_H + i(\alpha + \tilde{k}_{q,\Omega})\Omega}{\omega_H + i\alpha\Omega} \chi_{xx}(q, \Omega), \\ \chi_{xz}(q, \Omega) &= -\zeta_{q,\Omega}\chi_{xx}(q, \Omega) = -\chi_{zx}. \end{aligned} \tag{18}$$

The coefficients $\kappa'_{q,\Omega}$ and $\zeta_{q,\Omega}$ are given by

$$\kappa'_{q,\Omega} = \kappa \left(1 - \frac{q^4 l^4}{q^4 l^4 + \Omega^2 \tau^2} \right), \quad \zeta_{q,\Omega} = 1 + \kappa \frac{q^2 l^2 \Omega \tau}{q^4 l^4 + \Omega^2 \tau^2}. \tag{19}$$

Hence, $\kappa'_{q,\Omega}$ and $\zeta_{q,\Omega}$ depend on q and Ω . If $q = 0$, $\kappa'_{q,\Omega}$ and $\zeta_{q,\Omega}$ go to $\kappa'_{q,\Omega} \rightarrow \kappa$ and $\zeta_{q,\Omega} \rightarrow 1$, respectively. Then, the magnetic permeability is isotropic. In $q = 0$, χ_{xx} and χ_{zz} go to the same value and $\chi_{xz} = -\chi_{zx}$ is satisfied. On the other hand, in nonzero q the magnetic permeability is anisotropic: $\chi_{xx} \neq \chi_{zz}$.

Figure 3(a) shows the dependence of Ω on the imaginary part of the longitudinal magnetic permeability for several q . The resonance frequency Ω_r and the half-width value $\Delta\Omega$ are slightly changed by the nonzero q . **Figure 3(b)** shows change in the resonance frequency for several f_H in greater detail— f_H is the frequency described by the static magnetic field H_0 . The resonance frequency decreases with increasing ql from $ql = 0$ into $ql = q_0 l$, where q_0 satisfies $q_0^2 l^2 \sim \Omega\tau$. In

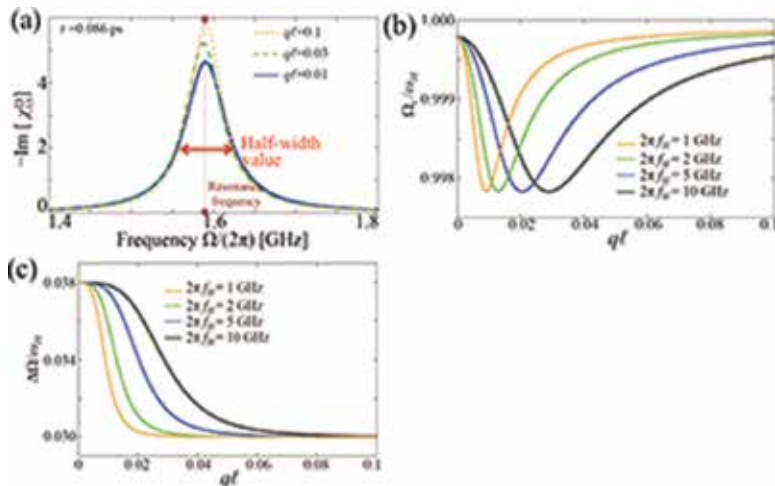


Figure 3. (a) Frequency dependence of the imaginary part on the longitudinal magnetic permeability of several ql . The half-width value and resonance frequency change according to ql . (b) Dependence of ql on the resonance frequency for several frequencies of the applied static magnetic field. (c) Dependence of ql on the half-width of several frequencies of the static magnetic field [49].

addition, when ql takes a large value the resonance frequency returns to that frequency at $ql=0$. **Figure 3(c)** shows the momentum dependence of the half-width value on renormalization by the angular frequency of the applied magnetic field for several $\omega_H = 2\pi f_H$ frequencies when realistic parameters on the surface of the TI are taken into account [31]. Change in the normalized half-width value $\Delta\Omega/\omega_H(ql)$ decreases from $\Delta\Omega/\omega_H(ql=0) = 0.038$ to $\Delta\Omega/\omega_H(ql \sim 0.1) = 0.030$ with increasing ql .

Any change in the half-width value $\Delta\Omega$ indicates an induced charge current on the surface of the TI because $T_e^L + T_e^D$ is proportional to the induced charge current [29–31]. In addition, the half-width value $\Delta\Omega$ of T_e^D represents a contribution from the spatial gradient of the spin current. These relations can be useful for the detection of spin current. For example, let us suppose that in a finite ql , $\Delta\Omega$ includes the contribution from the whole of the spin torque T_e and the contribution from the nonlocal term T_e^D is reduced by the large magnetic field. In a higher magnetic field the inhomogeneous spin texture would be expected to be aligned along the magnetic field direction and the spin texture to be spatially uniform; hence, the value of ql decreases and reaches zero. Then, the half-width value $\Delta\Omega(T_e^D = 0)$ has no contribution from T_e^D . The difference $\Delta\Omega(T_e^D \neq 0) - \Delta\Omega(T_e^D = 0)$ includes a pure contribution from T_e^D .

Any contribution from the applied magnetic field is of course a concern. Note that an in-plane static magnetic field contributes no finite charge current generation or spin polarization [49], whereas the contribution from the applied magnetic field is negligible.

3. Spin pumping in a Weyl–Dirac semimetal

3.1. Model

We now consider spin pumping in a Weyl–Dirac semimetal subjected to magnetism. To do this, a Weyl–Dirac semimetal subjected to spin and momentum locking, such as a superlattice heterostructure constructed from a TI/normal insulator/TI [39, 46–48], is considered. The low-energy effective Hamiltonian describing the Weyl–Dirac semimetals that have a spin–exchange interaction is given by [50–52]

$$H = H_{\text{Weyl}} + H_{\text{ex}} + H_{\text{imp}}. \quad (20)$$

The first term takes the form

$$H_{\text{Weyl}} = \sum_k \Psi_k^\dagger [\hbar v_F \tau^z \otimes (\bar{k} - \tau^z \bar{b}) \cdot \sigma - \mu \tau^0 \otimes \sigma^0 - \mu^5 \tau^z \otimes \sigma^0] \Psi_k, \quad (21)$$

where $\Psi_k = {}^t(\Psi_{\uparrow,+}, \Psi_{\downarrow,+}, \Psi_{\uparrow,-}, \Psi_{\downarrow,-})$ is the annihilation operator of an electron with spin (\uparrow, \downarrow) and helicity $\tau(+, -)$ degrees of freedom; $\tau^{\alpha=0,x,y,z}$ and $\sigma^{\alpha=0,x,y,z}$ are Pauli matrices of the helicity and spin, respectively; v_F is the Fermi velocity; μ is the chemical potential of the Weyl–Dirac semimetal;

and \mathbf{b} and μ^5 denote the difference in position between each Weyl cone in momentum and energy space, respectively. In Dirac semimetals, we set $\mathbf{b} = 0$ and $\mu^5 = 0$.

The second term of Eq. (20) indicates the spin–exchange interaction:

$$H_{\text{ex}} = -J_{\text{ex}} \int dx \psi^\dagger [\tau^0 \otimes \vec{S} \cdot \vec{\sigma}] \psi, \quad (22)$$

where J_{ex} is the coefficient of the exchange interaction; and \mathbf{S} is the localized spin that depends on space and time in the Weyl semimetal. This exchange interaction is independent of the helicity index. H_{imp} shows the nonmagnetic impurity scattering in the Weyl–Dirac semimetal:

$$H_{\text{imp}} = \int dx u_{\text{imp}} \psi^\dagger [\tau^0 \otimes \sigma^0] \psi. \quad (23)$$

This Hamiltonian is similar to that on the surface of the TI—see Eq. (4). In the following calculations, H_{ex} and H_{imp} are treated as perturbations within the same formalism as laid out in Section 2.2. This treatment is allowed when the energy scale of the exchange interaction is smaller than the bandwidth of Eq. (21). Then, the low-energy effective Hamiltonian in Eq. (21) gives a good approximation.

3.2. Response function within the linear response to the exchange interaction

To calculate the charge and spin current within the linear response to H_{ex} , we use Green's functions. From Eq. (20) the charge current $\langle j^i \rangle$ ($i = x, y, z$) can be defined by

$$\langle j^i(x, t) \rangle = ev_F \langle \psi^\dagger(x, t) (\tau^z \otimes \sigma^i) \psi(x, t) \rangle. \quad (24)$$

where $\langle \rangle$ denotes the expectation value in Eq. (20). Such a charge current can be decomposed as $\langle j \rangle = \langle j_+ \rangle + \langle j_- \rangle$, where $\langle j_\pm \rangle = \pm ev_F \langle \Psi_\pm^\dagger \sigma \Psi_\pm \rangle$ and $\Psi_\pm = (\Psi_{1,\pm}, \Psi_{2,\pm})$ is the annihilation operator around each helicity $\tau = \pm 1$. Since there is no mixing between $\Psi_{1,+}^\dagger$ and $\Psi_{1,-}$ in the Hamiltonian in Eq. (20) the charge current around each helicity can be calculated separately. Because of spin–momentum locking in the Weyl–Dirac semimetal the charge current links to the spin polarization. The charge current of each helicity is proportional to the spin polarization of each helicity as

$$\langle j_\pm^i(x, t) \rangle = \pm \frac{ev_F}{2} \langle s_\pm^i(x, t) \rangle. \quad (25)$$

The spin current in the Weyl–Dirac semimetal can be defined from the Heisenberg equation for the spin operator:

$$\partial_t s_\alpha + \partial_i j_{s,\alpha}^i = T_{r,\alpha}, \quad (26)$$

where $j_{s,\alpha}^i$ is the spin current operator; and $T_{r,\alpha}$ is the spin relaxation term. Spin current density can also be decomposed into the spin current density of each helicity and can be calculated separately:

$$\langle j_{s,\alpha,\pm}^i \rangle = \pm \frac{\hbar v_F}{2} \delta_\alpha^i \langle \psi_\pm^\dagger \psi_\pm \rangle = \pm \frac{\hbar v_F}{2e} \delta_\alpha^i \langle \rho_\pm \rangle. \quad (27)$$

The superscript and subscripts of $j_{s,\alpha}^i$ denote the direction of flow and spin of the spin current of each helicity, respectively. The direction of spin is perfectly parallel to that of the flow, and the spin current density is proportional to the charge density of each helicity.

The relaxation term can also be decomposed by $\langle T_r \rangle = \langle T_{r,+} \rangle + \langle T_{r,-} \rangle$ and can be given by $\langle T_{r,\pm} \rangle$:

$$\langle T_{r,\pm} \rangle = \mp \frac{i\hbar v_F}{2} \varepsilon^{\alpha\beta} \langle \psi_\pm^\dagger \sigma^\beta (\partial^i \psi_\pm) - (\partial^i \psi_\pm^\dagger) \sigma^\beta \psi_\pm \rangle. \quad (28)$$

The charge and spin current can be obtained by calculating the response function (**Figure 4**):

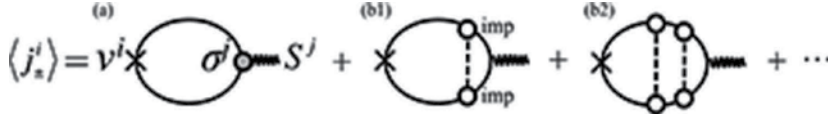


Figure 4. Diagrammatic representation of the charge current of each helicity within the linear response to the exchange interaction. The bold line is Green's function; v^i is the velocity operator; and S^j is the localized spin (wavy lines). (a) A bubble diagram without taking impurity scattering from the exchange interactions into account. (b1) and (b2) Bubble diagrams that take impurity scattering within the ladder approximation into account.

$$\begin{aligned} \langle j_\pm^i \rangle &= \pm \frac{ie\hbar v_F J_{\text{ex}}}{L^3} \sum_{\vec{q}, \Omega} e^{i(\Omega t - \vec{q} \cdot \vec{x})} \text{tr}[\sigma^i \Pi_\pm^j(\vec{q}, \Omega)] S_{\vec{q}, \Omega}^j, \\ \langle j_{s,\alpha,\pm}^i \rangle &= \mp \frac{i\hbar v_F J_{\text{ex}}}{2L^3} \delta_\alpha^i \sum_{\vec{q}, \Omega} e^{i(\Omega t - \vec{q} \cdot \vec{x})} \text{tr}[\Pi_\pm^j(\vec{q}, \Omega)] S_{\vec{q}, \Omega}^j, \end{aligned} \quad (29)$$

where \vec{q} and Ω are the momentum and frequency of the localized spin, respectively; L^3 is the volume of the system; and Π_\pm^j is the response function within the helicity index:

$$\Gamma_\pm^j \equiv n_c u_1^2 \sum_{\omega, \vec{k}} g_{\omega-\Omega/2, \vec{k}-\vec{q}/2, \pm}^R \sigma^j g_{\omega-\Omega/2, \vec{k}-\vec{q}/2, \pm}^A = \Gamma_\pm^{jn} \sigma^n. \quad (30)$$

where f_{ω} , $g_{\omega, k_{\pm}}^R = ([g_{\omega, k_{\pm}}^A]^\dagger) = [\hbar v_F / (2\pi) + \mu_{\pm} - \hbar v_F \mathbf{k} \cdot \boldsymbol{\sigma} / (2\pi) + i\hbar / (4\pi\tau_{\pm})]^{-1}$, and Λ_{\pm}^i are the Fermi distribution function, the retarded (advanced) Green's function, and the vertex correction of the ladder diagram at each helicity \pm , respectively; and τ_{\pm} is the relaxation time of nonmagnetic impurities in the material, which depends on the helicity, because it depends on the chemical potential μ_{\pm} . When $\Omega\tau_{e,\pm} \ll 1$ and $qv_F\tau_{e,\pm} \ll 1$ are satisfied the vertex function Λ_{\pm}^i is given by $\Lambda_{\pm}^i = [\Gamma_{\pm} + \Gamma_{\pm}^2 + \Gamma_{\pm}^3 + \dots]^n \sigma^n = [(1 - \Gamma_{\pm})^{-1}]^n \sigma^n$ with

$$\Gamma_{\pm}^j \equiv n_c u_i^2 \sum_{\omega, \mathbf{k}} g_{\omega - \Omega/2, \mathbf{k} - \mathbf{q}/2, \pm}^R \sigma^j g_{\omega + \Omega/2, \mathbf{k} + \mathbf{q}/2, \pm}^A = \Gamma_{\pm}^{jn} \sigma^n \quad (31)$$

where Γ_{\pm}^{jn} ($|\Gamma_{\pm}^{jn}| < 1$) is a 4×4 matrix ($j, n = 0, x, y, z$). As a result, Π_{\pm}^i can be represented by

$$\begin{pmatrix} \Pi_{\pm}^0 \\ \Pi_{\pm}^x \\ \Pi_{\pm}^y \\ \Pi_{\pm}^z \end{pmatrix} = \begin{pmatrix} \Pi_{\pm}^{00} & \Pi_{\pm}^{0x} & \Pi_{\pm}^{0y} & \Pi_{\pm}^{0z} \\ \Pi_{\pm}^{x0} & \Pi_{\pm}^{xx} & \Pi_{\pm}^{xy} & \Pi_{\pm}^{xz} \\ \Pi_{\pm}^{y0} & \Pi_{\pm}^{yx} & \Pi_{\pm}^{yy} & \Pi_{\pm}^{yz} \\ \Pi_{\pm}^{z0} & \Pi_{\pm}^{zx} & \Pi_{\pm}^{zy} & \Pi_{\pm}^{zz} \end{pmatrix} \begin{pmatrix} \sigma^0 \\ \sigma^x \\ \sigma^y \\ \sigma^z \end{pmatrix} \quad (32)$$

where the above matrix component ($m, m' = x, y, z$) is

$$\begin{aligned} \Pi_{\pm}^{00} &= -\frac{\Omega}{4\pi} \frac{2 + i\Omega\tau_{e,\pm}}{q^2 v_F^2 \tau_{e,\pm} / 2 + i\Omega}, \\ \Pi_{\pm}^{m0} = \Pi_{\pm}^{0m} &= \mp \frac{\Omega}{4\pi} \frac{iv_F q^m}{q^2 v_F^2 \tau_{e,\pm} / 2 + i\Omega} \\ \Pi_{\pm}^{mm'} &= -\frac{\Omega}{4\pi} \left(1 - \frac{v_F^2 \tau_{e,\pm}^2 q^m q^{m'}}{q^2 v_F^2 \tau_{e,\pm} / 2 + i\Omega} \right). \end{aligned} \quad (33)$$

As a result, the charge current and spin current can be obtained by

$$\langle j_{\pm}^i \rangle = \pm \frac{ev_F J_{\text{ex}} \nu_{\pm}^{\text{WS}} \tau_{e,\pm}}{2} \partial_i \bar{S} - \frac{1}{6} v_F^2 \tau_{\pm} \bar{\nabla} \langle \rho_{\pm} \rangle, \quad (34)$$

$$\langle j_{s, \alpha, \pm}^i \rangle = \pm \frac{\hbar v_F}{2e} \delta_{\alpha}^i \langle \rho_{\pm} \rangle, \quad (35)$$

where ν_{\pm}^{WS} and $\langle \rho_{\pm} \rangle$ are the charge density of state and the induced charge density of each helicity, respectively:

$$\langle \rho_{\pm} \rangle = \mp \frac{1}{2} e v_F J_{\text{ex}} v_{\pm}^{\text{WS}} \tau_{e,\pm} \left(\vec{\nabla} \cdot \partial_t \langle \vec{S} \rangle_{\text{D},\pm} \right) \quad (36)$$

where $\langle \mathbf{S} \rangle_{\text{D},\pm}$ is the convolution between the localized spin and diffusive propagation of each helicity. $\langle \mathbf{S} \rangle_{\text{D},\pm}$ can be defined by

$$\begin{aligned} \langle \vec{S} \rangle_{\text{D},\pm} &\equiv \frac{1}{\tau_{e,\pm}} \int_{-\infty}^{\infty} dt' \int dx' D_{\text{W},\pm}(x-x', t-t') \vec{S}(x', t'), \\ D_{\text{W},\pm}(x-x', t-t') &= \frac{1}{L^3} \sum_{\vec{q}, \Omega} \frac{1}{q^2 v_F \tau_{e,\pm} / 2 + i\Omega} e^{i(\Omega t - \vec{q} \cdot \vec{x})}. \end{aligned} \quad (37)$$

Note that the above results are obtained when $\mathbf{b} = 0$. These results are easily generalized when $\mathbf{b} \neq 0$. Because \mathbf{b} behaves like a static Zeeman field acting on the whole of the band of H_{Weyl} , it can shift as a result of Pauli paramagnetism. However, \mathbf{b} cannot drive a net current because \mathbf{b} is static [49]. On the other hand, the dynamics of the localized spin are only effective near the Fermi surface, the structure of which does not depend on \mathbf{b} . Therefore, we obtain the same charge and spin current in Eqs. (33)–(35) even when $\mathbf{b} \neq 0$.

3.3. Charge and spin current due to spin pumping effects

From the above results the total charge current can be given by

$$\langle \mathbf{j}^i \rangle = \frac{e v_F J_{\text{ex}}}{2} (v_+^{\text{WS}} \tau_{e,+} - v_-^{\text{WS}} \tau_{e,-}) \partial_i S^i + \frac{e v_F^3 J_{\text{ex}}}{12} \nabla^i \left[\vec{\nabla} \cdot \partial_t (v_+^{\text{WS}} \tau_{e,+}^2 \langle \vec{S} \rangle_{\text{D},+} - v_-^{\text{WS}} \tau_{e,-}^2 \langle \vec{S} \rangle_{\text{D},-}) \right]. \quad (38)$$

The charge current is triggered by the dynamics of localized spin. The first term indicates the local term of the dynamics of localized spin. Its direction is parallel to $\partial_t \mathbf{S}$. The second term shows the nonlocal term, which is generated by the convolution between localized spin and the diffusion propagator. A nonzero nonlocal term is given when the spin texture of localized spin depends on space. Thus, the driving force needed to induce the charge current is the same as localized spin dynamics, which plays the role of driving the charge current on the surface of the TI. Note that the charge current in a Weyl–Dirac semimetal depends strongly on the valley index. When the difference between τ_+ and τ_- as well as between v_+^{WS} and v_-^{WS} is realized, there is a population imbalance between two of the bands of each helicity. Then, nonzero $\langle \mathbf{j} \rangle$ is induced when $v_+^{\text{WS}} \tau_{e,+} \neq v_-^{\text{WS}} \tau_{e,-}$ or $\mu^5 = 0$.

Note that the property of the charge current at each helicity links to that of spin polarization because of spin–momentum locking. However, after summation of the indices of helicity the relation between total charge current and total spin polarization is changed. As a result, even in the absence of population imbalance, nonzero spin polarization can be given by Eq. (25) as

$$\langle s^i \rangle = \frac{J_{\text{ex}}}{2} (\nu_+^{\text{WS}} \tau_{e,+} + \nu_-^{\text{WS}} \tau_{e,-}) \partial_t S^i + \frac{v_F^2 J_{\text{ex}}}{24} \nabla^i \left[\bar{\nabla} \cdot \partial_t \left(\nu_+^{\text{WS}} \tau_{e,+}^2 \langle \bar{S} \rangle_{D,+} + \nu_-^{\text{WS}} \tau_{e,-}^2 \langle \bar{S} \rangle_{D,-} \right) \right]. \quad (39)$$

Local spin polarization is along $\partial_t S$ and nonlocal spin polarization is along the spatial gradient of $\partial_t(\partial^i S^i)$.

Total spin current can be represented from Eqs. (35) and (36) as

$$\langle j_{s,\alpha}^i \rangle = -\frac{\hbar v_F^2 J_{\text{ex}}}{4} \delta_\alpha^i \bar{\nabla} \cdot \partial_t \left[\nu_+^{\text{WS}} \tau_{e,+} \langle \bar{S} \rangle_{D,+} + \nu_-^{\text{WS}} \tau_{e,-} \langle \bar{S} \rangle_{D,-} \right]. \quad (40)$$

Total spin current can be generated by spatial divergence of localized spin dynamics, where localized spin is the convolution with diffusion. As a result, the spin current can be regarded as a nonlocal spin current. Note that a nonzero spin current is generated when localized spin depends on space. Such a spin current becomes nonzero even in the absence of population imbalance.

The nonlocal spin current in this case is obtained from the diffusive motion of spin density, which is driven by the dynamics of localized spin, where localized spin depends on space. The spin diffusive motion of each helicity can be given from Eqs. (25), (34), (37) as

$$\left(\partial_t - \frac{1}{2} v_F^2 \tau_{e,\pm} \right) \langle s_\pm^i \rangle = \frac{e v_F^3 \tau_{e,\pm}^2 J_{\text{ex}}}{2} \nu_\pm^{\text{WS}} \partial_t \nabla (\nabla \cdot S). \quad (41)$$

As a result, the diffusive motion of total spin becomes:

$$\left[\partial_t (\langle s_+^i \rangle + \langle s_-^i \rangle) - \frac{1}{2} v_F^2 (\tau_{e,+} \langle s_+^i \rangle + \tau_{e,-} \langle s_-^i \rangle) \right] = \frac{e v_F^3 J_{\text{ex}}}{2} (\tau_+^2 \nu_{e,+}^{\text{WS}} + \tau_-^2 \nu_{e,-}^{\text{WS}}) \partial_t \nabla (\nabla \cdot S) \quad (42)$$

Time-dependent and spatial-dependent localized spin, $\partial[\partial_t(\partial^i S^i)]$, triggers the diffusive motion of total spin density. When there is no population imbalance between each helicity, diffusive motion can accompany total spin density without any charge flow. Hence, a pure spin current can be generated.

4. Conclusion

Our results on the charge and spin current due to spin pumping on the surface of a three-dimensional TI (Section 2) [28] and in the bulk of a three-dimensional Weyl–Dirac semimetal (Section 3) [51] are summarized in this chapter.

Section 2 summarizes our results on spin pumping on the surface of a TI attached to an MI. The results are calculated using the standard Keldysh–Green function method within the linear response to the exchange interaction between the conduction spin and localized spin of an MI. The purpose of this work is to derive charge and spin current generation due to localized spin dynamics on the disordered surface of a TI; in particular, when the localized spin depends on space on the surface. The main results on the surface of a TI are summarized in **Table 1**. Time-dependent localized spin on the surface is a prerequisite to obtaining nonzero charge and spin current generation. Moreover, **Table 1** shows that when the spin texture is spatially inhomogeneous, not only the local charge but also the nonlocal charge and spin current are generated by time-dependent localized spin. The flow and spin polarization of the spin current are perfectly perpendicular to each other because of spin–momentum locking. The magnitude of the spin current is proportional to the charge density, which is induced by divergence between time-dependent localized spin and the diffusive propagator on the surface—see Eqs. (10) and (11). Such pumping effects are caused by time-dependent localized spin, which plays a role in driving the charge current and can be regarded as an effective electric field E_s^{TI} .

	$\langle j \rangle$	$\langle j_{s,\alpha}^i \rangle$	$\langle s \rangle$	$\langle p \rangle$	Ref.
Local	$z \times \partial_t S^{\parallel}$		$\partial_t S^{\parallel}$		[29–31]
Nonlocal	$\nabla[\nabla \times \partial_t S^{\parallel}_{\text{D}}]_z$	$\epsilon^{z\alpha i}[\nabla \times \partial_t S^{\parallel}_{\text{D}}]_z$	$\nabla[\nabla \times \partial_t S^{\parallel}_{\text{D}}]_z$	$[\nabla \times \partial_t S^{\parallel}_{\text{D}}]_z$	This work [28]
Driving force	$z \times \epsilon_s^{\text{TI}}$	$[\nabla \times \epsilon_s^{\text{TI}} D]_z$	$z \times \epsilon_s^{\text{TI}}$	$[\nabla \times \epsilon_s^{\text{TI}} D]_z$	This work [28]
$\epsilon_s^{\text{TI}} \equiv -\frac{J_{\text{ex}}}{\epsilon v_F} \partial_t S^{\parallel}$	$\nabla[\nabla \times \langle \epsilon_s^{\text{TI}} \rangle_{\text{D}}]_z$		$\nabla[\nabla \times \langle \epsilon_s^{\text{TI}} \rangle_{\text{D}}]_z$		

Table 1. Brief summary of the charge current, spin current, spin, and charge density induced by localized spin dynamics on the disordered surface of a TI. The charge current and spin density have both a local and nonlocal contribution. The spin current and charge density are described by the nonlocal contribution.

Recently, it has been reported that the localized spin texture at the junction of the TI/MI is spatially inhomogeneous [34]. We suppose that the spin current we have obtained at the junction is generated when the spin texture moves temporally.

On the basis of these results, in Section 2.3 we discussed a way of detecting the charge current and spin current induced on the surface of a TI attached to an MI by using ferromagnetic resonance. We assume that the dynamics of localized spin is triggered by the applied static and AC magnetic field of the microwave. The dynamics of the localized spin induced both the charge current and the spin current. Such induced currents are related to spin density, and spin polarization acts on the localized spin in much the same way as spin torque—see Eq. (14). Hence, the half-width of ferromagnetic resonance changes as shown in **Figure 3**.

Spin pumping in a Weyl–Dirac semimetal hosting massless Weyl–Dirac fermions is summarized in section 3. The results are obtained within the same formalism as laid out in Sections 2.1 and 2.2. The charge and spin current as well as the charge and spin density are given in **Table 2**. Semimetals are subject to spin–momentum locking. The spin direction of Weyl–Dirac fermions brought about by spin–momentum locking is perfectly parallel/antiparallel to its momentum and its locking is determined by the helicity degrees of freedom of Weyl–Dirac fermions. As a result, the charge current and spin polarization induced depend on the helicity indices. Eqs. (38) and (39) show that localized spin dynamics induces the charge current and spin polarization, respectively; hence, localized spin plays the role of an effective electric field $E_{s,\pm}^{\text{WDS}}$ acting on electrons [51]. Moreover, $E_{s,\pm}^{\text{WDS}}$ depends on the helicity index, whereas total charge current is proportional to μ^5 . As a result, a nonzero charge current is generated when there is population imbalance between each helicity. On the other hand, localized spin dynamics also drives the spin current when localized spin depends on time and position in a Weyl–Dirac semimetal. The spin current is finite even in the absence of population imbalance. Then, the spin current does not accompany charge flow. These results may be of use to next-generation spintronics devices based on Weyl–Dirac semimetals.

	$\langle j_z \rangle_{\alpha\pm} \langle S_z \rangle$	$\langle j_{s,\alpha,\pm}^i \rangle_{\alpha\pm} \delta_{i,\alpha} \langle \rho_{\pm} \rangle$	Ref.
Local	$\mp \partial_t S$		[51]
Nonlocal	$\mp \nabla [\nabla \cdot \partial_t S_{D,\pm}]$	$\delta_{i,\alpha} \nabla \cdot \partial_t \langle s \rangle_{D,\pm}$	[51]
Driving force	$\epsilon_{s,\pm}^{\text{WDS}}$ and $\nabla [\nabla \cdot (\epsilon_s^{\text{WDS}})_{D,\pm}]$	$\nabla \cdot (\epsilon_s^{\text{WDS}})_{D,\pm}$	This work [51]
	$\epsilon_{s,\pm}^{\text{WDS}} \equiv \mp \frac{J_{ex}}{ev_p} \partial_t S$		
Total	$\langle j \rangle_{\text{local}} \alpha \mu^5 \partial_t S$ $\langle j \rangle_{\text{nonlocal}} \alpha \partial_t \nabla [\nabla \cdot (\langle s \rangle_{D,+} - \langle s \rangle_{D,-})]$	$\langle j_{s,\alpha}^i \rangle_{\text{nonlocal}} \alpha \delta_{i,\alpha} \partial_t \nabla \cdot (\langle s \rangle_{D,+} + \langle s \rangle_{D,-})$	This work

Table 2. Brief summary on charge and spin current generation by spin pumping in a Weyl–Dirac semimetal with the dynamics of localized spin, where \pm denotes the helicity index. Because of spin–momentum locking the charge (spin) current is proportional to the spin (charge) density with each helicity. Time-dependent localized spin drives the local and nonlocal charge and spin current. The nonzero population imbalance between each helicity μ^5 is a prerequisite to obtaining the nonzero charge current. The nonzero spin current (charge density) is triggered by time-dependent and spatial-dependent localized spin dynamics even when $\mu^5 = 0$.

Acknowledgements

This work was supported by a Grant-in-Aid for JSPS Fellows (Grant No. 13J03141), by a Grant-in-Aid for Challenging Exploratory Research (Grant No. 15K13498), and by the Core Research for Evolutional Science and Technology (CREST) of Japan Science.

Author details

Katsuhisa Taguchi

Address all correspondence to: taguchi@rover.nuap.nagoya-u.ac.jp

Department of Applied Physics, Nagoya University, Nagoya, Japan

References

- [1] Tserkovnyak Y, Brataas A, Bauer GEW. Enhanced gilbert damping in thin ferromagnetic films. *Phys Rev Lett.* 2002;88(11):117601. DOI: 10.1103/PhysRevLett.88.117601
- [2] Saitoh E, Ueda M, Miyajima H, Tataru G. Conversion of spin current into charge current at room temperature: Inverse spin-Hall effect. *Appl Phys Lett.* 2006;88(18):13–6. DOI: 10.1063/1.2199473
- [3] Hasan MZ, Kane CL. Colloquium: Topological insulators. *Rev Mod Phys.* 2010;82(4):3045–67. DOI:10.1103/RevModPhys.82.3045
- [4] Qi XL, Zhang SC. Topological insulators and superconductors. *Rev Mod Phys.* 2011;83(4). DOI: 10.1103/RevModPhys.83.1057
- [5] Ando Y. Topological insulator materials. *J Phys Soc Japan.* 2013;82(10):1–32. DOI: 10.7566/JPSJ.82.102001
- [6] Hsieh D, Xia Y, Qian D, Wray L, Dil JH, Meier F, et al. A tunable topological insulator in the spin helical Dirac transport regime. *Nature.* 2009;460(7259):1101–5. DOI: 10.1038/nature08234
- [7] Yokoyama T, Tanaka Y, Nagaosa N. Anomalous magnetoresistance of a two-dimensional ferromagnet/ferromagnet junction on the surface of a topological insulator. *Phys Rev B.* 2010;81(12):3–6. DOI: 10.1103/PhysRevB.81.121401
- [8] Schwab P, Raimondi R, Gorini C. Spin-charge locking and tunneling into a helical metal. *Europhysics Lett.* 2011;93(6):67004. DOI: 10.1209/0295-5075/93/67004
- [9] Mondal S, Sen D, Sengupta K, Shankar R. Magnetotransport of Dirac fermions on the surface of a topological insulator. *Phys Rev B.* 2010;82(4):1–11. DOI: 10.1103/PhysRevB.82.045120
- [10] Ma MJ, Jalil MBA, Tan SG, Li Y, Siu ZB. Spin current generator based on topological insulator coupled to ferromagnetic insulators. *AIP Adv.* 2012;2(3). DOI: 10.1063/1.4751255

- [11] Kong BD, Semenov YG, Krowne CM, Kim KW. Unusual magnetoresistance in a topological insulator with a single ferromagnetic barrier. *Appl Phys Lett*. 2011;98(24):96–9. DOI: 10.1103/PhysRevB.89.201405
- [12] Kandala A, Richardella A, Rench DW, Zhang DM, Flanagan TC, Samarth N. Growth and characterization of hybrid insulating ferromagnet–topological insulator heterostructure devices. *Appl Phys Lett*. 2013;103(20):2011–5. DOI: 10.1063/1.4831987
- [13] Taguchi K, Yokoyama T, Tanaka Y. Giant magnetoresistance in the junction of two ferromagnets on the surface of diffusive topological insulators. *Phys Rev B*. 2014;89(8):1–5. DOI: 10.1103/PhysRevB.89.085407
- [14] Fischer MH, Vaezi A, Manchon A, Kim E-A. Spin–Torque generation in topological–insulator-based Heterostructures. *Phys Rev B*. 2016;93(12):1–4. DOI: 10.1103/PhysRevB.93.12530
- [15] Jamali M, Lee JS, Lv Y, Zhao Z, Samarth N, Wang JP. Room Temperature Spin Pumping in Topological Insulator Bi₂Se₃. [Internet.] 2014. Available from: <http://arxiv.org/abs/1407.7940>
- [16] Qi XL, Hughes TL, Zhang SC. Topological field theory of time-reversal invariant insulators. *Phys Rev B*. 2008;78(19):1–43. DOI: 10.1103/PhysRevB.78.195424
- [17] Garate I, Franz M. Inverse spin-galvanic effect in the interface between a topological insulator and a ferromagnet. *Phys Rev Lett*. 2010;104(14):1–4. DOI: 10.1103/PhysRevLett.104.146802
- [18] Nomura K, Nagaosa N. Electric charging of magnetic textures on the surface of a topological insulator. *Phys Rev B*. 2010;82(16):3–6. DOI: 10.1103/PhysRevB.82.161401
- [19] Ueda HT, Takeuchi A, Tataru G, Yokoyama T. Topological charge pumping effect by the magnetization dynamics on the surface of three-dimensional topological insulators. *Phys Rev B*. 2012;85(11):1–6. DOI: 10.1103/PhysRevB.85.115110
- [20] Linder J. Improved domain-wall dynamics and magnonic torques using topological insulators. *Phys Rev B*. 2014;90(4):1–5. DOI: 10.1103/PhysRevB.90.041412
- [21] Taguchi K, Shintani K, Tanaka Y. Electromagnetic effect on disordered surface of topological insulators. *J Magn Magn Mater*. 2015;400:188–10. DOI: 10.1103/PhysRevB.92.035425
- [22] Burkov AA, Hawthorn DG. Spin and charge transport on the surface of a topological insulator. *Phys Rev Lett*. 2010;105(6):6–9. DOI: 10.1103/PhysRevLett.105.066802
- [23] Fujimoto J, Sakai A, Kohno H. Ultraviolet divergence and Ward–Takahashi identity in a two-dimensional Dirac electron system with short-range impurities. *Phys Rev B*. 2013;87(8):1–5. DOI: 10.1103/PhysRevB.87.085437
- [24] Sakai A, Kohno H. Spin torques and charge transport on the surface of topological insulator. *Phys Rev B*. 2014;89(16). DOI: 10.1103/PhysRevB.89.165307

- [25] Liu X, Sinova J. Reading charge transport from the spin dynamics on the surface of a topological insulator. *Phys Rev Lett*. 2013;111(16):1–5. DOI: 10.1103/PhysRevLett.111.166801
- [26] Tserkovnyak Y, Loss D. Thin-film magnetization dynamics on the surface of a topological insulator. *Phys Rev Lett*. 2012;108(18):1–5. DOI: 10.1103/PhysRevLett.108.187201
- [27] Tserkovnyak Y, Pesin DA, Loss D. Spin and orbital magnetic response on the surface of a topological insulator. *Phys Rev B*. 2015;91(4):041121. DOI: 10.1103/PhysRevB.91.041121
- [28] Taguchi K, Shintani K, Tanaka Y. Spin-charge transport driven by magnetization dynamics on disordered surface of doped topological insulators. *Phys Rev B*. 2015;035425:1–34. DOI: 10.1103/PhysRevB.92.035425 [Figure 4(b) in reference [28] is a misprint: The values 0.38, 0.34, and 0.30 on the vertical axis in the figure should be 0.038, 0.034, and 0.030, respectively. Figure 3(c) in this chapter is revised.]
- [29] Semenov YG, Duan X, Kim KW. Voltage-driven magnetic bifurcations in nanomagnet-topological insulator heterostructures. *Phys Rev B*. 2014;89(20):1–5. DOI: 10.1103/PhysRevB.89.201405
- [30] Deorani P, Son J, Banerjee K, Koirala N, Brahlek M, Oh S, et al. Observation of inverse spin Hall effect in bismuth selenide. *Phys Rev B*. 2014;094403:1–19. DOI: 10.1103/PhysRevB.90.094403
- [31] Shiomi Y, Nomura K, Kajiwara Y, Eto K, Novak M, Segawa K, et al. Spin–electricity conversion induced by spin injection into topological insulators. *Phys Rev Lett*. 2014;113(19):7–11. DOI: 10.1103/PhysRevLett.113.196601
- [32] Mizukami S, Ando Y, Miyazaki T. Effect of spin diffusion on Gilbert damping for a very thin permalloy layer in Cu/permalloy/Cu/Pt films. *Phys Rev B*. 2002;66(10):1–9. DOI: 10.1103/PhysRevB.66.104413
- [33] Gilbert TL. Classics in magnetic: A phenomenological theory of damping in ferromagnetic materials. *IEEE Trans Magn*. 2004;40(6):3443–9. DOI: 10.1109/TMAG.2004.836740
- [34] Wei P, Katmis F, Assaf BA, Steinberg H, Jarillo-Herrero P, Heiman D, et al. Exchange-coupling-induced symmetry breaking in topological insulators. *Phys Rev Lett*. 2013;110(18):1–5. DOI: 10.1103/PhysRevLett.110.186807
- [35] Coop G, Przeworski M, Wall JD, Frisse LA, Hudson RR, Di Rienzo A, et al. Observation of skyrmions in a multiferroic material. *Science*. 2012;336(April):198–201. DOI: 10.1126/science.1214143
- [36] White JS, Prša K, Huang P, Omrani AA, Živković I, Bartkowiak M, et al. Electric-field-induced skyrmion distortion and giant lattice rotation in the magnetoelectric insulator Cu₂OSeO₃. *Phys Rev Lett*. 2014;113(10):1–5. DOI: 10.1103/PhysRevLett.113.107203

- [37] Murakami S. Phase transition between the quantum spin Hall and insulator phases in 3D: Emergence of a topological gapless phase. *New J Phys.* 2007;9. DOI: 10.1088/1367-2630/9/9/356
- [38] Yang B, Nagaosa N. Classification of stable three-dimensional Dirac semimetals with nontrivial topology. *Nat Commun.* 2014;5:4898. DOI: 10.1038/ncomms5898
- [39] Burkov AA, Balents L. Weyl semimetal in a topological insulator multilayer. *Phys Rev Lett.* 2011;107(12):1–4. DOI: 10.1103/PhysRevLett.107.127205
- [40] Brahlek M, Bansal N, Koirala N, Xu SY, Neupane M, Liu C, et al. Topological-metal to band-insulator transition in $(\text{Bi}_{1-x}\text{In}_x)_2\text{Se}_3$ thin films. *Phys Rev Lett.* 2012;109(18):1–5. DOI: 10.1103/PhysRevLett.109.186403
- [41] Wu L, Brahlek M, Valdés Aguilar R, Stier AV, Morris CM, Lubashevsky Y, et al. A sudden collapse in the transport lifetime across the topological phase transition in $(\text{Bi}(1-x)\text{In}(x))_2\text{Se}_3$. *Nat Phys.* 2013;9(7):410–4. DOI: 10.1038/nphys2647
- [42] Liu ZK, Jiang J, Zhou B, Wang ZJ, Zhang Y, Weng HM, et al. A stable three-dimensional topological Dirac semimetal Cd_3As_2 . *Nat Mater.* 2014;13(7):677–81. DOI: 10.1038/nmat3990
- [43] Neupane M, Xu S-Y, Sankar R, Alidoust N, Bian G, Liu C, et al. Observation of a three-dimensional topological Dirac semimetal phase in high-mobility Cd_3As_2 . *Nat Commun.* 2014;05:3786- May 7;5. DOI: 10.1038/ncomms4786
- [44] Novak M, Sasaki S, Segawa K, Ando Y. Large linear magnetoresistance in the Dirac semimetal TlBiSSe . *Phys Rev B.* 2015;91(4):1–5. DOI: 10.1103/PhysRevB.91.041203
- [45] Huang S-M, Xu S-Y, Belopolski I, Lee C-C, Chang G, Wang B, et al. A Weyl Fermion semimetal with surface Fermi arcs in the transition metal monopnictide TaAs class. *Nat Commun.* 2015;6:7373. DOI: 10.1038/ncomms8373
- [46] Tominaga J, Kolobov AV, Fons P, Nakano T, Murakami S. Ferroelectric order control of the Dirac–semimetal phase in $\text{GeTe-Sb}_2\text{Te}_3$ superlattices. *Adv Mater Interfaces.* 2013;1:1-7. DOI: 10.1002/admi.201300027
- [47] Zyuzin AA, Wu S, Burkov AA. Weyl semimetal with broken time reversal and inversion symmetries. *Phys Rev B.* 2012;85(16):1–9. DOI: 10.1103/PhysRevB.85.165110
- [48] Zyuzin AA, Burkov AA. Topological response in Weyl semimetals and the chiral anomaly. *Phys Rev B.* 2012;86(11):1–8. DOI: 10.1103/PhysRevB.86.115133
- [49] Vazifeh MM, Franz M. Electromagnetic response of Weyl semimetals. *Phys Rev Lett.* 2013;111(2):1–5. DOI: 10.1103/PhysRevLett.111.027201
- [50] Taguchi K. Equilibrium axial current due to a static localized spin in Weyl semimetals. *J Phys Conf Ser.* 2014;568(5):052032. DOI: 10.1088/1742-6596/568/5/052032

- [51] Taguchi K, Tanaka Y. Axial current driven by magnetization dynamics in Dirac semimetals. *Phys Rev B*. 2015;91(5):1–5. DOI:10.1103/PhysRevB.91.054422
- [52] Nomura K, Kurebayashi D. Charge-induced spin torque in anomalous Hall ferromagnets. *Phys Rev Lett*. 2015;115(12):1–5. DOI: 10.1103/PhysRevLett.115.127201
- [53] Chan C-K, Lee P A, Burch KS, Han JH, Ran Y. When chiral photons meet chiral fermions: Photoinduced anomalous Hall effects in Weyl semimetals. *Phys Rev Lett*. 2015;1(7):1–5. DOI: 10.1103/PhysRevLett.116.026805
- [54] Taguchi K, Imaeda T, Sato M, Tanaka Y. Photovoltaic chiral magnetic effect in a Weyl semimetal. *Phys Rev B(R)*. 2016;93(20):1–5. DOI: 10.1103/PhysRevB.93.201202
- [55] Haug H, Jauho A-P. *Quantum Kinetics in Transport and Optics of Semiconductors*. [Internet.] 2008. 362 pp. Available from: <http://www.springer.com/physics/complexity/book/978-3-540-73561-8>
- [56] Tokura Y, Kida, N. Dynamical magnetoelectric effects in multiferroic oxides. *Phil. Trans. R. Soc. A*. 2011;369:3679–3694. DOI: 10.1098/rsta.2011.0150

Metamaterial Properties of 2D Ferromagnetic Nanostructures: From Continuous Ferromagnetic Films to Magnonic Crystals

Roberto Zivieri

Additional information is available at the end of the chapter

<http://dx.doi.org/10.5772/64070>

Abstract

In recent years the study of low-dimensional magnetic systems has become topical not only for its several technological applications but also for achieving a deep understanding of the underlying physics of magnetic nanostructures. These efforts have considerably advanced the field of magnetism both theoretically and from an experimental point of view. Very recently, for their challenging features, great attention has been given to the investigation of the static and dynamical properties of magnetic nanostructures with special regard to magnonic crystals, a class of periodic magnetic systems. As shown by micromagnetic and analytical methods, the ferromagnetic materials composing magnonic crystals can be regarded as metamaterials since they exhibit effective properties directly linked, for instance, to the definition of an effective magnetization, an effective permeability, and an effective wavelength. Hence, the aim of this chapter is to give an overview of the recent results obtained on the study of metamaterial properties of two-dimensional ferromagnetic nanostructures ranging from those of thin films to the ones of two-dimensional magnonic crystals. Some possible applications based on the effective properties for tailoring new magnetic devices are suggested.

Keywords: metamaterials, ferromagnetic nanostructures, magnonic crystals, effective properties, magnonic devices

1. Introduction

In this chapter, an overview of recent theoretical results on metamaterial properties of ferromagnetic nanostructures is presented. These results have been found according to micromag-

netic simulations based on a finite difference method called dynamical matrix method (DMM) with implemented two-dimensional (2D) boundary conditions and extended to periodic magnetic systems [1] and via simple analytical calculations. We first review some challenging properties arising from the study of spin dynamics in in-plane magnetized ferromagnetic thin films that can be regarded as the simplest example of ferromagnetic nanostructures. Indeed, they are un-patterned and infinitely extended systems in the xy plane but are confined along the z direction with thickness of a few nanometers. There are several studies carried out on spin-wave modes propagation in ferromagnetic films with both in-plane and out-of-plane magnetization and different classes of excitations based on the propagation features have been studied (see e.g., [2, 3]). Special emphasis is devoted to the investigation of backward volume spin-wave modes (BVMSWs) characterized by a “negative” group velocity (antiparallel to the propagation wave vector) and a negative dynamic permeability in the magnetostatic limit (see e.g., [3, 5]). This analysis is done for the sake of simplicity in the absence of losses but it can be easily generalized also to spin dynamics where intrinsic damping is taken into account. It is shown that the inclusion of the exchange interaction suppresses the backward nature of BVMSWs leading to a “positive” group velocity, namely a group velocity parallel to the propagation wave vector, and the analytical expressions of the group velocity are given in both the dipole and dipole-exchange regimes [4]. Moreover, it is demonstrated that BVMSWs are spin-wave modes characterized by a negative dynamic effective permeability and its behavior is studied as a function of the spin-wave mode frequency and magnetic parameters [5]. In view of these results, ferromagnetic thin films with in-plane magnetization can be regarded as metamaterials and can be put on a similar footing as other classes of metamaterials such as electromagnetic backward-wave media where, since the first prediction by Veselago [6], the simultaneous presence of a negative permeability and permittivity was investigated (see e.g., [7, 8]).

Then, the analysis focuses on periodic two-dimensional (2D) magnetic nanostructures with periodic modulation, the so-called magnonic crystals (MCs) [9–17], by giving special emphasis to their metamaterial properties arising from the 2D spatial periodicity. Specifically, effective quantities such as the notions of effective magnetization, effective wavelength, and effective wave vector are introduced for different kinds of 2D magnonic crystals. In particular, these properties are discussed for square arrays of antidot lattices (ADLs) where holes are embedded into a ferromagnetic matrix (single component systems) and binary systems composed by periodic arrangements of dots etched into a ferromagnetic matrix of a different material. General relations involving the effective wavelength and effective wave vector with the corresponding Bloch wavelength and Bloch wave vector are proposed for in-plane [17] and perpendicularly magnetized ADLs [18], and it is shown that their validity can be extended to periodic and binary systems [19, 20]. An effective relation involving the effective wave vector and completing the well-known Bloch rule for periodic systems is also presented. Frequency dispersion and band gaps of collective modes are discussed for different geometries and comparisons with the frequencies calculated via an effective description are performed. The definition of effective “surface magnetic charges” is introduced for describing the magnetic interactions in binary ferromagnetic systems in terms of an effective magnetic potential and experiment for tailoring magnetic devices and for mapping the spatial profiles of collective spin-wave modes based on the studied effective properties is proposed [17].

2. Metamaterial properties of ferromagnetic films

In this section, we review the metamaterial properties of ferromagnetic thin films that can be considered as the simplest example of ferromagnetic nanostructures. In particular, we focus on some recent theoretical results on the dynamical properties related to a class of volume spin-wave modes whose wave vector is parallel to the static magnetization \mathbf{M} and to the external magnetic field \mathbf{H} , sometimes called BVMSW. These modes are characterized by a “negative” group velocity \mathbf{v}_g [4]. The word “negative” refers to the fact that, for this class of spin-wave modes, the group velocity is opposite to the propagation wave vector \mathbf{k} and to the phase velocity. As a result, BVMSW frequency decreases with increasing the modulus of the propagating wave vector. This unusual behavior is associated to their propagation that is along the direction of the in-plane magnetic field and of the magnetization leading to a reduction of their magnetostatic energy with increasing the modulus of the wave vector.

2.1. BVMSWs and group velocity

BVMSWs are thermally excited waves typical of the in-plane magnetized ferromagnetic thin film depicted in **Figure 1**, having the following features:

1. They are classified as volume spin waves because they have a real perpendicular to the plane wave vector component.
2. They are characterized by a “negative” group velocity satisfying the condition $\mathbf{k} \cdot \mathbf{v}_g < 0$ according to which the group velocity $\mathbf{v}_g = (0, v_g)$ is antiparallel to the in-plane wave vector $\mathbf{k} = (0, k_y)$ and to the phase velocity.
3. They are transverse plane waves, that is $\mathbf{k} \cdot \delta \mathbf{m} = 0$ with $\delta \mathbf{m}(\mathbf{x}) = \delta \mathbf{m}_0 \exp^{i(\mathbf{k} \cdot \mathbf{x} - \omega t)}$ where $\delta \mathbf{m} = (\delta m_x, \delta m_z)$ is the dynamic magnetization, $\delta \mathbf{m}_0 = (\delta m_{0x}, \delta m_{0z})$ is the dynamic magnetization amplitude with $\mathbf{x} = (x, y)$ for \mathbf{M} and \mathbf{H} oriented along the y axis. The corresponding band of frequencies lies below that of the surface waves, the so-called Damon-Eshbach modes.

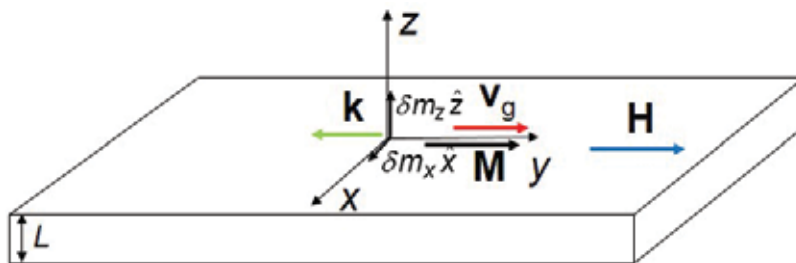


Figure 1. Sketch of the ferromagnetic film. The directions of \mathbf{H} , \mathbf{M} , \mathbf{k} , and \mathbf{v}_g of BVMSW are shown. The dynamic magnetization components δm_x and δm_z are also indicated. The symbol L denotes the thickness.

Note that in ferromagnetic thin films, there exists also volume modes having $\mathbf{k} = (k_x, k_y)$ even though they cannot be classified, at all effects, as BVMSWs that have a propagating wave vector along the direction of \mathbf{M} and \mathbf{H} .

The spectrum of BVMSWs in dimensionless units in the dipole-exchange regime for a purely conservative dynamics (no Gilbert damping) and assuming the dynamic magnetization uniform along z takes the form [3]:

$$\Omega_k^2 = (\Omega_{\text{Heff}} + \Omega_{\text{Hexch}}) \left(\Omega_{\text{Heff}} + \Omega_{\text{Hexch}} + \frac{1 - e^{-kL}}{kL} \right). \quad (1)$$

where $\Omega_k = \omega/\omega_M$ with ω the angular frequency and $k = |k_y|$, $\omega_M = 4\pi\gamma M$ with γ the gyromagnetic ratio (in modulus) and M the saturation magnetization, $\Omega_{\text{Heff}} = H_{\text{eff}}/4\pi M$ and $\Omega_{\text{Hexch}} = H_{\text{exch}}/4\pi M$. H_{eff} is the effective field including in this case the external magnetic field H only, namely $H_{\text{eff}} = H$ and $\Omega_{\text{Heff}} = \Omega_H$ being the demagnetizing field for in-plane magnetization equal to zero and, for the sake of simplicity, within this description the anisotropy is neglected, $H_{\text{exch}} = Dk^2$ (D is the exchange constant) is the dynamic non-uniform exchange field. The term effective field is used in this framework to underline the metamaterial and effective properties characterizing this family of spin waves such as the “negative” group velocity or the negative permeability depending on H_{eff} . Strictly speaking, the purely magnetostatic regime occurring when $H_{\text{exch}} = 0$ corresponds to angular frequencies in the microwave range and wave vectors between 30 and 10^5 cm^{-1} where electromagnetic retardation effects are neglected. In this regime, in the limit of infinite wave vector, the angular frequency is the Larmor resonance frequency, viz. $\omega = \gamma H_{\text{eff}}$ that becomes $\omega = \gamma H$ when anisotropy is not included. In a realistic calculation also exchange effects should be taken into account for wave vectors larger than 10^5 cm^{-1} . From Eq. (1), the group velocity $\mathbf{v}_g = \nabla_k \omega$, where ∇_k denotes the gradient with respect to the wave vector can be calculated. For the geometry shown in **Figure 1**, it is $\mathbf{v}_g = (0, v_g)$ with $v_g = \partial\omega/\partial k$. In the magnetostatic limit, we get:

$$v_g = -\frac{\omega_M}{2} \frac{\Omega_{\text{Heff}}}{\Omega_k} \frac{1 - e^{-kL}}{k} \frac{(1 + kL)}{kL}, \quad (2)$$

with $v_g < 0$. The behavior of the group velocity given in Eq. (2) as a function of the modulus of the in-plane wave vector is illustrated in **Figure 2** for $L = 10 \text{ nm}$ and for two different values of the effective field, $\Omega_{\text{Heff}} = 0.1$ and $\Omega_{\text{Heff}} = 1$, respectively. In the calculations, typical parameters of ferromagnetic materials were used: $\gamma = 1.76 \times 10^7 \text{ rad}/(\text{G s})$, $4\pi M = 10^4 \text{ G}$, and $D = 0$. The group velocity is of the order of hundreds of meters per second, has its minimum value in the long wavelength limit ($k = 0$), increases with increasing k tending asymptotically to zero (negatively) for large wave vectors in proximity of the Larmor resonance frequency. At fixed magnetic parameters, the group velocity increases (negatively) with increasing the thickness L of the ferromagnetic film.

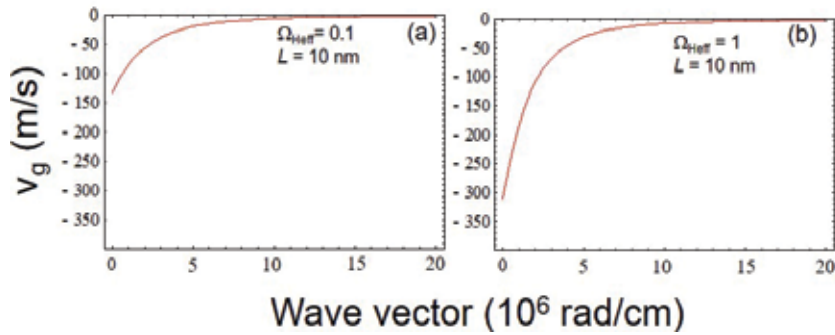


Figure 2. Group velocity v_g of BVMSWs as a function of the in-plane wave vector in the magnetostatic limit for $L = 10$ nm. (a) v_g for $\Omega_{\text{Heff}} = 0.1$. (b) v_g for $\Omega_{\text{Heff}} = 1$.

In the presence of exchange effects, BVMSWs propagation is studied in the dipole-exchange regime. From Eq. (1), we get the corresponding group velocity that depends also on the exchange field, namely:

$$v_g = \frac{\omega_M}{2} \frac{1}{\Omega_k} \frac{1}{k} \frac{(4\Omega_{\text{Hexch}}^2 + 4\Omega_{\text{Heff}}\Omega_{\text{Hexch}} + \Omega_{\text{Hexch}}e^{-kL} + \Omega_{\text{Heff}}e^{-kL})kL + (\Omega_{\text{Hexch}} - \Omega_{\text{Heff}})(1 - e^{-kL})}{kL} \quad (3)$$

Group velocity is still “negative” for small values of the wave vector, but this behavior is suppressed by the presence of exchange effects. Above a certain value of the wave vector, group velocity becomes parallel to the phase velocity due to the effect of $H_{\text{exch}} = Dk^2$. For a given $k = k^*$, depending on the geometric and magnetic parameters and in the range of $10^4 \div 10^5$ rad/cm, it is $v_g(k^*) = 0$ for a typical exchange constant $D = 2.51 \times 10^{-9}$ Oe cm². For $k = k^*$, the envelope of the wave form stops as a consequence of the vanishing of the group velocity, while the corresponding phase velocity remains different from zero. For wave vectors larger than k^* , the backward nature of these volume waves is suppressed.

2.2. BVMSWs and effective permeability studied in the magnetostatic approximation and with no losses

The dynamic permeability tensor referred to the BVMSWs geometry sketched in **Figure 1** is derived from the linearization of the Landau-Lifshitz equation of motion in the magnetostatic limit and in the absence of losses and can be expressed in the form of magneto-gyrotropic media as [8]

$$\mu_{ij} = \begin{pmatrix} \mu_R & 0 & i\mu_I \\ 0 & 1 & 0 \\ -i\mu_I & 0 & \mu_R \end{pmatrix}, \quad (4)$$

where the effective dynamic dependence is separated from the static one ($\mu_{yy} = 1$). The tensor is of rank two and is hermitian. The diagonal components μ_{xx} and μ_{zz} are real with $\mu_{xx} = \mu_{zz} = \mu_R$, where μ_R is the real part of the effective dynamic permeability. We do not deal with the imaginary part that has less physical meaning. Instead, we discuss the trend of μ_R that takes the form [5]:

$$\mu_R(\omega) = \frac{\Omega_{\text{Heff}}(1 + \Omega_{\text{Heff}}) - \Omega^2}{\Omega_{\text{Heff}}^2 - \Omega^2}. \quad (5)$$

We restrict ourselves to the underlying physics arising from μ_R for the range of Ω , where it is negative corresponding to the band of BVMSWs. μ_R has a singularity at the Larmor resonance frequency $\Omega = \Omega_{\text{Heff}}$ where it diverges negatively, increases for $\Omega_{\text{Heff}} < \Omega < (\Omega_{\text{Heff}}(1 + \Omega_{\text{Heff}}))^{1/2}$ and vanishes in correspondence of the ferromagnetic resonance frequency, namely for $\Omega = (\Omega_{\text{Heff}}(1 + \Omega_{\text{Heff}}))^{1/2}$. In **Figure 3**, the dependence of μ_R on the angular frequency in the interval $\Omega_{\text{Heff}} < \Omega < (\Omega_{\text{Heff}}(1 + \Omega_{\text{Heff}}))^{1/2}$ is displayed for $\Omega_{\text{Heff}} = 0.05$ and $\Omega_{\text{Heff}} = 1$ corresponding to frequencies of a few gigahertz for typical magnetic material parameters: $4\pi M = 10^4$ G and $\gamma = 1.76 \times 10^7$ rad/(G s).

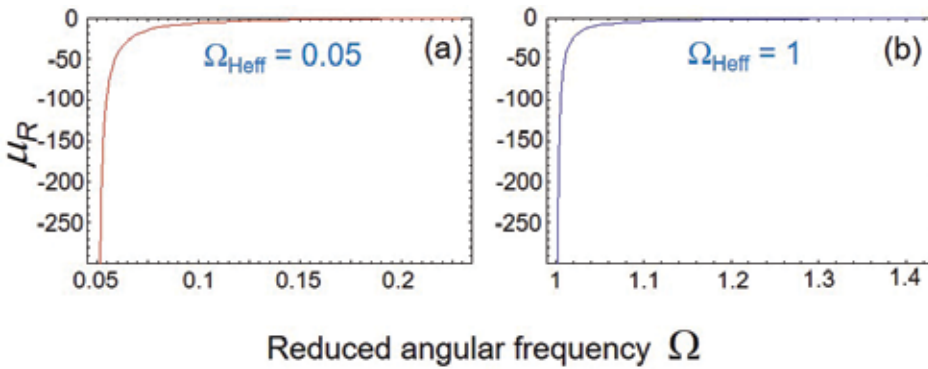


Figure 3. Effective dynamic permeability μ_R for two different values of the effective field. (a) μ_R for $\Omega_{\text{Heff}} = 0.05$. (b) μ_R for $\Omega_{\text{Heff}} = 1$.

Looking at the two curves, it can be noted that μ_R can be tuned by the external magnetic field intensity.

In conclusion, the study of the peculiar dynamical properties characterizing BVMSWs propagating in ferromagnetic films allows using them as media for coupling electromagnetic radiation in the microwave range with spin excitations. From this point of view, ferromagnetic films can be considered as magnetic metamaterials having properties analogous to those of plasmonic metamaterials where photons are coupled to plasmons.

3. Metamaterial properties of 2D magnonic crystals

This section reports on some recently found metamaterial properties of 2D magnonic crystals (MCs). MCs are prototypes of artificially periodic magnetic systems where the effect of the artificial periodicity is to modify the energy spectrum of collective excitations. MCs can be arranged in one-dimensional (1D), two-dimensional (2D), and three-dimensional (3D) arrays of magnetic nanostructures. In the following sections, the effective properties of 2D antidot lattices (ADLs) recently found by means of micromagnetic simulations and simple analytical calculations are first reviewed and their behavior as metamaterials is highlighted. Finally, bicomponent systems are presented and their interesting recently found effective and metamaterial properties are discussed.

3.1. Magnonic crystals: an introduction

Magnonic crystals are artificially periodic magnetic systems where the artificial periodicity modifies the energy spectrum of collective excitations. Frequency dispersion as a function of the Bloch wave vector strictly depends on the periodicity constant and on the interplay between the dipolar and exchange energy stored in collective modes. At the border of Brillouin zones (BZs), frequency gaps can open such that the propagation is forbidden for specific frequency ranges. There are different kinds of 1D MCs.

The 1D MCs most recently studied in the literature are

1. chains of interacting nanodots of different shapes (see e.g., [12, 13]),
2. arrays of nanostripes (see e.g., [14]).

Instead, the most relevant examples of 2D MCs recently investigated are

3. periodically arranged ferromagnetic nanodots of different shapes interacting along the two in plane directions (see e.g., [15]),
4. antidot lattices (ADLs) where nanoholes of different shapes are periodically embedded into a ferromagnetic matrix (see e.g., [13, 16, 17]),
5. binary systems either composed by nanodots of various shapes and different ferromagnetic materials [21] or formed by nanodots etched into a ferromagnetic matrix of a different material [19, 20].

Finally, note that also 3D MCs consisting of periodic arrangements of ferromagnetic elements of different nature along the three spatial directions have been recently studied (see e.g., [22] where a theoretical analysis on their dynamical properties based on the plane wave method has been performed).

The above-described periodic systems have been also extensively studied experimentally, for instance, by means of Brillouin light-scattering technique and vector network analyzer ferromagnetic resonance technique [11].

In the following section, we focus our attention on recent effective and metamaterial properties found via micromagnetic simulations and supported by analytical calculations. This was done

for ADLs and 2D periodic binary systems. In particular, the static properties have been studied by using Object Oriented MicroMagnetic Framework (OOMMF) code with periodic boundary conditions [23] able to determine the ground-state magnetization for any geometry. Instead, the DMM with implemented 2D periodic boundary conditions [1] has been employed to investigate the dynamical properties with special emphasis on the dynamics of collective modes characterizing these periodic magnetic systems. The DMM is a finite-difference micromagnetic method representing an eigenvalue/eigenvector problem solved in the conservative regime and therefore, for the purposes of the investigation, it aimed to focus on effective and metamaterial properties by neglecting dissipative effects. The frequencies and the profiles of magnonic modes are associated to the eigenvalues and eigenvectors, respectively, of a dynamical matrix obtained in the linear approximation and containing the second-order derivatives of the total energy density calculated at equilibrium. For technical details on the micromagnetic formalism [13]. In these numerical simulations, the equilibrium corresponds to the ground-state magnetization determined via the OOMMF code.

3.2. 2D antidot lattices with in-plane magnetization

In this section, we present some recent theoretical results obtained for the effective properties characterizing 2D ADLs based on the effective medium approximation [17]. Specifically, we deal with a square array of circular holes having nanometric size embedded into a ferromagnetic Permalloy (Py, $\text{Ni}_{80}\text{Fe}_{20}$) film. The lattice constant is $a = 800$ nm with holes having diameter $d = 120$ nm. The Py film thickness is $L = 22$ nm [16]. Both static and dynamical properties were investigated. To study the system in the effective medium approximation and to extract the effective field, micromagnetic simulations were performed by using OOMMF code for a system composed by 5×5 supercells. It has been found that the results of these calculations were exactly reproduced by using the OOMMF code with 2D periodic boundary conditions that were available after these numerical calculations were performed for the first time [23]. The system was subdivided into $5 \text{ nm} \times 5 \text{ nm} \times 22 \text{ nm}$ prismatic cells. In the calculation, the typical Py magnetic parameters were used: $4\pi M_s = 9.4$ kG, $\gamma/2\pi = 2.95$ GHz/kOe and $A = 1.3 \times 10^{-6}$ erg/cm with M_s the saturation magnetization, γ the gyromagnetic ratio, and A the exchange stiffness constant.

For the study of the effective properties the magnetostatic surface wave (MSSW) scattering geometry illustrated in **Figure 4** was considered in the calculations. In this geometry, \mathbf{H} was applied along the y direction with $\mathbf{H} \perp \mathbf{K}$ where \mathbf{K} is the Bloch wave vector of collective modes along the x direction. A magnetic field having intensity $H = 200$ Oe sufficient to saturate the system (static magnetization \mathbf{M} parallel to \mathbf{H} apart from the regions close to the holes) was applied. We denote with region 1 (2), the one in correspondence of (between) vertical rows of holes (see **Figure 4(a)**). The corresponding first Brillouin zone (1 BZ) with the high-symmetry direction ΓX and the high-symmetry points are shown in **Figure 4(b)**.

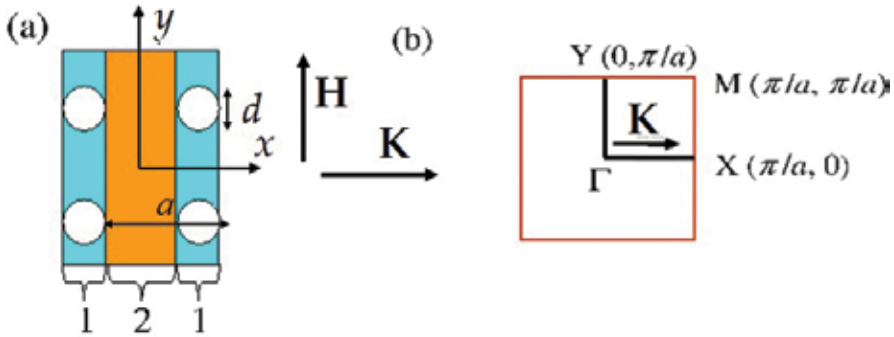


Figure 4. (a) A sketch of the sample regions. Region 1 (blue) corresponds to the vertical rows of ADs. Region 2 (brown) is comprised between the vertical rows of ADs. An in-plane reference frame is also shown together with the directions of \mathbf{H} and of \mathbf{K} . (b) 1 BZ with the high-symmetry points and the high-symmetry direction ΓX .

The system can be treated as if it were a continuous magnetic film and effective parameters can be introduced incorporating the effective properties in an effective field arising from the demagnetizing effects associated with holes. For this metamaterial, the dispersion can be written in the approximated form in dimensionless units as

$$\Omega_{MM}^2 = (\Omega_{\text{Heff}} + \Omega_{\text{Hexch}} + f)(\Omega_{\text{Heff}} + \Omega_{\text{Hexch}} + 1 - f), \quad (6)$$

where $\Omega_{MM} = \omega_{MM}/\omega_M$ with ω_{MM} the angular frequency of the metamaterial (MM) wave, $\omega_M = 4\pi\gamma M_s$ and $\Omega_{\text{Heff}} = H_{\text{eff}}/4\pi M_s$.

Here, $H_{\text{eff}} = H + \langle H_{\text{dem}} \rangle$ is the intensity of the effective field given by the sum of the external magnetic field and of the mean demagnetizing (internal) field calculated as an average of its y component over the 128 prismatic cells along the channels comprised between the rows of holes. According to the numerical calculations with OOMMF, it has been found $\langle H_{\text{dem}} \rangle \cong -60$ Oe, so that $H_{\text{eff}} \cong 140$ Oe. Instead, $\Omega_{\text{Hexch}} = H_{\text{exch}}/4\pi M_s$ with $H_{\text{exch}} = Dk^2$ ($D = 2A/M_s$ is the exchange constant) is the dynamic non-uniform exchange field magnitude and $f = 1 - (1 - \exp(-KL))/KL$ with the Bloch wave vector $\mathbf{K} = (K, 0)$ aligned along the x direction.

A comparison of the dispersion of the extended modes, the so-called Damon-Eshbach-like ($\text{DE}_{n\text{BZ}}$) extended collective modes with $n = 1, 2, \dots$ (see Section 3.2.1 for a description), calculated by using the DMM, to the one of the metamaterial mode propagating in the channel according to Eq. (6) was made. The DMM micromagnetic calculations were performed in the linear approximation, viz. under the assumption that $\mathbf{M} = \mathbf{M}_0 + \delta\mathbf{m}$, where \mathbf{M} is the total magnetization, \mathbf{M}_0 is its static part and the complex dynamic magnetization $\delta\mathbf{m} = (\delta m_x, \delta m_z)$ expresses the small deviations from the ground state. A comparison with the frequencies of the Damon-Eshbach surface mode of the corresponding continuous film calculated in the dipole-exchange regime [3] has also been performed. The results of these calculations are shown in **Figure 5**, and the calculated frequencies are in the microwave range.

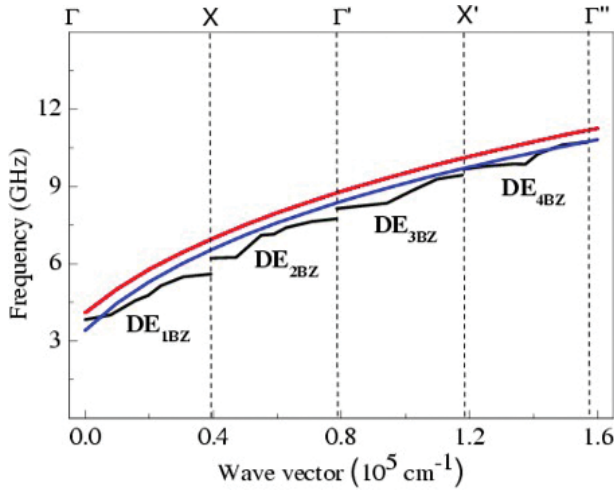


Figure 5. Calculated DMM dispersion of the DE_{nBZ} of the AD lattice (black lines) [16] compared to the calculated Damon-Eshbach dispersion of the unpatterned film (red line) [3] and to the calculated DE dispersion of the MM (blue line) by means of Eq. (6). The edges of BZs are indicated by dashed lines.

At small Bloch wave vectors, the ADL collective mode dynamics (black lines) significantly deviates from the dispersion of the Damon-Eshbach surface mode of the continuous film (red line), while at large Bloch wave vectors, the ADL frequency is closer to that of the Damon-Eshbach mode. Due to demagnetizing effects, the frequencies of the MM mode (blue line) are downshifted with respect to those of the Damon-Eshbach surface mode of the continuous film. The opening of frequency band gaps can be seen at the border of $nBZs$ with $n = 1, 2, 3, \dots$ that can be regarded as another metamaterial property resulting from the artificial periodicity with the band gap amplitude decreasing with increasing n . The band gap opening is mainly due to the inhomogeneity of the internal field in correspondence of the holes, where there is a Bragg diffraction of the Bloch wave for the different families of collective modes including the collective localized modes (not shown) [13, 16].

From an application point of view, because of the explicit dependence on the effective field, the collective mode dispersion calculated according to Eq. (6) could be useful for measuring the internal field experienced by magnonic modes in order to control spin wave propagation in arrays of ADs.

3.2.1. Effective quantities

We now introduce some effective quantities characterizing collective modes. For the sake of simplicity, we restrict ourselves to the analysis of the stationary regime (edges of BZs), but effective quantities can be defined also in the propagative regime (far from BZs edges).

By inspecting spatial profiles, a characteristic wavelength directly related to the scattering with holes can be defined for every collective mode. For hole diameters and for nanometric periodicities, the characteristic wavelength is much larger than hole size. Hence, the charac-

teristic wavelength can be identified as an effective wavelength λ_{eff} defined as the distance between either two maxima or two minima corresponding to the effective periodicity of the wave. In this respect, it is at all effects the wavelength of the wave. Unlike the Bloch wavelength that can assume fractional values of the periodicity, at the edges of the n BZs with $n = 1, 2, \dots$ the effective wavelength is always commensurable with the array periodicity (it is either equal to a or $2a$). In particular, λ_{eff} characterizes each mode of the spectrum and it is not necessarily equal to the Bloch wavelength $\lambda_B = 2\pi/K$, which decreases with increasing K and becomes comparable to d at high-order n BZs. In the special case studied, d/λ_{eff} is less equal than 0.15 for the whole range of Bloch wave vectors investigated. Correspondingly, collective modes have also a small effective wave vector \mathbf{k} of modulus $k = 2\pi/\lambda_{\text{eff}}$ that is not necessarily equal to the Bloch wave vector of modulus $k = 2\pi/\lambda_B$. By means of this small effective wave vector, the influence of holes acting as scattering centers on collective spin modes is expressed in an even more direct way with respect to that of the effective wavelength.

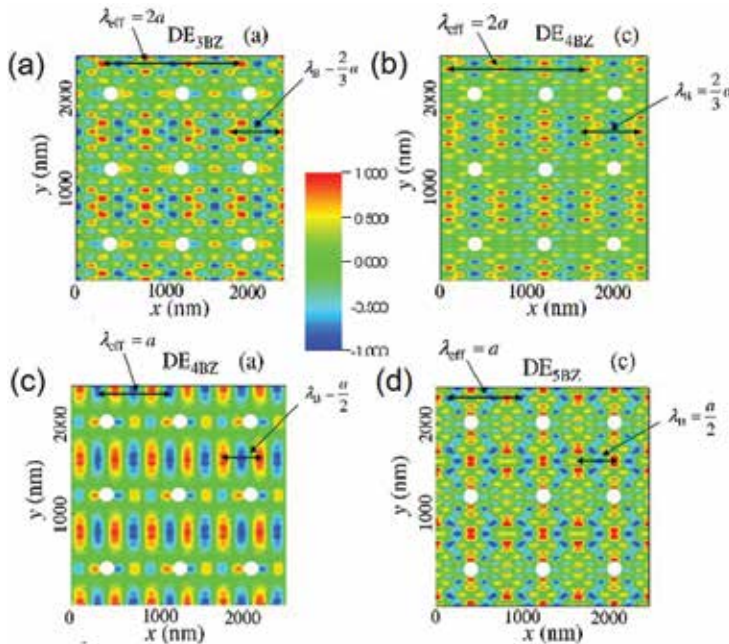


Figure 6. Spatial profiles ($\text{Re}[\delta m_x]$) of collective modes. (a) $\text{DE}_{3\text{BZ}}$ mode at the edge of the 3 BZ. (b) $\text{DE}_{4\text{BZ}}$ mode at the edge of the 3 BZ. (c) $\text{DE}_{4\text{BZ}}$ mode at the edge of the 4 BZ. (d) $\text{DE}_{5\text{BZ}}$ mode at the edge of the 4 BZ. For each collective mode the effective wavelength λ_{eff} and the Bloch wavelength λ_B are indicated.

Two examples underlining the difference between the meaning of the effective wavelength and of the Bloch wavelength and the corresponding wave vectors for the array of ADs studied are shown in **Figure 6**, where two couples of the so-called extended modes exhibiting large amplitude in the horizontal channels comprised between hole rows and non-negligible amplitude in the rows are depicted at n BZs edges with $n = 3, 4$. In particular, the calculated spatial profiles of the couple of extended modes $\text{DE}_{3\text{BZ}}$ and $\text{DE}_{4\text{BZ}}$ at the X' point (border of 3

BZ, $n = 3$) and of the couple of extended modes DE_{4BZ} and DE_{5BZ} at the Γ'' point (border of 4 BZ) are shown. The numerical frequencies are $\nu = 9.44$ GHz for the DE_{3BZ} and $\nu = 9.67$ GHz for the DE_{4BZ} with a band gap of amplitude of 0.23 GHz. Looking at the spatial profiles of DE_{3BZ} and DE_{4BZ} , their effective wavelength is three times the Bloch wavelength λ_B both in the horizontal rows and in the horizontal channels, namely $\lambda_{\text{eff}} = 2a$. Instead, from the inspection of the spatial profiles, the effective wavelength of DE_{4BZ} and DE_{5BZ} modes is $\lambda_{\text{eff}} = a$, both in the horizontal rows and horizontal channels, and is twice the Bloch wavelength. The numerical frequencies are $\nu = 10.70$ GHz for DE_{4BZ} and $\nu = 10.83$ GHz for DE_{5BZ} with a band gap of amplitude of 0.13 GHz. For each couple of modes, the amplitudes are phase shifted of $\pi/2$. Similar conclusions are drawn by studying the spatial profiles of collective localized modes whose spatial profiles have larger amplitudes in the horizontal rows of holes [13, 16].

For a discussion of other effective properties characterizing ADLs [17]. The same features remain valid for other types of ADLs in the nanometric and submicrometric ranges having different hole shape, periodicity, type of unit cell, and ferromagnetic materials. They remain valid also for other scattering geometries depending on the relative orientation of \mathbf{K} with respect to \mathbf{H} including the BVMSW scattering geometry ($\mathbf{K} \parallel \mathbf{H}$) and for other high-symmetry directions in the reciprocal space [17, 24].

Moreover, similar numerical results have been obtained for perpendicularly magnetized thin CoFeB ADLs with strong uniaxial perpendicular anisotropy [18]. This means that the effective description of ADLs dynamics does not depend on the ground-state magnetization. For a quantitative description of the relations between the effective quantities and the corresponding Bloch quantities together with other general rules valid for the types of 2D periodic systems reviewed in this chapter (see Section 3.4).

3.3. Binary and periodic ferromagnetic systems: Py/Co and Co/Py

In this section, we describe the recent results found according to micromagnetic simulations carried out by means of DMM on the effective properties of binary and periodic ferromagnetic systems [19, 20] that can be regarded as another class of magnetic metamaterials. In particular, it is shown that also in these systems, the dynamics of the most representative collective modes in the effective medium approximation can be described in terms of an MM propagating wave. This is done in analogy with what occurs in ADLs with, in addition, the definition of other effective quantities directly related to the presence of two ferromagnetic materials. We report here the geometry of a Py/Co binary and periodic system with periodicity $a = 600$ nm, where a periodic arrangement of Co circular dots are embedded into a Py matrix. The Co circular dots have diameters $d = 310$ nm and are totally etched into the Py film while the thickness of the continuous film is $L_{\text{Py}} = 16$ nm for every system. The ground-state magnetization has been determined by using the OOMMF code with periodic boundary conditions [23]. In the simulations, prismatic cells of $7.5 \text{ nm} \times 7.5 \text{ nm} \times 8 \text{ nm}$ size have been used subdividing the thickness into a stack of two layers. The magnetic parameters used in the simulations range within the typical values of the literature. For Py, $\gamma_{\text{Py}}/2\pi = 2.96$ GHz/kOe, $M_{s,\text{Py}} = 740$ emu/cm³, and $A_{\text{exch}}^{\text{Py}} = 1.3 \times 10^{-6}$ erg/cm, while for Co, $\gamma_{\text{Co}}/2\pi = 3.02$ GHz/kOe, $M_{s,\text{Co}} = 1000$ emu/cm³, and

$A_{\text{exch}}^{\text{Co}} = 1.5 \times 10^{-6}$ erg/cm (this value is typical of polycrystalline Co). Micromagnetic simulations have been carried out for an external in-plane magnetic field \mathbf{H} applied along the y direction having intensity $H = 500$ Oe.

In order to find the frequency dispersion of the metamaterial wave, it is useful to define an effective magnetization by means of the filling ratio $\eta = \pi R^2/a^2$ where R is the dot radius, namely:

$$M_{\text{eff}} = M_{s,\text{Py}}(1 - \eta) + M_{s,\text{Co}}\eta. \quad (7)$$

In addition, it can be defined also an effective magnetic field that plays the role of an internal field experienced by the MM wave and depends on both materials:

$$H_{\text{eff}} = H + \langle H_{\text{dem}}^y \rangle, \quad (8)$$

where $\langle H_{\text{dem}}^y \rangle$ denotes the average of the y component of the static demagnetizing field over the 80 prismatic cells of the unit cell along both x and y directions due to its uniformity along the z direction. Because of its small contribution, the static exchange field can be safely neglected. The effective gyromagnetic ratio and the effective stiffness constant are $\gamma_{\text{eff}} \approx \gamma_{\text{Py}}$ and $A_{\text{eff}} \approx A_{\text{exch}}^{\text{Py}}$ respectively.

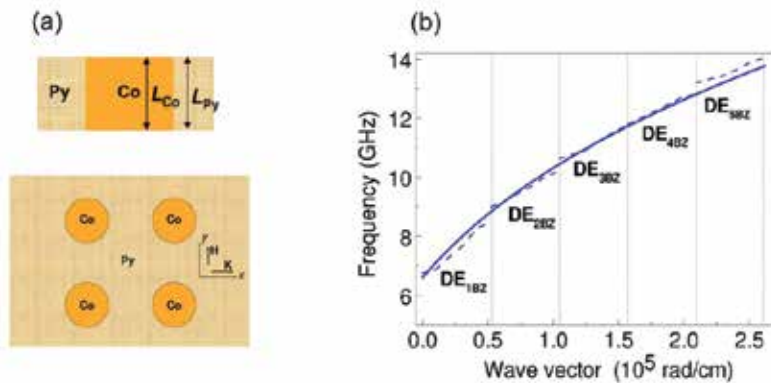


Figure 7. (a) Pictorial sketch and top view of the Py/Co system and (b) calculated DMM frequency dispersion of the DE_{nBZ} modes (dashed blue lines) for Py/Co system compared to the Damon-Eshbach dispersion of the MM mode (solid blue line) calculated according to Eq. (6) and accounting for Eqs. (7) and (8).

The frequency dispersion of the MM wave can be calculated according to Eq. (6) by taking into account Eqs. (7) and (8), $L = L_{\text{Py}}, L_{\text{Co}}, \gamma \approx \gamma_{\text{Py}}$, and $A \approx A_{\text{exch}}^{\text{Py}}$ and corresponds to the effective medium description of the DE_{nBZ} collective modes having an appreciable amplitude in the whole unit cell. **Figure 7(a)** shows a sketch of the Py/Co system studied. In **Figure 7(b)**, the

MM wave dispersion is compared to the DE_{nBZ} dispersion obtained according to DMM with implemented 2D boundary conditions and extended to systems composed by several materials [20]. The numerical values obtained from micromagnetic simulations are $H_{\text{eff}} = 476$ Oe being $\langle H_{\text{dem}}^y \rangle = -24$ Oe, and $M_{\text{eff}} = 794$ emu/cm³. The calculated frequency intersects, at the nBZ borders, the middle frequency of the corresponding band gaps determined by means of DMM with the only exception of the 5 BZ. For the micromagnetic simulations on the other families of collective modes and on the other types of binary periodic Py/Co and Co/Py systems with different filling fractions [19, 20].

3.3.1. Effective “surface magnetic charges”

In this section, we recall the definition of effective “surface magnetic charges” recently introduced [20] that can be applied to binary and periodic ferromagnetic systems. As an example, we discuss their distribution for the Py/Co system of the previous paragraph and of the Co/Py system obtained by interchanging the two ferromagnetic materials. By considering the Py/Co system at the border of Co cylindrical dots, an effective “surface magnetic charge” density can be defined as the linear superposition of the “surface magnetic charge” densities of the two ferromagnetic materials, viz. $\sigma_{\text{eff}} = \mathbf{M}_{\text{Py}} \cdot \hat{n} + \mathbf{M}_{\text{Co}} \cdot \hat{n}'$. Here, \hat{n} is the unit vector associated to \mathbf{M}_{Py} external to Py film, but internal to Co cylindrical dot, while \hat{n}' is the corresponding unit vector associated to \mathbf{M}_{Co} external to Co cylindrical dot, but internal to Py film.

σ_{eff} can be expressed in the simple form:

$$\sigma_{\text{eff}} = \Delta \mathbf{M}_{\text{Co-Py}} \cdot \hat{n}', \quad (9)$$

via $\hat{n} = -\hat{n}'$ with the vector $\Delta \mathbf{M}_{\text{Co-Py}} = \mathbf{M}_{\text{Co}} - \mathbf{M}_{\text{Py}}$. The effective “surface magnetic charge” density is thus proportional to the difference between the magnetizations of the two ferromagnetic materials.

In **Figure 8(a)**, the distribution of the “surface magnetic charges” is depicted together with the direction of \mathbf{H} for the Py/Co system. The magnetic field applied along the y axis orients along the same direction both the static magnetization in the Py film and the one inside the Co cylindrical dots, \mathbf{M}_{Py} and \mathbf{M}_{Co} respectively. This leads to the formation of “surface magnetic charges” of opposite sign, but of different magnitude at the interface between Py and Co. The net effect is the formation of what we call effective “surface magnetic charges” that take the signs of the “surface magnetic charges” due to \mathbf{M}_{Co} because of the larger value of $M_{s,\text{Co}}$ with respect to $M_{s,\text{Py}}$. This effect is pictorially shown in **Figure 8**. Note that the ground-state magnetization exhibits a slight deviation from the collinear state close to the dot surface at the border between the two materials as found according to micromagnetic simulations performed with OOMMF and this effect is not shown in **Figure 8**.

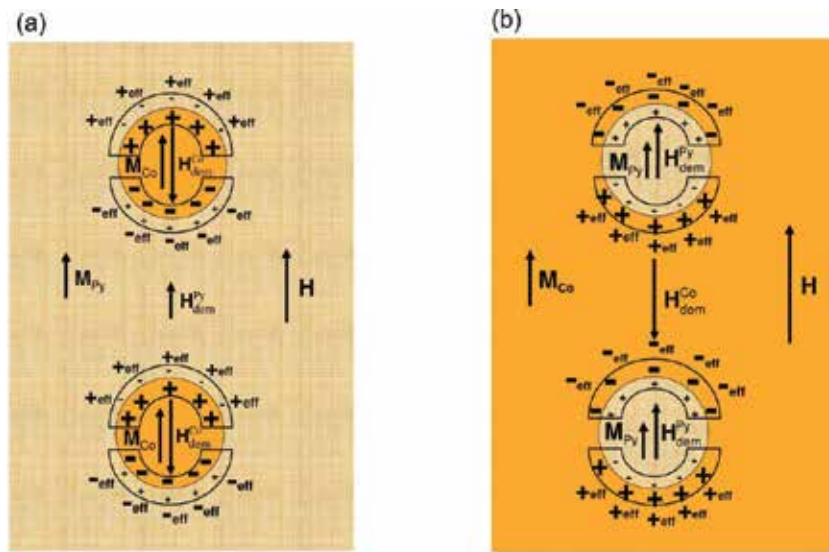


Figure 8. (a) Top view of the distribution of “surface magnetic charges” for the Py/Co system. The positive and negative effective “surface magnetic charges” are shown. The subscript “eff” stands for “effective.” The directions of M_{Py} , M_{Co} , and H together with those of the Co and Py static demagnetizing fields H_{dem}^{Co} and H_{dem}^{Py} , respectively, are also displayed. (b) As in panel (a) but for the Co/Py system. The meaning of the symbols is the same.

By interchanging the two ferromagnetic materials (Co/Py system), the corresponding distribution of effective “surface magnetic charges” becomes opposite to that of Py/Co system (see **Figure 8(b)**). Again, the effective “surface magnetic charges” at the interface between Py and Co take the sign of those of Co, because the “surface magnetic charge” density due to Co at the interface is higher with respect to that of Py. As a result, there is a reversal of the orientations of H_{dem}^{Py} and H_{dem}^{Co} static demagnetizing fields with respect to the corresponding H_{dem}^{Co} and H_{dem}^{Py} ones of Py/Co system, respectively. As a consequence of the formation of effective “surface magnetic charges,” in both systems shown in **Figure 8**, the Py static demagnetizing field is parallel to M_{Py} , while the Co static demagnetizing field H_{dem}^{Co} is antiparallel to M_{Co} . Note that, for both Py/Co and Co/Py systems, H_{dem}^{Py} (H_{dem}^{Co}) is not only due to Py (Co) but also due to their combined effect mainly related to the nonlocal nature of demagnetizing fields. For a discussion about the effective “surface magnetic charges” of other types of Py/Co or Co/Py systems characterized by other filling fractions [20].

The definition of effective “surface magnetic charges” allows to introduce an effective magnetic potential that is expressed in terms of both the “volume magnetic charges” and the effective “surface magnetic charges.” By taking into account the non-collinearity of the ground-state magnetization that gives rise to volume contributions and its three-dimensional spatial dependence, the effective magnetic potential gets its contributions from two volume integrals, one for each ferromagnetic material, and from one surface integral. For Py/Co system, it reads:

$$\Phi_M^{\text{Py/Co}}(\mathbf{r}) = - \int_{V_{\text{cell-Vdot}}} \frac{\nabla \cdot \mathbf{M}_{\text{Py}}}{|\mathbf{r} - \mathbf{r}''|} d\mathbf{r}'' - \int_{V_{\text{dot}}} \frac{\nabla \cdot \mathbf{M}_{\text{Co}}}{|\mathbf{r} - \mathbf{r}''|} d\mathbf{r}'' + \int_S \frac{\sigma_{\text{eff}}}{|\mathbf{r} - \mathbf{r}''|} dS'', \quad (10)$$

where $\mathbf{r} = (x, y, z)$ and S is the lateral surface in common between the two ferromagnetic materials. For the sake of simplicity, the dependence on the spatial coordinate in the integrand functions on the second member appearing at the numerators is omitted. It is interesting to note a main difference between the volume contributions and the surface contributions. While for the volume contributions it is possible to separate the first two terms on the second member coming from the two ferromagnetic materials, this is not anymore true for the last term related to the surface contribution. Indeed, the last term is proportional to the effective “surface magnetic charge” density depending on the contrast between the magnetizations of the two ferromagnetic materials expressed by Eq. (9). By interchanging the two ferromagnetic materials, the effective magnetic potential of Eq. (10) is not invariant, that is $\Phi_M^{\text{Co/Py}} \neq \Phi_M^{\text{Py/Co}}$. The lack of invariance is due to the two volume contributions appearing in the first and second integral on the second member that change their values upon interchanging Py with Co. Instead, the effective potential is invariant if it is supposed a quasi-collinear distribution of the magnetization leading to the neglect of the volume contributions. In this case, it is:

$$\Phi_M^{\text{Py/Co}}(\mathbf{r}) = \Phi_M^{\text{Co/Py}}(\mathbf{r}) = \int_S \frac{\sigma_{\text{eff}}}{|\mathbf{r} - \mathbf{r}''|} dS''. \quad (11)$$

Indeed, the magnetic potential depends only on the difference in modulus of the saturation magnetization of the two materials according to the definition of σ_{eff} (Eq. (9)).

3.4. General quantitative relations for effective quantities in ferromagnetic ADLs and binary and periodic magnonic crystals

For the two types of 2D magnonic crystals studied previously and represented by square lattices, it is possible to express some general quantitative relations involving the effective quantities characterizing the dynamics of collective modes for the scattering geometries investigated and for the two different ground-state magnetizations (either in-plane or perpendicular to the plane). First, some general rules between the effective quantities and the corresponding Bloch quantities have been found. These rules have been rigorously proved looking at the spatial profiles of each family of collective modes in the stationary regime (at $n\text{BZs}$ boundaries). They are summarized as follows:

- a. The effective wavelength is a function of the Bloch wavelength [19], viz.

$$\lambda_{\text{eff}}^{n\text{BZ}} = \begin{cases} n\lambda_{\text{B}}^{n\text{BZ}} & \text{if } n \text{ is odd} \\ \frac{n}{2}\lambda_{\text{B}}^{n\text{BZ}} & \text{if } n \text{ is even} \end{cases} \quad (12)$$

At the $n\text{BZs}$ edges, the effective wavelength is commensurable with the periodicity and assumes either the value $2a$ or a depending on n with $n = 1, 2, \dots$

- b.** The small effective wave vector can be written in terms of the Bloch wave vector for odd and even BZs edges, respectively [17]:

$$\mathbf{k}^{(2l+1)\text{BZ}} = \mathbf{K}^{(2l+1)\text{BZ}} - \mathbf{G}; \quad \mathbf{k}^{(2l+2)\text{BZ}} = \mathbf{K}^{(2l+2)\text{BZ}} - \mathbf{G} \quad (13)$$

where $\mathbf{G} = (l b^x, 0)$, $l = 0, 1, 2, \dots$ and $b^x = 2\pi/a$. The small effective wave vector \mathbf{k} can be interpreted as a Bloch wave vector shifted by a reciprocal lattice vector \mathbf{G} , but not necessarily shifted into the 1 BZ and at the $n\text{BZs}$, edges assumes either the value $\mathbf{k} = (\pi/a, 0)$ for n odd with $n = 1, 3, \dots$ or the value $\mathbf{k} = (2\pi/a, 0)$ for n even with $n = 2, 4, \dots$ It has been found that as the hole size tends to zero (about 10 nm), the effective wavelength becomes equal to the Bloch wavelength (and the same for the corresponding effective wave vectors) and, in this limit, the description of the spin dynamics in terms of effective properties is not anymore valid [17]. This is also true when the size of the inclusion (dot) in a binary magnonic crystal becomes very small, but it is still not zero. When the size of the defect vanishes, the role of the Bloch quantities is replaced by those of the wavelength of the surface Damon-Eshbach wave and of the corresponding propagating wave vector in a continuous ferromagnetic film. In principle, the above relations between the effective quantities and the Bloch quantities expressed by Eq.(12) and Eq.(13) can be extended also to the case when \mathbf{H} and \mathbf{K} are, for example, along the diagonal of the square cell in the MSSW scattering geometry corresponding to the ΓM direction in the reciprocal space. However, in this latter case, it has been proved, according to symmetry arguments for the case of square ADLs, that the effective wavelength of the collective modes is twice the effective periodicity and is not anymore commensurable with it [24].

As a consequence of the previous described effective rules, some further general relations can be extracted in the stationary regime [17]. In particular,

- i.** An effective rule on the dynamic magnetization.
- ii.** An inequality between the effective wavelength and the Bloch wavelength and as a consequence between the small effective wave vector and the Bloch wave vector.
- iii.** A quantitative representation of the dynamic magnetization components of collective modes in terms of the effective wavelength.

Concerning (i), it is possible to prove an effective rule on the dynamic magnetization, analogous to the well-known Bloch rule where the small effective wave vector appears in place of the Bloch wave vector, viz.

$$\delta\mathbf{m}_{\mathbf{k}}(\mathbf{r} + \mathbf{R}) = \delta\mathbf{m}_{\mathbf{k}}(\mathbf{r}) \exp^{i\mathbf{k}\cdot\mathbf{R}}, \quad (14)$$

where \mathbf{R} is the translational vector of the periodic system and, for the sake of simplicity, the superscript in the small effective wave vector has been omitted. Indeed, according to Eq. (13), it is always $\exp^{i\mathbf{k}\cdot\mathbf{R}} = \exp^{i\mathbf{k}\cdot\mathbf{R}} = \mp 1$, where -1 refers to odd edges of $n\text{BZs}$ ($n = 1, 3, \dots$) and $+1$ to even edges of BZs ($n = 2, 4, \dots$). Therefore, at the edges of $n\text{BZs}$, the phase factor of the Bloch function remains unchanged if the Bloch wave vector is replaced by the corresponding small effective wave vector. Straightforwardly, from the effective rule expressed by Eq. (14), it can be shown that the well-known Bloch rule is fulfilled. Indeed, by using Eq. (13) and omitting the superscripts, Eq. (14) takes the form:

$$\delta\mathbf{m}_{\mathbf{k}}(\mathbf{r} + \mathbf{R}) = \delta\mathbf{m}_{\mathbf{k}}(\mathbf{r}) \exp^{i(\mathbf{k}-\mathbf{G})\cdot\mathbf{R}} = \delta\mathbf{m}_{\mathbf{k}}(\mathbf{r}) \exp^{i\mathbf{k}\cdot\mathbf{R}}, \quad (15)$$

since $\exp^{-i\mathbf{G}\cdot\mathbf{R}} = 1$ for each reciprocal lattice vector \mathbf{G} . Notice that the vector \mathbf{G} does not necessarily coincide with the well-known \mathbf{G} used to pass from the extended to the reduced zone scheme.

We now discuss (ii). A general relation can be found from the analysis of the effective wavelength and of the corresponding small effective wave vector. Independently of the collective mode considered, the effective wavelength is always larger than or equal to the Bloch wavelength, viz.

$$\lambda_{\text{eff}} \geq \lambda_{\text{B}}. \quad (16)$$

Hence, a scattering selection rule can be established. Due to the presence of a periodic arrangement of finite size defects (either in the form of holes or in the form of dots having size in the nanometric range and smaller than the lattice constant of the 2D magnonic crystal), it is not allowed for a magnonic wave that scatters on the defect to have an effective wavelength smaller than the Bloch wavelength. Even though not yet investigated in detail, this rule is fulfilled in 2D square arrays of ADLs and in binary and periodic systems independently of the holes shape and of the dots shape and material. It has been proved to be independent also on the studied scattering geometry, viz. MSSW ($\mathbf{K} \perp \mathbf{H}$) or MSBVW ($\mathbf{K} \parallel \mathbf{H}$) with \mathbf{H} oriented either along the rows of holes in ADLs and of dots in binary periodic systems or along the diagonal of the square cell. This can be regarded as a general metamaterial property of 2D periodic magnetic systems where finite size defects act as scattering centers. From the inequality of Eq.

(16), the following general inequality between the magnitude of the small effective wave vector and that of the Bloch wave vector \mathbf{K} can be written, viz.

$$k \leq K. \tag{17}$$

For both relations, the equality holds at the edge of 1 BZ and 2 BZ, while from the edge of 3 BZ ahead, the strict inequality is fulfilled.

Regarding (iii), strictly related to the effective rule discussed in (i) and to the above relations involving the effective quantities described in (ii), also a quantitative representation of the dynamic magnetization of collective modes in terms of the effective wavelength can be given. It is possible to give a simple representation of the components of the dynamic magnetization associated to collective modes for both types of 2D magnonic crystals presented and for the MSSW scattering geometries described at the edges of BZs (including the one along the ΓM high-symmetry direction) in terms of the effective quantities. In particular:

$$\delta m_i = A_i \sin(\mathbf{k} \cdot \mathbf{r}) = A_i \sin(\mathbf{k} \cdot (\mathbf{r} + \mathbf{r}_{\text{eff}})), \tag{18}$$

$$\delta m_i = A_i \cos(\mathbf{k} \cdot \mathbf{r}) = A_i \cos(\mathbf{k} \cdot (\mathbf{r} + \mathbf{r}_{\text{eff}})), \tag{19}$$

with $i = x, z$. Here, A_i is a complex amplitude (either purely real or purely imaginary) and in the MSSW scattering geometry with the Bloch wave vector \mathbf{K} along the x direction, it is $\mathbf{r} = (x, 0)$, $\mathbf{k} = (k_x, 0)$, and $\mathbf{r}_{\text{eff}} = (x_{\text{eff}}, 0)$ so that $\lambda_{\text{eff}} = x_{\text{eff}}$. This representation is not only valid for describing collective modes in 2D ADLs whose dynamics is studied in the MSSW scattering geometry [17], but it can be also extended to the MSBVW scattering geometry and to the collective mode dynamics in the binary periodic magnetic systems discussed previously for the same scattering geometries.

4. Applications of 2D magnonic crystals as metamaterials

In this section, we briefly discuss some possible future applications of 2D magnonic crystals based on their metamaterial properties [17]. First, we describe the realization of a magnonic device exploiting the definition of the small effective wave vector that could potentially open the route for experiments on collective modes mapping. Second, we propose a technique based on the Fourier analysis for mapping the spatial profiles of magnonic modes as already done for spin-wave modes in isolated magnetic vortex-state disks [25] and in 2D arrays of saturated magnetic nanoelements [26].

4.1. Magnonic metamaterial device

The fabrication of a magnonic device able to exploit the definition of the small effective wave vector is proposed. As usual, the magnonic device consists of three regions. The first region is an input region, represented by an antenna producing a small magnetic field $\mathbf{h}(\mathbf{r}, t)$ having a spatial dependence proportional to $\exp^{i\mathbf{\kappa} \cdot \mathbf{r}}$ with $\mathbf{\kappa}$ the wave vector and a time dependence of the form $\exp^{i\omega_R t}$ with a resonance angular frequency ω_R . Instead, the second region is a functional region manipulated by the external magnetic field containing the 2D magnonic crystal under study, while the last region is an output region where the microwave signal is collected. Importantly, the resonance condition on the wave vector can be expressed in terms of the small effective wave vector previously discussed, namely $\mathbf{\kappa} = \mathbf{k}$. Hence, it is sufficient to use the only two values $\mathbf{k} = (\pi/a, 0)$ and $\mathbf{k} = (2\pi/a, 0)$ corresponding to wavelengths of $2a$ and a , respectively, to excite all the couples of modes of interest separated by band gaps at the border of the n BZ. Indeed, the number of values of Bloch wave vectors $\mathbf{K} = (n\pi/a, 0)$ with $n = 1, 2, 3, \dots$ at n BZ edges that should be employed would be greater. Exploiting the resonance condition on the frequency ω_R of the oscillating field, the frequencies of a couple of modes corresponding to a BZ edge and separated by a gap can be obtained and distinguished from the frequencies of another couple of modes belonging to another BZ edge. Therefore, the spatial and temporal resonance mechanism could permit to make a mapping of the frequencies of collective modes of 2D magnonic crystals independently of the geometry studied.

4.2. Imaging of collective modes

We suggest an experiment to confirm the predictions of micromagnetic simulations obtained by means of the DMM about the main features of spatial profiles of collective modes. The proposed experiment is similar to the one carried out, for example, for mapping spin-wave modes in isolated disks in the vortex state [25] or in 2D arrays of magnetic nanoelements in the saturated state [26]. By applying a magnetic field pulse with an in-plane component and by Fourier transforming the time domain signal recorded at each location of the unit cell into the frequency domain, the modal structure of the most representative collective excitations in the 2D magnonic crystals previously described could be measured. From this procedure, a spatial map of Fourier amplitudes and phases of collective modes could be determined and compared to micromagnetic spatial profiles. By means of this experimental analysis, it could be also investigated for 2D periodic magnetic systems the role of point defects in the form of either holes or magnetic dots of different shapes in determining the effective properties of collective modes like, for instance, the effective wavelength and its commensurability with the periodicity of the system. This experimental analysis could highlight further effective properties not yet theoretically investigated.

5. Conclusions

In summary, in this chapter, a systematic overview of the static and dynamical properties of 2D magnetic nanostructures has been made. The overview has included the theoretical analysis

of spin-wave modes having backward character and the investigation of effective properties of collective modes in 2D periodic systems. According to the presented results, a description of the dynamical features of continuous films and 2D magnonic crystals in terms of effective and metamaterial properties has been done. In the case of continuous ferromagnetic films, special emphasis has been given mainly to the metamaterial properties related to BVMSWs having “negative” group velocity in the purely dipolar regime and negative effective dynamic permeability. Instead, for the 2D magnonic crystals investigated, effective quantities and effective rules have been found starting from the inspection of the spatial profiles of collective modes and the role of holes and of ferromagnetic inclusions acting as scattering centers has been highlighted. In this respect, 2D magnetic nanostructures can be regarded as a new class of metamaterials that can be put on a similar footing as, for instance, other classes of widely studied metamaterials such as plasmonic, dielectric, and electromagnetic metamaterials. The found properties could open the route for further experimental investigations in the field of magnonic crystals such as, for instance, the mapping of collective excitations of different kinds and for different geometries and can be exploited for tailoring a magnonic device able to confirm the theoretical predictions on the effective quantities and effective properties characterizing collective spin-wave modes.

Acknowledgements

This work was partially supported by National Group of Mathematical Physics (GNFM-INDAM). The author acknowledges L. Giovannini for making available the DMM micromagnetic code.

Author details

Roberto Zivieri

Address all correspondence to: roberto.zivieri@unife.it

Department of Physics and Earth Sciences, University of Ferrara, Ferrara, Italy

References

- [1] Giovannini L, Montoncello F, Nizzoli F: Effect of interdot coupling on spin-wave modes in nanoparticle arrays. *Phys. Rev. B.* 2007; 75: 024416. DOI: 10.1103/PhysRevB.75.024416
- [2] Damon RW, Eshbach JR: Magnetostatic modes of a ferromagnet slab. *J. Phys. Chem. Solids.* 1961; 19: 308–320. DOI: 10.1016/0022-3697(61)90041-5

- [3] Kalinikos BA, Slavin AN: Theory of dipole-exchange spin wave spectrum for ferromagnetic films with mixed exchange boundary conditions. *J. Phys. C.* 1986; 19: 7013–7033. DOI: 10.1088/0022-3719/19/35/014
- [4] Zivieri R. Magnetic matter spin waves with “negative” group velocity. In: Proceedings of the 9th International Congress on Advanced Electromagnetic Materials and Optics (Metamaterials’ 2015); 7–10 September 2016; Oxford. 2015. pp. 529–531. DOI: 10.1109/MetaMaterials.2015.7342512 04/04/2016 <http://ieeexplore.ieee.org/xpl/articleDetails.jsp?arnumber=7342512>
- [5] Zivieri R. Dynamic negative permeability in a lossless ferromagnetic medium. In: Proceedings of the 9th International Congress on Advanced Electromagnetic Materials and Optics (Metamaterials’ 2015); 7–10 September 2016; Oxford. 2015. pp. 532–534. DOI: 10.1109/MetaMaterials.2015.7342513 04/04/2016 <http://ieeexplore.ieee.org/xpl/articleDetails.jsp?arnumber=7342513>
- [6] Veselago VG: The electrodynamics of substances with simultaneously negative values of ϵ and μ . *Sov. Phys. Usp.* 1968; 10: 509–515. DOI: 10.1070/PU1968v010n04ABEH003699
- [7] Alù A, Engheta N: Pairing an epsilon-negative slab with a mu-negative slab: resonance, tunneling and transparencies. *IEEE Trans. Antennas Propag.* 2003; 51: 2558–2571. DOI: 10.1109/TAP.2003.817553
- [8] Mikhaylovskiy RV, Hendry E, Kruglyak VV: Negative permeability due to exchange spin-wave resonances in thin magnetic films with surface pinning. *Phys. Rev. B* 2010; 82: 195446. DOI: 10.1103/PhysRevB.82.195446
- [9] Nikitov SA, Tailhades P, Tsai CS: Spin waves in periodic magnetic structures magnonic crystals. *J. Magn. Magn. Mater.* 2001; 236: 320–330. DOI: 10.1016/S0304-8853(01)00470-X
- [10] Elachi C: Magnetic wave propagation in a periodic medium. *IEEE Trans. Magn. Magn.* 1975; 11: 36–39. DOI: 10.1109/TMAG.1975.1058546
- [11] Kruglyak VV, Demokritov SO, Grundler D: Magnonics. *J. Phys. D: Appl. Phys.* 2010; 43: 264001. DOI: 10.1088/0022-3727/43/26/264001
- [12] Zivieri R, Montoncello F, Giovannini L, Nizzoli F, Tacchi S, Madami M, Gubbiotti G, Carlotti G, Adeyeye AO: Collective spin modes in chains of dipolarly interacting rectangular magnetic dots. *Phys. Rev. B* 2011; 83: 054431. DOI: 10.1103/PhysRevB.83.054431
- [13] Zivieri R: Metamaterial properties of one-dimensional and two-dimensional magnonic crystals. *Sol. State Phys.* 2012; 63: 151–216. DOI: 10.1016/B978-0-12-397028-2.00003-5
- [14] Wang ZK, Zhang VL, Lim HS, Ng SC, Kuok MH, Jain S, Adeyeye AO: Observation of frequency band gaps in a one-dimensional nanostructured magnonic crystal. *Appl. Phys. Lett.* 2009; 94: 083112. DOI: 10.1063/1.3089839

- [15] Tacchi S, Montoncello F, Madami M, Gubbiotti G, Carlotti G, Giovannini L, Zivieri R, Nizzoli F, Jain S, Adeyeye AO, Singh N: Band diagram of spin waves in a two-dimensional magnonic crystal. *Phys. Rev. Lett.* 2011; 107: 127204. DOI: 10.1103/PhysRevLett.107.127204
- [16] Zivieri R, Tacchi S, Montoncello F, Giovannini L, Nizzoli F, Madami M, Gubbiotti G, Carlotti G, Neusser S, Duerr G, Grundler D: Bragg diffraction of spin waves from a two-dimensional antidot lattice. *Phys. Rev. B* 2012; 85: 012403. DOI: 10.1103/PhysRevB.85.012403
- [17] Zivieri R, Giovannini L: Effective quantities and effective rules in two-dimensional antidot lattices. *Photon. Nanostruct. Fundam. Appl.* 2013; 11: 191–202. DOI: 10.1016/j.photonics.2013.07.002
- [18] Malagò P, Giovannini L, Zivieri R. Perpendicularly magnetized antidot lattice as a two-dimensional magnonic metamaterial. In: *Proceedings of the 9th International Congress on Advanced Electromagnetic Materials and Optics (Metamaterials' 2016)*; 7–10 September 2016; Oxford. 2015. pp. 532–534. DOI: 10.1109/MetaMaterials.2015.7342513 04/04/2016 <http://ieeexplore.ieee.org/xpl/articleDetails.jsp?arnumber=7342514>
- [19] Malagò P, Giovannini L, Zivieri R. Effective properties of a binary magnonic crystal. In: *Proceedings of the 8th International Congress on Advanced Electromagnetic Materials and Optics (Metamaterials' 2014)*; 25–30 August 2014; Copenhagen. 2014. pp. 316–318. DOI: 10.1109/MetaMaterials.2015.7342513
- [20] Zivieri R, Malagò P, Giovannini L: Band structure of collective modes and effective properties of binary magnonic crystals. *Photon. Nanostruct. Fundam. Appl.* 2014; 12: 398–418. DOI: 10.1016/j.photonics.2014.04.001
- [21] Gubbiotti G, Malagò P, Fin S, Tacchi S, Giovannini L, Bisero D, Madami M, Carlotti G, Ding J, Adeyeye AO, Zivieri R: Magnetic normal modes of bicomponent permalloy/cobalt structures in the parallel and antiparallel ground state. *Phys. Rev. B* 2014; 90: 024419. DOI: 10.1103/PhysRevB.90.024419
- [22] Krawczyk M, Puzzkarski H: Plane-wave theory of three-dimensional magnonic crystals. *Phys. Rev. B* 2008; 77: 054437. DOI: 10.1103/PhysRevB.77.054437
- [23] Donahue M, Porter D (Eds): *OOMMF User's Guide Version 1.0*. In: *Interagency Report NISTIR 6376*, National Institute of Standards and Technology, Gaithersburg, MD, 1999.
- [24] Zivieri R. Metamaterial description of magnonic modes along ΓM direction in a 2D antidot lattice. In: *Proceedings of the 7th International Congress on Advanced Electromagnetic Materials and Optics (Metamaterials' 2013)*; 16–21 September 2016; Bordeaux. 2013. pp. 181–183. DOI: 10.1109/MetaMaterials.2013.6808993 04/04/2016 <http://ieeexplore.ieee.org/xpl/articleDetails.jsp?arnumber=6808993>

- [25] Buess M, Höllinger R, Haug T, Perzmaier K, Krey U, Pescia D, Scheinfein MR, Weiss D, Back CH: Fourier transform imaging of spin vortex eigenmodes. *Phys. Rev. Lett.* 2004; 93: 077207. DOI: 10.1103/PhysRevLett.93.077207
- [26] Kruglyak VV, Keatly PS, Neudert A, Hicken RJ, Childress JR, Katine JA: Imaging collective magnonic modes in a 2D arrays of magnetic nanoelements. *Phys. Rev. Lett.* 2010; 104: 027201. DOI: 10.1103/PhysRevLett.104.027201

Molecular Magnetism Modeling with Applications in Spin Crossover Compounds

Mihai Dimian and Aurelian Rotaru

Additional information is available at the end of the chapter

<http://dx.doi.org/10.5772/64281>

Abstract

Molecular magnetic materials have become flourishing fields for research and technological developments due to their novel behavior compared to classical magnetic materials. Molecular magnetism modeling has reached a certain degree of maturity, although several experimental findings are still open problems. This chapter is aimed at providing a general introduction to physical modeling in molecular materials with a special emphasis placed on spin crossover compounds. This presentation includes Ising-type models and their generalizations, such as Wajnflasz and Pick, Bousseksou et al., Zimmermann and König, Sorai and Seki, and Nasser et al., along with their applications to the characterization of phase transition, hysteresis behavior, and thermal relaxations in spin crossover compounds. Recent experimental findings are explained in this context and the relevance of theoretical results for technological applications is also discussed.

Keywords: molecular magnetism, spin crossover compounds, hysteresis, phase transitions, thermal relaxations, modeling and simulations

1. Introduction

Molecular magnetic materials have been in the research spotlight since the current silicon based devices and conventional magnetic storage devices approached their technological and physical limits [1, 2]. In this context, spin crossover (SCO) materials present a special interest due to their unique properties, high versatility, and a wide variety of potential technical applications [3, 4].

The most widely studied SCO materials involve transition metal centers ($3d^4$ – $3d^7$) in an octahedral O_h symmetry of ligands. These materials present molecular bistability that can be triggered by various external stimuli such as temperature, pressure, light, magnetic and electric field, and gas absorption [5–16]. The molecular bistability results from the balance between the spin pairing energy and the crystal field that leads to the possibility to populate the 3d orbitals in two different ways characterized by different values of the total spin S . These two situations are known in the literature as high-spin (HS) and low-spin (LS) states, respectively. Schematic representation of 3d electron configurations in an octahedral ligand field for Fe (II) complexes in the low-spin ($S = 0$) and the high-spin ($S = 4$) states are presented in **Figure 1**.

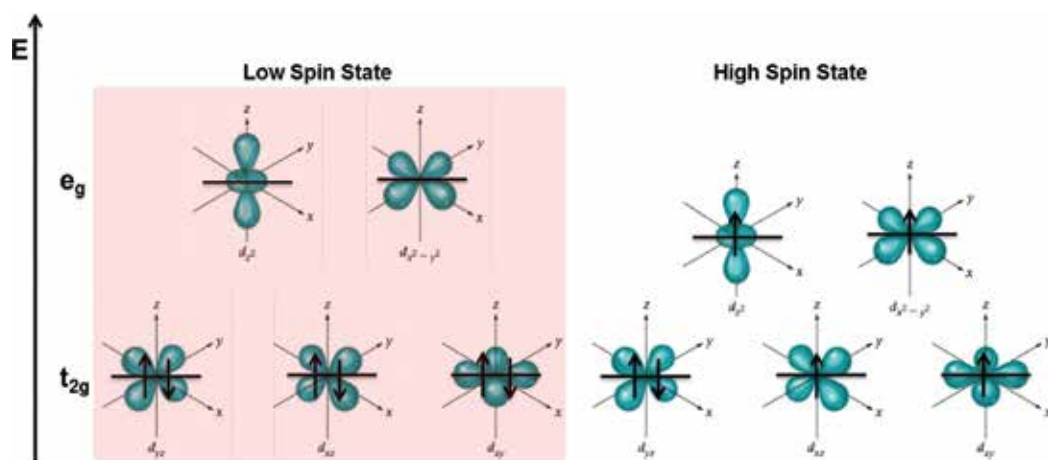


Figure 1. 3d electron configurations in an octahedral ligand field for Fe (II) complexes in the low-spin ($S = 0$) and the high-spin ($S = 4$) states, respectively.

The two stable states may feature different magnetic, optical, electrical, and vibrational/structural properties. In the solid state, the structural changes associated to the spin transition propagate in a cooperative manner, which can lead to a hysteretic behavior. From an applicative point of view, SCO materials have been proposed for various technological applications such as recording media, sensors (thermal, pressure, or gas) [17–21], displays [4], molecular switches [22, 23], memristor devices [24–28], or actuators [29, 30].

Molecular magnetism modeling has reached a certain degree of maturity, although several experimental findings are still open problems from theoretical point of view. Here, we provide a review of physical modeling in molecular materials with a special emphasis placed on spin crossover compounds, including Ising-type models and their generalizations, such as Slichter and Drickamer [9], Bousseksou et al. [31], Sorai and Seki [32], and Nasser et al. [33, 34], along with the novel approaches developed in our research group and applied to the characterization of phase transition and hysteresis behavior in molecular magnets [35–41]. Recent experimental findings are explained in this context and the relevance of theoretical results for technological applications is also discussed.

2. Modeling of spin crossover compounds

The theoretical analysis of SCO materials has been developed in two main directions: the molecular approach [31–34, 42–64] and macroscopic approach [9, 65–70], respectively. In the case of the “molecular” models, the interactions between molecules disturb the molecular system and, thus, the statistical thermodynamics can be used to correlate the microscopic parameters of the system with the experiments. The “macroscopic” models use the laws of thermodynamics (phenomenological equations and/or mixture theory) and do not reflect the intrinsic structure of the molecular system.

The first model based on the concept of intermolecular interaction, which was able to qualitatively simulate the spin transition in SCO materials, was proposed by Wajnflasz and Pick in the early 1970s [42, 43]. They assumed that each metal center is a four-level system (two ion beams, each one of them having two spin states) and introduced a fictitious charge to characterize each spin state. The interaction between ionic centers was described by an Ising-like coupling term and the corresponding Hamiltonian was resolved in the mean-field approximation. This model was able to predict both discontinuous and continuous $HS \leftrightarrow LS$ transitions, but its main limitation is related to the nature of the interaction term that is not entirely justified.

The main macroscopic model accounting intermolecular interactions was proposed during the same period by Slichter and Drickamer [9]. This model successfully described the effect of an external applied pressure on the spin transition phenomena and represented the starting point for many macroscopic models attempting to describe the origin of the interactions (atom-phonon coupling, elastic energy, etc.). It is based on the theory of regular solutions assuming a random distribution of molecules in the material. This model was also able to reproduce hysteresis phenomena accompanying discontinuous spin transitions in SCO materials.

In 1974, Sorai and Seki [32] proposed an alternative thermodynamic model by considering that the molecules of the same spin state are organized in spin-like domains, assumed to be independent from each other. The model is similar to the theory of heterophase fluctuations developed by Frenkel and is widely used when the calorimetric data for SCO transition are available. However, their model is rather limited since it is not able to reproduce a hysteretic transition.

In 1977, Zimmermann and König [45] developed a novel model that takes explicitly into account the lattice vibrations. Intramolecular interactions were introduced by using an Ising-like Hamiltonian that was resolved in the Bragg-Williams approximation. The vibration modes were assumed in the Debye approximation, regardless of their intra- or intermolecular origin. The authors also showed a formal equivalence between the two-level models approached in the mean-field approximation and the macroscopic thermodynamic models based on the theory of regular solutions.

The next step was made by Kambara [46] in 1979. This model, based on the theory of the ligand field, assumes that the $HS \rightarrow LS$ transition is induced by the Jahn-Teller coupling between the 3d electrons and the local distortion of the base complex Fe.

The link between the thermodynamic model and the experimental results was made by Gutlich et al. [70], changing the input parameters of the Sorai and Seki model.

The first real physical approach of the cooperativity origin was proposed by Onishi and Sugano [65] and Spiering et al. [66], respectively. The authors consider the active molecules, which are susceptible of undergoing a spin transition, as hard spheres inserted into an elastic medium. Indeed, it has been observed that the spin transition was accompanied by a volume change of the SCO molecules. This change will induce a stress field that will propagate in the whole crystallographic lattice due to its elasticity. These spheres were treated as point defects.

A new approach for two-level models was proposed by Bousseksou et al. in the 1990s [31, 71]. They consider that the degeneracy of the two-spin states is much higher than the spin degeneracy ratio. Such degeneracy results from the entropy variation during the spin transition. This new approach allows fitting of the experimental data using input parameters from calorimetric measurements.

Ising-like models can be easily applied, but the nature of the interactions, introduced to describe the cooperativity among the molecules, is not specified. In this regard, in recent years, another series of elastic-like models was proposed. Here, we can distinguish two different approaches. The first approach was proposed by Nishino et al. [58] and Enachescu et al. [60], where they consider that the interactions are elastic in their nature, i.e., the molecules are interacting via the change of the molecular volume. The second approach is proposed by Nasser et al. [33, 34], which is known in the literature as “atom-phonon coupling” (APC) model. The basic idea of the APC model is that the elastic constants that characterize the coupling between neighboring molecules depend on their spin state. This model has proven its complexity, being able to reproduce a wide range of characteristic behaviors to spin transition compounds [35–37, 39, 41, 72, 73].

2.1. Slichter and Drickamer model

The model proposed by Slichter and Drickamer assumes a mixture of both HS and LS constituents in the solid. If we denote by n_{LS} and n_{HS} the associated mole fractions of the LS and HS states, respectively, the free enthalpy of the interacting ions centers can be then expressed as

$$G = n_{LS}G_{LS} + n_{HS}G_{HS} - TS_{mix} + \Gamma n_{HS}n_{LS}, \quad (1)$$

where Γ is the term of intermolecular interaction and S_{mix} is the mixed entropy of an ideal mixing solution of LS and HS molecules, given by $S_{mix} = -R(n_{LS} \ln n_{LS} + n_{HS} \ln n_{HS})$ with R being the gas constant ($= 8.3144598(48) \text{ J K}^{-1} \text{ mol}^{-1}$). If G_{LS} is considered as origin level for energies, then $G_{LS} = 0$, while $G_{HS} = \Delta G = \Delta H - T\Delta S$, with ΔH and ΔS being the entropy and the enthalpy variations, respectively, during the spin transition. As a consequence, the free enthalpy can be written as follows:

$$G = n_{HS}\Delta H - \Gamma n_{HS}(1 - n_{HS}) + RT \left[(1 - n_{HS}) \ln(1 - n_{HS}) + n_{HS} \ln n_{HS} + n_{HS} \frac{\Delta S}{R} \right]. \quad (2)$$

The equilibrium condition of the system, $\left(\frac{\partial G}{\partial n_{HS}}\right)_{T,p} = 0$, leads to the implicit expression of n_{HS} as a function on T

$$T = \frac{\Delta H + \Gamma(1 - 2n_{HS})}{R \ln \left(\frac{1 - n_{HS}}{n_{HS}} \right) + \Delta S}. \quad (3)$$

The solution of Eq. (3) for HS molar fraction as a function of temperature is plotted in **Figure 2**, for several values of intermolecular interaction constants considering variations of enthalpy and entropy specific to Fe(II) SCO compounds.

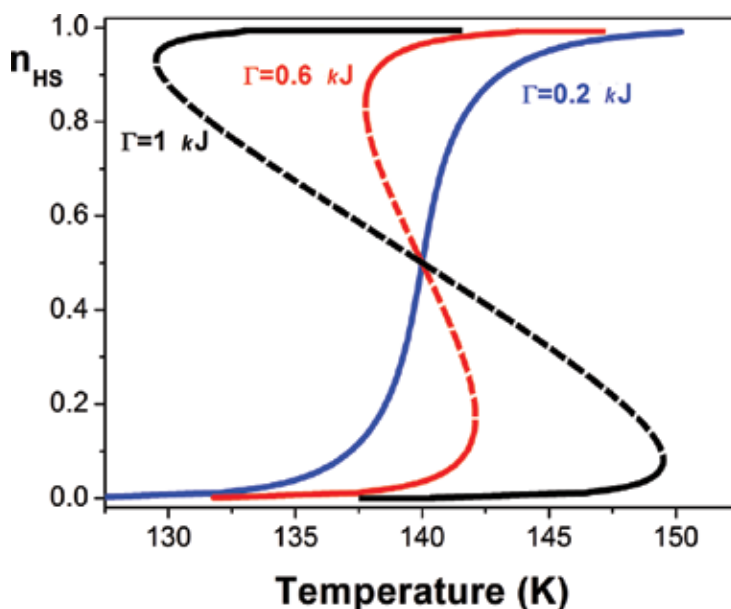


Figure 2. Thermal variations of the HS molar fraction for three selected values of the intermolecular interaction constant $\Gamma = 0.2, 0.6$, and 1 kJ. The following values have been used for the enthalpy and entropy variations: $\Delta H = 7$ kJmol⁻¹ and $\Delta S = 50$ JK⁻¹mol⁻¹.

2.2. Sorai and Seki model

The model proposed by Sorai and Seki considers that LS and HS molecules are not randomly distributed but organized in spin-like domains, i.e., regions of molecules having the same spin state. Thus, the SCO system consists of several noninteractive domains having the same

number of molecules (n) and transition temperature around a critical temperature $T_c (= \Delta H / \Delta S)$. The equilibrium condition leads to the following explicit expression of n_{HS} as a function on T :

$$n_{HS} = \frac{1}{1 + \exp\left(\frac{n\Delta H}{R}\left(\frac{1}{T} - \frac{1}{T_c}\right)\right)}. \quad (4)$$

For single-molecule domain, the solution is the same with the one found from Eq. (3) in the case of noninteractive particles. The introduction of spin-like domains in the model leads to a better control of the spin transition path, as reflected by **Figure 3(a)**, where the thermal variation of HS molar fraction is plotted for various numbers of molecules included in a spin-like domain. The Sorai and Saki model is widely used in the case when the calorimetric data of the SCO compounds are available. From calorimetric measurements, such as molar heat capacity at constant pressure as a function of temperature, $C_p = f(T)$, the number of molecules per domain can be calculated by using the following formula:

$$n = \frac{4RT_c^2}{(\Delta H)^2} \left(C_p(T_c) - \frac{1}{2}(C_{LS}(T_c) + C_{HS}(T_c)) \right), \quad (5)$$

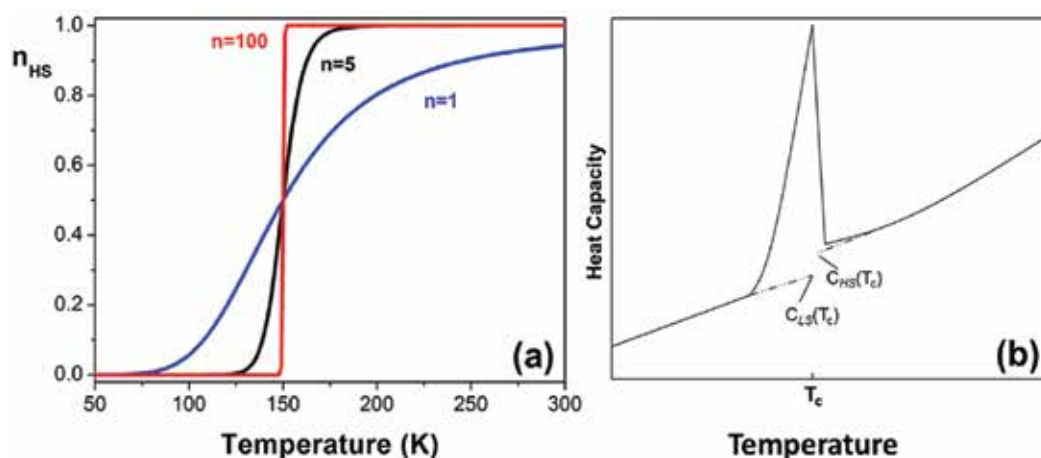


Figure 3. (a) Thermal variations of the HS molar fraction for three selected values of the number of molecules per domain $n = 1, 5$, and 100 . The following values have been used for the enthalpy variations and critical temperature: $\Delta H = 7 \text{ kJmol}^{-1}$ and $T_c = 150 \text{ K}$ and (b) typical heat capacity variation as a function of temperature and definitions of C_{LS} and C_{HS} .

where C_{LS} and C_{HS} are defined as “normal” heat capacities of LS and HS states as described in **Figure 3(b)**. Although n is considered a relevant measure of the spin cooperativity during phase transition, the lack of interaction between domains leads to an important limitation of Sorai and Seki model, since it is not able to reproduce hysteretic transition.

2.3. Ising-like model

The model proposed by Varret research group [31] has taken into account the degenerate energy levels and it was successfully used to describe both static and dynamic properties of SCO compounds under different external stimuli such as temperature, pressure, magnetic, and electric fields [74, 75]. The model Ising-like Hamiltonian can be written as follows:

$$H = \frac{1}{2} \sum_i (\Delta - k_B T \ln g) \hat{\sigma}_i - \sum_{\langle i,j \rangle} J_{ij} \hat{\sigma}_i \hat{\sigma}_j - L \langle \hat{\sigma} \rangle \sum_i \hat{\sigma}_i, \quad (6)$$

where $\hat{\sigma}_i$ is the fictitious spin operator associated to molecule i having the eigenvalues +1 (when the molecule is in the HS state) and -1 (when the molecule is in the LS state), Δ is the internal energy gap between the HS and LS states, k_B is the Boltzmann constant ($= 1.38064852(79) \times 10^{-23} \text{ J K}^{-1}$), g is the degeneracy ratio between HS and LS energy levels (>1), J_{ij} stands for the short-range interaction parameter representing the cooperative interaction that only exists between the nearest-neighboring pairs (J_{ij} includes the nearest-neighbors number), i, j denotes the fact that the sum is only made over the nearest-neighbors pairs, and L stands for long-range interaction parameter that is expressed here in a mean-field approach with $\langle \hat{\sigma} \rangle$ being the average fictitious spin.

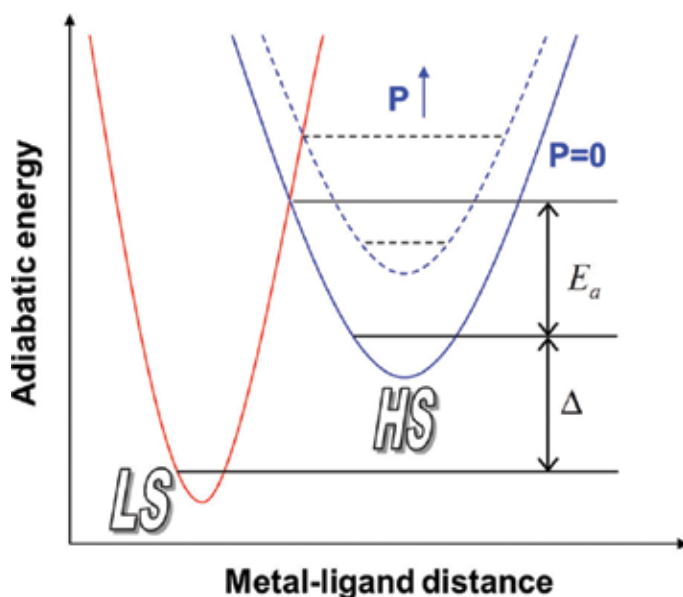


Figure 4. Pressure effect on the configuration diagram.

Hamiltonian (6) takes into account both short- and long-range interactions, while spin and energy degeneracies are considered as a temperature-dependent effective field $(\Delta - k_B T \ln g)/2$ acting on each spin. In noninteractive system, the critical temperature T_{0c} at which

$n_{\text{HS}} = n_{\text{LS}} = 0.5$, corresponds to a zero effective field and, consequently, it is related to the energy gap and degeneracy ratio as follows: $T_{0c} = \Delta/k_B \ln g$. Let us now denote by T_{1c} the critical temperature at which phase transition happens in purely ferromagnetic Ising systems formed by the second term in Hamiltonian (6) with J_{ij} positive. If the critical temperature in purely Ising model is smaller than the critical temperature in noninteractive model ($T_{1c} < T_{0c}$), then a gradual spin transition from LS to HS takes place by increasing the temperature. Otherwise, the spin transition is discontinuous and is associated to a first-order phase transition. The addition of long-range interactions, the last term in Hamiltonian (6), can significantly change the system behavior.

For example, purely one-dimensional Ising systems generate no phase transition, and, consequently, the addition of degeneracy term does not contribute to the appearance of phase transition (since T_{0c} is larger than $T_{1c} = 0$). However, when long-range interactions are introduced, various types of spin transition are possible, including multiple-step transitions and hysteretic transitions [76–79].

Next, we will discuss how this model can be adapted and applied to analyze the effects of external pressure on SCO behavior. It was experimentally observed that variations of the external pressure can give rise to transitions between HS state and LS state. This process, governed by entropy, can be better understood by assuming two potential wells, each representing a possible spin state as a function of a configuration coordinate (metal-ligand distance), as represented in **Figure 4**. The application of an external pressure decreases intermolecular distances and, by consequence, the metal-ligand distances. Since the ligand field is inversely proportional to the metal-ligand distance (to the sixth power), the application of external pressure has a similar effect as the substitution of ligands to the central metal, so the potential wells can move vertically and horizontally by changing the metastable state [9, 31, 43, 74, 80].

The energy gap dependence on the pressure can be expressed as:

$$\Delta(p) = \Delta(p=0) + p\delta V, \quad (7)$$

where δV is the volume variation of the SCO molecules during the spin transition phenomenon and p is the externally applied pressure. By considering the mean-field approach, the behavior of the system described by Eq. (6) coupled with Eq. (7) can be approximated by behavior of a noninteracting system of spins with one-site Hamiltonian H_{mf} written as

$$H_{mf} = \frac{\Delta(p) - k_B T \ln g}{2} \hat{\sigma} - (qJ + L) \hat{\sigma} \langle \hat{\sigma} \rangle, \quad (8)$$

where q is the number of nearest neighbors. The average fictitious spin $\langle \hat{\sigma} \rangle$ is also known as “fictitious magnetization” and will be further denoted by m . The resulting mean-field equation m has the following form:

$$m = \tanh\left(\frac{(qJ + L)m}{k_B T} + \frac{k_B T \ln g - \Delta(p)}{2k_B T}\right). \quad (9)$$

For the sake of simplicity, in the following calculations we use several normalizations, namely, the energy gap $\Delta = \Delta(p)/k_B$, the interaction parameter $\Gamma = (qJ + L)/k_B$ (which includes both short- and long-range interaction), and the volume variation $\alpha = \delta V \cdot 10^{-5}/k_B$ (where the factor 10^{-5} stands for the conversion of the pressure units from *pascal* to *bar*). Sample results for hysteretic transitions driven by temperature and pressure variations are presented in **Figure 5**, for $\Delta = 1000\text{K}$, $\ln g = 7$, $\Gamma = 400\text{K}$, $\alpha = 4\text{K}/\text{bar}$, where the HS fraction n_{HS} is simply related to the fictitious magnetization m by $n_{\text{HS}} = (1 + m)/2$.

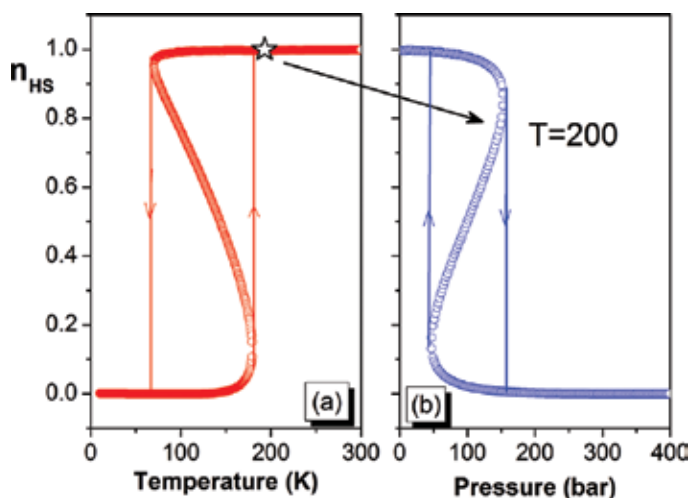


Figure 5. (a) Thermal hysteresis loop computed for pressure $p = 1$ bar and (b) pressure hysteric loop for $T = 200\text{K}$. The normalized parameters used in these calculations are $\Delta = 1000\text{K}$, $\ln g = 7$, $\Gamma = 400\text{K}$, $\alpha = 4\text{K}/\text{bar}$.

By increasing the applied pressure, the switching temperatures will shift to higher values, thus making it possible to control the system switching temperature by external inputs. However, the width of hysteric loop is reduced by this action and, at some critical value of the applied pressure, the SCO system will lose its cooperativity, i.e., the hysteric loop disappears leading to a continuous spin transition. The 3D phase diagrams' (T, p, n_{HS}) coordinates are presented in **Figure 6**, for a system with noninteractive molecule (left) and for a cooperative system with interaction constant $\Gamma = 400\text{K}$ (right). The other parameters are the same as in the previous discussion $\Delta = 1000\text{K}$, $\ln g = 7$, $\alpha = 4\text{K}/\text{bar}$. In order to separate the hysteric part from nonhysteric part of the phase diagram, let us observe that the transition temperatures (pressures) can be obtained as maxima and minima of the temperature (pressure) as a function of n_{HS} , or, equivalently, as a function of m . The expression of temperature in terms of m can be obtained by inverting Eq. (9) as follows:

$$T = \frac{\Delta(0) + \alpha p - 2\Gamma m}{\ln g - \ln\left(\frac{1+m}{1-m}\right)}. \quad (10)$$

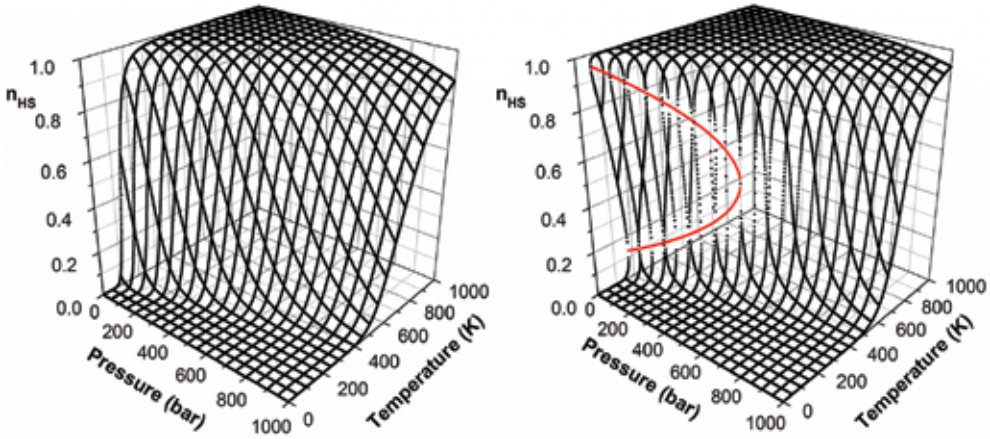


Figure 6. The 3D phase diagram for a system of noninteractive spins (left) and for a cooperative system with $\Gamma = 400\text{K}$ (right). The red curve from the right image represents the spinodal curve. The normalized parameters used in these calculations are $\Delta = 1000\text{K}$, $\ln g = 7$, $\alpha = 4\text{K}/\text{bar}$.

In order to find the extrema of T as a function of m , the derivative dT/dm is set to be zero, leading to the following algebraic equation:

$$\frac{1}{2}(m^2 - 1)\left(\ln\left(\frac{1+m}{1-m}\right) - \ln g\right) + 2m = \frac{1}{\Gamma}(\Delta(0) + \alpha p). \quad (11)$$

By varying pressure, the solution of this equation describes in (T, p, n_{HS}) space, a critical curve, also known as spinodal curve, which delimits the hysteretic part of the phase diagram from the nonhysteretic one, as presented from **Figure 6**.

2.4. Atom-phonon coupling model

Atom-phonon coupling model has been proposed by Nasser et al. [33, 34], with the aim to overcome some deficiencies of Ising-like models concerning the origin of the interaction parameter. Moreover, APC model is taking into account the results of Sorai and Seki, regarding the dependence of the Debye temperature as a function of the HS fraction [32]. In Sorai and Seki model, the importance of the contribution of phonons in the transition phenomenon is emphasized. A similar approach has been also discussed by other authors in Refs. [81, 82].

Although the APC model was initially proposed for the characterization of the thermal behavior of the SCO compounds, its applicability has been extended afterwards in order to describe the process of photoexcitation observed at low temperature light-induced excited spin

state trapping (LIESST) [37, 39, 41], the relaxation process of the photo-excited metastable states and light-induced thermal hysteresis (LITH) [35], as well as the effect of externally applied pressure [36, 37].

In the APC model, the spin crossover molecules are modeled as atoms linked by springs, i.e., the intramolecular vibrations are not taken into account. As in the Ising-like model, a fictitious spin $\hat{\sigma}_i$ is associated to each molecule that can take two eigenvalues: -1 , corresponding to the fundamental level LS, and $+1$, corresponding to the HS level. According to the spin state of the neighbor atoms, three values of the elastic constants taken into account are denoted by λ when both molecules are in the LS state, ν when both molecules are in the HS state, and μ when one atom is in the LS state and the other is in the HS state. From Brillouin and Mossbauer spectroscopy [83, 84] data, it was shown that the elastic constants are smaller in the HS state than in the LS state. Thus, at a given temperature, phonons promote the HS state while the HS-LS energy gap promotes the LS state, leading to an interesting competition between two mechanisms. Consequently, in the APC model, it is considered as $\nu < \mu < \lambda$.

The APC Hamiltonian is given by the sum of two contributions: electronic and vibrational:

$$H = H_{spin} + H_{ph} = \left(\sum_{i=1}^N \frac{\Delta}{2} \hat{\sigma}_i \right) + (E_c + E_p) , \quad (12)$$

where N is the number of spins in the system, Δ is the energy gap between these LS and HS states, and E_c and E_p are the kinetic energy and the potential energy of the system, respectively. The kinetic energy is simply written as:

$$E_c = \sum_{i=1}^N \frac{p_i^2}{2m_a} , \quad (13)$$

where i is the impulse of atom and m_a is the mass of the SCO atom. For a chain of N atoms, the potential energy can be written as:

$$E_p = \sum_{i=1}^N \frac{1}{2} e_{i,i+1} (u_{i+1} - u_i)^2 , \quad (14)$$

where u_i is the longitudinal displacement of the i th atom from its equilibrium position that is assumed to be independent of the electronic state of the atom i and its neighbors and $e_{i,i+1}$ is the elastic constant between the i th atom and the $(i+1)$ th atom. By taking into account the previous discussion related to the state-dependent elastic constants, a concise formula can be obtained for $e_{i,i+1}$ in terms of λ , μ , ν and the fictitious neighboring spins $\hat{\sigma}_i$ and $\hat{\sigma}_{i+1}$:

$$e_{i,i+1} = \frac{\lambda + 2\mu + \nu}{4} + \frac{\nu - \lambda}{4} (\hat{\sigma}_i + \hat{\sigma}_{i+1}) + \frac{\lambda - 2\mu + \nu}{4} \hat{\sigma}_i \hat{\sigma}_{i+1} . \quad (15)$$

The periodic boundary conditions are considered, as apparent from **Figure 7**, so $\hat{\sigma}_{N+1}$ is actually $\hat{\sigma}_1$. By plugging Eq. (15) in Eq. (14), the potential energy can be rewritten as the sum of three terms V_0 , V_1 , and V_2 where:

$$V_0 = \sum_{i=1}^N \frac{\lambda + 2\mu + \nu}{8} (u_{i+1} - u_i)^2, \quad (16)$$

$$V_1 = \sum_{i=1}^N \frac{\nu - \lambda}{8} [(u_i - u_{i-1})^2 + (u_{i+1} - u_i)^2] \sigma_i, \quad (17)$$

$$V_2 = \sum_{i=1}^N \frac{\lambda - 2\mu + \nu}{8} (u_{i+1} - u_i)^2 \sigma_i \sigma_{i+1}. \quad (18)$$

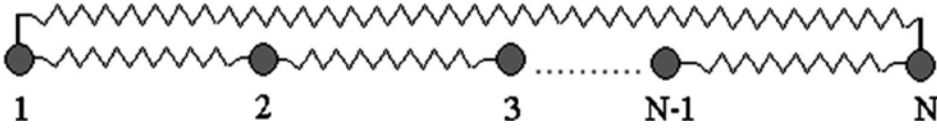


Figure 7. Chain of atoms bound together by springs with periodic boundary conditions.

It is apparent from Eq. (17) that V_1 has the expression of Zeeman-like energy, each spin $\hat{\sigma}_i$ being subject to an effective field h_i given by:

$$h_i = \frac{\nu - \lambda}{8} [(u_i - u_{i-1})^2 + (u_{i+1} - u_i)^2]. \quad (19)$$

where $\nu < \lambda$ in this field promotes the HS state (eigenvalue +1). It is apparent from Eq. (18) that V_2 has the expression of exchange-like energy, so an effective exchange parameter $J_{i,i+1}$ can be defined as follows:

$$J_{i,i+1} = \frac{\lambda - 2\mu + \nu}{8} (u_{i+1} - u_i)^2. \quad (20)$$

The sign of exchange constant depends on the relation between μ and $(\nu + \lambda)/2$, and the exchange term disappears when the elastic constant for HS-LS case is the average of the elastic constants for LS-LS and HS-HS states, i.e., $\mu = (\nu + \lambda)/2$.

In the mean-field approximation, the elastic constant $e_{i,i+1}$ can be replaced by an effective elastic constant K that does not depends on site i . Thus, the effective field h_i generated by the phonons is uniform throughout the chain and the effective exchange parameter $J_{i,i+1}$ is the same for each pair of neighboring spins. The system can be studied by using transfer-matrix method [85], and the resulting mean value for the phonon Hamiltonian can be expressed as follows:

$$\langle H_{phon}(K) \rangle_T = \frac{\hbar \omega_M(\lambda)}{2} \sqrt{\frac{K}{\lambda}} \cdot \sum_{i=1}^N \left| \sin \frac{i\pi}{N} \right| \coth \left(\frac{\hbar \omega_M(\lambda)}{2k_B T} \sqrt{\frac{K}{\lambda}} \left| \sin \frac{i\pi}{N} \right| \right), \quad (21)$$

where \hbar is the reduced Planck constant ($= 1.054571800(13) \times 10^{-34}$ J s⁻¹) and $\omega_M(\lambda)$ is the maximum phonon angular frequency for a periodic chain with an elastic constant λ ($\omega_M(\lambda) = 2\sqrt{\lambda/m_a}$). The effective elastic constant K can be obtained by applying the variational method [86]:

$$K = \frac{2\mu + \lambda + \nu}{4} + 4h_0 \cdot m + 2J_0 \cdot s, \quad (22)$$

where $h_0 = \frac{\nu - \lambda}{8}$, $J_0 = \frac{\lambda - 2\mu + \nu}{8}$ and $m = \langle \hat{\sigma}_i \rangle$, $s = \langle \hat{\sigma}_i \hat{\sigma}_{i+1} \rangle$ are the two-order parameters known as the fictitious magnetization and correlation parameter, respectively. From the transfer matrix method [85], the following system of two nonlinear equations is obtained for the two unknown m and s :

$$\begin{cases} m = \frac{\exp(J/k_B T) \sinh(h_g/k_B T)}{\sqrt{\exp(2J/k_B T) \sinh^2(h_g/k_B T) + \exp(-2J/k_B T)}} \\ s = 1 - \frac{2m^2 \exp(-4J/k_B T)}{\sinh(h_g/k_B T) (m \cosh(h_g/k_B T) + \sinh(h_g/k_B T))} \end{cases}, \quad (23)$$

where the implicit dependencies of the right-hand side terms on m and s are presented in h_g and J that depend on K (see also Eqs. (21) and (22)) as follows:

$$\begin{cases} h_g = -\frac{\Delta}{2} - \frac{2h_0}{K} \frac{\langle H_{phon}(K) \rangle_T}{N} + k_B T \frac{\ln g}{2} \\ J = -\frac{J_0}{K} \frac{\langle H_{phon}(K) \rangle_T}{N} \end{cases}, \quad (24)$$

where g is the degeneracy factor equal to the ratio between the degeneracy of the HS energy level and the degeneracy of the LS energy level. In conclusion, once the SCO parameters are given, namely, Δ , g , N , h_0 , J_0 , λ , m_a , the formula (23) contains two self-consistent equations for m and s that can be solved for each value of the temperature T .

Since the HS fraction n_{HS} is simply related to the fictitious magnetization m by the formula $n_{HS} = (1+m)/2$, the dependence of n_{HS} on temperature is thus obtained. For the sake of simplicity in the following calculations, we use several normalizations, namely:

- the reduced temperature $t_r = \frac{k_B T}{\hbar \omega_M(\lambda)}$;
- the dimensionless electronic excitation energy $\delta = \frac{\Delta}{\hbar \omega_M(\lambda)}$;
- the elastic constant ratio $x = \frac{\nu}{\lambda}$; and
- the dimensionless parameter y defined by $\mu = \frac{\lambda + \nu}{2} + \frac{\lambda - \nu}{2} y$.

The dimensionless parameter x is a measure of the interaction intensity in the system, a small value of x implying strong interactions in the system. The dimensionless parameter y shows how close is μ to λ as compared to ν , a positive value of y implying that μ is closer to λ while a negative value of y implying that μ is closer to ν . It is apparent that for $y = 0$, μ is the mean value of λ and ν . By using this normalization and the property of the above algebraic system that uses only ratios of elastic constants to λ , the 8-parameter problem is now reduced to 6-parameter problem: 4 normalized parameters presented above along with the number of atoms N and degeneracy ratio g . An example of hysteretic transition for a SCO chain driven by temperature, computed in the APC model, is plotted in **Figure 8**.

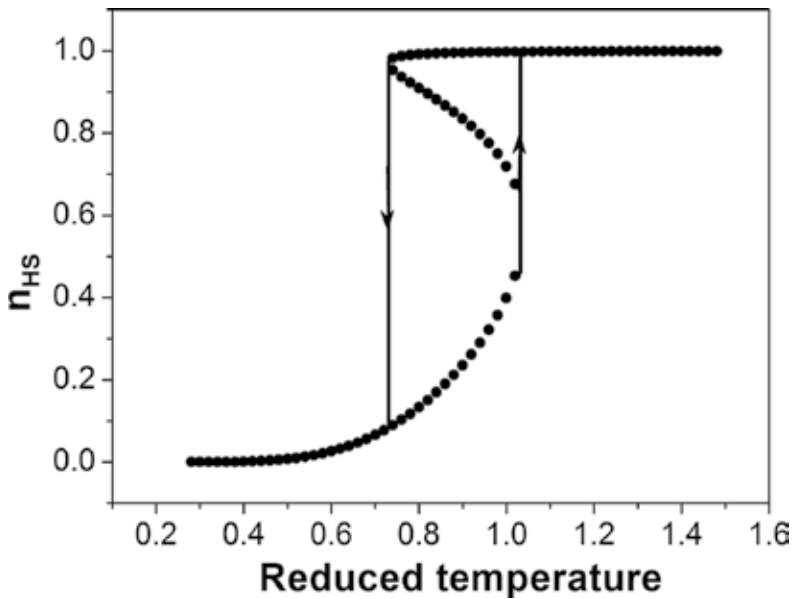


Figure 8. Thermal hysteresis loop for a SCO chain computed in the APC model. The reduced parameters used in these calculations are $x = 0.2$, $y = 0$, $\delta = 0.606$, while $\ln g = 5$, $N = 2000$.

The size effect plays a very important role in applications such as information storage technology. The problem is to estimate the minimum size for which the system still maintains its hysteretic properties. An important advantage of the APC model is that the system size appears naturally in the Hamiltonian, allowing a direct analysis of the size effect, i.e., the dependence

of the hysteresis loop width on the number of atoms N . Since the intermolecular interactions also play a crucial role in the width of hysteresis loop, we present in **Figure 9**, the variation of hysteresis loop width with the system size for two values of the elastic constant ratio x . As expected, the hysteretic loop is wider when stronger interactions are present in the system (i.e., x is smaller), but it is interesting to observe that critical system size for hysteretic behavior is also decreasing with the increase in the interaction strength. A saturation phenomenon in hysteretic loop width is also observed with the increase in system size. A more detailed analysis of this important topic can be found in Refs. [36, 80].

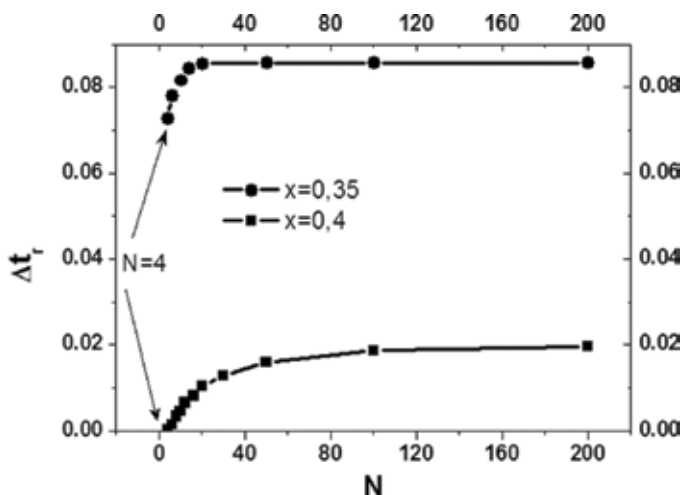


Figure 9. Size dependence of the SCO hysteresis width computed in the APC model for two different values of the elastic constant ratio x . The other reduced parameters used in these calculations are $\gamma = 0$, $\delta = 0.606$, while $\ln g = 5$.

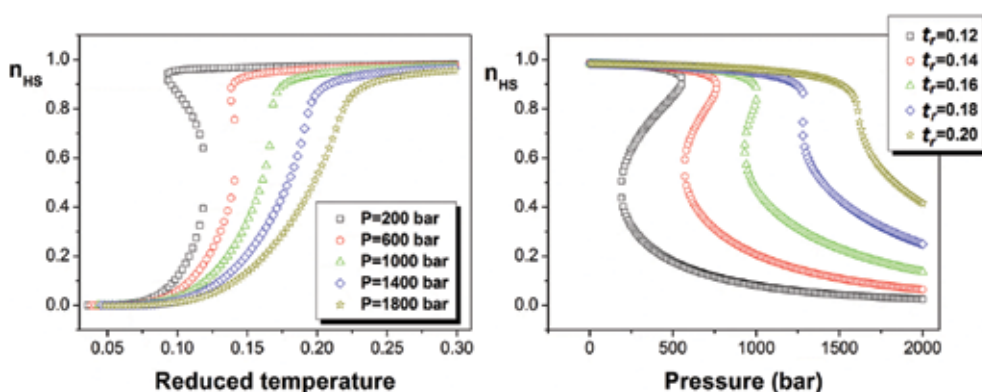


Figure 10. (Left) Thermally driven transitions computed for selected values of pressure indicated in the figure. (Right) Pressure-driven transitions computed for selected values of the reduced temperature indicated in the figure. The parameters used in these calculations are $x = 0.4$, $\gamma = 0.8$, $\delta_0 = 0.525$, $\alpha = 10^{-4} \text{bar}^{-1}$, $\ln g = 5$, and $N = 2000$.

Next, we will focus on the *pressure effect* on the spin transition driven by temperature as well as on the *temperature effect* on the spin transition driven by external pressure. Based on several results obtained by Raman spectroscopy, the vibrational properties of SCO systems seem to remain stable when external pressure is applied [84]. Thus, we can assume that the ratio of the elastic constants does not depend on pressure and the pressure effect will be accounted only in the energy gap: $\Delta_p = \Delta_0 + p\delta V$, as it was also considered in the Ising-like model. By substituting the new expression for the energy gap in Eq. (28), the solution for the fictitious magnetization will be dependent on the external pressure. The dimensionless electronic excitation energy will be now defined as $\delta_0 = \Delta_0/\hbar\omega_M(\lambda)$ and a normalized volume variation is introduced as $\alpha = \delta V \cdot 10^{-5}/\hbar\omega_M(\lambda)$ (where the factor 10^{-5} stands for the conversion of the pressure units from *pascal* to *bar*). Sample results for spin transitions driven by temperature and pressure variations are presented in **Figure 10**, for $x = 0.4$, $y = 0.8$, $\delta_0 = 0.525$, $\alpha = 10^{-4}\text{bar}^{-1}$, $\ln g = 5$, and $N = 2000$.

It should be noted that the pressure hysteresis loops computed in the APC model present an elongation at high pressure, in good agreements with the experimental observations [87]. However, in some coordination compounds, the electronic transitions do not always arise from a simple configuration. The external pressure can also induce a crystallographic phase transition, giving rise to an unusual behavior, such as the increase of the hysteretic loop width with the increase in the applied pressure [16].

2.4.1. Relaxation process of the photo-excited HS metastable states at low temperature

The bistable nature of spin crossover materials coupled to their sensitivity to light irradiation is of particular interest for the development of data-recording media. At low temperatures (typically below 40 K), the system can be switched from the ground low-spin state to the metastable high-spin state using appropriate wavelengths known as light-induced excited spin state trapping effect [6]. The relaxation from high-spin state to low-spin state (HS \rightarrow LS) appears if, after photoexcitation, the light is switched off.

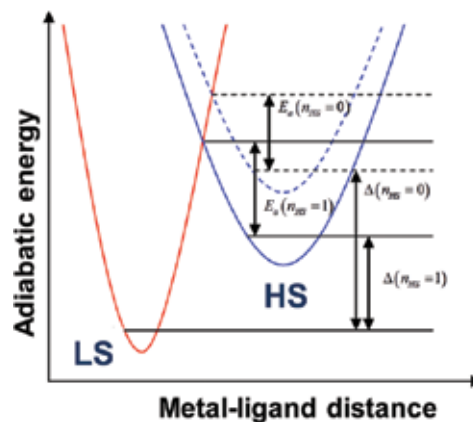


Figure 11. Configuration diagram of a spin crossover molecule showing the energy barrier variation.

At low temperature (<30 K), the relaxation process occurs by tunneling, while at higher temperature (>40 K), this process is thermally activated and consequently it is very fast at room temperature, where the life time is in the order of 10^{-8} to 10^{-6} s [88]. The relaxation process from high-spin state to low-spin state was studied in detail by Andreas Hauser and the Mainz group [88–90]. This analysis was based on the energy barrier properties of the state (HS) and led to the understanding of the main properties of the SCO cooperative relaxation. As illustrated in **Figure 11**, the energy gap Δ is increasing and the activation energy E_a is decreasing with the decrease of the molar high-spin fraction n_{HS} . Consequently, the relaxation (HS \rightarrow LS) becomes faster with the decrease of n_{HS} leading to a self-accelerating process.

The expression of the relaxation rate, K_{HL} , was introduced by Hauser, on experimental and theoretical bases, by considering a linear dependence of the barrier energy with n_{HS} . In APC model, a more realistic formula for the energy barrier was derived and used to describe the relaxation process. Thus, the activation energy can be expressed as follows:

$$E_a = E_0 - E_{HS} = E_0 - \frac{\Delta}{2} - \frac{2\hbar_0}{K} \frac{\langle H_{phon}(K) \rangle_T}{N}, \quad (25)$$

where E_0 is the level of the energetic barrier. In the thermal activation regime, the relaxation rate is given by the standard relation:

$$K_{HL}(T, n_{HS}) = k_\infty \exp\left(-\frac{E_a}{k_B T}\right), \quad (26)$$

where k_∞ is the high-temperature relaxation rate (associated to vibrational frequencies). The variation in time of the high-spin fraction is given by the master equation

$$\frac{dn_{HS}}{dt} = -n_{HS} K_{HL}(T, n_{HS}), \quad (27)$$

where $K_{HL}(T, n)$ is given by Eq. (26) in which E_a is given by Eq. (25).

Sample results for the SCO relaxation curves calculated by using the above formulas derived in the APC model are presented in **Figure 12**, for several values of the interaction parameter χ , and in **Figure 13**, for several values of the temperature at which relaxation process occurs. The values for the reduced parameters of the system (introduced above) used in these calculations are given in the figures' captions. In addition, a new normalized parameter is introduced and denoted by A , which is defined by $A = E_0/\hbar\omega_M(\lambda)$.

As can be seen from **Figure 12**, the relaxation process is getting slower when the interaction between the molecules is getting stronger (i.e., smaller values of χ). It is important to observe the sigmoidal shape of the relaxation curve which is in good agreement with the experimental data. Moreover, APC model also resolves one of the weaknesses of Hauser model, which was

not able to reproduce the so-called “tail-effect,” i.e., the slow-relaxation effect observed for small values of molar high-spin fraction. Since these results were derived in the framework of classical Arrhenius-type activation, the relaxation process of the photo-excited metastable states can also be analyzed by using the Arrhenius representation $\ln(K_{HL}) = f(n_{HS})$, as shown in **Figure 14**. Here, the shape of the resulting Arrhenius diagram shows two slopes, in good agreement with the experimental data, unlike the Hauser model, where the Arrhenius diagram is a straight line [91].

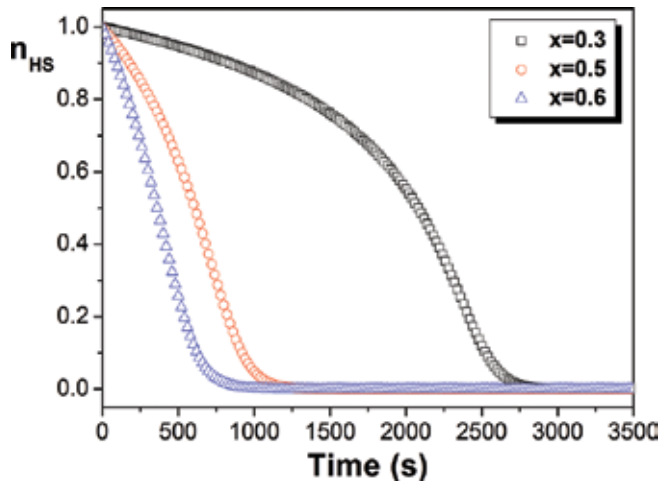


Figure 12. Relaxation curves recorded in dark for selected values of interaction parameter x . The parameters used in the calculations are $y = 0$, $\delta_0 = 0.6$, $t_r = 0.03$, $\ln g = 5$, $N = 2000$, $A = 0.8$, and $k_\infty = 100$.

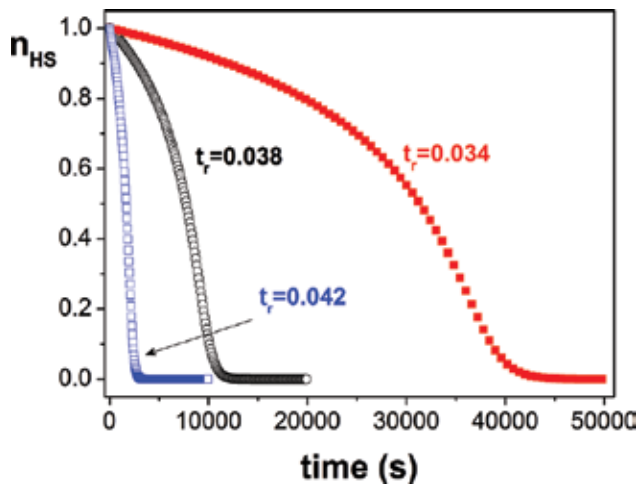


Figure 13. Relaxation curves recorded in dark for selected values of the reduced temperature t_r , at which relaxation process occurs. Parameters used in the calculations are $y = 0$, $\delta_0 = 0.6$, $x = 0.2$, $\ln g = 5$, $N = 2000$, $A = 0.8$, $k_\infty = 100$.

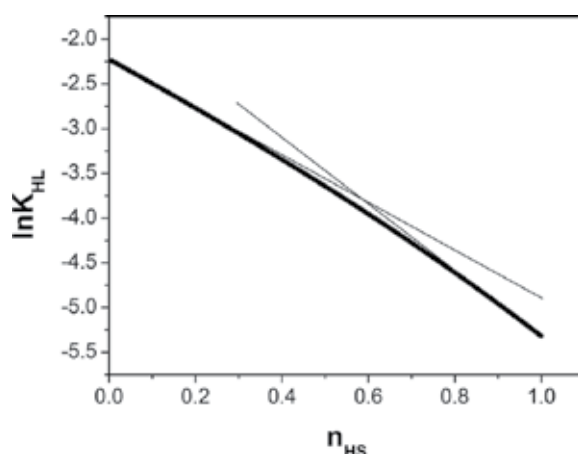


Figure 14. Arrhenius diagram of the relaxation process in SCO compounds in APC model.

Since we focused on thermally activated relaxations, it is apparent that the relaxation process speeds up with the increase of temperature, as shown in **Figure 13**, as well. In practice, the switch from HS state to LS state can be achieved either by direct nonradiative relaxation or by the reverse LIESST effect when the samples is irradiating in the HS state absorption band [8].

2.4.2. Light-induced thermal hysteresis

Experiments under permanent light irradiation illustrate the competition between the *noncooperative* photoexcitation (generating LS → HS transitions) and the cooperative relaxations (HS → LS) that are thermally activated. This competition leads to hysteretic transition known as light-induced thermal hysteresis. Light-induced thermal hysteresis was discovered almost simultaneously by the groups of F. Varret from Versailles [88] and O. Kahn from Bordeaux [92], respectively.

The LITH explanation given by Varret's group goes as follows: at low temperatures, the metastable HS states are populated by LIESST effect; by increasing the temperature, while maintaining the light irradiation, thermally activated relaxations (HS → LS transitions) get stronger leading the system into a metastable state where thermal relaxations balance the LIESST effect. Quantitatively, this situation can be expressed by introducing in relaxation Eq. (27) an additional term accounting for the effect of continuous light irradiation:

$$\frac{dn_{HS}}{dt} = -n_{HS}(t)K_{HL}(t, n_{HS}(t)) + I_0\sigma_a(1 - n_{HS}(t)) \quad (28)$$

where $I_0\sigma_a$ counts as the LS → HS switching probability rate (I_0 is the light beam intensity and σ_a is the light absorption cross section). Depending on the temperature change rate, two cases can be identified

- *Static LITH*: when the temperature change rate is small as compared to the rate of the other processes involved, so it can be neglected. The metastable states can be identified as fixed points of Eq. (28), which is equivalent to solving, for each value of temperature (t_r), the algebraic equation:

$$K_{HL}(t_r, n_{HS}) = I_0 \sigma_a \left(\frac{1}{n_{HS}} - 1 \right) \quad (29)$$

Sample results for the metastable states calculations are plotted versus (reduced) temperature in **Figure 15**, for two values of the interaction parameter x . The static LITH phenomenon is apparent in these two examples. As expected, the intermolecular interaction has an important role in LITH, due to the cooperative nature of the relaxation process.

- *Dynamic LITH*: where the temperature change interferes with the other processes and, consequently, the temperature change rate cannot be neglected. Typical hysteretic loops obtained by using Eq. (28) and APC model for K_{HL} are plotted in **Figure 16**, for several values of temperature change rate v_r . The APC model can successfully reproduce the main features of the experimental data reported in LITH properties [93]. By increasing the cooperativity of a SCO system, the LITH width increases accordingly. A similar effect can be obtained “artificially” by increasing the temperature change rate; thus, by increasing the temperature change rate, the system does not have enough time to react at the light effect, so the hysteresis loop is widened.

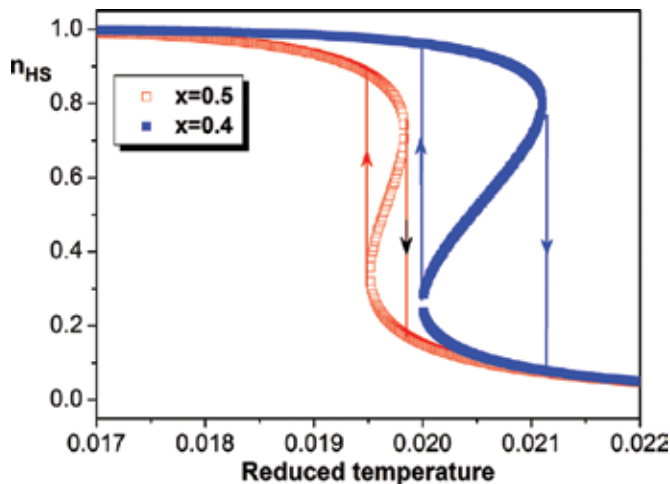


Figure 15. Static LITH for two values of the interaction parameter x . Parameters used in these calculations are $y = 0$, $\delta_0 = 0.6$, $x = 0.1$, $\ln g = 5$, $N = 2000$, $A = 0.8$, $k_\infty = 100$, $I_0 \sigma_a = 5 \times 10^{-4} \text{ s}^{-1}$.

Although the APC model is able to reproduce a wide range of phenomena, experimentally observed in molecular SCO compounds, it also has some limitations that need to be addressed

by further studies. The first physical limitation of the APC model consists the difficulty of measuring the elastic constants and consequently, the impossibility of measuring the reduced parameter y . This constraint leads to the application of the *trial-and-error* method for identifying a proper value of this parameter needed in a quantitative study instead of a physical identification that would make the model more focused on technical applications. Another important limitation of this model concerns the analysis of the spin-like domains spreading in spin crossover single crystals. Indeed, the spin crossover molecules are considered in APC model as fixed atoms that limit the analysis of the local distortions. These distortions are not only affecting the nearest neighbors but also causing long-range interactions between the system molecules. It is important to notice that some limitations were overcome by newly developed models, such as mechanoelastic model designed by Enachescu et al. [60], where the molecular volume change during the spin transition is taken into account.

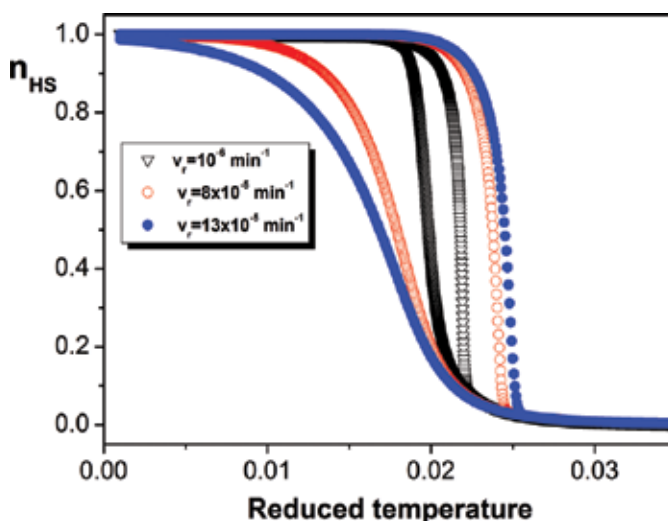


Figure 16. Dynamics LITH for three values of the temperature change rate v_r . Parameters used in the calculations are $x = 0.5$, $y = 0$, $\delta_0 = 0.6$, $\alpha = 0.1$, $\ln g = 5$, $N = 2000$, $A = 0.8$, $k_{\infty} = 100$, $I_0\sigma_a = 5 \times 10^{-4} \text{ s}^{-1}$.

3. Conclusions

This chapter provided a general introduction of physical modeling in molecular materials with a special emphasis placed on spin crossover compounds. It covered multiple types of spin crossover compounds and analyzed intermolecular interactions, size effects, thermal behavior, pressure effects, the photoexcitation processes (such as LIESST), relaxation process, and light-induced thermal hysteresis. Numerous illustrations were provided to help the reader in grasping highly abstract concepts, explaining molecular materials behavior, and designing various applications. In this way, we try to support students and young researchers get acquainted to this research area and to facilitate the communication between the mathematical

and physical communities, chemical experimentalists, and engineering practitioners in this field.

Although the models presented here are able to reproduce a wide range of phenomena, experimentally observed in molecular SCO compounds, they also have some limitations that emphasize the need for further research in this area. However, an attentive analysis of the bibliography is needed before deciding to work on a specific problem, since several generalizations have not been explicitly addressed in this short introduction to this novel and dynamic area of research.

Author details

Mihai Dimian^{1,2} and Aurelian Rotaru^{2*}

*Address all correspondence to: aurelian.rotaru@usm.ro

1 Department of Electrical and Computer Engineering, Howard University, Washington, DC, USA

2 Department of Computers, Electronics and Automation and MANSiD Research Center, Stefan cel Mare University, Suceava, Romania

References

- [1] S. Sanvito, *Molecular spintronics*, Chemical Society Reviews, 40 (2011) 3336–3355.
- [2] S. Sanvito, *Molecular spintronics: The rise of spinterface science*, Nature Physics, 6 (2010) 562–564.
- [3] A. Bousseksou, G. Molnar, L. Salmon, W. Nicolazzi, *Molecular spin crossover phenomenon: recent achievements and prospects*, Chemical Society Reviews, 40 (2011) 3313–3335.
- [4] O. Kahn, C.J. Martinez, *Spin-transition polymers: From molecular materials toward memory devices*, Science, 279 (1998) 44–48.
- [5] P. Gutlich, *Spin crossover in Iron (II)-complexes*, Structure and Bonding, 44 (1981) 83–195.
- [6] S. Decurtins, P. Gutlich, C.P. Kohler, H. Spiering, A. Hauser, *Light induced excited spin state trapping in a transition-metal complex – the hexa-1-propyltetrazole-Iron (II) tetrafluoroborate spin crossover system*, Chemical Physics Letters, 105 (1984) 1–4.
- [7] S. Decurtins, P. Gutlich, K.M. Hasselbach, A. Hauser, H. Spiering, *Light induced excited spin state trapping in Iron (II) spin crossover systems – optical spectroscopic and magnetic susceptibility study*, Inorganic Chemistry, 24 (1985) 2174–2178.

- [8] A. Hauser, *Reversibility of light-induced excited spin state trapping in the $\text{Fe}(\text{ptz})_6(\text{BF}_4)_2$ and the $\text{Zn}_{1-x}\text{Fe}_x(\text{ptz})_6(\text{BF}_4)_2$ spin-crossover systems*, *Chemical Physics Letters*, 124 (1986) 543–548.
- [9] C.P. Slichter, H.G. Drickamer, *Pressure-Induced Electronic Changes in Compounds of Iron*, *Journal of Chemical Physics*, 56 (1972) 2142–2160.
- [10] E. König, G. Ritter, J. Waigel, H.A. Goodwin, *The effect of pressure on the thermal hysteresis of 1st-order spin transition in bis(1,10-phenanthroline-2-carbaldehyde phenylhydrazone) iron (II) complexes*, *Journal of Chemical Physics*, 83 (1985) 3055–3061.
- [11] A. Bousseksou, N. Negre, M. Goiran, L. Salmon, J.P. Tuchagues, M.L. Boillot, K. Boukheddaden, F. Varret, *Dynamic triggering of a spin-transition by a pulsed magnetic field*, *European Physical Journal B*, 13 (2000) 451–456.
- [12] N. Negre, M. Goiran, A. Bousseksou, J. Haasnoot, K. Boukheddaden, Askenazy, F. Varret, *High magnetic field induced spin transition, HMFIST effect, in $[\text{Fe}_{0.52}\text{Ni}_{0.48}(\text{btr})_2(\text{NCS})_2]\text{H}_2\text{O}$* , *Synthetic Metals*, 115 (2000) 289–292.
- [13] C. Bartual-Murgui, A. Cerf, C. Thibault, C. Vieu, L. Salmon, G. Molnar, A. Bousseksou, *SERS-active substrates for investigating ultrathin spin-crossover films*, *Microelectronic Engineering*, 111 (2013) 365–368.
- [14] C. Bartual-Murgui, A. Akou, L. Salmon, G. Molnar, C. Thibault, J. Real, A. Bousseksou, *Guest effect on nanopatterned spin-crossover thin films*, *Small*, 7 (2011) 3385–3391.
- [15] X. Bao, H.J. Shepherd, L. Salmon, G. Molnar, M.L. Tong, A. Bousseksou, *The effect of an active guest on the spin crossover phenomenon*, *Angewandte Chemie-International Edition*, 52 (2013) 1198–1202.
- [16] A. Rotaru, F. Varret, E. Coddjovi, K. Boukheddaden, J. Linares, A. Stancu, P. Guionneau, J.F. Letard, *Hydrostatic pressure investigation of the spin crossover compound $[\text{Fe}(\text{PM-BiA})(2)(\text{NCS})(2)]$ polymorph I using reflectance detection*, *Journal of Applied Physics*, 106 (2009) 053515.
- [17] P. Gutlich, *Thermal and optical switching of bistable iron compounds and possible applications*, *Nuclear Instruments & Methods in Physics Research Section B-Beam Interactions with Materials and Atoms*, 76 (1993) 387–396.
- [18] J. Linares, E. Coddjovi, Y. Garcia, *Pressure and temperature spin crossover sensors with optical detection*, *Sensors*, 12 (2012) 4479–4492.
- [19] J. Dai, S. Kanegawa, Z. Li, S. Kang, O. Sato, *A switchable complex ligand exhibiting photoinduced valence tautomerism*, *European Journal of Inorganic Chemistry*, 2013 (2013) 4150–4153.
- [20] A. Vallee, C. Train, C. Roux, *Synthesis and properties of a thermochromic spin crossover Fe-II complex: an undergraduate coordination chemistry laboratory experiment*, *Journal of Chemical Education*, 90 (2013) 1071–1076.

- [21] A. Lapresta-Fernandez, S. Titos-Padilla, J.M. Herrera, A. Salinas-Castillo, E. Colacio, L.F.C. Vallvey, *Photographing the synergy between magnetic and colour properties in spin crossover material Fe(NH(2)trz)(3) (BF4)(2): a temperature sensor perspective*, Chemical Communications, 49 (2013) 288–290.
- [22] V. Meded, A. Bagrets, K. Fink, R. Chandrasekar, M. Ruben, F. Evers, A. Bernand-Mantel, J.S. Seldenthuis, A. Beukman, H.S.J. van der Zant, *Electrical control over the Fe(II) spin crossover in a single molecule: Theory and experiment*, Physical Review B, 83 (2011) 245415.
- [23] F.-L. Yang, M.-G. Chen, X.-L. Li, J. Tao, R.-B. Huang, L.-S. Zheng, *Two-dimensional iron(II) networks – guest-dependent structures and spin-crossover behaviors*, European Journal of Inorganic Chemistry, 2013 (2013) 4234–4242.
- [24] A. Rotaru, I.A. Gural'skiy, G. Molnar, L. Salmon, P. Demont, A. Bousseksou, *Spin state dependence of electrical conductivity of spin crossover materials*, Chemical Communications, 48 (2012) 4163–4165.
- [25] A. Rotaru, J. Dugay, R.P. Tan, I.A. Gural'skiy, L. Salmon, P. Demont, J. Carrey, G. Molnar, M. Respaud, A. Bousseksou, *Nano-electromanipulation of spin crossover nanorods: Towards switchable nanoelectronic devices*, Advanced Materials, 25 (2013) 1745–1749.
- [26] F. Setifi, C. Charles, S. Houille, F. Thetiot, S. Triki, C.J. Gomez-Garcia, S. Pillet, *Spin crossover (SCO) iron(II) coordination polymer chain: Synthesis, structural and magnetic characterizations of Fe(abpt)(2)(mu-M(CN)(4)) (M = Pt-II and Ni-II)*, Polyhedron, 61 (2013) 242–247.
- [27] Y. Qu, *Quantum-chemical investigation of the spin crossover complex Fe(mbpzbp)(NCS)(2)*, Spectrochimica Acta Part A-Molecular and Biomolecular Spectroscopy, 113 (2013) 427–431.
- [28] Y. Li, C.-G. Zhang, L.-Y. Cai, Z.-X. Wang, *Synthesis, crystal structure, Hirshfeld surfaces, and spectral properties of Cu(II) and Co(II) complexes with 3-phenoxymethyl-4-phenyl-5-(2-pyridyl)-1,2,4-triazole*, Journal of Coordination Chemistry, 66 (2013) 3100–3112.
- [29] V. Vrdoljak, B. Prugovecki, D. Matkovic-Calogovic, T. Hrenar, R. Dreos, P. Siega, *Three polymorphic forms of a monomeric Mo(VI) complex: Building blocks for two metal-organic supramolecular isomers. Intermolecular interactions and ligand substituent effects*, Crystal Growth & Design, 13 (2013) 3773–3784.
- [30] S. Sanvito, *Strategy for detection of electrostatic spin-crossover effect in magnetic molecules*, Physical Review B, 88 (2013) art. no. 054409.
- [31] A. Bousseksou, J. Nasser, J. Linares, K. Boukheddaden, F. Varret, *Ising-like model for the 2-step spin-crossover*, Journal of Physics I, 2 (1992) 1381–1403.
- [32] M. Sorai, S. Seki, *Phonon coupled cooperative low-Spin 1A1-high spin 5 T2 transition in [Fe(phen)2(NCS)2] and [Fe(phen)2(NCSe)2] crystals*, Journal of Physical Chemistry Solids, 35 (1974) 555–570.

- [33] J.A. Nasser, *First order high-spin/low-spin phase transition induced by acoustic-phonons*, European Physical Journal B, 21 (2001) 3–10.
- [34] J.A. Nasser, K. Boukheddaden, J. Linares, *Two-step spin conversion and other effects in the atom-phonon coupling model*, European Physical Journal B, 39 (2004) 219–227.
- [35] A. Rotaru, J. Linares, *Relaxation and light induced thermal hysteresis (LITH) behaviours in the atom-phonon coupling model for spin crossover compounds*, Journal of Optoelectronics and Advanced Materials, 9 (2007) 2724–2730.
- [36] A. Rotaru, J. Linares, E. Codjovi, J. Nasser, A. Stancu, *Size and pressure effects in the atom-phonon coupling model for spin crossover compounds*, Journal of Applied Physics, 103 (2008) 07B908.
- [37] A. Rotaru, J. Linares, S. Mordelet, A. Stancu, J. Nasser, *Re-entrance phase and excited metastable electronic spin states in one-dimensional spin crossover compounds explained by atom-phonon coupling model*, Journal of Applied Physics, 106 (2009) 043507.
- [38] A. Rotaru, A. Carmona, F. Combaud, J. Linares, A. Stancu, J. Nasser, *Monte Carlo simulations for 1-and 2D spin crossover compounds using the atom-phonon coupling model*, Polyhedron, 28 (2009) 1684–1687.
- [39] A. Gindulescu, A. Rotaru, J. Linares, M. Dimian, J. Nasser, *Excited metastables electronic spin states in spin crossover compounds studies by atom-phonon coupling model: Gradual and two-step transition cases*, Journal of Applied Physics, 107 (2010) 09A959.
- [40] M.P. Espejo, A. Gindulescu, J. Linares, J. Nasser, M. Dimian, *Phase diagram of two-dimensional spin crossover systems using the atom-phonon coupling model*, Journal of Applied Physics, 109 (2011) art. no. 07B102.
- [41] A. Gindulescu, A. Rotaru, J. Linares, M. Dimian, J. Nasser, *Metastable states at low temperature in spin crossover compounds in the framework of the atom-phonon coupling model*, Polyhedron, 30 (2011) 3186–3188.
- [42] J. Wajnflasz, *Study of “Low Spin” – “High Spin” transition in octahedral transition ion complexes*, Physica Status Solidi (b), 40 (1970) 537–545.
- [43] J. Wajnflasz, R. Pick, *“Low Spin” – “High Spin” transitions in Fe²⁺ complexes*, Le Journal de Physique Colloques, 32 (1971) C1–91.
- [44] R.A. Bari, J. Sivardiere, *Low-spin-high-spin transitions in transition-metal-ion-compounds*, Physical Review B, 5 (1972) 4466–4471.
- [45] R. Zimmermann, E. König, *Model for high-spin low-spin transitions in solids including effect of lattice vibrations*, Journal of Physics and Chemistry of Solids, 38 (1977) 779–788.
- [46] T. Kambara, *Theory of high-spin reversible low-spin transitions in transition-metal compounds induced by the Jahn-Teller effect*, Journal of Chemical Physics, 70 (1979) 4199–4206.

- [47] T. Kambara, *The effect of iron concentration on the high-spin reversible low-spin transitions in iron compounds*, Journal of the Physical Society of Japan, 49 (1980) 1806–1811.
- [48] T. Kambara, *Theory of high-spin reversible low-spin transitions in transition-metal compounds induced by cooperative molecular distortions and lattice strains*, Journal of Chemical Physics, 74 (1981) 4557–4565.
- [49] J. Linares, J. Nasser, K. Boukheddaden, A. Bousseksou, F. Varret, *Monte-Carlo simulations of spin-crossover transitions using the 2-level model. 1: mononuclear single sublattice case*, Journal of Magnetism Magnetic Materials, 140 (1995) 1507–1508.
- [50] A.L. Tchougreeff, A.V. Soudackov, I.A. Misurkin, H. Bolvin, O. Kahn, *High-spin low-spin transitions in Fe(II) complexes by effective Hamiltonian method*, Chemical Physics, 193 (1995) 19–26.
- [51] H. Bolvin, O. Kahn, *Ising-model for low-spin high-spin transitions in molecular compounds – within and beyond the mean-field approximation*, Chemical Physics, 192 (1995) 295–305.
- [52] J. Linares, H. Spiering, F. Varret, *Analytical solution of 1D Ising-like systems modified by weak long range interaction – Application to spin crossover compounds*, European Physical Journal B, 10 (1999) 271–275.
- [53] K. Boukheddaden, J. Linares, H. Spiering, F. Varret, *One-dimensional Ising-like systems: An analytical investigation of the static and dynamic properties, applied to spin-crossover relaxation*, European Physical Journal B, 15 (2000) 317–326.
- [54] K. Boukheddaden, I. Shteto, B. Hoo, F. Varret, *Dynamical model for spin-crossover solids. I. Relaxation effects in the mean-field approach*, Physical Review B, 62 (2000) 14796–14805.
- [55] K. Boukheddaden, *Anharmonic model for phonon-induced first-order transition in 1-D spin-crossover solids*, Progress of Theoretical Physics, 112 (2004) 205–217.
- [56] K. Boukheddaden, M. Nishino, S. Miyashita, F. Varret, *Unified theoretical description of the thermodynamical properties of spin crossover with magnetic interactions*, Physical Review B, 72 (2005) 014467.
- [57] K. Boukheddaden, S. Miyashita, M. Nishino, *Elastic interaction among transition metals in one-dimensional spin-crossover solids*, Physical Review B, 75 (2007) 094112.
- [58] M. Nishino, K. Boukheddaden, Y. Konishi, S. Miyashita, *Simple two-dimensional model for the elastic origin of cooperativity among spin states of spin-crossover complexes*, Physical Review Letters, 98 (2007) art. no. 247203.
- [59] A. Dobrinescu, C. Enachescu, A. Stancu, *Ising-like model study of size dependence relaxation in spin crossover complexes*, Journal of Magnetism and Magnetic Materials, 321 (2009) 4132–4138.
- [60] C. Enachescu, L. Stoleriu, A. Stancu, A. Hauser, *Model for elastic relaxation phenomena in finite 2D hexagonal molecular lattices*, Physical Review Letters, 102 (2009) 257204.

- [61] T.D. Oke, F. Hontinfinde, K. Boukheddaden, *Bethe lattice approach and relaxation dynamics study of spin-crossover materials*, Applied Physics A-Materials Science & Processing, 120 (2015) 309–320.
- [62] W. Nicolazzi, S. Pillet, C. Lecomte, *Two-variable anharmonic model for spin-crossover solids: A like-spin domains interpretation*, Physical Review B, 78 (2008) 174401.
- [63] G. Felix, W. Nicolazzi, M. Mikolasek, G. Molnar, A. Bousseksou, *Non-extensivity of thermodynamics at the nanoscale in molecular spin crossover materials: A balance between surface and volume*, Physical Chemistry Chemical Physics, 16 (2014) 7358–7367.
- [64] I. Gudyma, V. Ivashko, J. Linares, *Diffusionless phase transition with two order parameters in spin-crossover solids*, Journal of Applied Physics, 116 (2014) art. no. 173509.
- [65] S. Ohnishi, S. Sugano, *Strain interaction effects on the high-spin low-spin transition of transition-metal compounds*, Journal of Physics C-Solid State Physics, 14 (1981) 39–55.
- [66] H. Spiering, E. Meissner, H. Koppen, E.W. Muller, P. Gutlich, *The effect of the lattice expansion on high-spin reversible low-spin transitions*, Chemical Physics, 68 (1982) 65–71.
- [67] N. Willenbacher, H. Spiering, *The elastic interaction of high-spin and low-spin complex-molecules in spin-crossover compounds*, Journal of Physics C-Solid State Physics, 21 (1988) 1423–1439.
- [68] H. Spiering, N. Willenbacher, *The elastic interaction of high-spin and low-spin complex-molecules in spin-crossover compounds. 2*, Journal of Physics-Condensed Matter, 1 (1989) 10089–10105.
- [69] R. Zimmermann, *A model for high-spin low-spin transitions with an interpretation of thermal hysteresis effects*, Journal of Physics and Chemistry of Solids, 44 (1983) 151–158.
- [70] P. Gutlich, H. Koppen, R. Link, H.G. Steinhauser, *Interpretation of high-spin reversible low-spin transition in iron(II) complexes. 1. Phenomenological thermodynamic model*, Journal of Chemical Physics, 70 (1979) 3977–3983.
- [71] A. Bousseksou, H. Constantmachado, F. Varret, *A simple Ising-like model for spin-conversion including molecular vibrations*, Journal De Physique I, 5 (1995) 747–760.
- [72] A. Gîndulescu, A. Rotaru, J. Linares, M. Dimian, J. Nasser, *Analysis of phase transitions in spin-crossover compounds by using atom – phonon coupling model*, Journal of Physics: Conference Series, 268 (2011) 012007.
- [73] A. Rotaru, A. Graur, G.-M. Rotaru, J. Linares, Y. Garcia, *Influence of intermolecular interactions and size effect on LITH-FORC diagram in 1D spin crossover compounds*, Journal of Optoelectronics and Advanced Materials, 14 (2012) 529–536.
- [74] F. Varret, S.A. Salunke, K. Boukheddaden, A. Bousseksou, E. Codjovi, C. Enachescu, J. Linares, *The Ising-like model applied to switchable inorganic solids: discussion of the static properties*, Comptes Rendus Chimie, 6 (2003) 385–393.

- [75] K. Boukheddaden, J. Linares, E. Codjovi, F. Varret, V. Niel, J.A. Real, *Dynamical Ising-like model for the two-step spin-crossover systems*, Journal of Applied Physics, 93 (2003) 7103–7105.
- [76] D. Chiruta, J. Linares, P.R. Dahoo, M. Dimian, *Analysis of long-range interaction effects on phase transitions in two-step spin-crossover chains by using Ising-type systems and Monte Carlo entropic sampling technique*, Journal of Applied Physics, 112 (2012) 074906.
- [77] D. Chiruta, J. Linares, Y. Garcia, M. Dimian, P.R. Dahoo, *Analysis of multi-step transitions in spin crossover nanochains*, Physica B: Condensed Matter 434 (2014) 134–138.
- [78] D. Chiruta, J. Linares, Y. Garcia, P.R. Dahoo, M. Dimian, *Analysis of the hysteretic behaviour of 3D spin crossover compounds by using an Ising-like model*, European Journal of Inorganic Chemistry, 21 (2013) 3601–3608.
- [79] D. Chiruta, J. Linares, M. Dimian, Y. Alayli, Y. Garcia, *Role of edge atoms in the hysteretic behaviour of 3D spin crossover nanoparticles revealed by an Ising-like model*, European Journal of Inorganic Chemistry, 29 (2013) 5086–5093.
- [80] A. Rotaru, *Theoretical and experimental study of the effect of pressure and size on bistable compounds: thermal behavior and relaxation study*, PhD Thesis, GEMaC, Universite de Versailles et Saint Quentin en Yvelines, 2009.
- [81] Z. Yu, C. Li, X.Z. You, H. Spiering, P. Gutlich, Y.F. Hsia, *Debye-Waller factor in the spin crossover complex $Fe(ppi)_2(NCS)_2$* , Materials Chemistry and Physics, 48 (1997) 150–155.
- [82] M.M. Dirtu, Y. Garcia, M. Nica, A. Rotaru, J. Linares, F. Varret, *Iron(II) spin transition 1,2,4-triazole chain compounds with novel inorganic fluorinated counteranions*, Polyhedron, 26 (2007) 2259–2263.
- [83] J. Jung, H. Spiering, Z. Yu, P. Gutlich, *The Debye-Waller factor in spin crossover molecular crystals – a Mossbauer study on $[Fe_xZn_{1-x}(ptz)_6](BF_4)_2$* , Hyperfine Interactions, 95 (1995) 107–128.
- [84] J. Jung, G. Schmitt, L. Wiehl, A. Hauser, K. Knorr, H. Spiering, P. Gutlich, *The cooperative spin transition in $[Fe_xZn_{1-x}(ptz)_6](BF_4)_2$. 2. Structural properties and calculation of the elastic interaction*, Zeitschrift Fur Physik B-Condensed Matter, 100 (1996) 523–534.
- [85] J.M. Yeomans, *Statistical Mechanics of Phase Transitions*, Oxford University Press: Oxford, 1992.
- [86] R. Balian, *From Microphysics to Macrophysics. Methods and Applications of Statistical Physics*, Springer: Berlin, 1991.
- [87] C.-M. Jureschi, I. Rusu, E. Codjovi, J. Linares, Y. Garcia, A. Rotaru, *Thermo- and piezochromic properties of $[Fe(hyptrz)]A_2 \cdot H_2O$ spin crossover 1D coordination polymer: Towards spin crossover based temperature and pressure sensors*, Physica B: Condensed Matter, 449 (2014) 47–51.

- [88] A. Hauser, P. Gutlich, H. Spiering, *High-spin low-spin relaxations kinetics and cooperative effects in the hexakis(1-propyltetrazole)iron bis(tetrafluoroborate) and $[Zn_{1-x}Fe_x(ptz)_6](BF_4)_2$ ($ptz = 1$ -propyltetrazole) spin crossover systems*, *Inorganic Chemistry*, 25 (1986) 4245–4248.
- [89] A. Hauser, *Intersystem crossing in Fe(II) coordination-compounds*, *Coordination Chemistry Reviews*, 111 (1991) 275–290.
- [90] A. Hauser, *Cooperative effects on the HS–LS relaxation in the $[Fe(ptz)_6](BF_4)_2$ spin-crossover system*, *Chemical Physics Letters*, 192 (1992) 65–70.
- [91] C. Enachescu, *Phd Thesis, Contributions to the study of instability induced by light in photomagnetic inorganic solids, LMOV*, Universite de Versailles et Saint Quentin en Yvelines, 2003.
- [92] J.F. Letard, P. Guionneau, L. Rabardel, J.A.K. Howard, A.E. Goeta, D. Chasseau, O. Kahn, *Structural, magnetic, and photomagnetic studies of a mononuclear iron(II) derivative exhibiting an exceptionally abrupt spin transition. Light-induced thermal hysteresis phenomenon*. *Inorganic Chemistry*, 37 (1998) 4432–4441.
- [93] C. Enachescu, H.C. Machado, N. Menendez, E. Codjovi, J. Linares, F. Varret, A. Stancu, *Static and light induced hysteresis in spin-crossover compounds: experimental data and application of Preisach-type models*, *Physica B-Condensed Matter*, 306 (2001) 155–160.

Proteresis of Core-Shell Nanocrystals: Investigation through Theoretical Simulation and Experimental Analysis

Jhong-Yi Ji and Sheng Yun Wu

Additional information is available at the end of the chapter

<http://dx.doi.org/10.5772/62398>

Abstract

A study of proteresis (inverted hysteresis) in core-shell nanocrystals is presented. A core-shell anisotropic energy (CSAE) model is established to describe the observed proteretic behavior in Ni/NiO core-shell nanocrystals. The magnetic compositions of core-shell nanocrystals can be selected for ferromagnetic, antiferromagnetic, or paramagnetic materials where the exchange intercoupling between them results in both a large effective anisotropic energy and intercoupling energy. Simulation of the magnetization of core-shell nanocrystals reveals the existence of an exchange in the intercoupling energy between the interface of the core and shell moments that, surprisingly, is tuneable in both hysteresis and proteresis. Observations have shown a distinct proteresis, which is related to the spin-flip and exchange intercoupling energy between Ni and NiO. Our approach shows that the processing-dependent technology plays an important role when the grain size decreases to the order of nanometers and when the magnets are reduced from the single domain to core-shell domain. Integrated studies of process-dependent, theoretical modeling and core-shell nanocrystal fabrication technology will lead to more encouraging development in the overunity industry.

Keywords: proteresis, hysteresis, core-shell nanocrystals, exchange inter-coupling, spin flipping

1. Introduction

Traditionally, the change in free energy that occurs at a constant temperature is attributed to the mechanical work by the system and the magnetic work by the applied magnetic field. The

integral of the magnetic work gives the energy of the magnetization, which is always positive, because work must be done in the system in order for the magnetic field to establish the magnetization. Consequently, in an inverted hysteresis, the so-called proteretic system, the area of the inverted hysteresis loop $\oint HdM$ represents the energy dissipation for each cycle. At the nanoscale, the various temperatures and size of the hysteresis $M(H)$ loop influence the loop direction, such as whether it is counterclockwise (hysteresis) or clockwise (inverted hysteresis). Interestingly, the modulation of hysteresis and inverted hysteresis breaks the conception of the magnetic system [1]. Recently, a clockwise $M(H)$ loop has also been observed in $\text{CrO}_2/\text{Cr}_2\text{O}_3$ and Co/CoO core-shell particle systems. Zheng et al. [2] observed a series of inverted hysteresis loops between 261 and 292 K in CrO_2 [ferromagnetic (FM)] core particles coated with a Cr_2O_3 [antiferromagnetic (AFM)] surface layer. Wei et al. [3] observed an inverted hysteresis loop in Co (FM) with a core size of 3–4 nm and a CoO (AFM) shell with a thickness of ~ 3 nm, only giving an example at a temperature $T=70$ K. When the Co core size is smaller than 3 nm and larger than 4 nm, the $M(H)$ loop leads to an ordinary hysteresis loop. They provided a possible explanation that the proteretic behavior and its size effect dependence reflect the magnetic interaction between various anisotropies and exchange intercouplings in the Co and CoO phases [3]. In another work, Ohkoshi et al. [4] reported the observation of an inverted hysteresis loop that can be reasonably explained by competition between the spin-flip transitions and the uniaxial magnetic anisotropy. The competing anisotropy theory has been extended to systems involving competing cubic and uniaxial anisotropies [5] and two competing uniaxial anisotropies [6]. In the present work dealing with Ni/NiO core-shell nanoparticles, we ignore the influence of intracoupling to simplify the complex interactions and only discuss the intercoupling between Ni core and NiO shell. We design a core-shell anisotropic energy (CSAE) model, tuning the competition between the magnetic anisotropy and exchange intercoupling in the system, to describe the observation of hysteretic and proteretic behaviors in Ni/NiO core-shell nanoparticles. Recently, the tuning of the exchange intercoupling in core-shell magnetic nanocrystals has received intense attention because it allows the control of the interfaces in nanoscale building blocks and inverted hysteresis. The magnetic compositions of core-shell nanocrystals can be selected as FM, AFM, or paramagnetic (PM) materials, so that the exchange intercoupling between them results in a large effective anisotropic energy [7] and intercoupling energy. We also integrate some magnetic models including the Langevin function, the CSAE, and the Stoner-Wohlfarth (SW) model, providing a convenient simulation for the description of the hysteresis and proteretic loops.

2. Stoner-Wohlfarth model

The evolution of the magnetic theory model for the description of the hysteresis loop starts with the SW model [8], which was developed by Edmund Clifton Stoner and Erich Peter Wohlfarth in 1948. The basic hypotheses in this SW model include the following: (a) single-domain particles, (b) spherical geometry, (c) magnetic anisotropy along the easy axis (EA), and (d) non- or weak-interaction between small particles. Additionally, the sources of magnetic anisotropy can be divided into three parts: magnetocrystalline anisotropy, shape anisotropy,

and exchange anisotropy [9]. In the first case, magnetocrystalline anisotropy, the preferential direction for magnetization, arises from the atomic structure of the crystal. In shape anisotropy, it originates from the nonuniform spherical particle shapes, which cause the demagnetizing field to be unequal in all directions, creating one or more EAs. Third, in exchange anisotropy, magnetization originates from the interaction between AFM and FM materials. The SW model is considered to relate to uniaxial magnetic anisotropy, which may originate from magnetocrystalline anisotropy and shape anisotropy. As a magnetic field is applied to a single-domain particle, the moment M of a single-domain particle is subjected to two competing forces: one is due to a uniaxial anisotropy characterized by K toward an EA and the other is due to an external magnetic field H_a , as shown in **Figure 1a**. The total energy is the sum of the anisotropic energy E_A and the Zeeman energy $E_Z = -M \cdot H_a$. At absolute zero $T=0$ K, the energy is then expressed as

$$E = E_Z + E_A = -MH_a \cos \theta + K \sin^2(\theta - \varphi), \quad (1)$$

where M indicates the saturation magnetization, θ indicates the deviation of M from the field direction, φ indicates the deviation of the corresponding easy axis (EA) from the field direction, and K is the corresponding uniaxial magnetic anisotropy strengths. For the moment, we select an angle θ_m , which is oriented toward either a stable or a bistable state, giving the minimum energy E_m and magnetic field H_f , respectively. The total energy of $E(\theta, H_a)$ may be derived by solving the equations

$$\left(\frac{\partial E}{\partial \theta} \right)_{\theta=\theta_m} = 0 \quad \text{and} \quad \left(\frac{\partial^2 E}{\partial \theta^2} \right)_{\theta=\theta_m} > 0, \quad (2)$$

Moreover, the angle of a magnetic moment dependent on total energy exhibits an energy barrier in a selective applied magnetic field H_a , such as $H_a=0$, $H_a>0$, or $H_a>H_f$, as shown in **Figure 1b**. When the field H_a is zero, the energy barrier exhibits a saddle shape, giving both stable solutions. When the field H_a increases, the energy barrier between the stable and bistable states decreases, implying that the field H_a provides Zeeman energy E_Z to compete with the anisotropic energy E_A . The spin direction in the bistable state gradually becomes more unstable. When the field H_a reaches H_f , the energy barrier between the stable and bistable states disappears. In this condition, the Zeeman energy E_Z is larger than the anisotropic energy E_A . The moment of a single-domain particle will then switch from spin-up to spin-down and orient itself toward the direction of the applied field, giving only one solution. As for the initial state of the magnetic moment M , it will make a choice between the stable and bistable states following a pattern like water flowing downhill. The ideal is to establish a loop process, which can be used to describe a transitional hysteresis loop. Its magnetization can readily be calculated by evaluating $M(H_a)=M_s \cos \theta_m$. Thus, the SW model provides the basis for the description of the hysteresis loop, which can be further extended to a CSAE system.

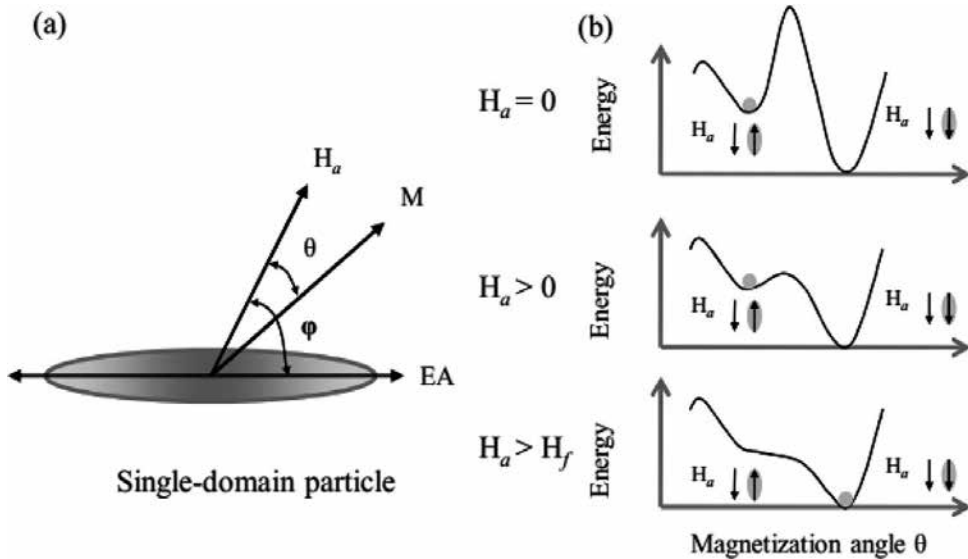


Figure 1. (a) Schematic illustration of a single-domain particle with the magnetic moment (M) and EA under an applied field (H_a). (b) Variation of the energy landscape with angle θ in a selective applied magnetic field, such as $H_a=0$, $H_a>0$, and $H_a>H_f$.

3. Core-shell anisotropic energy model

Neel [10] described the thermal fluctuations of the magnetic moment of a single-domain FM particle and its decay towards thermal equilibrium, neglecting the contribution of magnetic anisotropy. The further development of the thermal activated magnetization is described by the Brown model [11]. Fluctuations in the thermal energy $k_B T$ cause continual changes in the orientation of the moment of an individual nanoparticle. An ensemble of such nanoparticles maintains a distribution of orientation characteristics of statistical equilibrium. The thermal fluctuations are important in superparamagnetism, which can be described by a “Langevin function,” providing a description of the thermal activated magnetization. A number of models have been established [12–14] to explain the phenomena of inverted hysteresis for germanium nanostructures [15] and hysteresis for Mackay icosahedral gold nanoparticles [16], using the competing anisotropy model, and based on the SW model [8]. In the case studied here, the general picture of the core-shell system established in the Ni core (FM) coated with a NiO shell (AFM) can be described as two nonidentical phases [17], as shown in **Figure 2a**. Usually, in the macroscopic view, most of the native oxide shells of transition metals (Co, Ni) are either AFM or FM. The magnetism on the FM core has been either neglected or reported to be effective only at low temperatures [18, 19].

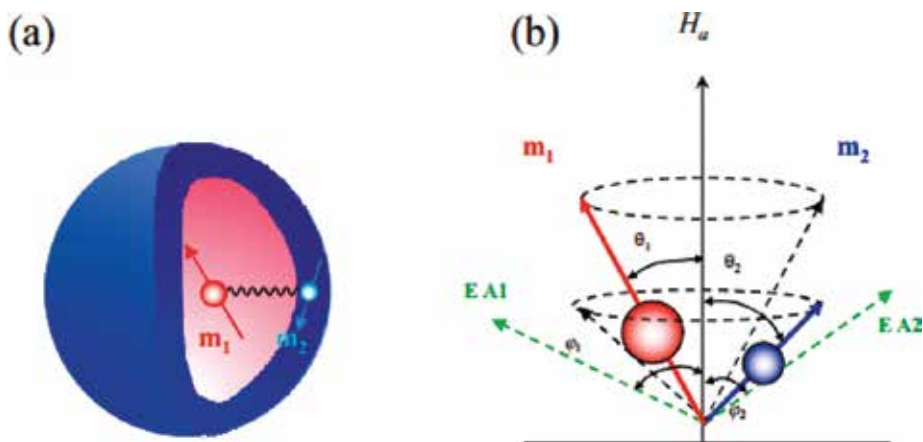


Figure 2. (a and b) Schematic illustration of a core-shell particle with two interacting magnetic moments m_1 and m_2 and EAs EA1 and EA2 under an applied field H_a . They couple at an angle $(\theta_1 - \theta_2)$ and exchange intercoupling energy E_j between the surface and inner moments.

Because most of the AFM spins are arranged collinearly and the number of sublattices are the same, the resulting magnetization is zero and the coupling vanishes to the first order [20, 21]. However, in the present core-shell system, the existence of correlated magnetic exchange intercoupling between the core-shell moments can be treated as an “exchange spring,” which can create an exchange field, inducing a canting of the AFM surface layer that “cannot” be neglected. The interpretation of the occurrence of exchange intercoupling between the surface and the core further indicates that magnetism develops not only in the core atoms but also extends into the surface ones. Treating the surface atoms and the inner atoms gives rise to a net surface macromoment m_2 and a net inner macromoment m_1 that will couple at angles $(\theta_1 - \theta_2)$ and will lead to the development of exchange intercoupling energy E_j between the surface and inner moments. We believe that the associated magnetism is indeed an intrinsic property of Ni/NiO core-shell nanoparticles. The extrinsic factors, such as the shape and temperature, are thus neglected in the considerations of the model. Conducting quantitative analysis of the intercoupling of the core-shell system, and neglecting the contribution of intracoupling, we can express the CSAE E triggered by various magnetic applied fields H_a as

$$E = -m_1 V_1 H_a \cos \theta_1 - m_2 V_2 H_a \cos \theta_2 + k_1 V_1 \sin^2(\theta_1 - \varphi_1) + k_2 V_2 \sin^2(\theta_2 - \varphi_2) + E_j \cos(\theta_1 - \theta_2). \quad (3)$$

where V_1 and V_2 indicate the volume of the Ni core and NiO shell for each nanoparticle, θ_1 and θ_2 indicate the deviations of m_1 and m_2 from the field direction, φ_1 and φ_2 indicate the deviations of the corresponding EAs from the field direction, and k_1 and k_2 are the corresponding uniaxial magnetic anisotropy strengths, as shown in **Figure 2b**. E_j is defined as $\sigma_{ex} V_s$, where σ_{ex} indicates

the exchange intercoupling energy per area and V_s indicates the interfacial area between the Ni core and NiO shell. The magnetization can readily be calculated by solving $M(H_a) = m_1 \cos \theta_{1m} + m_2 \cos \theta_{2m}$, where θ_{1m} and θ_{2m} are the θ_1 and θ_2 , respectively, that minimize E_m at each H_a . Depending on the relative strength between m_1 and m_2 and between k_1 and k_2 , the value of E_j and the bistable energy of $E(\theta_{1m}, \theta_{2m}, H_a)$ may be derived by solving the following equations: $\partial E / \partial \theta_1 = \partial E / \partial \theta_2 = 0$ [15, 22]. **Figure 3** shows an example of the dependence of the energy E of angles θ_1 and θ_2 on the selection of the applied magnetic field, such as $H_a = 0$, $H_a > 0$, or $H_a > H_f$, giving a two-dimensional energy barrier. Here, different colors are used to differentiate the energy intensity, with red indicating high energy and purple low energy. When the field H_a is zero, the energy barrier exhibits two whirlpools, indicating stable and bistable solutions. A two-dimensional and high-energy barrier appears between the two whirlpools. With an increase of the field H_a , the energy barrier between the stable and bistable states decreases, implying that the field H_a provides Zeeman energy to compete with the magnetic anisotropies and the exchange intercoupling. The magnetic directions of the core and shell moments in the bistable state gradually become more unstable. When the field H_a reaches H_f , the energy barrier between the stable and bistable states disappears. In this condition, the Zeeman energy is larger than the magnetic anisotropies and the exchange intercoupling. The core and shell moments will switch from bistable to stable states, and the core moment (FM) then becomes oriented toward the applied field direction, giving only one solution. The initial state of the core and shell moments m_1 and m_2 can assume either a stable or bistable state following a pattern like water flowing downhill. Observe the energy barrier along the dashed line in **Figure 4**. The simplified energy barrier clearly exhibits stable and bistable states, which is similar to the SW model. The exchange intercoupling between the core and shell moments in the CSAE model also plays an important role on the $M(H)$ loop process for the modulation of the hysteresis and inverted hysteresis loops. Huang et al. [15] reported the $M(H)$ loop processes and the modulation of the magnetic anisotropies and exchange intercoupling describing proteresis.

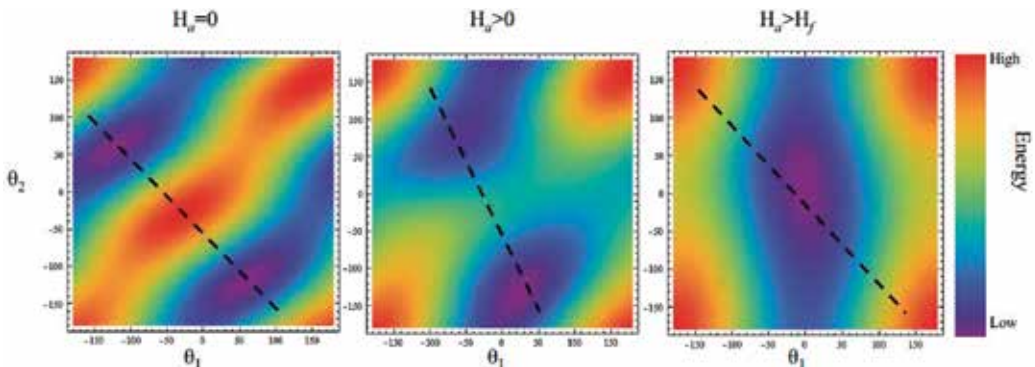


Figure 3. Variation of the energy landscape with angles θ_1 and θ_2 in a selective applied magnetic field, such as $H_a = 0$, $H_a > 0$, and $H_a > H_f$, giving a two-dimensional energy barrier.

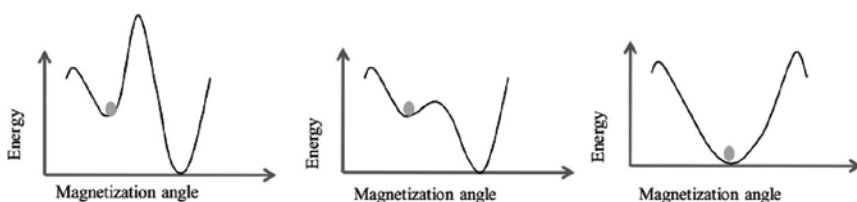


Figure 4. Observation of the energy barrier along the dashed line (**Figure 3**) clearly shows the stable and bistable states in the one-dimensional energy barrier.

4. Spin dynamics

In the Ni/NiO core-shell nanoparticle system, treating the inner Ni atoms and surface NiO atoms gives rise to a net inner macromoment m_1 and a net surface macromoment m_2 . The strength of the exchange intercoupling $E_j = \sigma_{\text{ex}} V_s$ is between the two moments of m_1 and m_2 . Moreover, the fluctuation in the thermal energy $k_B T \neq 0$ causes continual changes in the orientation of the moment of an individual nanoparticle, giving a thermally activated magnetization. Thus, to provide good simulation results, the magnetic model of the Ni/NiO core-shell nanoparticle system requires combining the CSAE model with the Langevin function. **Figure 5** shows an example of the field dependence of the magnetization. The inverted hysteresis for the 13.9(2) nm sample appears at $T=150$ K. The black open circles (experimental data) can be described by a magnetic model with a blue line (decreasing field) and a red line (increasing field). An examination of the bottom of **Figure 5** shows the process of spin dynamics from $H_a=1$ kOe to $H_a=-1$ kOe, indicating a decreasing field. In the field $H_a=1$ kOe, the Ni core moment m_1 is toward the field direction, showing coupling at an angle $|\theta_1 - \theta_2| = 88.3^\circ$ between m_1 (red line) and m_2 (blue line). When the field decreases to zero, the m_1 magnetization along the vertical direction component decreases, and the coupling angle between m_1 and m_2 increases to $|\theta_1 - \theta_2| = 172.8^\circ$. As the field decreases to $H_a=-1$ kOe, the Ni core moment m_1 moves toward the negative field direction, and the coupling angle decreases to $|\theta_1 - \theta_2| = 115.6^\circ$. For an increasing field, the process of spin dynamics is similar to the results for a decreasing field, but the directions of m_1 and m_2 at $H_a=1$ kOe are not the same. The explanation is that one solution is still in a bistable state. Thus, the field H_a has a great impact on the coupling angle between m_1 and m_2 . For the $M(H)$ loop direction, the parameters in the simulation, $m_1 > m_2$, $k_1 < k_2$, and $E_j \neq 0$, apply to the description of inverted hysteresis in the low field. In the higher field, the exchange intercoupling between m_1 and m_2 will be destroyed by the Zeeman energy, which changes the $M(H)$ loop direction to counterclockwise. A similar $M(H)$ loop has been reported in a germanium nanostructure system [15]. The exchange intercoupling strength E_j between the core and shell plays an important role in guiding the direction of the $M(H)$ loop. If there is no interaction between the core and shell moments, the $M(H)$ loop only exhibits hysteresis. If the exchange intercoupling strength E_j is larger than the magnetic anisotropies KV , the binding energy between m_1 and m_2 can be treated as a single nanoparticle system, giving rise to the hysteretic behavior. When the exchange intercoupling strength E_j is comparable to the magnetic anisotropy $K_1 V_1$ or $K_2 V_2$, the $M(H)$ loop will be guided to be proteretic.

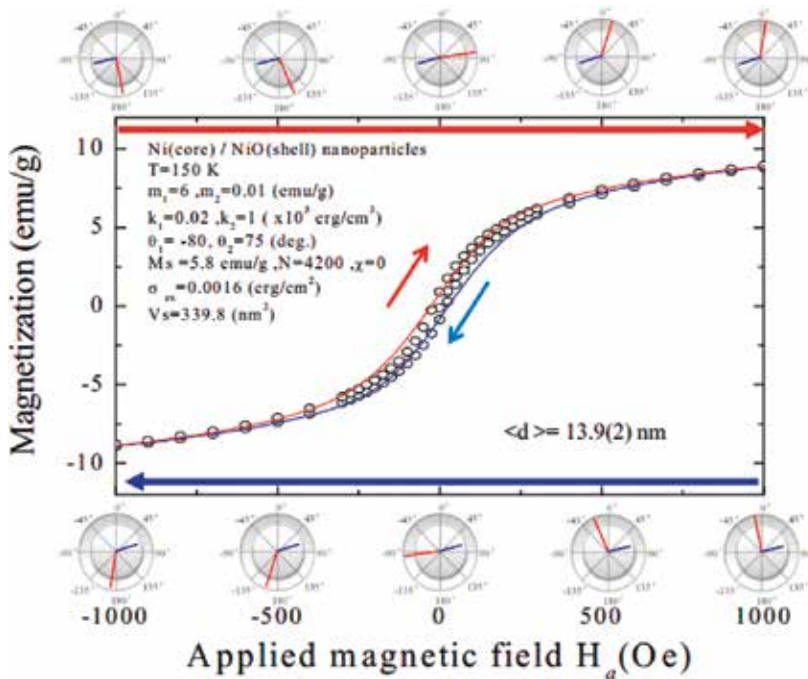


Figure 5. Field dependence of the magnetization, giving an example of inverted hysteresis for the 13.9(2) nm sample at $T=150 \text{ K}$. The black circle (experimental data) can be described by a magnetic model with a blue line (decreasing field) and a red line (increasing field).

In the example illustrated in **Figure 5**, the parameters used in the simulation, $E_f = \sigma_{\text{ex}} V_s = 3.4 \text{ meV}$, $K_1 V_1 = 0.74 \text{ meV}$, and $K_2 V_2 = 51 \text{ meV}$, give a proteretic loop, which corresponds to the above description. In terms of the spin dynamics, the angles θ_1 and θ_2 for each field provide spin processes that lead to an increasing field, as shown in **Figure 6a**, and a decreasing field as shown in **Figure 6b**. The CSAE simulation produces proteretic behavior in the 13.9(2) nm sample after solving the spin dynamics for the decreasing field and increasing field. This result suggests that the spin-orientation results in proteretic behavior. Applying the process-dependent summary of angles θ_1 and θ_2 , we consider a decreasing-field process below and above the blocking temperature T_B for two selected samples [$\langle d \rangle = 7.2(3) \text{ nm}$ and $19.0(2) \text{ nm}$], as shown in **Figures 7** and **8**. **Figure 7** shows the spin processes for the decreasing field for angles θ_1 and θ_2 in the 7.2(3) nm sample. Two examples of the field-dependent spin dynamics at temperatures below and above $T_B = 20 \text{ K}$, $T = 2 \text{ K}$, and $T = 50 \text{ K}$, respectively, are given. The spin dynamics exhibit a spin-flip for the angle θ_1 at $T = 2 \text{ K}$ and spin-orientation at $T = 50 \text{ K}$ for the angle θ_1 , implying a change of the Ni core moment m_1 . However, the phenomenon of spin-orientation was not found in the 19.0(2) nm sample, as shown in **Figure 8**, where the temperature is above the blocking temperature. Based on the observed field-dependent spin dynamics for $T = 2 \text{ K}$ to $T = 300 \text{ K}$, we give a summary of the region for spin-flip (white region) and spin-orientation (gray region), which corresponds to the distinction between hysteresis and proteresis (see **Figure 9**). The phase diagram of the spin dynamics implies a limit of the

proteretic behavior and spin-orientation below a mean size of $\langle d \rangle = 15.8$ nm, which indirectly indicates a limit to the magnetic instability in the Ni (FM) core particles coated with NiO (AFM) shells. It also reveals the reason why there is no proteresis when the mean size is large. Controlling the proteretic behavior requires a mean size below $\langle d \rangle = 15.8$ nm and temperature above T_p . The proteretic behavior relates to the spin-orientation, which has a rotation along EA. This will cause the destruction of the magnetic record. The result helps us to understand the limitations of recording data for the Ni/NiO core-shell nanoparticles on the size effect, which will affect the development of the magnetic industry in the future.

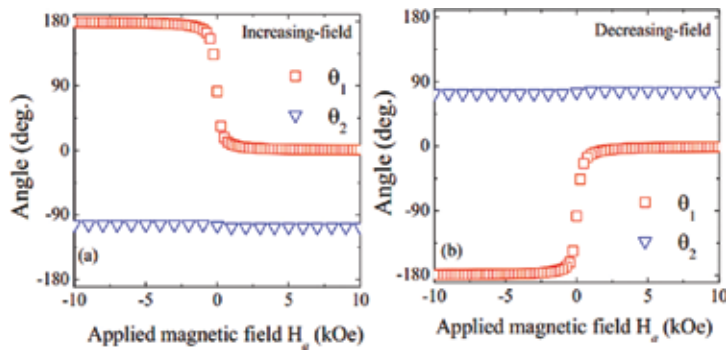


Figure 6. Simulation results provide a possible solution to elaborate spin dynamics for (a) the increasing field and (b) the decreasing field in the Ni/NiO core-shell nanoparticles.

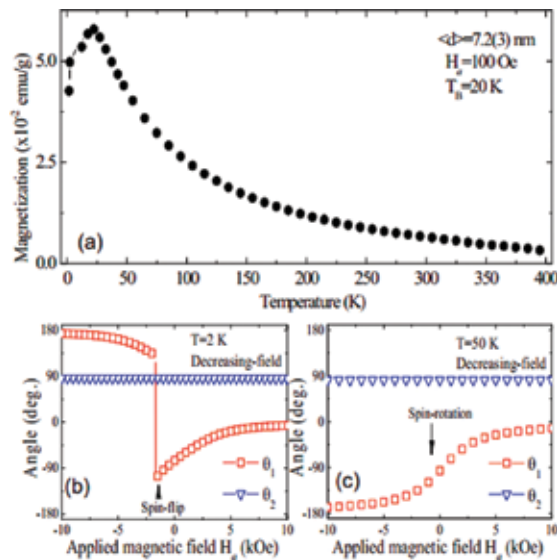


Figure 7. (a) Temperature dependency of magnetization. (b and c) Magnetic field-dependent summary of the angles θ_1 and θ_2 for the decreasing-field process below ($T = 2$ K) and above ($T = 50$ K) the blocking temperature T_b for $\langle d \rangle = 7.2(3)$ nm sample.

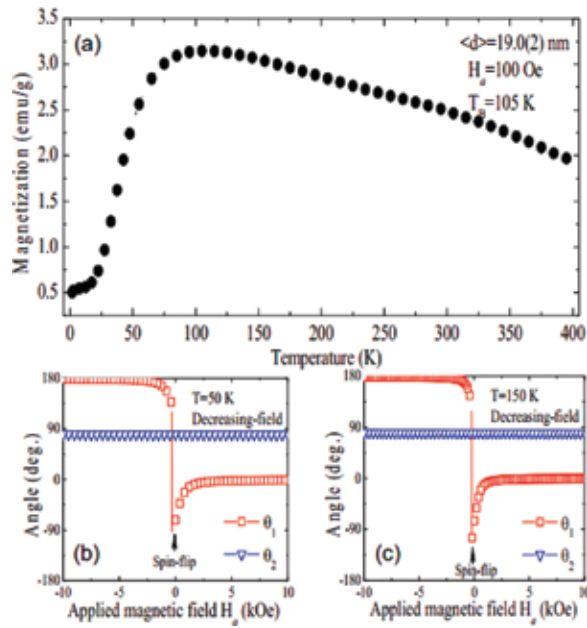


Figure 8. (a) Temperature dependence of magnetization. (b and c) Magnetic field-dependent summary of the angles θ_1 and θ_2 for the decreasing-field process below ($T=50 \text{ K}$) and above ($T=150 \text{ K}$) the blocking temperature T_B for the $\langle d \rangle = 19.0(2) \text{ nm}$ sample.

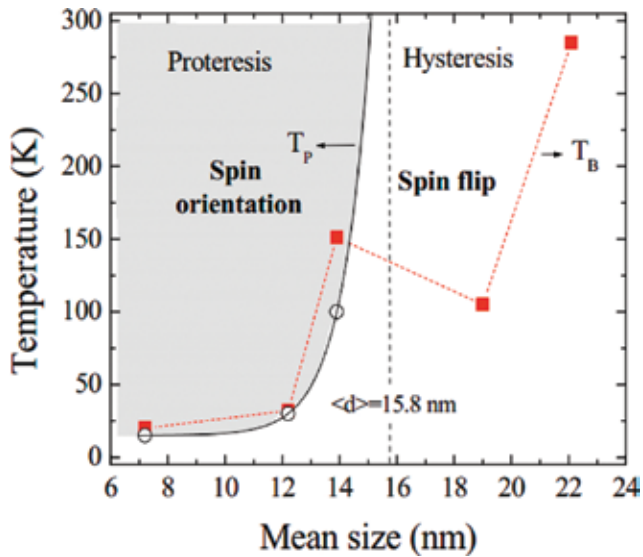


Figure 9. Summary of the $M(H)$ loop direction for hysteresis and proteresis at a series of temperatures for each sample and resulting spin-flip or spin-orientation.

5. Conclusion

Analysis of the results leads to some interesting conclusions. First, the impact of the size effect on the temperature-dependent $M(H)$ loop allows the modulation of hysteresis and proteresis, which breaks the concept of a magnetic system. The $M(H)$ loop between hysteresis and proteresis can be distinguished through analysis of the difference in magnetization ΔM , giving a summary of T_p , which results in an appearance of the proteretic behavior. In addition, we design a CSAE model, tuning the competition between magnetic anisotropy and exchange intercoupling, to describe the observation of hysteretic and proteretic behaviors in Ni/NiO core-shell nanoparticles. The CSAE simulation results show how the spin dynamics in the hysteresis and proteresis loops give rise to a spin-flip and spin-orientation, respectively. Finally, the phase diagram of the spin dynamics suggests a limit to the proteretic behavior and spin-orientation below a mean size of $\langle d \rangle = 15.8$ nm, which indirectly indicates a limit to the magnetic instability of Ni (FM) core particles coating the NiO (AFM) shells. It also explains why no proteresis occurs when the mean particle size is large. Controlling the proteretic behavior requires a mean particle size below $\langle d \rangle = 15.8$ nm and temperature above T_p . Finally, the results of magnetic analysis help us to understand the limitations of recording data for the Ni/NiO core-shell nanoparticles on the size effect, which will have implications for the development of the magnetic industry in future.

Acknowledgements

We would like to thank the Ministry of Science and Technology (MOST) of the Republic of China for their financial support of this research through project numbers MOST-103-2112-M-259-005 and MOST-104-2112-M-259-001.

Author details

Jhong-Yi Ji and Sheng Yun Wu*

*Address all correspondence to: sywu@mail.ndhu.edu.tw

Department of Physics, National Dong Hwa University, Taiwan

References

- [1] Wu SY, Ji J-Y, Shih P-H, Gandhi AC, Chan TS. Proteresis of $\text{Cu}_2\text{O}/\text{CuO}$ core-shell nanoparticles: Experimental observations and theoretical considerations. *J Appl Phys* 2014;116:193906. DOI: 10.1063/1.4902524s.

- [2] Zheng RK, Liu H, Wang Y, Zhang XX. Inverted hysteresis in exchange biased Cr_2O_3 coated CrO_2 particles. *J Appl Phys* 2004;96:5370–5372. DOI: 10.1063/1.1795983
- [3] Wei XH, Skomski R, Sun ZG, Sellmyer DJ. Proteresis in Co:CoO core-shell nanoclusters. *J Appl Phys* 2008;103: 07D514. DOI: 10.1063/1.2829239.
- [4] Ohkoshi SI, Hozumi T, Hashimoto K. Design and preparation of a bulk magnet exhibiting an inverted hysteresis loop. *Phys Rev B* 2001;64:132404. DOI: 10.1103/PhysRevB.64.132404.
- [5] Geshev J, Viegas ADC, Schmidt JE. Negative remnant magnetization of fine particles with competing cubic and uniaxial anisotropies. *J Appl Phys*. 1998;84:1488–1492. DOI: 10.1063/1.368214.
- [6] Valvidares SM, Alvarez-Prado LM, Martin JI, Alameda JM. Inverted hysteresis loops in magnetically coupled bilayers with uniaxial competing anisotropies: Theory and experiments. *Phys Rev B* 2001;64:134423. DOI: 10.1103/PhysRevB.64.134423.
- [7] Gao Y, Shindo D, Bao Y, Krishnan K. Electron holography of core-shell Co/CoO spherical nanocrystals. *Appl Phys Lett* 2007;90:233105. DOI: 10.1063/1.2747052.
- [8] Stoner EC, Wohlfarth EP. A mechanism of magnetic hysteresis in heterogeneous alloys. *Philos Trans A* 1948;240:599–642. DOI: 10.1098/rsta.1948.0007.
- [9] Schüler K. McCaig: Permanent magnets in theory and practice. *Physikalische Blätter* 1979;35:423. DOI: 10.1002/phbl.19790350913.
- [10] Neel LCR. Influence des fluctuations thermiques sur l'aimantation de grains ferromagnétiques très fins. *Acad Science (Paris), Series B* 1949; 228 : 664–666.
- [11] Brown WF. Thermal fluctuations of a single-domain particle. *Phys Rev* 1963;130:1677. DOI: 10.1103/PhysRev.130.1677.
- [12] Gao C, O'Shea MJ. Inverted hysteresis loops in CoO-based multilayers. *J Magnet Magnet Mater* 1993;127:181–189. DOI: 10.1016/0304-8853(93)90213-L.
- [13] Thiaville A. Coherent rotation of magnetization in three dimensions: A geometrical approach. *Phys Rev B* 2000;61:12221–12232. DOI: 10.1103/PhysRevB.61.12221.
- [14] Wernsdorfer W. Classical and quantum magnetization reversal studied in nanometer-sized particles and clusters. *Adv Chem Phys* 2007;118:99–190. DOI: 10.1002/9780470141786.
- [15] Huang YL, Wang HL, Chan KC, Wu SY, Wong MS, Yeh SF, Lin CI. Size-effect induced short-range magnetic ordering in germanium nanostructures. *J Nanosci Nanotechnol* 2010;10:4629–4634. DOI: 10.1166/jnn.2010.1698.
- [16] Wu CM, Li CY, YT Kuo, Wang CW, Wu SY, Li W-H. Quantum spins in Mackay icosahedral gold nanoparticles. *J Nanoparticles Res* 2010;12:177–185. DOI: 10.1007/s11051-009-9592-3.

- [17] Ji J-Y, Shih P-H, TS Chan, Ma Y-R, Wu SY. Magnetic properties of cluster glassy Ni/NiO core-shell nanoparticles: An investigation of their static and dynamic magnetization. *Nanoscale Res Lett* 2015;10:243. DOI: 10.1186/s11671-015-0925-0.
- [18] Sharrock MP. Recent advances in metal particulate recording media: Toward the ultimate particle. *IEEE Trans Magnet* 2000;36:2420–2425. DOI: 10.1109/20.908453
- [19] Nogues J, Sort J, Langlais V, Skumryev V, Surinach S, Munoz JS, Baro MD. Exchange bias in nanostructures. *Phys Rep* 2005;422:65–117. DOI: 10.1016/j.physrep.2005.08.004.
- [20] Fröbrich P, Kuntz PJ, Jensen PJ. Coupled ferro-antiferromagnetic Heisenberg bilayers investigated by many-body Green function theory. *J Phys Condensed Matter* 2005;17:5059. DOI: 10.1088/0953-8984/17/33/010.
- [21] Jensen PJ, Dreyssé H, Kiwi M. Magnetic reordering in the vicinity of a ferromagnetic/antiferromagnetic interface. *Eur Phys J B* 2005;46:541–551. DOI: 10.1140/epjb/e2005-00287-y.
- [22] Xu C, Li ZY, Hui PM. Monte Carlo studies of hysteresis curves in magnetic composites with fine magnetic particles. *J Appl Phys* 2001;89:3403. DOI: 10.1063/1.1348326.

Radiation and Propagation of Waves in Magnetic Materials with Helicoidal Magnetic Structure

Igor V. Bychkov, Dmitry A. Kuzmin and
Vladimir G. Shavrov

Additional information is available at the end of the chapter

<http://dx.doi.org/10.5772/64014>

Abstract

In this chapter, we are shortly reviewing some problems of electromagnetic and acoustic wave propagation and radiation in the magnets with helicoidal spin structure. We show the band structure of the coupled wave spectrum in the materials. The band gap width depends on the spiral angle (or, equivalently, on external magnetic field value). Interaction of spin and electromagnetic waves leads to opening the gap in spin-electromagnetic dispersion. This gap leads to opacity window in reflection spectrum of spiral magnet plate. The opacity window closes at phase transition into collinear ferromagnetic state and reaches a maximum at simple spiral state. At the frequencies near band gap boundaries, the rotation of polarization plane of propagating electromagnetic wave is observed. Account of interaction of spin and electromagnetic waves with acoustic subsystem leads to opening the gap in spin-acoustic spectrum. This gap leads to some features in electromagnetic reflectance spectrum and to rotation of acoustic wave polarization plane, i.e. to acoustic Faraday effect. We also show the possibility of acoustic and electromagnetic wave radiation by helicoidal magnets at phase transition into collinear ferromagnetic state. Some features of electromagnetic waves generation by spiral magnets placed in homogeneous magnetic field with harmonical time-dependence are also discussed.

Keywords: spiral magnets, helicoidal magnetic structure, electromagnetic waves, spin waves, acoustic waves, Faraday effect, acoustic Faraday effect

1. Introduction

The magnets with spiral (helical, or modulated) magnetic structure have been under investigation for a long time [1, 2]. These materials include the rare-earth metals, compounds based on them, and some of the compounds based on transition metals. Such materials may be semiconductors, as well as dielectrics. The reasons of such ordering may be the following: competing exchange interaction of atoms in the first and the second coordination spheres, asymmetric exchange, relativistic interaction (Dzyaloshinskii-Moriya interaction). The main characteristic of modulated structures is a modulation wave number $q = 2\pi/L$, where L is the modulation period. The modulation period of such structures is much greater than the lattice constant of the crystal. Modulation period of helical magnets usually changes continuously with the change of temperature. It may be incommensurable with the crystal's lattice constants. This is the reason why modulated, or long-periodic, magnetic structures are frequently called "incommensurable" ones.

Modulated magnetic structure leads to sufficient features of dynamical properties of helical magnets comparing with the properties of collinear ferro- and anti-ferromagnets. Thus, the spectrum of spin waves has a band structure. It has no activation frequency when wave number of propagating wave is equal to the modulation wave number [2], i.e. $k = q$, while in collinear ferro- and anti-ferromagnets this situation is observed at $k = 0$. Magnetoelastic waves in ferromagnets with spiral structure have been studied in details, for example, in works [3–8]. Works [4–6] are devoted to investigation of spin and acoustic oscillations interaction in spiral magnets without taking into account the spontaneous deformations in the ground state. These deformations were consistently considered in work [8]. Interaction of spin and electromagnetic waves in magnetic dielectrics with collinear magnetic structure has been investigated in [9]. Peculiarities of spin waves and helicons hybridization have been considered in [10]. The result of this work has been generalized for the case of arbitrary propagation direction in [11]. Later, coupled spin-Alfvén waves in ferromagnetic metals [12], and coupled plasmon-spin-electromagnetic waves in ferromagnetic semiconductors and metals with different anisotropy types [13] have been studied. These investigations show that interaction of the spin subsystem with the electromagnetic waves usually leads to the shift of activation frequency of quasi-spin branch: an additional term of electromagnetic nature, namely magnetostatic frequency, appears. This interaction may also lead to reduce the phase speed of electromagnetic wave.

Modulated magnetic structure may manifest itself in the modulation of electromagnetic characteristics of the magnet. Phenomenological approach has been successfully applied to investigate the magneto optical effects in the medium with the simple spiral structure [14]. Some features of light propagation have been predicted in works [15, 16]. Authors of these works have not taken into account the dynamics of magnetic subsystem. Such approach is valid for optical frequencies, when magnetic subsystem does not keep pace with changes of field's magnetic component. As for investigation of electro-dynamical processes at lower frequencies, taking into account dynamics of magnetic subsystem may lead to qualitatively new effects.

Coupled spin-electromagnetic and spin-acoustic-electromagnetic waves have been investigated in detail for magnets with the simple spiral structure in [17, 18]. Wave hybridization in such magnets leads to opening the gaps in spectrums of electromagnetic waves, as well as in acoustic ones. Due to the band structure of the spectrum, some features in electromagnetic and acoustic reflectance may be observed. All these features should have a place in magnets with conical spiral ordering as well.

A special kind of dynamic effects in materials with a modulated magnetic structure can occur during phase transitions, accompanied by appearance/disappearance of the modulated structure. Similar effects are well known for periodically distributed sources of different nature and they usually consist of different wave radiation. Thus, nanostructured metallic films may be sources of radiation when they are irradiated by laser pulses [19, 20]. Theoretical model for describing this effect has been proposed in [21]. Terahertz wave radiation may occur when magnons are excited by femtosecond laser pulses in anti-ferromagnets [22], or by infrared pulses in diluted magnetic semiconductors [23]. In helicoidal magnets, the spin structure is reorganized during phase transition. This may also lead to radiation of electromagnetic waves and sound. Recently [24], we have observed experimentally electromagnetic waves radiation by Heusler alloy during magneto-structural phase transition, possible mechanisms and theory of this effect have been discussed as well. We have supposed that the main contribution is caused by moving dislocations with dipole moment. Here, we show that in spiral magnets during orientational magnetic phase transition, electromagnetic radiation may be comparable to and even be more than in Heusler alloys.

Nowadays, scientific interest on the investigation of helicoidal magnets is caused by the fact that in such magnets, spontaneous polarization may appear frequently due to specific magnetic ordering. Such materials, combining both electric and magnetic properties, are called multiferroics. First, in 2003 such effect was observed in TbMnO_3 [25], then in 2004 in TbMn_2O_5 [26], and many other materials. Experiments clearly show the coupling between spontaneous polarization and modulated magnetic ordering. Phenomenologically, coupling of polarization and non-uniform magnetic ordering may be described by energy term of third order $PM\partial M$, which is allowed by symmetry. This coupling is linear according to polarization. Thus, even weak interaction of such type will lead to electric polarization at corresponding magnetic arrangement. In this chapter we will not consider multiferroic materials, but qualitatively all results are valid even in case of multiferroics. Details of peculiarities of wave interaction in helicoidal multiferroics may be found, for example, in our previous works [27–29].

This chapter consists of introduction, two sections and conclusions. In the first section, we review some peculiarities of electromagnetic and acoustic wave propagation in helical magnets. The results cover the coupled wave spectrum, electromagnetic reflection from half-space and plate of magnet with the spiral magnetic structure, Faraday rotation, and acoustic Faraday rotation (i.e. rotation of polarization plane of acoustic wave). In the second section, we consider the possibility of electromagnetic and acoustic wave radiation in spiral magnets during the phase transition. An infinitely fast phase transition and the linear change of the transverse magnetization component are considered as model processes.

2. Influence of electromagnetic-spin-acoustic interaction on wave propagation

This section is mainly based on results of our previous investigations [30–33].

Let us consider the magnet with spiral magnetisation distribution at the ground state. Such magnetic order may be realized if free energy of the crystal has the following form:

$$F = \frac{\alpha}{2} \left(\frac{\partial M_i}{\partial x_i} \right)^2 + \frac{\beta_1}{2} M_z^2 + \frac{\beta_2}{2} M_z^4 - M_z H + b_{ijlm} M_i M_j u_{lm} + c_{ijkl} u_{ij} u_{lm} + F_{in}, \quad (1)$$

where $\mathbf{M} = (M_x, M_y, M_z)$ is the magnetization of the crystal, α is the exchange constant, β_1 and β_2 are anisotropy constants, b_{ijlm} are magnetostriction constants, c_{ijkl} are elasticity constants, $i, j, l, k = x, y, z$. The sum is assumed where indexes are repeated. The term F_{in} corresponds to inhomogeneous magnetization distribution at the ground state. It may have an exchange nature (such structures we will call “exchange spiral”): $F_{in} = \gamma (\partial^2 M_i / \partial x_i^2) / 2$. Another reason may be relativistic interaction (such situation we will call “relativistic spiral”): $F_{in} = \alpha_1 \mathbf{M} \text{rot} \mathbf{M}$. In (1) we suppose that external magnetic field is directed along z -axis, which corresponds to anisotropy axis.

For concreteness, we will assume that crystal with exchange spiral structure is from hexagonal crystal system ($D_{3d}, C_{3v}, D_{6d}, D_{6h}$). Magnets with relativistic spiral structure will be assumed as isotropic ones. Their elastic properties may be defined by two characteristics (Lamé constants λ and μ), and magnetostriction will be characterized by one “effective” constant b .

Spiral magnetization distribution may be described by the following coordinate dependence of magnetization components:

$$M_x = M_0 \sin \theta \cos qz, \quad M_y = M_0 \sin \theta \sin qz, \quad M_z = M_0 \cos \theta. \quad (2)$$

In (2), $q = 2\pi/L$ is the spiral wave number, L is the spiral period, θ is the spiral angle, M_0 is the magnetization amplitude. In case of $\theta = 0$, one will have a ferromagnetic ground state, while $\theta = \pi/2$ corresponds to simple spiral structure. When $0 < \theta < \pi/2$, the “ferromagnetic spiral” phase is realized.

Minimizing the free energy (1) with appropriate expression for F_{in} , taking into account ground state magnetization distribution of spiral type (2), we will get the conditions of the phase stability. For crystals with exchange spiral, these conditions are the following: $\gamma > 0$, $\alpha < 0$, $q = (-\alpha/2\gamma)^{1/2}$. For relativistic spiral, one will have $\alpha_1 \neq 0$, $\alpha > 0$, $q = \alpha_1/\alpha$. In both cases an external magnetic field is coupled with the spiral angle:

$$M_0 \cos \Theta \left[\tilde{\beta}_1 + h_{me} + (\tilde{\beta}_2 - h_{me}/M_0^2) M_0^2 \cos^2 \Theta + \alpha q^2 + \tilde{\Delta} \right] + H = 0,$$

where β_1 and β_2 are anisotropy constants renormalized by magnetostriction [28], and $h_{me} = (b_{11} - b_{12})^2 M_0^2 / (c_{11} - c_{12})$, $\tilde{\Delta} = \gamma q^4$ for magnets with exchange spiral structure, while $h_{me} = b^2 M_0^2 / 2\mu$, $\tilde{\Delta} = -2\alpha_1 q$ for relativistic ones.

There is a critical magnetic field value H_{cr} , when the phase transition into collinear ferromagnetic state occurs. Diagonal components of the equilibrium stress tensor are homogeneous and depend on the spiral angle, while the components u_{xz} and u_{yz} depend on both spiral angle and z -coordinate, $u_{xy} = 0$.

To obtain the spectrum of coupled spin, acoustic and electromagnetic waves, one should use the Landau-Lifshitz and Maxwell equations with equation of motion of the elastic medium. Simplifying such system of equations by small oscillations method, linearizing and taking the circular components, one will obtain the following:

$$\begin{aligned} \pm \omega m_{\pm}(k) &= \cos \theta \left[\omega_{2k}^{\pm} + \frac{1}{2} \omega_{me4} \sin^2 \theta \right] m_{\pm}(k) + \frac{1}{2} \omega_{me4} \sin^2 \theta \cos \theta m_{\pm}(k \mp 2q) - \\ &- \omega_{1k \pm q} \sin \theta m_z(k \mp q) + igb_{44} M_0^2 k \left[\frac{1}{2} - \frac{3}{2} \sin^2 \theta \right] u_{\pm}(k) - \\ &- \frac{i}{2} g M_0^2 b_{44} \sin^2 \theta (k \pm 2q) u_{\pm}(k \mp 2q) - ig(b_{33} - b_{31}) M_0^2 \sin 2\theta (k \pm q) u_z(k \mp q) + \\ &+ g M_0 \sin \theta h_z(k \mp q) - g M_0 \cos \theta h_{\pm}(k), \\ \omega m_z(k) &= \frac{1}{2} \sin \theta \left[\omega_{2k-q}^- m_-(k-q) - \omega_{2k+q}^+ m_+(k+q) \right] - \\ &- \frac{i}{4} gb_{44} M_0^2 \sin 2\theta \left[(k-q) u_-(k-q) - (k+q) u_+(k+q) \right] + \\ &+ \frac{1}{2} g M_0 \sin \theta \left[h_+(k+q) - h_-(k-q) \right], \\ \left[\omega^2 - s_l^2 k^2 \right] u_{\pm}(k) &= \frac{i}{\rho} kb_{44} M_0 \left[\sin \theta m_z(k \mp q) + \cos \theta m_{\pm}(k) \right], \\ \left[\omega^2 - s_l^2 k^2 \right] u_z(k) &= -2i(b_{33} - b_{31}) k M_0 \cos \theta m_z(k) / \rho, \\ \left[\omega^2 - k^2 v^2 \right] h_{\pm}(k) &= -\omega^2 4\pi m_{\pm}(k), \quad h_z(k) = -4\pi m_z(k). \end{aligned}$$

This system of equations should be complemented by the condition of magnetization vector permanence $|\mathbf{M}| = \text{const}$, which for Fourier components has a form:

$$\sin \theta [m_-(k-q) + m_+(k+q)] + 2 \cos \theta m_z(k) = 0.$$

In all equations above we have used the following notations: $\mathbf{h}(k)$, $\mathbf{m}(k)$, $\mathbf{u}(k)$ are Fourier components of corresponding vector \mathbf{h} , \mathbf{m} , \mathbf{u} ; $v=c/\sqrt{\varepsilon}$ is electromagnetic wave speed in the medium; ε is permittivity of the crystal; $\omega_{2k}^{\pm} = \omega_{20} + gM_0L_{\perp}^{\pm}(k)$, $\omega_{1k} = \omega_{10} + gM_0\sin^2\theta L_{\parallel}(k) = 0$, $L_{\perp}^{\pm}(k) = -\alpha(q^2 - k^2) - \gamma(q^4 - k^4) + 2\alpha_1(q \mp k)$, $L_{\parallel}(k) = -\alpha(q^2 - k^2) - \gamma(q^4 - k^4) + 2\alpha_1q$, $s_t^2 = c_{44}/\rho$, $s_l^2 = c_{33}/\rho$, $\omega_{me4} = gM_0h_{me4} = gb_{44}^2M_0^3/c_{44}$, $\omega_{10} = gM_0[h_{me4} - \sin^2\theta(\beta_1 + (\beta_2 + 2\beta_2)M_0^2\cos^2\theta + h_{me}\sin^2\theta)]$.

Dispersion equation may be obtained from this system of equations. Solution of dispersion equation gives the propagation constant k for the waves with opposite circular polarization. We should note that due to the symmetry of the problem, the propagation of the wave with fixed circular polarization along z -axis is similar to the propagation of the wave with opposite circular polarization in inverse direction. Detailed investigation shows that waves with opposite circular polarizations have different propagation constants. This situation is valid for electromagnetic waves, as well as for acoustic ones. The difference in propagation constants will lead to different speed of waves with opposite circular polarization, hence, the rotation of polarization plane of linearly polarized wave. Rotation angle may be calculated as $\Delta\varphi = (k_+ - k_-)l/2$, where k_+ and k_- are propagation constants of the waves with corresponding circular polarization, and l is the distance, which the wave goes in the medium.

For investigation of electromagnetic wave reflection from the plate of magnet with spiral magnetic structure, one should add the boundary conditions: $H_{x,y}^{(out)} = H_{x,y}^{(in)}$, $E_{x,y}^{(out)} = E_{x,y}^{(in)}$, $D_z^{(out)} = D_z^{(in)}$, $\partial m_i / \partial z = 0$, and $\sigma_{jz} = 0$. Indexes (*in*) and (*out*) denote the fields inside and outside the magnet. We suppose that the outer medium is a vacuum. When one investigates the reflection of electromagnetic waves from semi-infinite structure, these boundary conditions should be applied to the single boundary.

For numerical estimations we will use following constant values [2]: $b_{ij} \sim 20 \text{ erg}/(\text{Oe} \times \text{cm}^4)$, $q \sim 10 \text{ g}/\text{cm}^3$, $v_t \sim 3 \times 10^5 \text{ cm/s}$, $v_l \sim 5 \times 10^5 \text{ cm/s}$, $M_0 \sim 500 \text{ Oe}$. The period of the structure for relativistic interaction-caused spiral magnet is usually much larger than in case of exchange-caused spiral structures. For example, $\text{Fe}_x\text{Co}_{1-x}\text{Si}$ alloys, which symmetry allows Dzyaloshinskii-Moriya interaction, for $x = 0.3$ in spiral state has a modulation period $L = 230 \text{ nm}$ ($q \sim 3 \times 10^5 \text{ cm}^{-1}$) [34]. Other examples of the magnets with Dzyaloshinskii-Moriya interaction-caused spiral structures are FeGe ($L = 70 \text{ nm}$, $q \sim 8 \times 10^5 \text{ cm}^{-1}$) [35], and MnSi ($L = 18 \text{ nm}$, $q \sim 3 \times 10^6 \text{ cm}^{-1}$) [36]. Different modulated states exist in erbium single crystal due to the competing exchange interaction. In conical state, wave number of the structure is $5c^*/21$ ($c^* = 2\pi/c$ is inverse lattice constant, $c = 0.56 \text{ nm}$ is lattice constant) [37], i.e. $q \sim 3 \times 10^7 \text{ cm}^{-1}$. We will use $q \sim 10^5 \text{ cm}^{-1}$ and $q \sim 10^8 \text{ cm}^{-1}$, consequently.

First of all, let us discuss the influence of spin-electromagnetic interaction on wave propagation. For such purposes, the problem may be simplified. We may neglect the elasticity and magnetostriction terms in free energy (1). In such case, dispersion equation may be calculated in form:

$$\left[2\omega^2 (\omega^2 - v^2 k^2) + \left((\omega^2 - v^2 k^2) \Omega_k^+ - \omega^2 \omega_M \right) (\Omega_{1M} \sin^2 \theta - 2\omega \cos \theta) \right] \times$$

$$\left[2\omega^2 (\omega^2 - v^2 (k - 2q)^2) + \left((\omega^2 - v^2 (k - 2q)^2) \Omega_{k-2q}^- - \omega^2 \omega_M \right) (\Omega_{1M} \sin^2 \theta + 2\omega \cos \theta) \right] -$$

$$- \Omega_{1M}^2 \sin^4 \theta \left((\omega^2 - v^2 k^2) \Omega_k^+ - \omega^2 \omega_M \right) \left((\omega^2 - v^2 (k - 2q)^2) \Omega_{k-2q}^- - \omega^2 \omega_M \right) = 0.$$

Here, $\omega_M = 4\pi g M_0$ is magnetostatic frequency, $\Omega_{1M} = \Omega_{1k-q} + \omega_M$, $\Omega_{k-2q}^- = g M_0 (\alpha(q^2 - (k - 2q)^2) + \gamma(q^4 - (k - 2q)^4) - 2\alpha_1(k - q))$, $\Omega_k^+ = g M_0 (\alpha(q^2 - k^2) + \gamma(q^4 - k^4) + 2\alpha_1(k - q))$, $\Omega_{1k-q} = g M_0 (\beta_1 + 3\beta_2 M_0^2 \cos^2 \theta - \alpha(q^2 - (k - q)^2) + \gamma(q^4 - (k - q)^4) + 2\alpha_1 q)$. For relativistic spiral, one should put $\alpha_1 = 0$, while in exchange spiral case $\gamma = 0$.

Results of calculations are shown in **Figure 1**.

Figure 1a shows the dispersion of coupled spin-electromagnetic waves in spiral magnets with different spiral angles (or external magnetic field values). One can see that the spectrum has a band structure. The band gap is observed near the point where non-interacting dispersion curves are crossed. This band gap appears due to the resonant interaction of spin and electromagnetic waves in a magnet. From **Figure 1a** we can see that with decrease of angle, the gap shifts toward lower frequencies and its width decreases. Calculations show that in case of exchange spiral, a zone of opacity is much narrower than in case of relativistic spiral, and lies at higher frequencies. It should be also noted that the magnitude of the interaction of spin and electromagnetic waves depends on the spiral angle.

Figure 1b shows the frequency dependence of the reflectance of electromagnetic wave from the plate of spiral magnet with width $l = 100 \mu\text{m}$ for different spiral angles. One can see that reflectance is near to unit at frequencies corresponding to the band gap of the spectrum of coupled waves, i.e. opacity window is observed. This window exists only for spiral states with $\theta \neq 0$, while it disappears in the collinear ferromagnetic state.

The results of calculating polarization plane rotation are shown in **Figure 1c** and **d**. One can see that rotation angle depends on external magnetic field almost linearly at frequencies upper and lower the band gap. The maximum values of rotation correspond to the band gap boundaries.

Let us now investigate the effect of acoustic subsystem on wave propagation in the magnet. For such purposes we should solve all equations for exact free energy expression (1). The details of this investigation may be found in work [33].

Calculations of the spectrum of coupled spin-electromagnetic-acoustic waves in spiral magnets show that despite the gap corresponding to spin-electromagnetic interaction, an additional gap corresponding to spin-acoustic interaction is opened. This gap reaches a maximal width at ferromagnetic spiral state with $\theta = \pi/4$. The spectrum of coupled waves near $k = 0$ is shown in **Figure 2a**.

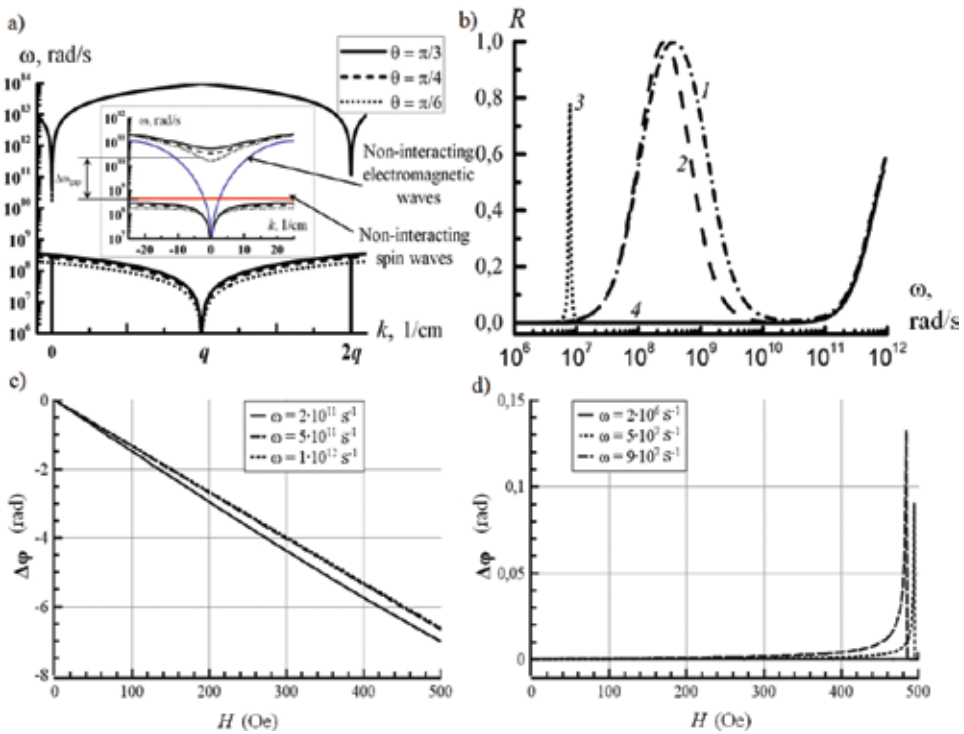


Figure 1. Dispersion of coupled spin-electromagnetic waves in spiral magnets with different spiral angles (a). On the inset the small k region is shown. Frequency dependence of the reflectance of electromagnetic wave from the plate of spiral magnet with width $l = 100 \mu\text{m}$ for different spiral angles (b). Electromagnetic waves polarization plane rotation: near upper frequency of band gap (c), and near lower frequency of band gap (d).

Figure 2b shows results of investigation of electromagnetic waves reflection from semi-infinite spiral magnet. One can see that besides the opacity window corresponding to spin-electromagnetic interaction, there are some features at the frequencies of spin-acoustic interaction. This effect corresponds to resonant interaction of electromagnetic, spin and acoustic waves. The width of such acoustically caused electromagnetic opacity window depends on the spiral angle (or, equivalently, on external magnetic field value), as well.

The gap opening in spin-acoustic spectrum leads to the possibility of polarization plane rotation for acoustic waves, i.e. acoustic Faraday effect. The results of calculation of rotation angle at the sample distance of 1 cm for different frequencies are shown in **Figure 2c**. The breaks on the curves correspond to band gap in the spectrum, which moves with the change of the external magnetic field. One can see that maximal rotation of the polarization plane is observed near the band gap.

The results we have discussed in this section show that spiral magnets may be perspective materials for electromagnetic and acoustic wave manipulation (such as filtering, polarizing, and phase shifting).

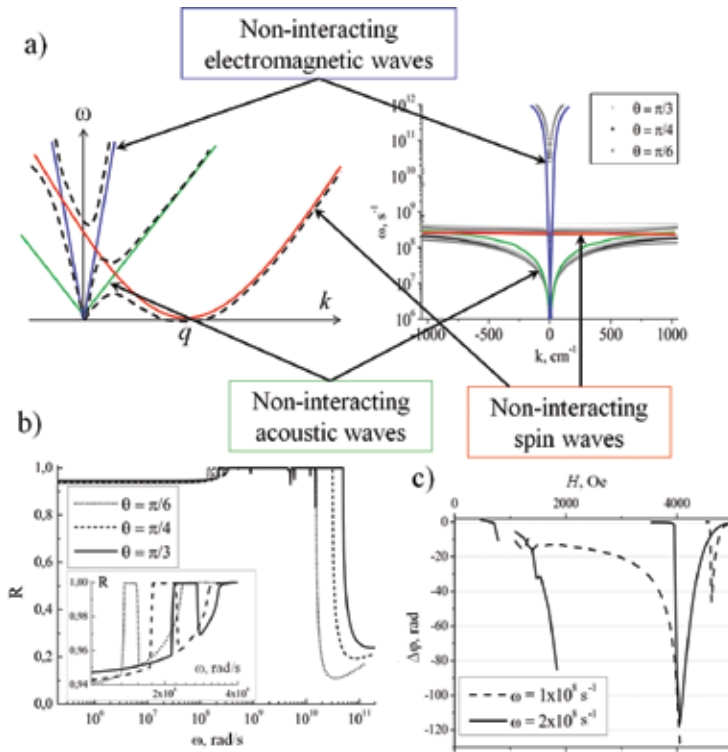


Figure 2. Spectrum of coupled waves (a) (left – schematic spectrum, right – calculated spectrum near $k = 0$). Electromagnetic waves reflection from semi-infinite spiral magnet (b). On the inset the feature associated with the acoustic gap is shown. Acoustic Faraday effect (c).

3. Radiation of electromagnetic and acoustic waves by helicoidal magnets at phase transitions

In this section we partly follow our previous works [38, 39].

In context of macroscopic electrodynamics, electromagnetic wave radiation may be described by the following equation:

$$\Delta \mathbf{E} - \frac{1}{c^2} \frac{\partial^2 \mathbf{E}}{\partial t^2} = \frac{4\pi}{c^2} \left[\frac{\partial}{\partial t} \left(\mathbf{j} + \frac{\partial \mathbf{P}}{\partial t} + c \text{rot } \mathbf{M} \right) + c^2 \text{grad div}(\mathbf{P}) \right] \quad (3)$$

In (3) \mathbf{E} is electric field strength, \mathbf{P} and \mathbf{M} are polarization and magnetization of the medium, consequently, \mathbf{j} is the current density, c is speed of light in the vacuum. Assuming magnetic material to be non-conductive with dielectric constant ϵ , Eq. (3) may be simplified:

$$\Delta \mathbf{E} - \frac{\varepsilon}{c^2} \frac{\partial^2 \mathbf{E}}{\partial t^2} = \frac{4\pi}{c^2} \frac{\partial \mathbf{j}_M}{\partial t} \quad (4)$$

In (4) magnetic current density has been introduced: $\mathbf{j}_M = c \cdot \text{rot}(\mathbf{M})$. For spiral magnets with magnetization distribution given by (2), one may calculate magnetic current density $\mathbf{j}_M = (j_0 \cos(qz), j_0 \sin(qz), 0)$, $j_0 = -cqM_0 \sin(\theta)$. So, we may conclude that any process with changing the spiral wave number q , the amplitude of magnetization vector M_0 , or the spiral angle θ will be accompanied by electromagnetic radiation.

The form of radiation Eq. (4) allows one to see that time-varying non-uniform magnetization distribution is equivalent to time-varying distributed conductive currents. Generally, this equation should be solved together with the magnetization motion equation (usually, Landau-Lifshitz equation with additional relaxation terms). This system of equations can be solved only numerically. However, it is known that the frequency of precession of the magnetization vector in ferromagnetic materials (ferromagnetic resonance frequency) is about 10–100 GHz, and the relaxation time of magnetization to equilibrium state is of the order of few microseconds at usual conditions. In this case, if we are interested in processes with characteristic frequencies far from resonance, the motion of magnetization can be neglected, and one can assume that magnetization has always ground state value (2). This makes reasonable the assumption that only spiral angle changes during magnetic field induced phase transition.

For investigation of sound waves generation, we should solve equation of motion for elastic medium:

$$\rho \partial^2 u_i / \partial t^2 = \partial \sigma_{ij} / \partial x_j, \quad \sigma_{ij} = \partial F / \partial u_{ij}. \quad (5)$$

In (5), F denotes free energy density defined by Eq. (1) for spiral magnets. Eq. (5), similarly to the case of electromagnetic waves, may be transformed into wave equations with non-zero source functions, which in general may depend on both coordinate and time. It is convenient to introduce circular components $(u, M)_{\pm} = (u, M)_x \pm i(u, M)_y$, transversal and longitudinal sound velocities $v_t = (2c_{44})^{1/2}$ and $v_l = (c_{33})^{1/2}$, consequently. Calculations show that only transverse sound will be excited. We will have

$$\frac{\partial^2 u_{\pm}}{\partial t^2} - v_t^2 \frac{\partial^2 u_{\pm}}{\partial z^2} = \pm \frac{iqb_{44}M_0^2}{\rho} \sin(2\theta) \exp(\pm iqz). \quad (6)$$

Let's consider an infinite crystal. At initial time, it will be assumed that there was no electromagnetic radiation, i.e., we should solve the Eq. (4) or (6) with zero initial conditions. In this case, solutions of Eq. (4) or (6) can be obtained from the Duhamel's principle [40].

Here, we would not solve the problem of phase transition kinetics. We will consider only two simplest cases: an infinitely fast phase transition and linear variation of source functions. Comparing Eqs. (6) and (4) one may note that source function for radiation of electromagnetic waves is proportional to time derivative of $\sin[\theta(t)]$, while in case of acoustic waves it is defined by time dependence of $\sin[2\theta(t)]$. Thus, maximal radiation of electromagnetic waves may be expected at phase transition from simple spiral state to collinear ferromagnetic one, while maximal acoustic radiation should be observed at phase transition from “ferromagnetic spiral” phase with $\theta = \pi/4$ to collinear ferromagnetic state.

Let us assume that $\sin[\theta(t)] = \Theta(-t)$; $\Theta(t)$ is the step-like Heaviside function; $\partial\Theta(-t)/\partial t = -\delta(t)$; $\delta(t)$ is the Dirac’s delta function. This situation corresponds to instantaneous actuation of magnetic field with the value H_{cr} at time $t = 0$, and collapse of the spin spiral. Such a process is quite unreal since magnetization requires finite relaxation time to get to the final collinear ferromagnetic state. However, despite the unreality of the case, its analysis allows us to estimate an upper limit of emitted wave amplitude. Calculations show that electromagnetic field has a form:

$$E_{\pm}(z, t) = E_x(z, t) \pm iE_y(z, t) = \mp 4\pi i M_0 \varepsilon^{-1/2} \sin(qvt) \exp[\mp iqz] \quad (7)$$

In case of linear time dependence of $\sin[\theta(t)]$: $\sin[\theta(t)] = Pt$, at $t \leq P^{-1}$, $P = const$, we will have:

$$E_{\pm}(z, t) = \pm 4\pi i M_0 P (qc)^{-1} [1 - \cos(qvt)] \exp[\mp iqz], t \leq P^{-1} \quad (8)$$

It is seen that in contrast to the fast actuation of the magnetic field, in addition to the standing wave, a constant component of the electric field appears as well. The amplitude and the constant component are directly proportional to the speed of the state change P .

Solutions given by expressions (7) and (8) are superposition of waves travelling to the left and to the right, which, due to unbound periodic source, give a standing wave by adding each other. In the real material, multiple reflections of the excited waves from the boundaries and some part of electromagnetic energy will be emitted beyond the material. If refractive index of the environment is the same as for crystal (i.e. mediums are ideally conjugated) with thickness d , two electromagnetic wave pulses with wave number q and frequency qv will be emitted from each sample’s side.

Maximum sound waves generation will take place at phase transition from $\theta = \pi/4$ to collinear ferromagnetic state. Mathematically, it may be expressed as $\sin[2\theta(t)] = \Theta(t)$. In such case, solution may be easily calculated:

$$u_{\pm}(z, t) = \pm i b_{44} M_0^2 \exp[\pm iqz] [1 - \cos(qv_t t)] / \rho q v_t^2 \quad (9)$$

Let us consider now the model process, when $\sin[2\theta(t)] = \eta t, t < \eta^{-1}$ (i.e. linear time-dependence of source function). Calculations show that the following sound oscillations will be excited:

$$u_{\pm}(z, t) = \pm \eta i b_{44} M_0^2 \rho^{-1} q^{-2} v_t^{-3} [q v_t t - \sin(q v_t t)] \exp[\pm i q z], t < \eta^{-1}. \quad (10)$$

The frequency of standing electromagnetic waves in formulas (7) and (8) is $\omega = qv \sim 10^{15} - 10^{16} \text{ s}^{-1}$. At “slow” change of the state, in mode determined by formula (8), the signal amplitude is proportional to P . For $P \sim 10^7 \text{ s}^{-1}$, the amplitude of emitted waves is small: $E \sim 10^{12} \text{ CGSE}$ (energy density is about 10^{-11} J/cm^3). For ultrafast magnetization reversal processes, the time of magnetization switch is usually about 10^{-12} s , or $P \sim 10^{12} \text{ s}^{-1}$, and we have $E \sim 10^2 \text{ CGSE}$ (energy density is about 10^{-3} J/cm^3). The maximal radiation corresponding to the situation of the instantaneous change of the state has amplitude of electric field $E \sim 10^3 \text{ CGSE}$ (energy density is about 0.1 J/cm^3). This radiation will be emitted like a pulse. Characteristic time length of this pulse is $d/v + P^{-1}$. For sample with $d \sim 1 \mu\text{m}$, we will have $d/v \sim 10^{-14} \text{ s}$. This time is much smaller than usual magnetization switching time, so in real experiments, characteristic time length of the pulse should be comparable with switching time for $d \ll vP^{-1}$. Despite low energy density of the pulse, it may have valuable power density. In case of $P = 10^{12} \text{ s}^{-1}$ this value may reach about 1 GW/cm^3 .

For acoustic wave generation in case of infinitely fast phase transition, we will have the oscillations frequency $\omega = qv_t$. For Dzyaloshinskii-Moriya interaction-caused spiral magnets the linear frequency $f = \omega/(2\pi) \sim 5 \text{ GHz}$, and amplitude is $u_{\pm} \sim 10^{-5} \text{ cm}$. In exchange-caused case $f \sim 5 \text{ THz}$, $u_{\pm} \sim 10^{-8} \text{ cm}$. Both cases correspond to hypersound oscillations. In case of “slow” phase transition sound oscillations with the same frequency are excited. Amplitude of excited oscillations linearly depends on the “phase transition speed” η . We may calculate that $u_{\pm} \sim 10^{-21} \times \eta \text{ cm}$ and $u_{\pm} \sim 10^{-27} \times \eta \text{ cm}$ for Dzyaloshinskii-Moriya and exchange interaction-caused spiral magnets, respectively. For example, ultrafast magnetization reversal processes have time of magnetization switch of about 10^{-12} s , or $\eta \sim 10^{12} \text{ s}^{-1}$. The amplitudes will have values $u_{\pm} \sim 10^{-9} \text{ cm}$ and $u_{\pm} \sim 10^{-15} \text{ cm}$ for Dzyaloshinskii-Moriya and exchange interaction-caused spiral magnets, consequently. One can see that in case of exchange spiral structure, the amplitude is negligibly small. In experiments it is possible to detect the pulse of sound with characteristic time length of about $\tau \sim d/v$, where d is the sample size. For sample size $d \sim 1 \text{ mm}$ we will have time length $\tau \sim 10^{-6} \text{ s}$.

The abovementioned results make one believe that a similar effect may be observed when the spiral magnet is placed in homogeneous periodic magnetic field, i.e. when the spiral angle periodically changes near its equilibrium value. For investigation of this problem, let us consider the spiral magnet in time-dependent external magnetic field $H_z(t) = H_0 + h_0(t)$, where H_0 is a constant magnetic field defining the ground state and equilibrium value of spiral angle, and $h_0(t) = h_0 \exp[i\Omega t]$ is a periodic component. For simplicity, we will assume that the periodic component of the field has small amplitude. In such context, magnetization may be described by static component \mathbf{M}_0 , which is described by Eq. (2) with the spiral angle defined by H_0 and

by dynamical component $m(z,t)$. Dynamical component may be obtained from Landau-Lifshitz equation. We will neglect relaxation processes for simplicity. Oscillated components may be assumed in form of Fourier series $m(z,t) = \Sigma m_n(t)\exp[-inqz]$. Calculations show that longitudinal periodic magnetic field will excite only harmonics of m_x and m_y with $n = \pm 1$. We will have the following:

$$\frac{\partial^2 m_{\pm}}{\partial z \partial t} = \frac{-gq\Omega M_0 \sin \theta h_{0z} e^{i\Omega t}}{\Omega_{res}^2 - \Omega^2} \left\{ \pm 2g\alpha_1 q M_0 \cos \theta e^{\mp iqz} + (\Omega \pm g\alpha_1 q M_0 \cos \theta) e^{\pm iqz} \right\}; \quad (11)$$

$$m_{\pm} = m_x \pm im_y; \Omega_{res}^2 = 5\alpha_1^2 g^2 q^2 M_0^2 \cos^2 \theta.$$

One can see that the source function defined by Eq. (11) has a resonance at $\Omega = \Omega_{res}$. This is due to resonant behaviour of corresponding susceptibility component. In real materials, due to unavoidable damping processes, the source function will have a finite value even at resonant frequency. We will take into account these processes formally by putting $\Omega + i\delta$ instead of Ω , where δ is a formal damping parameter.

Solving Eq. (4) with use of Green's function formalism for magnet's size d , we will have the following stationary electric field amplitudes at the left boundary of the sample:

$$E_{\pm}(0,t) = \frac{i2\pi g M_0 \sin \theta h_{0z} e^{i\Omega t} e^{-i\Omega d/v}}{\Omega_{res}^2 - (\Omega + i\gamma)^2} \times$$

$$\times \left\{ \frac{\Omega + i\gamma \pm g\alpha_1 q M_0 \cos \theta}{\Omega \mp qv} \left[qv(e^{i\Omega d/v} - 1) \pm \Omega(1 - e^{\pm iqd}) \right] \mp \right.$$

$$\left. \mp \frac{2g\alpha_1 q M_0 \cos \theta}{\Omega \pm qv} \left[qv(e^{i\Omega d/v} - 1) \mp \Omega(1 - e^{\mp iqd}) \right] \right\} \quad (12)$$

One may calculate the energy of emitted waves $W_{\pm} = |E_{\pm}|^2/8\pi$. Dependencies of this energy from the frequency and from the equilibrium spiral angle are shown in **Figure 3**.

One can see that intensities of left- and right-polarized emitted waves differ from each other. When $0 < \theta < \pi/2$ (i.e. when the static component of magnetization is tilted along spiral axis) the energy of negatively polarized waves is greater than that of positively polarized ones. When $\theta = \pi/2$, energies of waves for both polarizations are equal. When $\pi/2 < \theta < \pi$, the energy of positively polarized waves prevails. The increase of damping parameter leads to decrease of emitted wave energy, especially near the resonance. When the damping parameter becomes much greater than the resonant frequency, the energy of emitted waves slowly varies with the frequency, equal for waves of both polarizations, and has a maximum at $\theta = \pi/2$.

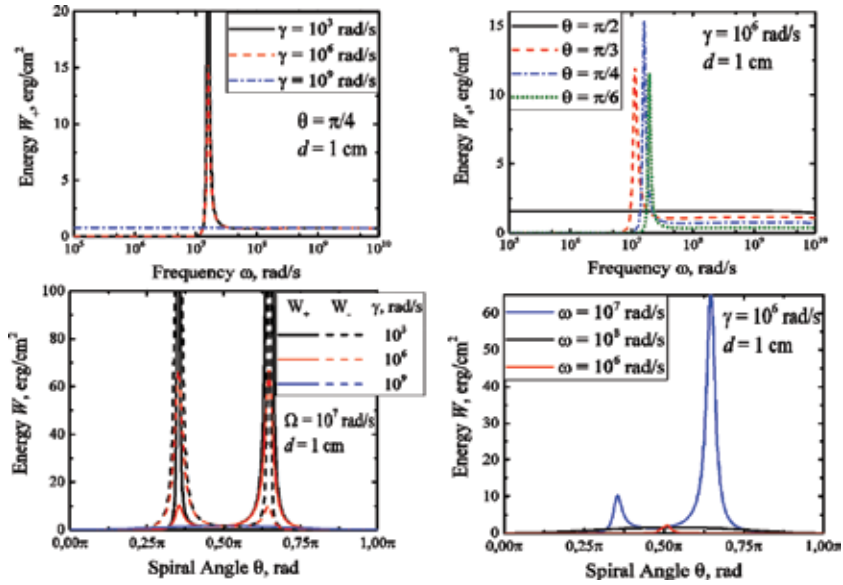


Figure 3. Energy of emitted electromagnetic waves versus frequency of exciting field and the static value of spiral angle.

Similarly, one may consider acoustic wave excitation in spiral magnets in homogeneous harmonical magnetic field. Wave equations may be written as follows:

$$\begin{aligned} \frac{\partial^2 u_{\pm}}{\partial z^2} - \frac{\ddot{u}_{\pm}}{v_l} &= -\frac{b_{44}}{c_{44}} \left(M_{z0} \frac{\partial m_{\pm}}{\partial z} + m_z \frac{\partial M_{\pm 0}}{\partial z} \right); \\ \frac{\partial^2 u_z}{\partial z^2} - \frac{\ddot{u}_z}{v_l} &= -\frac{2b_{13}}{c_{33}} \left(M_{x0} \frac{\partial m_x}{\partial z} + m_x \frac{\partial M_{x0}}{\partial z} + M_{y0} \frac{\partial m_y}{\partial z} + m_y \frac{\partial M_{y0}}{\partial z} \right). \end{aligned} \quad (13)$$

Both longitudinal and transversal acoustic waves may be excited. Transverse magnetization oscillations will excite both longitudinal and transverse sound, while longitudinal magnetization oscillations affect only transverse sound. Similar to calculations made in [41], for simplicity we will suppose that magnetization oscillations are uniform, i.e. $\partial m_i(z, t) / \partial z \approx m_{i0} [\delta(z) - \delta(z-d)] \exp(-i\omega t)$, here $\delta(z)$ is Dirac's delta-function, d is the sample size. Wave equations may be solved by Green's function formalism. Green's functions for longitudinal and transverse acoustic waves $G_{t,l}(z, z_0)$ consist of two terms. The first one $(i/2k_{t,l}) \exp(ik_{t,l}|z-z_0|)$ corresponds to the sound excited in point z_0 and propagating in $+z$ -direction. The second one $(i/2k_{t,l}) \exp(ik_{t,l}|z+z_0|)$ corresponds to the wave excited in the same point, but propagating in opposite direction. In both cases, $k_{t,l} = \omega/v_{t,l}$. Complete Green's function will be as follows:

$$G_{i,l}(z, z_0) = ik_{i,l}^{-1} \exp(-ik_{i,l}z) \cos(k_{i,l}z_0). \quad (14)$$

Calculations show that amplitudes of excited waves are:

$$u_{\pm} = -\frac{ib_{44}M_0}{k_l c_{44}} \left\{ \begin{array}{l} m_{\pm 0} \cos \theta [1 - \cos(k_l d)] \pm \\ \pm iq \frac{m_{\pm 0} \sin \theta}{q^2 - k_l^2} \left[\begin{array}{l} k_l \exp(\pm iqd) \sin(k_l d) \mp \\ \mp iq (1 - \exp(\pm iqd) \cos(k_l d)) \end{array} \right] \end{array} \right\}; \quad (15)$$

$$u_z = -\frac{4ib_{13}M_0 \sin \theta}{k_l c_{33}} \left\{ \begin{array}{l} m_{x0} \frac{k_l}{q^2 - k_l^2} [q \sin qd \sin k_l d - k_l \cos qd \cos k_l d] - \\ -m_{y0} \sin qd \left[\cos k_l d - \frac{q \sin k_l d}{q + k_l} \right] \end{array} \right\}.$$

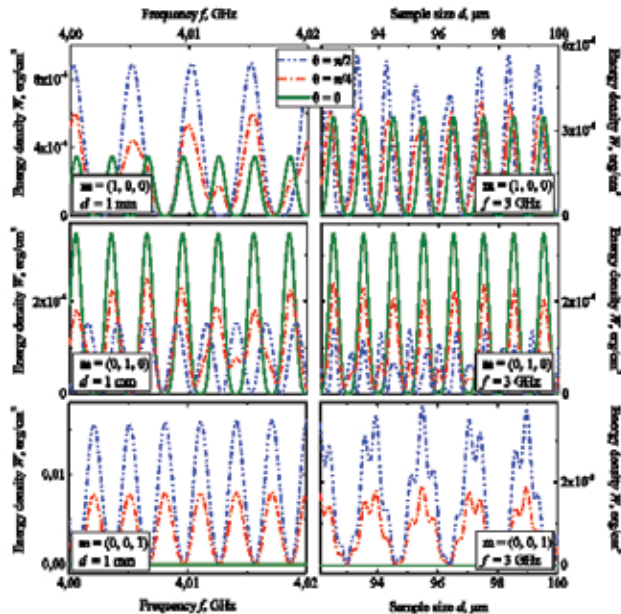


Figure 4. Fragments of acoustic waves energy density dependencies from frequency and sample size for different polarization of excited field. Wave number of spiral is $q = 10^5 \text{ cm}^{-1}$.

Energy density of excited waves is $W = c_{33}(u_{zz})^2/2 + 2c_{44}[(u_{xz})^2 + (u_{yz})^2]$. Fragments of its dependencies from frequency and sample size for different polarization of excited field are shown in **Figure 4**. One can see that these dependencies have a complex oscillating behaviour. Oscillations are caused by interference of sound waves propagating from opposite sample boundaries. Another reason of oscillations is periodicity of source function. Eq. (15) have resonances at $k_{t,l} = q$. At microwave frequencies these resonances may be observed in magnets with relativistic spiral structure ($q \sim 10^5 \text{ cm}^{-1}$, $\omega_{res} \sim qv_{t,l} \sim 10^{10} \text{ rad/s}$), while in magnets with exchange spiral structure, resonance frequencies correspond to terahertz frequency range ($q \sim 10^8 \text{ cm}^{-1}$, $\omega_{res} \sim qv_{t,l} \sim 10^{13} \text{ rad/s}$).

4. Conclusions

We have reviewed some features of electromagnetic and acoustic wave propagation in magnets with helicoidal spin order. There is an opacity window in reflectance spectrum of electromagnetic waves from the plate of spiral magnet. The width of this window has a maximal value at phase of simple spiral, and decreases with decrease of spiral angle (or, equivalently, with increase of external magnetic field). Field dependencies of polarization plane rotation angle have a resonant behaviour. Maximum rotation may be observed near boundaries of band gaps for both electromagnetic and acoustic waves. Both electromagnetic and acoustic waves may be radiated by spiral magnets during the phase transition. The amplitude of radiated waves strictly depends on the speed of phase transition.

In general, the results show the possibility of practical applications of spiral magnets for electromagnetic and acoustic wave manipulation and generation.

Acknowledgements

The work was supported partly by Russian Science Foundation Grant # 14-22-00279 and Russian Foundation for Basic Researches Grant # 15-07-99654.

Author details

Igor V. Bychkov^{1*}, Dmitry A. Kuzmin¹ and Vladimir G. Shavrov²

*Address all correspondence to: bychkov@csu.ru

1 Chelyabinsk State University, Chelyabinsk, Russian Federation

2 Kotelnikov Institute of Radio Engineering and Electronics of RAS, Moscow, Russian Federation

References

- [1] Hurd C.M. Varieties of magnetic order in solids. *Contemporary Physics*. 1982;23(5): 469–493. DOI: 10.1080/00107518208237096
- [2] Izyumov Yu. A. Modulated, or long-periodic, magnetic structures of crystals. *Soviet Physics Uspekhi*. 1984;27(11):845–867. DOI: 10.1070/PU1984v027n11ABEH004120
- [3] Tsvirko Yu. A. Properties of coupled magnetoelastic waves in magnets without an inversion center. *Fizika Tverdogo Tela (in Russian)*. 1968;10:3526.
- [4] Nagyar A.H., Sherringtin D. Magnon-phonon interaction in rare-earth metals with helical spin structures. *Journal of Physics F: Metal Physics*. 1972;2(5):893. DOI: 10.1088/0305-4608/2/5/013
- [5] Vlasov K.B., Bar'yakhtar V.G., Stephanovskii E.P. Propagation of sound waves in magnetically ordered crystals with a spiral magnetic structure. *Physics of the Solid State (in Russian)*. 1973;15:3656.
- [6] Vlasov K.B., Smorodinskii I.G. Elastic waves in magnetic materials with a conical spiral magnetic structure. *The Physics of Metals and Metallography (in Russian)*. 1978;45:903.
- [7] Buchelnikov V.D., Shavrov V.G. Magnetoelastic waves in helical magnetic materials. *Physics of the Solid State (in Russian)*. 1988;30:1167.
- [8] Buchelnikov V.D., Shavrov V.G. Magnetoelastic waves in crystals with a helical magnetic structure. *Physics of the Solid State (in Russian)*. 1989;31:81.
- [9] Akhiezer A.I., Bar'yakhtar V.G., Peletminskii S.V. *Spin Waves*. Amsterdam: Interscience (Wiley); 1968. 369 p.
- [10] Stern E.A., Callen E.R. Helicons and magnons in magnetically ordered conductors. *Physical Review*. 1963;131:512.
- [11] Blank Ya A. Electromagnetic waves in a metal under conditions of ferromagnetic resonance. *Soviet Physics JETP*. 1965;20(1):216–222.
- [12] Spector, H.N., Cfsselman T.N. Interaction of Alfvén waves and spin waves in a ferromagnetic metal. *Physical Review*. 1965;139:A1594.
- [13] Bar'yakhtar V.G., Savchenko M.A., Stepanov K.N. Interaction of plasma and spin waves in ferromagnetic semiconductors and metals. *Soviet Physics JETP*. 1966;23(3): 383–390.
- [14] Tyurnev V.V., Erukhimov M.S.H. Effect of absorption of light on the quadratic magneto-optical effects in media with a spiral magnetic structure. *Physics of the Solid State (in Russian)*. 1976;18:1635.
- [15] Sementsov D.I., Morozov A.M. Magneto-optical interaction of light with the structure of the "ferromagnetic helicoid" . *Fizika Tverdogo Tela (in Russian)*. 1978;20:2591.

- [16] Sementsov D.I. Features of light propagation in helical magnetic structures. *Optics and Spectroscopy* (in Russian). 1981;56:37.
- [17] Manzhos I.V., Chupis I.E. Electromagnetic-spin waves in crystals with a simple spiral magnetic structure. *Low Temperature Physics* (in Russian). 1988;14:606.
- [18] Buchelnikov V.D., Bychkov I.V., Shavrov V.G. Coupled magnetoelastic and electromagnetic waves in uniaxial crystals having spiral magnetic structure. *Journal of Magnetism and Magnetic Materials*. 1993;118(1–2):169–174. DOI: 10.1016/0304-8853(93)90173-Y
- [19] Welsh G.H., Wynne K. Generation of ultrafast terahertz radiation pulses on metallic nanostructured surfaces. *Optics Express*. 2009;17(4):2470–2480. DOI: 10.1364/OE.17.002470
- [20] Welsh G.H., Hunt N.T., Wynne K. Terahertz-pulse emission through laser excitation of surface plasmons in a metal grating. *Physical Review Letters*. 2007;98:026803. DOI: 10.1103/PhysRevLett.98.026803
- [21] Gladun A.D., Leiman V.G., Arsenin A.V. On the mechanism of generation of terahertz electromagnetic radiation upon irradiation of a nanostructured metal surface by femtosecond laser pulses. *Quantum Electronics*. 2007;37(12):1166–1168. DOI: 10.1070/QE2007v037n12ABEH013618
- [22] Nishitani J., Kozuki K., Nagashima T., Hangyo M. Terahertz radiation from coherent antiferromagnetic magnons excited by femtosecond laser pulses. *Applied Physics Letters*. 2010;96(22):221906. DOI: 10.1063/1.3436635
- [23] Rungsawang R., Perez F., Oustinov D., Gómez J., Kolkovsky V., Karczewski G., et al. Terahertz radiation from magnetic excitations in diluted magnetic semiconductors. *Physical Review Letters*. 2013;110(17):177203. DOI: 10.1103/PhysRevLett.110.177203
- [24] Bychkov I., Kuzmin D., Kalenov D., Kamantsev A., Koledov V., Kuchin D., et al. Electromagnetic waves generation in Ni₂14Mn0.81GaFe0.05 Heusler alloy at structural phase transition. *Acta Physica Polonica A*. 2015;127(2):588–590. DOI: 10.12693/APhysPolA.127.588
- [25] Kimura T., Goto T., Shintani H., Ishizaka K., Arima T., Tokura Y. Magnetic control of ferroelectric polarization. *Nature*. 2003;426:55–58. DOI: 10.1038/nature02018
- [26] Hur N., Park S., Sharma P.A., Ahn J.S., Guha S., Cheong S.W. Electric polarization reversal and memory in a multiferroic material induced by magnetic fields. *Nature*. 2004;429:392–395. DOI: 10.1038/nature02572
- [27] Bychkov I.V., Kuzmin D.A., Lamekhov S.J., Shavrov V.G. Magnetolectric susceptibility tensor of multiferroic TbMnO₃ with cycloidal antiferromagnetic structure in external field. *Journal of Applied Physics*. 2013;113:17C726. DOI: 10.1063/1.4798820
- [28] Bychkov I.V., Kuzmin D.A., Shavrov V.G. Spectrum of coupled waves in orthorhombic multiferroics with cycloidal antiferromagnetic structure in external electric and

- magnetic fields. *IEEE Transactions on Magnetics*. 2013;49(8):4695–4698. DOI: 10.1109/TMAG.2013.2261055
- [29] Buchelnikov V.D., Bychkov I.V., Kuzmin D.A., Lamekhov S.J., Shavrov V.G. Reflecting electromagnetic waves from a surface of TbMnO_3 with sinusoidal antiferromagnetic structure. *Bulletin of the Russian Academy of Sciences: Physics*. 2013;77(9):1120–1122. DOI: 10.3103/S1062873813090062
- [30] Bychkov I.V., Kuz'min D.A., Shadrin V.V., Sharov V.G. Electromagnetic waves reflected from the plate of a magnetic with a ferromagnetic spiral. *Bulletin of the Russian Academy of Sciences: Physics*. 2012;76(3):368–371. DOI: 10.3103/S1062873812030070
- [31] Bychkov I.V., Buchelnikov V.D., Kuzmin D.A., Shadrin V.V. Spectrum of the coupled waves in magnetics having the ferromagnetic spiral. *Solid State Phenomena*. 2012;190:257–260. DOI: 10.4028/www.scientific.net/SSP.190.257
- [32] Bychkov I.V., Kuzmin D.A., Sharov V.G. Coupled spin, elastic, and electromagnetic waves in the magnetic of a ferromagnetic spiral phase. *Bulletin of the Russian Academy of Sciences: Physics*. 2013;77(3):278–280. DOI: 10.3103/S1062873813030076
- [33] Bychkov I.V., Kuzmin D.A., Shavrov V.G. Hybridization of electromagnetic, spin and acoustic waves in magnetic having conical spiral ferromagnetic order. *Journal of Magnetism and Magnetic Materials*. 2013;329:142–145. DOI: 10.1016/j.jmmm.2012.10.021
- [34] Beille J., Voiron J., Roth M. Long period helimagnetism in the cubic B20 $\text{Fe}_x\text{Co}_{1-x}\text{Si}$ and $\text{Co}_x\text{Mn}_{1-x}\text{Si}$ alloys. *Solid State Communications*. 1983;47(5):399–402. DOI: 10.1016/0038-1098(83)90928-6
- [35] Lebech B., Bernhard J., Freltoft T. Magnetic structures of cubic FeGe studied by small-angle neutron scattering. *Journal of Physics: Condensed Matter*. 1989;1(35):6105–6122. DOI: 10.1088/0953-8984/1/35/010
- [36] Ishikawa Y., Tajima K., Bloch D., Roth M. Helical spin structure in manganese silicide MnSi. *Solid State Communications*. 1976;19(6):525–528. DOI: 10.1016/0038-1098(76)90057-0
- [37] McMorro D.F., Jehan D.A., Cowley R.A., Eccleston R.S., McIntyre G.J. On the magnetic phase diagram of erbium in a *c* axis magnetic field. *Journal of Physics: Condensed Matter*. 1992;4(44):8599. DOI: 10.1088/0953-8984/4/44/021
- [38] Bychkov I.V., Kuzmin D.A., Kamantsev A.P., Koledov V.V., Shavrov V.G. Waves generation by spiral magnets at phase transitions. *Materials Science Forum*. 2016;845:185–188. DOI: 10.4028/www.scientific.net/MSF.845.185
- [39] Bychkov I.V., Kuzmin D.A., Kamantsev A.P., Koledov V.V., Shavrov V.G. Magnetostrictive hypersound generation by spiral magnets in the vicinity of magnetic field

induced phase transition. *Journal of Magnetism and Magnetic Materials*. 2016. DOI: 10.1016/j.jmmm.2016.05.060

- [40] Tikhonov A.N., Samarskii A.A. *Equations of Mathematical Physics*. Oxford: Pergamon Press; 1963.
- [41] Tucker J.W., Rampton V.W. *Microwave Ultrasonics in Solid State Physics*. Amsterdam: North-Holland Publishing Company; 1972. 418 p.

Giant Magnetoimpedance Effect and AC Magnetic Susceptibility in Amorphous Alloys System of FeCoNbBSiCu

Zulia Isabel Caamaño De Ávila,
Amilkar José Orozco Galán and
Andrés Rosales-Rivera

Additional information is available at the end of the chapter

<http://dx.doi.org/10.5772/63024>

Abstract

The study of Giant Magnetoimpedance (GMI) effect of the amorphous alloys system of $\text{Fe}_{72-x}\text{Co}_x\text{Nb}_6\text{B}_{10}\text{Si}_{11}\text{Cu}_1$ (for $x = 35$ and $x = 40$ at. percent Co) and AC magnetic susceptibility for the amorphous alloy of $\text{Fe}_{37}\text{Co}_{35}\text{Nb}_6\text{B}_{11}\text{Si}_{10}\text{Cu}_1$ composition are presented in this chapter. The importance of GMI effect for the improvement of technological applications in sensor devices in amorphous magnetic Fe- and Co-based alloys is introduced; then it is described as the experimental procedure of magnetoimpedance and AC magnetic susceptibility measurements. The obtained results are discussed and finally the conclusions are presented.

Keywords: amorphous, soft magnetic alloys, magnetoimpedance, magnetic susceptibility, amorphous magnetic alloys

1. Introduction

Over the last decades, there has been a growing interest in research on amorphous soft magnetic materials, mainly because they present superior soft magnetic properties, which allowed the development of improved technological applications such as transformer cores, magnetic field sensors, motors, generators, electric vehicles, etc. [1, 2]. The current trend of this kind of materials is their use at high temperatures and high frequencies, for example, in high-frequency power electronics components and power conditioning systems [2].

More recently, the development of high-performance magnetic sensors has promoted the study of interesting magnetic phenomena such as Giant Magnetoimpedance (GMI) and AC Magnetic Susceptibility, in metal-based amorphous alloys.

The Magnetoimpedance (MI) effect has paid more attention in scientific community not only for its applications in sensors devices, especially for low-field detection [3], but also because it has constituted in a useful tool to investigate the magnetism physics.

The MI effect corresponds to the change of the real and imaginary components of electrical impedance $Z = R + iX$ of a ferromagnetic conductor caused by the action of an external static magnetic field [3], being R the Resistance and X the inductance.

The GMI effect consists of large changes in impedance when the materials are subjected to external DC magnetic field and it has been efficiently explained in the terms of classical electrodynamics through the influence of magnetic field on penetration depth of electrical current flowing through the soft magnetic material [4].

The GMI effect is expressed by:

$$\frac{\Delta Z}{Z} = \frac{Z(H) - Z(H_{\max})}{Z(H_{\max})} \times 100 \quad (1)$$

where $Z(H)$ is the impedance of the material in absence of the DC magnetic field and $Z(H_{\max})$ is the impedance at maximum DC field. H_{\max} is usually the external magnetic field sufficient to saturate the impedance [4].

In the case of amorphous ribbon, the skin depth, δ , is given by:

$$\delta = \sqrt{\frac{1}{\pi\mu\sigma f}} \quad (2)$$

where σ is the electrical conductivity, f the frequency of the AC current along the sample, and μ is the transverse permeability of the magnetic ribbon. The DC applied field changes the skin depth through the modification of μ which finally results in a change of the impedance [4].

The GMI effect was investigated for the first time in amorphous ribbons FeCoSiB based on their possible applications in the manufacture of magnetic sensors [5]. Subsequently, it was investigated in $\text{Co}_{70.4}\text{Fe}_{4.6}\text{Si}_{15}\text{B}_{10}$ amorphous ribbons [6] and $\text{Co}_{68.1}\text{Fe}_{4.4}\text{Si}_{12.5}\text{B}_{15}$ amorphous wires [7]. However, in 1994 the GMI effect was discovered in soft magnetic amorphous wires [8]. Since then, there have been numerous studies on the GMI effect in a wide variety of amorphous magnetic alloys in ribbons [1–4, 9–13], wires and microwires [1, 14], and films form [1, 3].

In the same way, AC magnetic susceptibility has been mainly studied for Co-based alloys in wire form [15, 16] and thin films [17]. Also, magnetic susceptibility studies of amorphous and nanocrystalline $\text{Fe}_{44.5}\text{Co}_{44.5}\text{Zr}_7\text{B}_4$ ribbons of 5 cm length and 2 mm width, have been reported

in [18]; however, it has been reported little in the literature about AC magnetic susceptibility in (FeCo)NbBSiCu amorphous alloys.

The magnetic susceptibility is the magnetization degree of a material in response to an applied magnetic field. The susceptibility χ is defined by the following expression:

$$\chi = M / H \quad (3)$$

where M is the magnetization and H is the applied DC magnetic field.

Similarly, AC susceptibility measurement involves an application of a varying magnetic field H_{ac} to a sample.

$$\chi_{AC} = \frac{dM}{dH_{AC}} \quad (4)$$

In the AC measurement, the magnetic moment of the sample is changing in response to an applied AC magnetic field. Therefore, the dynamics of the magnetic system, as the frequency dependence of the complex susceptibility can be studied. Then it is possible to obtain information about relaxation processes and the relaxation times of the magnetic system [19].

The used inductive method for magnetic susceptibility measurements do not need currents or voltages leads; an entire sample volume can be measured and therefore it can provide a volume average of the sample's magnetic response [19]. Hence, inhomogeneous systems as amorphous ribbons can be studied.

The measurement of AC susceptibility can provide important information about AC losses in polycrystalline high-Tc superconductors. In particular, the loss component or imaginary part of the complex susceptibility can be used to probe the nature of the coupling between grains. Also, ac susceptibility can be used to find the transition temperatures of inter- and intergranular regions, as in new granular oxides [19].

GMI and AC magnetic susceptibility are actually opening a new branch of research combining the micromagnetics of soft magnets with the classical electrodynamics.

This chapter presents the results of the GMI effect of amorphous alloys system of (Fe_{72-x}Co_x)Nb₆B₁₀Si₁₁Cu₁ (for $x = 35$ and $x = 40$ at. percent Co) and AC magnetic susceptibility for the amorphous alloy of Fe₃₇Co₃₅Nb₆B₁₁Si₁₀Cu₁ composition.

2. Experimental procedure

Amorphous ribbons were prepared by the melt-spinning technique. GMI effect measurements of the samples were performed on an electric impedance analyzer equipment, using a frequency range of the current applied from 0.5 to 20 MHz and with a magnetic field applied

parallel to the sample, in a range from -80 to 80 Oe. Amorphous ribbons of 7 cm long and 1.1 mm wide were used for the GMI measurements.

AC magnetic susceptibility measurements were performed on an AC susceptometer, using a frequency range between 10 Hz and 5 kHz and sample lengths between 0.4 and 1 cm, with a constant amplitude of about 1 Vrms. The magnetic field was varied from -74 to 74 Oe. The variation of the external magnetic field (H_{AC}) for each frequency was carried out in three stages: from 0 to 74 Oe, 74 – 74 Oe, and -74 to 74 Oe with a step of 1 Oe.

3. Results and discussion

3.1. Giant magnetoimpedance effect (GMI)

In **Figure 1**, the results of the GMI effect for the alloy of composition $\text{Fe}_{37}\text{Co}_{35}\text{Nb}_6\text{B}_{10}\text{Si}_{11}\text{Cu}_1$ ($x = 35$) are presented. It shows the dependence of the change ratio in total impedance, resistance, and reactance in the frequency range of 0.5 – 20 MHz. It obtains a maximum change ratio of 10.3% for the total impedance, 22.7% for the resistance, and 21.6% for the reactance [13].

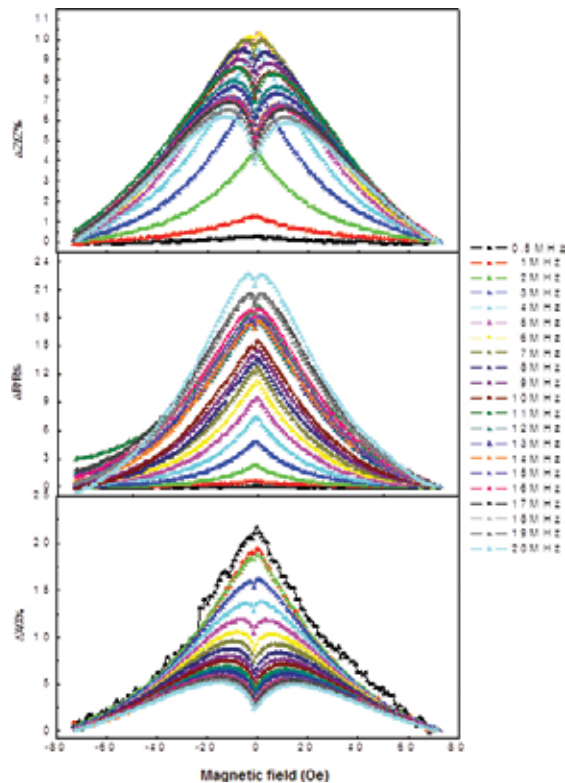


Figure 1. Change ratio in the total impedance $\Delta Z/Z$, the resistance $\Delta R/R$ and in the reactance $\Delta X/X$, as a function of the magnetic field for the amorphous alloy composition $x = 35$ at different frequencies.

The GMI spectra obtained in a frequency range 1–20 MHz for the alloy composition $\text{Fe}_{32}\text{Co}_{40}\text{Nb}_6\text{B}_{11}\text{Si}_{10}\text{Cu}_1$ ($x = 40$) are shown in **Figure 2**.

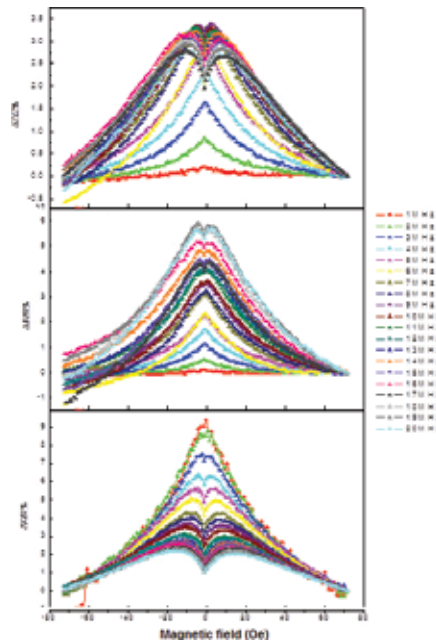


Figure 2. Change ratio in the total impedance $\Delta Z/Z$, the resistance $\Delta R/R$ and the reactance $\Delta X/X$, as a function of the magnetic field for the amorphous alloy composition $x = 40$ at different frequencies [13].

It obtains a maximum change ratio of 3.4% for the total impedance, 5.9% for the resistance, and 9.4% for the reactance [13].

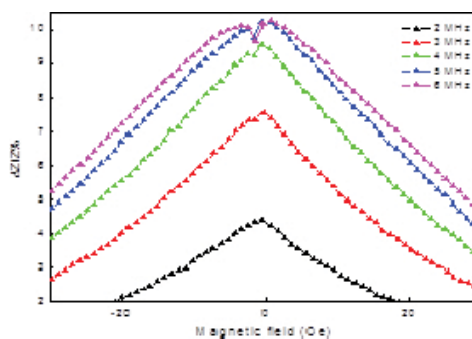


Figure 3. Change ratio of the magnetoimpedance versus magnetic field for the alloy composition $x = 35$ in a frequency range from 2 MHz to 6 MHz.

Figure 3 shows the change MI ratio for frequency range of 2–6 MHz. From the figure, it is observed that the change MI ratio present one peak behavior up to the frequency of 2 MHz;

above this frequency a double peak can be seen. The maximum change MI ratio, $(\Delta Z/Z)_{\max}$, reaches a maximum value in 6 MHz, which is the relaxation frequency, f_x , for this alloy [13].

For the alloy $x = 40$, a double peak is observed above the frequency of 4 MHz, as it can be seen in **Figure 4**. The value of the frequency where the maximum change ratio in the magnetoimpedance reaches is 9 MHz; this is the relaxation frequency for this sample [13].

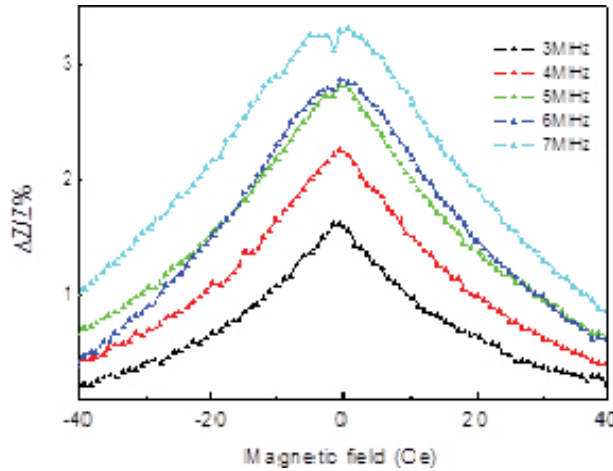


Figure 4. Change ratio of the magnetoimpedance versus magnetic field for the alloy of composition $x = 40$ in a frequency range from 3 MHz to 7 MHz.

The **Table 1** [13] shows the results of the GMI spectra for the alloys of study.

Composition (at. % Co)	$(\Delta Z/Z)_{\max}$ (%)	$(\Delta R/R)_{\max}$ (%)	$(X/X)_{\max}$ (%)	f_x (MHz)
$x = 35$	10.3	22.7	21.7	6
$x = 40$	3.4	5.9	9.4	9

Table 1. Maximum change ratio in the impedance, $(\Delta Z/Z)_{\max}$, in the resistance, $(\Delta R/R)_{\max}$, in the reactance, $(X/X)_{\max}$, and relaxation frequency, f_x , for the amorphous alloys system of $\text{Fe}_{72-x}\text{Co}_x\text{Nb}_6\text{B}_{11}\text{Si}_{10}\text{Cu}_1$.

MI ratio was calculated by the Equation (1):

$$\text{MI ratio} = \frac{\Delta Z}{Z(H_{\max})} \times 100 = \frac{Z(H) - Z(H_{\max})}{Z(H_{\max})} \times 100 \quad (5)$$

where $Z(H)$ is the impedance of the amorphous ribbon in absence of the DC magnetic field and $Z(H_{\max})$ is the impedance at maximum DC field.

The two peak behavior in the spectra of GMI for each composition is due to the rotation of the magnetization produced by the AC current across the ribbon, as it was reported in [12, 20].

The difference between the values of MI for each sample can be due to the modification of the magnetic structure of the material [12], when Fe atoms are substituted by Co atoms, affecting the magnetic permeability and consequently, the impedance of the material.

By the other hand, as it can be seen from the table, the values of the maximum change ratio in the magnetoimpedance for the alloys are very small in comparison with the obtained value (~30%) for the amorphous ribbon of composition $\text{Co}_{64}\text{Fe}_{21}\text{B}_{11}$ reported by Coisson in [21]. Even, it has reported changes in the magnetoimpedance up to 250% for amorphous wires of composition $(\text{Fe}_6\text{Co}_{94})_{72.5}\text{Si}_{12.5}\text{B}_{15}$ [22] and about 50% for amorphous microwires of composition $\text{Fe}_{4.5}\text{Co}_{80}\text{Si}_{10}\text{B}_{1.5}\text{Nb}_4$ [12].

Low values in the percentage change in Z , $(\Delta Z/Z)(\%)$, as a function of H_{dc} at a representative frequency of 2 MHz, were obtained for amorphous ribbons of $\text{Fe}_{68.5}\text{Si}_{18.5}\text{Cu}_1\text{Nb}_3\text{B}_9$ as it was reported by Trilochan Sahoo et al. in [10]. The obtained low values are believed to be related to the magnetostriction effect [10]. The MI effect is also closely related to the magnetic domain structure as well. The domain wall motion contributes to the change in transverse magnetic permeability during the interaction between exciting magnetic field produced by the alternating current flowing across the ribbon axis and the longitudinally applied dc magnetic field. The domain wall motion occurs in different directions and its net effect on transverse permeability is very low. This leads to very low values of $(\Delta Z/Z)$, as it was explained in [10].

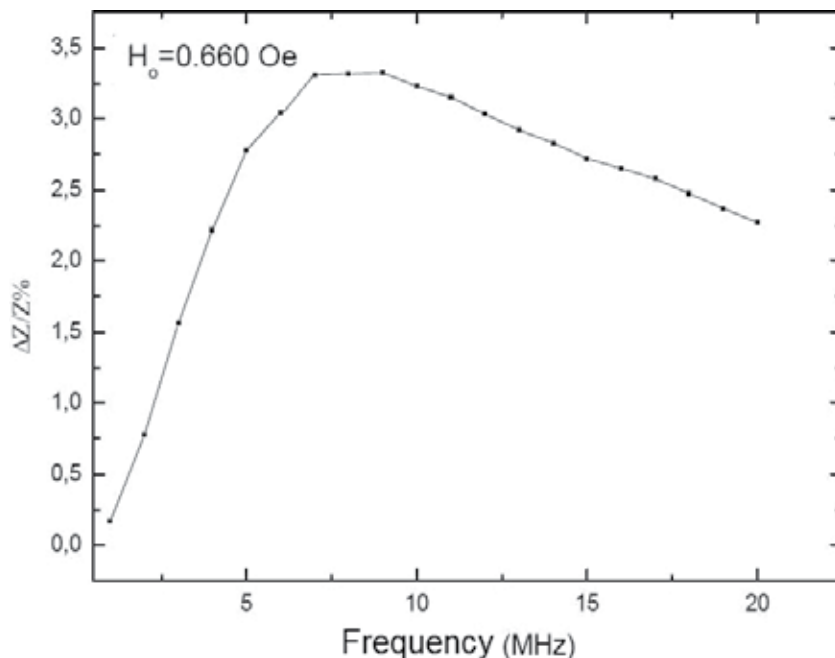


Figure 5. Change ratio of the magnetoimpedance versus frequency for the alloy composition $x = 35$ at DC field $H_c = 0.660$ Oe.

The behavior of the change ratio in the magnetoimpedance as a function of frequency for each alloy composition at constant magnetic field of 0.66 Oe is shown in **Figure 5** and **Figure 6**.

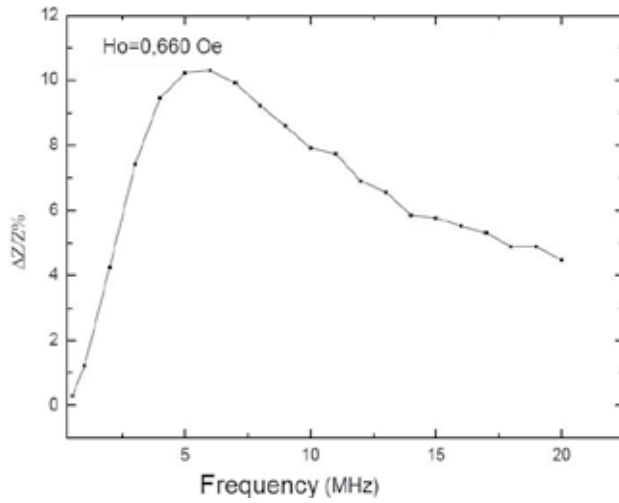


Figure 6. Change ratio of the magnetoimpedance versus frequency for the alloy composition $x = 40$ at DC field $H_c = 0.660$ Oe.

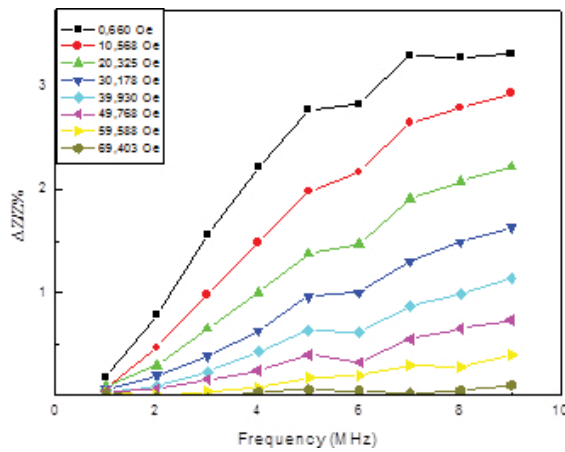


Figure 7. Change ratio of the magnetoimpedance versus frequency for the alloy composition $x = 40$ at DC field from 0.660 Oe until 69.403 Oe.

From these figures, it is observed that the change in the MI increases until to the relaxation frequency corresponding to each composition, and then it diminishes when frequency increases. The increasing in the change MI ratios up to the relaxation frequency is due to the electromagnetic skin effect, as it was reported by Rahman in [23]. However, the decreasing of the change MI ratio above the relaxation frequency is related with the decreasing of the

effective permeability, which is caused by the damping in the movement of the domain walls [12].

Figure 7 illustrates the change MI ratio in the frequency range 1–9 MHz, at constant magnetic fields for the alloy of composition $x = 40$.

It can be noted from the figure that the change ratio of MI decreases when the applied magnetic field is increased in the respective frequencies range. Similar behavior was observed for the alloy composition of $x = 35$ (see **Figure 8**).

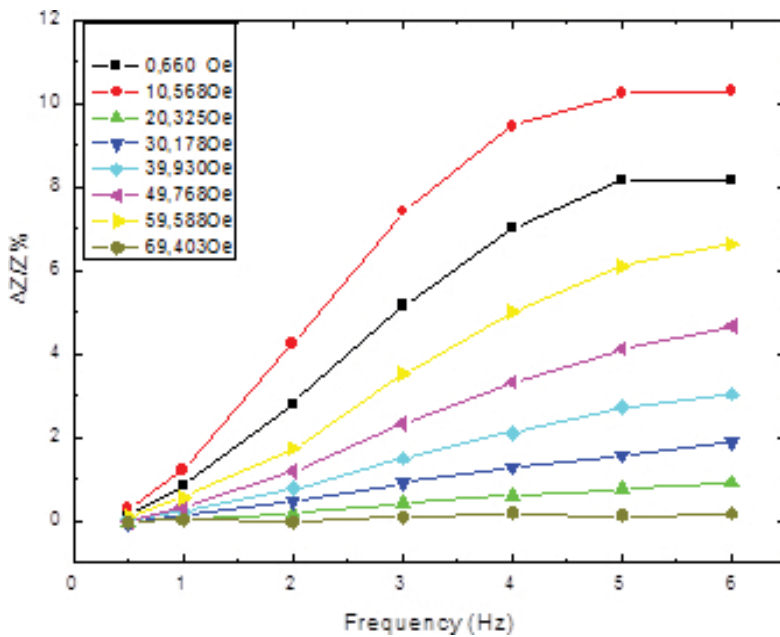


Figure 8. Change ratio of the magnetoimpedance versus frequency for the alloy composition of $x = 35$ at DC field from 0.660 Oe until 69.403 Oe.

3.2. AC Magnetic susceptibility measurements

Figure 9 shows (a) real and imaginary (b) components, χ'_{AC} and χ''_{AC} , of the AC magnetic susceptibility as a function of the applied magnetic field, for the $\text{Fe}_{37}\text{Co}_{35}\text{Nb}_6\text{B}_{11}\text{Si}_{10}\text{Cu}_1$ alloy at a frequency of 40 Hz at room temperature. From the figure, it is observed that the real and imaginary AC susceptibility decreases with increasing magnetic field, both the negative and positive side. A peak at zero magnetic field, corresponding to the maximum value of the AC magnetic susceptibility, is observed.

The continuous decrease of the susceptibility as the magnetic field increase, showing a maximum value at $H = 0$ is the result of the magnetization processes attributed to the domain walls movement, as it was indicated by O. Moscoso [15].

By the other side, the χ''_{AC} imaginary part of the AC magnetic susceptibility, allows to get information about energy losses in magnetization processes. It could be considered that the narrower peak observed in the χ''_{AC} imaginary part is due to the minimum energy loss, which is characteristic of soft magnetic materials and it is associated with the domain walls motion freedom in the material.

The AC magnetic susceptibility dependence on frequency and length of the sample is shown in **Figure 10**. It can be seen that the real AC magnetic susceptibility tends to widen as the frequency increases in **Figure 10(a)**, indicating the strong dependence of AC magnetic susceptibility on frequency, also demonstrating the minimum energy costs in the magnetization processes for this type of system.

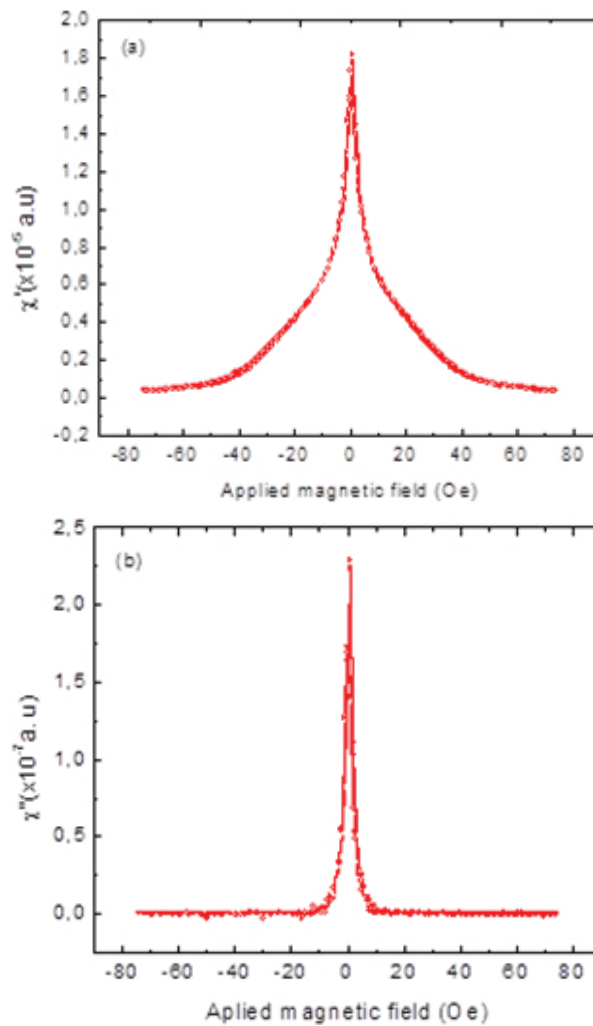


Figure 9. Real AC susceptibility (a) and imaginary AC susceptibility (b) versus applied magnetic field at 40 Hz [24].

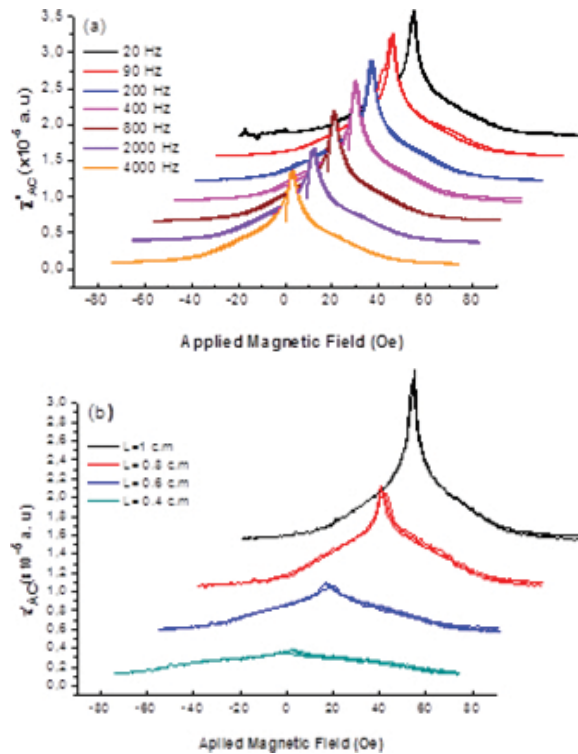


Figure 10. (a) Real part of AC magnetic susceptibility versus external magnetic field at different frequencies and (b) at different lengths of the amorphous alloy of $\text{Fe}_{37}\text{Co}_{33}\text{Nb}_6\text{B}_{11}\text{Si}_{10}\text{Cu}_1$ composition [24].

In **Figure 10(b)** is shown the AC magnetic susceptibility dependence on length of the sample. It can be seen that the AC magnetic susceptibility response enhances as the sample length increases, which is characterized by the emergence of a peak in susceptibility as the length of the sample increases, being more defined for the sample of 1 cm length. This behavior can be due to a possible magnetic hardening of the sample when the length is decreased. The magnetic domain configuration is strongly influenced by the demagnetizing field, because there is an increase in the demagnetization factor along the direction of the sample when the length is reduced; as it was explained by L. Goncalves et al. [16] for alloys of composition $\text{Co}_{70}\text{Fe}_5\text{Si}_{15}\text{B}_{10}$.

4. Conclusions

From the measurements of GMI effect of amorphous alloys system of $\text{Fe}_{72-x}\text{Co}_x\text{Nb}_6\text{B}_{11}\text{Si}_{10}\text{Cu}_1$ ($x = 35$ and 40 at. percent Co) is concluded:

1. The maximum MI ratios obtained for the alloys composition $x = 35$ and $x = 40$ were 10.3% and 3.4%, respectively. The difference between the values obtained can be attributed to the change in the magnetic structure of the material, when replacing Fe by Co, which affects the magnetic permeability and consequently the impedance of the material.

2. The studied amorphous ribbons does not present a “giant” MI effect as the present soft magnetic amorphous alloys such as Finemet- and Co-based alloys reported in literature.
3. The dependence of the MI ratios with the frequency and the applied magnetic field is mainly due to electromagnetic skin effect for low and intermediate frequencies.

From measurements of AC magnetic susceptibility of $\text{Fe}_{37}\text{Co}_{35}\text{Nb}_6\text{B}_{11}\text{Si}_{10}\text{Cu}_1$ amorphous alloy it is concluded that AC magnetic susceptibility depends strongly on the frequency and length of the sample and its response is closely related to a minimum energy loss, which is characteristic for this type of alloys.

Acknowledgements

To the group of Physics of Materials II of the Universidad Autónoma de Barcelona (Bellaterra, Spain), for the collaboration in the preparation of the samples by the melt-spinning technique.

To Universidad del Atlántico (Barranquilla, Colombia) for financial support for the internship of A. Orozco at the Universidad Nacional de Colombia, in Manizales, for AC magnetic susceptibility measurements.

The first author highly appreciates MSc. L. Costa Arzuza for his collaboration in some of the results of GMI effect.

Author details

Zulia Isabel Caamaño De Ávila^{1*}, Amilkar José Orozco Galán¹ and Andrés Rosales-Rivera²

*Address all correspondence to: zuliacaamano@mail.uniatlantico.edu.co

1 Physics Department, Basics Sciences Faculty, Universidad del Atlántico, Barranquilla, Colombia

2 Magnetism and Advanced Materials Laboratory, Exact Sciences and Natural Faculty, Universidad Nacional de Colombia, sede Manizales, Manizales, Colombia

References

- [1] Rajat Roy K, Ashis Panda K and Amitava M. In: Ahmad Z, editor. *New Trends in Alloy Development, Characterization and Application*. Intech (Croatia); 2015. pp. 39–60. DOI: 10.5772/60772.

- [2] Škorvánek I, Marcin J, Capik M, Varga M, Kováč J, Janotova I, Švec P, Idzikowski B. Soft Magnetic Melt-spun Ribbons for Energy and Sensor Applications. *Acta Electro-technica et Informatica*. 2013; 1:45–48. DOI: 10.2478/aei-2013-0009.
- [3] Silva E, Da Silva R, Gamino M, De Andrade A, Vázquez M, Corrêa M, Bohn F. Asymmetric magnetoimpedance effect in ferromagnetic multilayered biphasic films. *J. Magn. Mater.* 2015; 393:260–264.
- [4] Wei Lu, Yewen Xu, Jindan Shi, Yiming Song, Xiang Li. Soft magnetic properties and giant magnetoimpedance effect in thermally annealed amorphous $\text{Co}_{68}\text{Fe}_4\text{Cr}_3\text{Si}_{15}\text{B}_{10}$ alloy ribbons. *J. Alloys Compd.* 2015; 638:233–238.
- [5] Makhotkin V, Shurukhin B, Lopatin V, Marchukov Y, Levin Y. A magnetic field sensor based on rotating amorphous ribbons. *Sens. Actuators A*. 1992; 31:220–222.
- [6] Machado F, Lopes da Silva B, Montarroyos E. Magnetoresistance of the random anisotropic $\text{Co}_{70.4}\text{Fe}_{4.6}\text{Si}_{15}\text{B}_{10}$ alloy. *J. Appl. Phys.* 1993; 73:6387. DOI: 10.1063/1.352659.
- [7] Mandal K and Ghatak S. Large magnetoresistance in an amorphous $\text{Co}_{68.1}\text{Fe}_{4.4}\text{Si}_{12.5}\text{B}_{15}$ ferromagnetic wire. *Phys. Rev. B*. 1993; 47:14233.
- [8] Panina L and Mohri K. Magneto-impedance effect in amorphous wires. *Appl. Phys. Lett.* 1994; 65:1189.
- [9] Béron F, Valenzuela L, Knobel M, Melo L, Pirola K. Hysteretic giant magnetoimpedance effect analyzed by first-order reversal curves. *J. Magn. Mater.* 2012; 324:1601–1605.
- [10] Trilochan Sahoo, Majumdar B, Srinivas V, Srinivas M, Nath T, Agarwal G. Improved magnetoimpedance and mechanical properties on nanocrystallization of amorphous $\text{Fe}_{68.5}\text{Si}_{18.5}\text{Cu}_1\text{Nb}_3\text{B}_9$ ribbons. *J. Magn. Mater.* 2013; 343:13–20.
- [11] Ganesh Kotagiri and Markandeyulu G. Magnetoimpedance studies on as-quenched $\text{Fe}_{66-x}\text{Co}_x\text{Ni}_7\text{Si}_7\text{B}_{20}$ ($x=0, 33$ and 66) ribbons. *Physica B*. 2014; 448:20–23.
- [12] Rosales-Rivera A., Valencia, V. H, Pineda-Gómez P. Three-peak behavior in giant magnetoimpedance effect in $\text{Fe}_{73.5-x}\text{Cr}_x\text{Nb}_3\text{Cu}_1\text{Si}_{13.5}\text{B}_9$ amorphous ribbons. *Physica B*. 2007; 398:252–255.
- [13] Caamaño Z, Costa L, Rosales A. Giant Magnetoimpedance effect and magnetization in amorphous alloys system of FeCoNbBSiCu. *Rev. Mex. Fis. S.* 2012; 58:35–38.
- [14] Zhukov A, Ipatov M, Blanco J.M, Zhukova V. GMI Effect of Ultra-Soft Magnetic Soft Amorphous Microwires. *Open Mater Sci J.* 2012; 6:39–43.
- [15] Rosales-Rivera A, Moscoso-Londoño O, Muraca D. Magnetization dynamics and magnetic hardening in amorphous FeBSi alloys. *Rev. Mex. Fis. S.* 2012; 58:155–159.
- [16] Goncalves L, Soares J, Machado F, De Azebedo W. *Physica B*. 2006; 384:152–154.

- [17] Chen Yuan-Tsung, Hsieh W.H. Thermal, magnetic, electric, and adhesive properties of amorphous $\text{Co}_{60}\text{Fe}_{20}\text{B}_{20}$ thin films. *J. Alloys Compd.* 2013; 552:283–288.
- [18] Varga M, Varga R, Komova E, Csach K, Vojtanik P. Temperature evolution of magnetic susceptibility during devitrification of Cu-free HITPERM alloy. *J. Magn. Magn. Mater.* 2010; 322:2758-2761.
- [19] Nikolo M. Superconductivity: A guide to alternating current susceptibility measurements and alternating current susceptometer design. *Am. J. Phys.* 1995; 63:57–61.
- [20] Vázquez M, Kurlyandskaya G, Garcia-Benitez J, Sinnecker J. *IEEE Trans. Magn.* 1999; 35:3358–3360.
- [21] Coisson M, Kane S, Tiberto P, Vinai F. Influence of DC Joule-heating treatment on magnetoimpedance effect in amorphous $\text{Co}_{64}\text{Fe}_{21}\text{B}_{15}$ alloy. *J. Magn. Magn. Mater.* 2004; 271:312–317.
- [22] Pal S, Manik N, Mitra A. Dependence of frequency and amplitude of the ac current on the GMI properties of Co based amorphous wires. *Mater. Sci. Eng. A.* 2006; 415:195–201.
- [23] Rahman Z, Kamruzzaman M, Rahman M. A. *J. Mater. Process. Technol.* 2004; 153–154:791–796.
- [24] Orozco A, Caamaño Z, Rosales A. AC magnetic susceptibility and influence of heat treatment on obtaining the nanocrystalline structure for the amorphous alloy of $\text{Fe}_{37}\text{Co}_{35}\text{Nb}_6\text{B}_{11}\text{Si}_{10}\text{Cu}_1$ composition. *JPCS.* 2016; 687:1–4. DOI:10.1088/1742-6596/012109.

Magnetization Statics and Ultrafast Photoinduced Dynamics in Co/garnet Heterostructures

Andrzej Stupakiewicz

Additional information is available at the end of the chapter

<http://dx.doi.org/10.5772/62542>

Abstract

We demonstrate experimental studies of the magnetization behavior from statics to ultrafast photoinduced dynamics with high temporal resolution in ultrathin Co/garnet heterostructures with a sub-nanometer roughness at the interface. We report on modulation of spin precession in Co/garnet heterostructures with distinct frequencies and show that the excitation efficiency of these precessions strongly depends on the amplitude and the direction of external magnetic field. Furthermore, it is shown that the magnetization precession in the garnet film can be manipulated by the strong magneto-static coupling between Co and garnet layers. These findings could provide new possibilities in all-optical excitation and local spin manipulation by polarized femtosecond pulses for the application in nanodevices with high-speed switching.

Keywords: ultrafast magnetization dynamics, magneto-optical effect, magnetization reversal, magnetic anisotropy, magnetic domain structure, photomagnetism, ferromagnetic resonance, garnet, cobalt

1. Introduction

Control of magnetization with the help of femtosecond laser pulses is a hot topic in fundamental science [1–5]. Understanding ultrafast magnetization dynamics on an ultrashort timescale promises to enable technologies based on the quantum-level interplay of nonlinear optics and magnetism. All-optical control of the magnetism in novel magnetic materials is a particularly important issue for further development of faster magnetic information storage/processing and spintronic nanodevices. The thermal effect limits the application of the technology of heat-assisted magnetic recording due to relatively long cooling time (~1 ns) [6]. One of the solu-

tions to this problem can be all-optical nonthermal control of the magnetization. For fundamental research, hybrid structures give the unique possibility to engineer high-quality two-dimensional interfaces and create phenomena which do not exist in a bulk material. On the contrary, new functionalities may emerge from the coexistence of two materials with complementary properties, such as magnetism and ferroelectricity, metallic and dielectric, antiferromagnetic and ferromagnetic, etc.

An interesting combination is formed by a metallic ferromagnetic ultrathin film on top of a dielectric ferrimagnet, based on yttrium iron garnet (YIG) with different substitutions. The functionality of YIG systems has been shown to be very broad, with examples such as the excitation of surface plasmons [7], the propagation of nonlinear spin-waves [8, 9], Bose-Einstein condensation of a magnon gas [10], high-temperature photomagnetism [11], the observation of the inverse Faraday effect induced by an ultrafast laser pulse [12–14], and many others. A combination of a metal layer on a garnet system may create the possibility to modify different properties. Recently, it was reported that ion beam sputtered Fe films on a 100 nm-thick YIG layer possess a perpendicular magnetic anisotropy [15]. In the thickness range between 5 and 10 nm, the stripe domain structure of YIG was transferred into the Fe films due to the presence of strong interlayer exchange coupling [15]. Static and dynamic properties were also investigated for a 30-nm permalloy film on a $0.5 \mu\text{m}$ $(\text{YBiLu})_3(\text{FeAl})_5\text{O}_{12}$ layer that is characterized by a perpendicular anisotropy [16]. A strong direct exchange coupling is revealed via the formation of enlarged closure domains with a preferred orientation at the interface between the permalloy film and the garnet layer. As a result, the domain pattern of such a heterostructure shows an increased zero-field stripe period in comparison to the parent garnet layer [16]. The magnetization reversal process and magnetic domain structure were the focus points of these studies. YIG films with iron partially substituted with Co^{2+} and Co^{3+} ions [17] show interesting magnetic properties, such as several spin-reorientation phase transitions in a temperature range of 20–300 K [18], and both quasistatic [19] and ultrafast [20] light-induced changes in magnetic anisotropy. Light pulses excite large-angle magnetization precession in such garnets, the phase and the amplitude of the precession being determined by the polarization of the light. If coupled with a nanostructure ferromagnetic (metallic) overlayer, such photomagnetic effects in the garnet may also be transferred to the overlayer, thus creating new possibilities for ultrafast switching.

For instance, it is known for a metal/dielectric heterostructure that spin-orbital interaction may initiate a transfer of angular momentum between the layers and thus cause correlations in the magnetization dynamics [21]. Understanding optical control of the magnetism in magnetic heterostructures is a particularly important issue for further development of faster magnetic information storage/processing and spintronic nanodevices. Optical control of spins in Co/SmFeO₃ heterostructures by the X-ray pulse with duration 70 ps has been demonstrated using X-ray photoemission electron microscopy, revealing that the dynamics of the spins in the metallic Co and the dielectric SmFeO₃ are strongly coupled [22]. In the general case, a novel ultrafast magnetization dynamics in ferromagnetic metal/garnet heterostructures can be expected due to the coupling between the ferromagnetic and garnet films and/or the influence of the effective magnetic field of the ferromagnetic metallic film. Using the YIG:Co film in the

ferromagnetic/garnet heterostructures gives unique possibility to investigate light-induced magnetization dynamics at the sub-picosecond timescale.

This chapter describes experimental and theoretical studies of the magnetization behavior from statics to ultrafast light-induced magnetization dynamics in ultrathin 2 nm Co films deposited on Co-substituted yttrium iron garnet thin film. In particular, we demonstrate that ion beam sputtering can be used for the formation of Co/garnet heterostructures. The magnetization reversal process and magnetic anisotropy of the Co/garnet heterostructures are measured by both magneto-optical magnetometry and ferromagnetic resonance (FMR). To investigate the ultrafast magnetization dynamics in both garnet and Co/garnet heterostructure induced by femtosecond laser pulses, we carried out time-resolved measurements at room temperature using a magneto-optical pump-probe method. We demonstrated that the frequency of the spin precession in a Co/garnet bilayer can be modulated by exciting linearly polarized femtosecond pulses. The experimental results presented here were obtained on 2 nm Co/garnet heterostructure, which has a strong magnetostatic interlayer coupling. In this heterostructure, two distinct precession frequencies were observed. One is attributed to the magnetization precession of the 2 nm cobalt and the other to that of the 1.8- μm -thick garnet. The spin oscillation frequencies of the two layers differ by about a factor of two and are strongly dependent on the out-of-plane external magnetic field. We compared magnetization dynamics in the Co and bare garnet films separately via selective probing and showed that magnetization precession in the garnet via the photomagnetic effect can be manipulated by the magnetostatic interlayer coupling. The experimental results are discussed within the phenomenological model.

2. Heterostructure preparation

Initial garnet thin films composed of $\text{Y}_2\text{Ca}_1\text{Fe}_{3.9}\text{Co}_{0.1}\text{Ge}_1\text{O}_{12}$ (YIG:Co) were grown by liquid-phase epitaxy on $\text{Gd}_3\text{Ga}_5\text{O}_{12}$ (GGG) (001)-oriented substrate. The initial thickness of garnet films was 6.5 μm . The initial garnet surface was etching, and Co/YIG:Co heterostructures were formed using the dual ion beam sputtering technique [23] on the base of an A 700 Q Leybold vacuum system. The base pressure was below 8×10^{-6} mbar in the vacuum chamber. The damage-free etching of the garnet films and subsequent deposition of the Co layers were carried out *in situ* at a pressure of 2.5×10^{-4} mbar [24].

Figure 1 illustrates the stage of the heterostructure preparation. The initial garnet film was smoothed to 5.8 μm thickness with a 0.6-keV oxygen ion beam with current density of 0.2 mA/cm², corresponding to the ion flux of $3.2 \times 10^{15} \text{ cm}^{-2} \times \text{s}^{-1}$ [24]. The oxygen ions improve garnet transmittance in the energy range between 0.5 and 1 keV. The garnet films are sputtered at a near-normal incidence angle. At this angle, optimal smoothing of the optical materials (quartz, glass, ceramic) is achieved for up to sub-nanometer roughness [25]. The garnet sputtering rate is about 0.22 $\mu\text{m}/\text{h}$. A final smoothing of the garnet surfaces was completed using a 0.3-keV oxygen ion beam for over 10 minutes. Au and Co targets were sputtered with a 1.5-keV argon ion beam at 0.25 mA/cm² current density [24]. The incident angle of argon ions is 60° with

respect to the target normal, so that the sputtered flux is deposited onto substrate at near-normal incidence angle. The deposition rates of Au and Co are 8.4 and 5.4 nm/min, respectively. A 4-nm Au film was used to protect the 2-nm Co layer before oxidation. For this thickness, the Au film is continuous and exhibits surface roughness close to the substrate of about 0.2 nm [26]. The Co/YIG:Co heterostructures and reference YIG:Co films are prepared onto the same substrate and in the same experimental conditions.

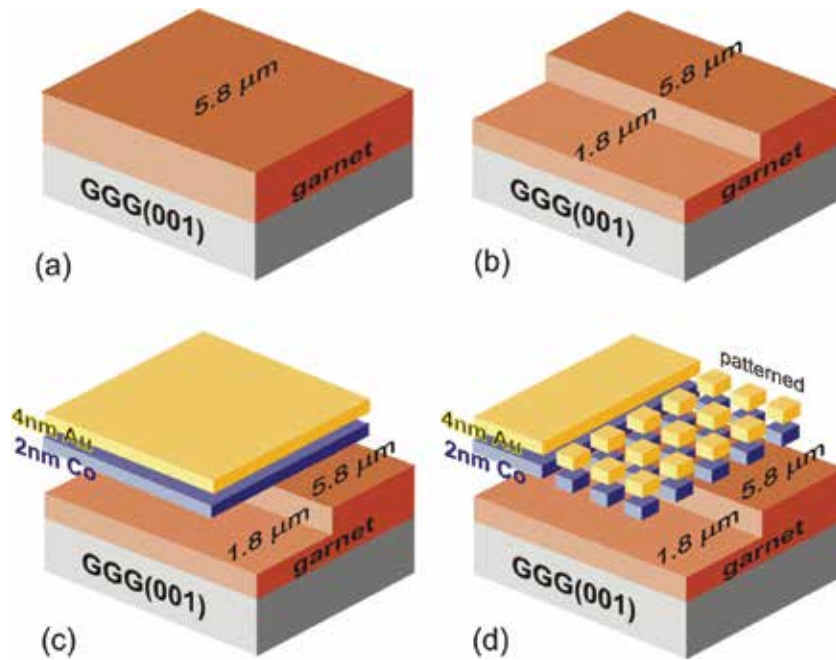


Figure 1. Schematic configuration of the heterostructure during preparation: (a) the YIG:Co film after smoothing from 6.5 μm to 5.8 μm thickness, (b) after ion beam etching to 1.8 μm on the garnet part, (c) after deposition of 4-nm Au/2 nm Co bilayer on the garnet part, and (d) the 20 × 20 μm pattern area on the Co/garnet part.

A 20 × 20 μm Au/Co pattern, for comparison of coupling between Co and garnet films and domain structures modifications on garnets, was fabricated by a lift-off photolithography. The photolithographic process can be represented as follows. In the first step, the garnet film was coated with the light-sensitive chemical photoresist to form a homogeneous layer of about 1 μm thickness. In the second step, the photoresist on garnet surface was exposed through a lithographic mask with high-intensity ultraviolet (UV) radiation. This mask contains the copy of pattern. The 20 × 20 μm windows are opened to the exposing UV light passes through the mask. The dose of UV exposure and the development process were precisely controlled to result in a sharp edge profile of resist patterns. In the third step, the irradiated photoresist area was washed away, leaving the photoresist in the unexposed area. In the fourth step, after deposition of the Au/Co bilayers, a chemical etching was used to remove the previously unexposed photoresist. In such way, the pattern from mask was transferred to the garnet film. As a result, the Co(homogeneous) and Co(pattern)/garnet heterostructures as well as reference

garnet films with discrete thicknesses were prepared onto the same GGG (001) substrate by combining the ion beam processing with photolithographic technique (see **Figure 1**).

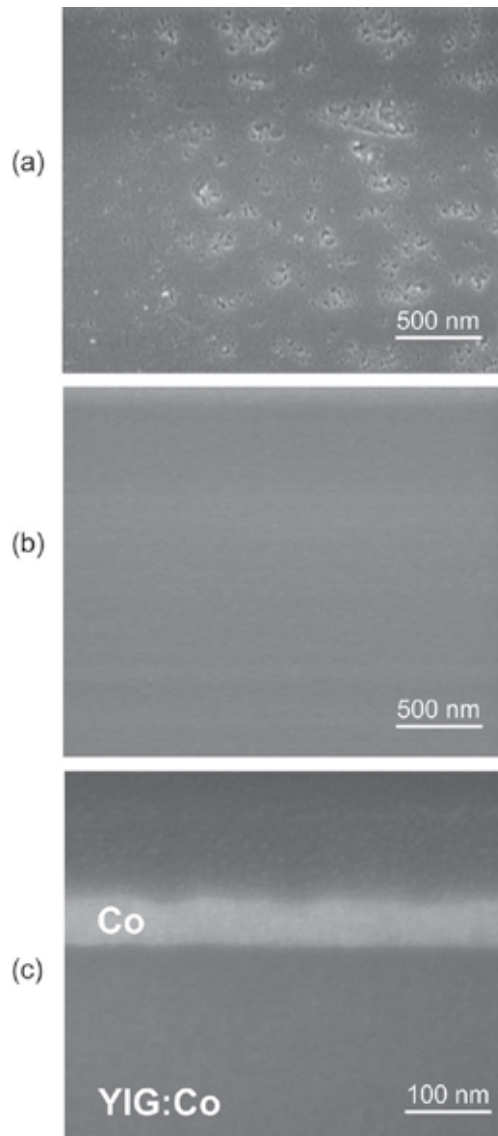


Figure 2. (a) SEM images of the initial 6.5 μm YIG:Co film, (b) 5.8 μm YIG:Co film after etching, of YIG:Co films, and (c) the cross-sectional image of the Co(50nm)/YIG:Co interface .

The surface morphology of both the bare YIG:Co film and Co/YIG:Co heterostructure was measured by high-resolution scanning electron microscopy (SEM) using a FEI's Helios NanoLab DualBeam system. The root mean square (rms) surface roughness was examined by atomic force microscope in tapping mode. The initial garnet surface is rough with protrusions,

while YIG:Co contains troughs of about 100–200 nm in diameter (see **Figure 2(a)**). The ion beam smoothing the garnet surface area showed significantly reduced rms parameters from 3.5 to 0.3 nm after etching the garnet film from 6.5 μm to 5.8 μm (see **Figure 2(b)**). The surface roughness remains approximately the same after ion beam etching down to 1 μm . Ion beam thinning of the garnet film also decreases the rms parameter to 0.25 nm. This is comparable to surfaces of roughness similar to high-quality Si substrate (0.18 nm).

The surfaces of the Co/garnet heterostructures are continuous and exhibit a slightly increased rms parameter from 0.3 to 0.37 nm after the deposition of Au(4nm)/Co(2 nm) bilayer structures on the ion beam-smoothed garnet surfaces. A cross section of the Co/garnet interface was observed using a 30-keV gallium-focused ion beam. The low contrast of the Co(≤ 5 nm)/garnet interfaces results from charge accumulation in the dielectric garnet film. Therefore, only for the SEM image observation, the thickness of the Co layer was increased up to 50 nm for the enhancement of the contrast at the Co/garnet interface. The Co/garnet interface is sharp, and the thickness of the transition layer is thinner than 1–2 nm (see inset of **Figure 2(c)**).

3. Optical and magnetic properties of Co/garnet heterostructures

The optical transmittance, magneto-optical both Kerr (θ_k) and Faraday (θ_f) rotations were performed on Co/YIG:Co heterostructures and reference YIG:Co film using light from a mode-locked Ti-sapphire laser (MaiTai HP, Spectra-Physics) operating within the 400–1040 nm range and a repetition rate of 80 MHz. For the detection of the angle of magneto-optical rotation, a lock-in amplifier was used in combination with a standard modulation technique with a photoelastic modulator.

3.1. Optical and magneto-optical spectra

The investigation of the optical absorption and the Faraday rotation spectra in YIG:Co garnet demonstrated that the contribution of Co ions in octahedral sites is substantially smaller than that of tetrahedral Co ions [27]. Furthermore, the latter can be observed in near-infrared range, where pure YIG is fully transparent. Both an optical transmittance and magneto-optical Faraday rotation spectra for YIG:Co film are shown in **Figure 3**. At wavelengths longer than about 800 nm, the absorption is small and is equal to about 10^2 cm^{-1} (see **Figure 3(b)**). Essentially in the wavelength range of 450–1300 nm, the absorption is caused by crystal field transitions of Fe^{3+} , Co^{2+} , and Co^{3+} ions in both tetrahedral and octahedral sites. The crystal field transitions in octahedral sites have weaker oscillator strength than that the tetrahedral ones. However, at wavelengths shorter than 450 nm, the strong optical absorption of the garnet film is related to charge transfer transitions from oxygen ligands O^{2-} to octahedral Fe^{3+} and Co^{3+} ions. The scheme of crystal field and charge transfer transitions for Co ions (**Figure 3(a)**) was obtained from experimental and theoretical investigations [27, 28]. In a band model, the charge transfer transition is connected with electron excitation from a valence band to conduction ones, which are created by O 2*p* and Fe (Co) 3*d* orbitals, respectively. Although a determination of band gap E_g is difficult owing to the garnets not exhibiting sharp absorption edge, the lowest charge transfer transitions of octahedral Co^{3+} (${}^1\text{A}_1 \rightarrow {}^1\text{T}_2$) ions give $E_g \approx 2.85$ eV. This value agrees well

with the band gap of pure YIG ($E_g = 2.9$ eV). In the general case, the optical absorption is correlated with the magneto-optical Faraday rotation (defined by rotation angle θ_F) (see **Figure 3(c)**). The energy levels of the Co ions do not coincide with the $3d$ levels of the Fe ions. Therefore, the optical excitation of YIG:Co film leads to additional transitions of Co ions as well as affect the Fe^{3+} ion transitions and consequently results in magneto-optical effects with spectral sensitivity.

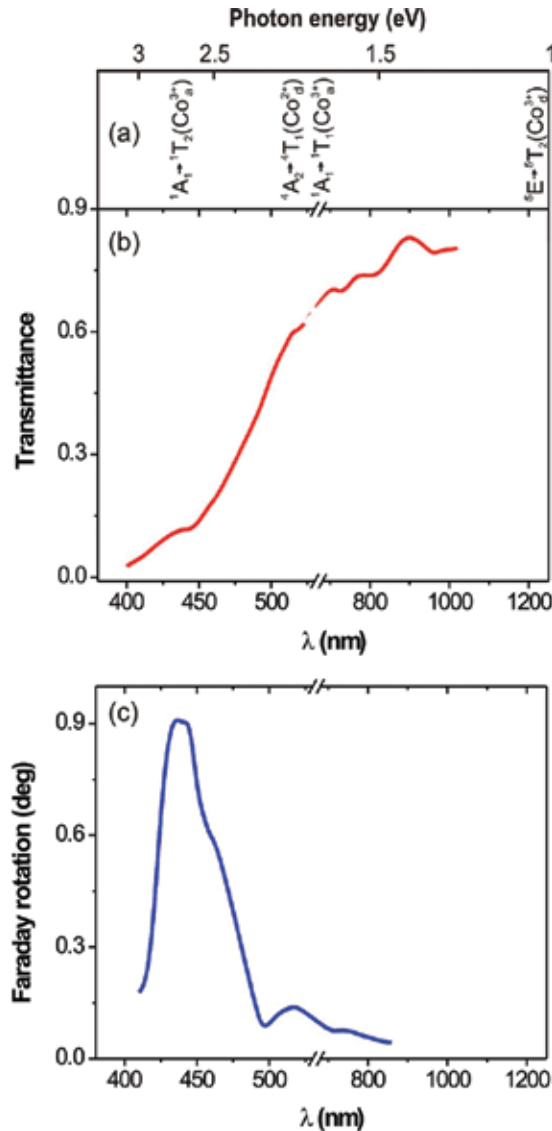


Figure 3. (a) Scheme of crystal field and charge transfer transitions according to Refs. [27, 28], (b) optical transmittance, and (c) magneto-optical Faraday rotation spectra of 1.8 μm YIG:Co film.

The contribution of Co ion transitions to magneto-optical Faraday rotation spectrum is clearly seen by comparison of previously reported spectra for both YIG [29] and YIG:Co films [27]. In our case, for the garnet film, we observed the reduction of θ_F close to the optical transitions of tetrahedral Co^{2+} and Co^{3+} ions as well as octahedral Co^{3+} ones. It is important to note that for different garnet thicknesses and both YIG and YIG:Co films reported, θ_F is practically the same in the wavelength range of 800–900 nm, where no optical transitions of Co ions are expected (see **Figure 3(b)**). This indicates that magnetic anisotropy (induced by the temperature, light, etc.) of the garnet can be modified due to inhomogeneous distribution of Co dopant in the garnet lattice. The contribution of low spin octahedral Co^{3+} ions to magnetic anisotropy is zero in single-ion approximation. Since tetrahedral Co^{2+} and Co^{3+} ions are responsible for growth-induced magnetic anisotropy [30], one can assume that the reduction in garnet thickness leads to a change in the uniaxial anisotropy and thus to a change in the magnetization reversal process. To confirm this, in the next sections we performed investigations of both the magnetic anisotropy and magnetization reversal processes in ultrathin Co layer and garnet thin films.

3.2. Magnetization reversal in static regime

The process of magnetization reversal has been studied at room temperature in reflection with the linear magneto-optic Kerr effect (MOKE) and in transmission with the Faraday effect. From the data, we separated different magneto-optical contributions from the Co layer and garnet-only films. The perpendicular magnetization component of the ultrathin Co layer was measured using the polar MOKE (P-MOKE) geometry, with the angle of incidence of the laser light close to the sample normal and the external magnetic field H_z perpendicular to the surface of the sample (see **Figure 4(a)**). The measurements of the in-plane magnetization components of the Co layer were performed in the longitudinal MOKE (L-MOKE) geometry, with a 49° angle of incidence of the light (see **Figure 5(a)**). The magnetic field H_x was applied in the sample plane for various orientations with respect to the garnet [100] direction. The process of magnetization reversal to the determination of Faraday rotation angle θ_F of the garnet-only films was studied in the magneto-optical Faraday geometry, with perpendicular and in-plane magnetic field orientation (**Figure 4**).

According to the optical absorption spectra in **Figure 3(b)**, Au/Co/garnet heterostructures are transparent enough to be investigated in transmission geometry, for example at 690 nm wavelength. From the experimental curves, we separated the different magneto-optical contributions of the Co layer and garnet films using vector magneto-optical magnetometry and measurements for reference garnet film [31]. The P-MOKE hysteresis loops observed for the 2-nm-thick Co film grown on garnet film indicate an in-plane magnetization of Co (see **Figure 4(c)**). **Figure 4(b)** and **5(b)** show Faraday rotation hysteresis loops measured for garnet film and a perpendicular applied field H_z and an in-plane field H_x , respectively. From the hysteresis loop shown in **Figure 4(b)**, one deduces a Faraday rotation from the garnet layer of about $\theta_F = 0.08$ degrees and a paramagnetic linear contribution from the GGG substrate. For the in-plane applied magnetic field in the garnet [100] direction, the saturating field is about 0.6 kOe (**Figure 5(b)**).

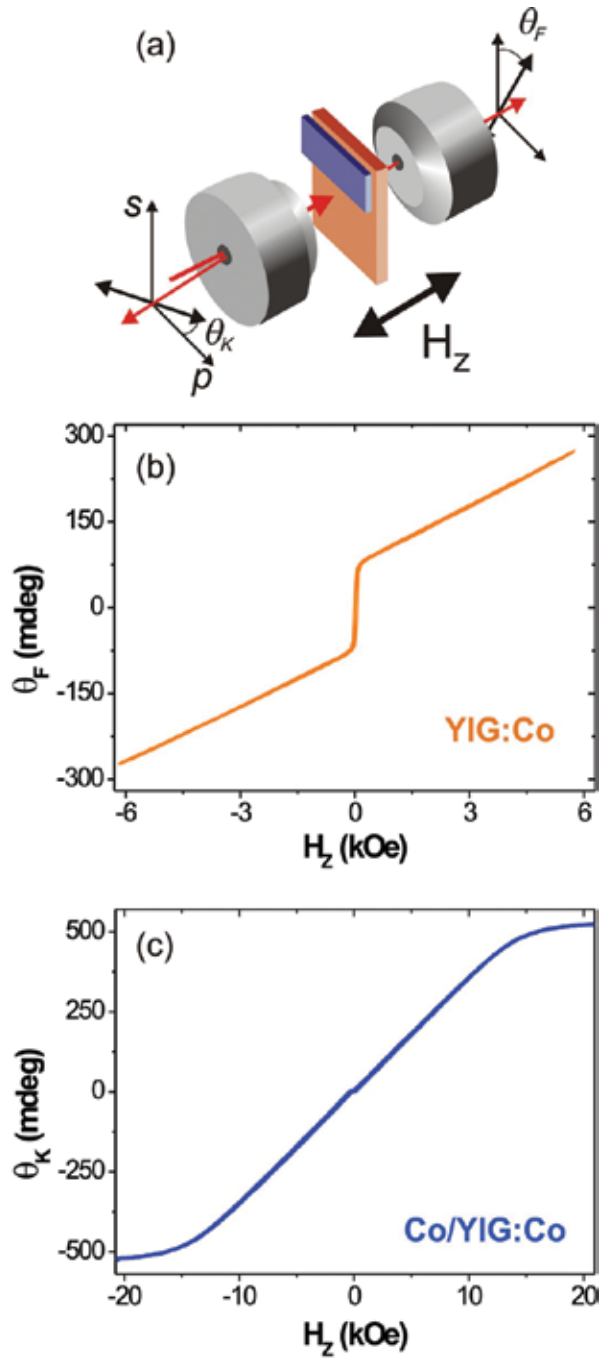


Figure 4. (a) The experimental configuration with Kerr and Faraday effects for perpendicular magnetic field orientation H_z to the sample plane. Hysteresis loops measured for YIG:Co and Co/YIG:Co at 690 nm wavelength in: (b) Faraday and (c) P-MOKE geometries.

The L-MOKE magnetization curve for the Co layer measured with the in-plane external magnetic field H_x are shown in **Figure 5(c)**. From L-MOKE hysteresis loops, the remanence parameter is plotted on inset of **Figure 5(c)** as a function of azimuthal angle ϕ_H . The shape of these loops is practically independent on the azimuthal sample orientation and confirms the “easy plane” type of the magnetic anisotropy with a saturation in-plane field of about 0.3 kOe. To determine magnetic anisotropy of both garnet films and Co layer, we performed FMR measurements at room temperature.

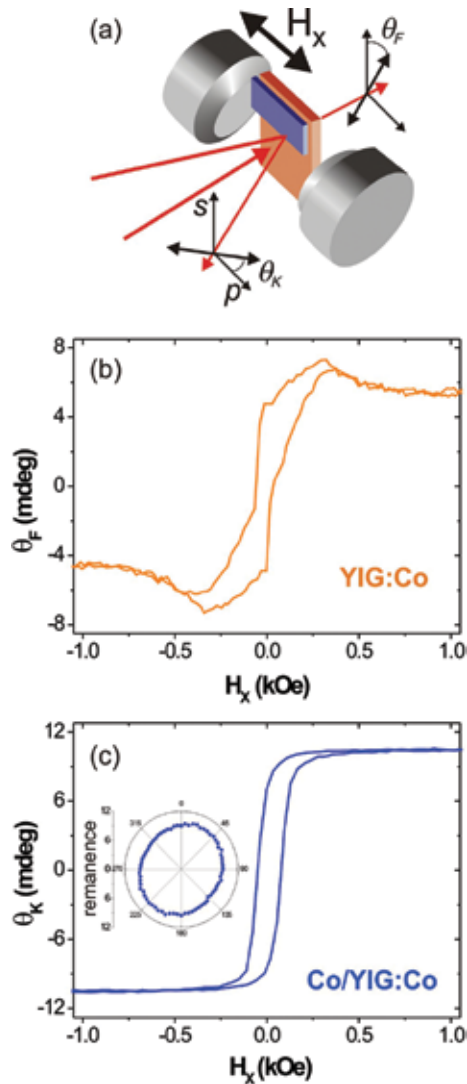


Figure 5. (a) The experimental configuration with Kerr and Faraday effects for sample in-plane magnetic field orientation H_x . Hysteresis loops measured for YIG:Co and Co/YIG:Co at 690 nm wavelength in: (b) Faraday and (c) L-MOKE geometries.

3.3. Magnetic anisotropy study

The typical FMR line measured in the external magnetic field applied to the sample at polar angle $\theta_H = 65^\circ$ is presented in **Figure 6**. The Co layer and garnet film contributions to this FMR line can be clearly seen. The linewidth values of Co and garnet films are different. The peak-to-peak FMR linewidth ΔH is related to the relaxation rate of magnetization motion, which is caused by intrinsic Gilbert damping α and magnetic inhomogeneities $\Delta H(0)$ in ferromagnet: $H = \frac{2}{\sqrt{3}} \frac{\alpha}{\gamma} 2\pi f_{\text{FMR}} + \Delta H(0)$, where γ is the gyromagnetic ratio, and f_{FMR} is the FMR frequency. The damping parameter estimated from above-mentioned ΔH values of Co and garnet films is equal to $\alpha_{\text{Co}} = 0.04$ and $\alpha_{\text{garnet}} = 0.19$. Nevertheless, the Gilbert damping of ultrathin Co layer grown on ultra-smoothed garnet film is comparable with the damping of high-quality single and polycrystalline Co layers obtained on metallic underlayers [32–34].

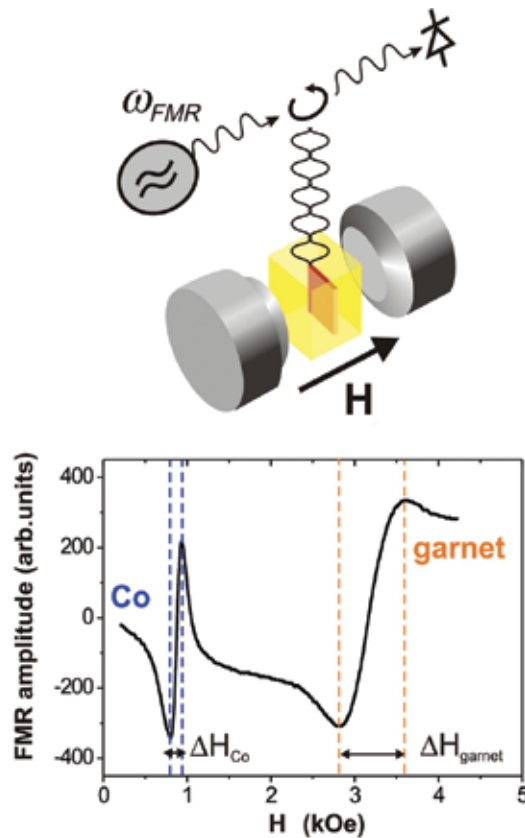


Figure 6. FMR lines for Co/YIG:Co heterostructure measured at $\theta_H = 65^\circ$ and $\phi_H = 0^\circ$ of the external magnetic field H .

The experimental dependencies of a resonance field H_R on the angles θ_H and ϕ_H for the garnet film and the Co layer are plotted in **Figures 7** and **8**, respectively. The existence of easy magnetization axes along the $\langle 111 \rangle$ directions for the garnet contributions was deduced by

analyzing $H_R(\theta_H, \phi_H)$ (see **Figure 7(a,b)**). This result correlates well with the Faraday experiments for garnet film, shown in **Figure 4(b)**. For the 2-nm Co layer, the easy magnetization axis lies in the sample plane (see **Figure 8(a)**) and is also connected with the "easy plane" type of the magnetic anisotropy (**Figure 8(b)**). As observed before, the magnetic anisotropy of the YIG:Co has two contributions [18]: magnetocrystalline cubic and growth-induced uniaxial ones. Hence, a qualitative analysis of the FMR and magnetization curves gives rise to the following description of the magnetic anisotropy energy E_A , which contains cubic, growth-induced and uniaxial anisotropies:

$$E_A(\vec{M}_{\text{garnet}}, \vec{M}_{\text{Co}}) = K_1 \left[(m_x m_y)^2 + (m_x m_z)^2 + (m_z m_y)^2 \right] + K_{\text{eff}}^{\text{garnet}} \sin^2 \theta + K_{\text{eff}}^{\text{Co}} \sin^2 \theta_M \quad (1)$$

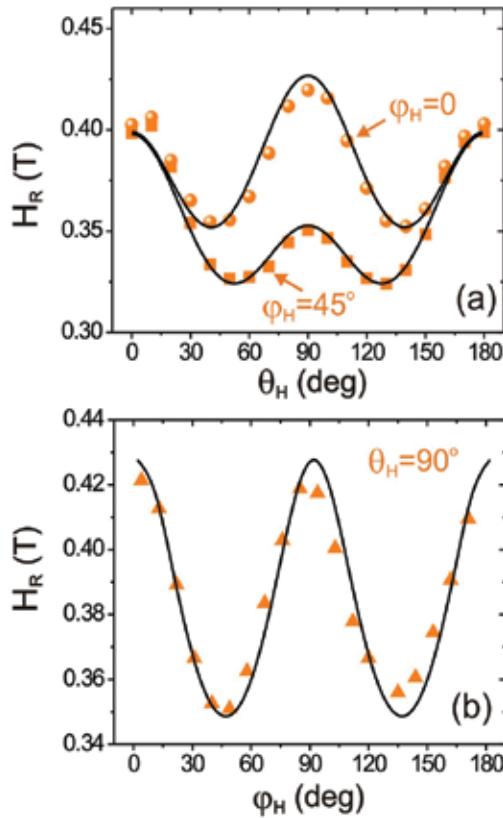


Figure 7. The polar (for $\phi_H = 0^\circ$ and 45°) and azimuthal (for $\theta_H = 90^\circ$) dependences of the resonance field H_R for YIG:Co film. The dots are experimental values, and solid lines were fitted using Eq. (1).

where \vec{M}_{garnet} and \vec{M}_{Co} are the magnetization vectors for garnet and Co films, respectively; K_C is the cubic anisotropy constant of garnet film; m_x , m_y , and m_z are the direction cosines of garnet magnetization vector along the principle crystallographic axes defined as $m_x = \sin\theta\cos\phi$, $m_y =$

$\sin\theta\sin\phi$, $m_z = \cos\theta$ (θ and ϕ are the polar and azimuthal angles of magnetization, respectively); $K_{\text{eff}}^{\text{garnet}}$ is the effective growth-induced (uniaxial) anisotropy constant for the garnet film, $K_{\text{eff}}^{\text{Co}}$ is the effective uniaxial anisotropy constant of the 2-nm Co layer defined by the polar angle θ_M . The bulk value of the saturation magnetization 1420 G was assumed for the 2-nm Co thickness. The saturation magnetization was 7 G [17]. For each resonance line of YIG:Co and ultrathin Co films, the magnetic anisotropy constants were fitted using Eq. (1) and standard FMR conditions [35, 36]:

$$f_{\text{FMR}} = \frac{1}{2\pi} \frac{\gamma}{M \sin\theta} \left[\frac{\partial^2 E_A}{\partial \theta^2} \frac{\partial^2 E_A}{\partial \phi^2} - \left(\frac{\partial^2 E_A}{\partial \theta \partial \phi} \right)^2 \right]^{1/2} \quad (2)$$

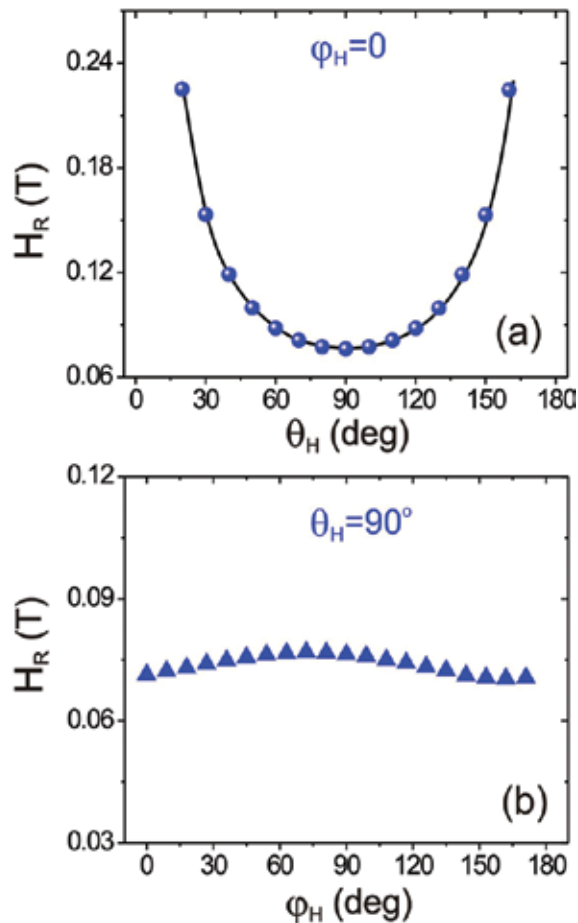


Figure 8. The polar (for $\phi_H = 0^\circ$ and 45°) and azimuthal (for $\theta_H = 90^\circ$) dependences of the resonance field H_R for 2-nm Co layer on YIG:Co film. The dots are experimental values, and the solid line was fitted using Eq. (1).

where f_{FMR} is the FMR frequency. The equilibrium angles θ and ϕ of the magnetization can be found by the minimization of E_A : $\frac{\partial E_A}{\partial \theta} = 0$ and $\frac{\partial E_A}{\partial \phi} = 0$. The FMR frequency was $f_{\text{FMR}} = 9.5$ GHz (X-band spectrometer). The gyromagnetic ratio of Co layer and garnet films is suggested to be equal to $\gamma_{\text{Co}} = 1.76 \times 10^6$ Hz/Oe and $\gamma_{\text{garnet}} = 1.65 \times 10^6$ Hz/Oe, respectively. The gyromagnetic ratio values of Co and garnet films correspond to the factors $g_{\text{Co}} = 2$ and $g_{\text{garnet}} \approx 1.9$, which are comparable to the previously reported experimental data for Co [35] and the similar garnet compositions [37, 38]. The reduction of g_{garnet} can be explained in terms of Wangsness model for the two-sublattice ferrimagnet [39]. The first sublattice is produced by tetrahedral and octahedral Fe^{3+} ions for which the g -factor is close to two, while second one is formed by high-spin octahedral Co^{2+} ions with $g \approx 2.9$ [38]. As a result, oppositely directed sublattices lead to the reduction of the effective g -factor. Solid lines in **Figures 7** and **8** show the results of the fitting procedure.

Thus, let us analyze, step by step, the magnetic anisotropy constants of the Co layer and garnet films from FMR field and magnetization loops. First, for the Co layer deposited on the garnet film, the effective anisotropy constant is $K_{\text{eff}}^{\text{Co}} = -9.9 \times 10^6 \text{ erg/cm}^3$ that corresponds to the case of in-plane magnetic anisotropy in the Co layer. Second, from the part of FMR spectrum which corresponds to garnet films, the cubic $K_C = -2 \times 10^3 \text{ erg/cm}^3$ anisotropy contribution for garnet film was deduced from the fitting procedure. In the case of negative K_C , four easy magnetization-axis orientations along a $\langle 111 \rangle$ -type of crystallographic direction to the sample plane in garnet films exist [39]. Third, cubic constants K_C determined by FMR technique were used for the fitting of Faraday loops measured for garnet parts of a sample. Since the direction of magnetization at equilibrium corresponds to the minimum of $E_A(M_{\text{garnet}})$, the effective growth-induced anisotropy constant $K_{\text{eff}}^{\text{garnet}} = K_{\text{J}}^{\text{garnet}} - 2\pi M_{\text{garnet}}^2$ can be determined from the minimization of $E_A(M_{\text{garnet}})$ with respect to the polar angle θ of magnetization: $\frac{\partial E_A(M_{\text{garnet}})}{\partial \theta} = 0$. After separation of the demagnetization contribution from the uniaxial anisotropy, the anisotropy constant $K_{\text{J}}^{\text{garnet}} = 10^3 \text{ erg/cm}^3$ for 1.8- μm -thick garnet film was obtained [40].

3.4. Magnetostatic interlayer coupling

Here, we report on an influence of the 2-nm Co layer on both the domain structure geometry and magnetization reversal processes in the YIG:Co film. The period and shape of domains in Co/YIG:Co heterostructure are explained by competition of different energies. Taking into account the domain period in garnet film of order of 10 μm , the $20 \times 20 \mu\text{m}$ Au/Co pattern is required for the observation of domain structure of garnet films under ultrathin Co layer [40], i.e., the size of pattern square is larger than domain period of garnet films. **Figure 9** shows the images of domain structure for patterned Co/garnet area recorded at $H_z = 0$ and $H_z = 40$ Oe, respectively.

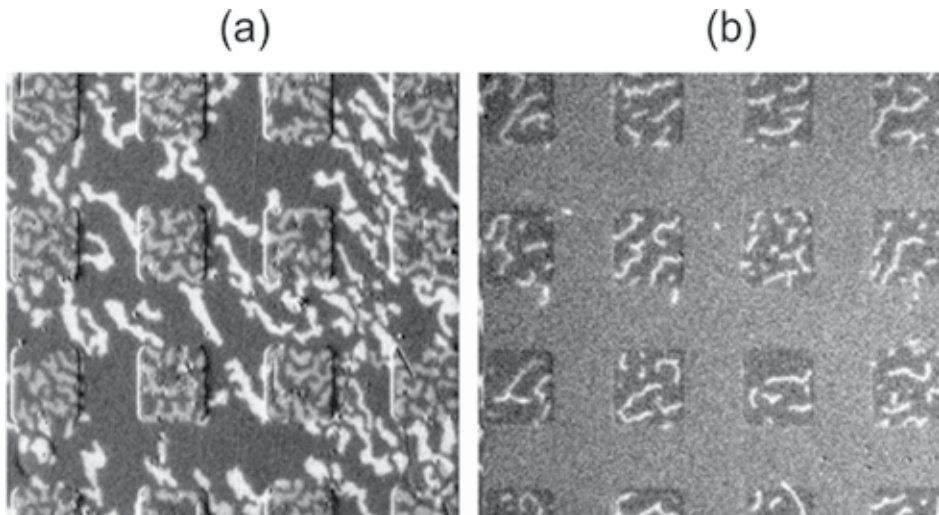


Figure 9. Images of magnetic domain structure in 2-nm Co/YIG:Co pattern area recorded at: (a) $H_z = 0$ and (b) $H_z = 40$ Oe. The image size is $140 \times 130 \mu\text{m}$.

In **Figure 9(a)**, both in garnet and Co/garnet (square areas) structures, stripe domain structures are observed. In this case, the period and the domain size in the Co/garnet structure is less than in the garnet film.

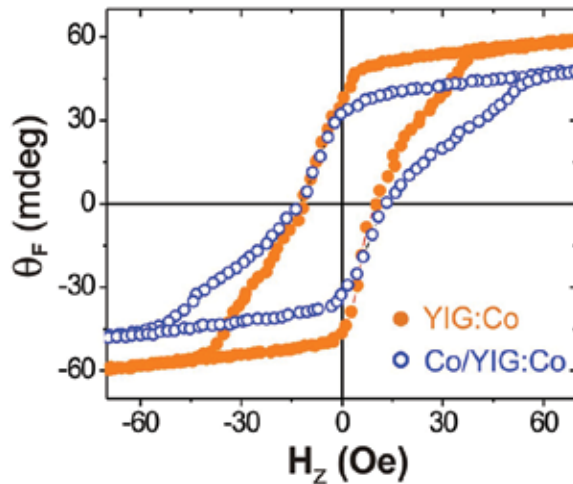


Figure 10. The hysteresis loops recorded for both bare YIG:Co (full points) and Co/YIG:Co (open points) films.

At $H_z = 40$ Oe, the domain structure was observed only at Co/garnet pattern (see **Figure 9(b)**). Moreover, the clear difference in the magnetization reversal process with and without the 2-

nm cover Co layer on garnet film was observed in the field range near the coercivity (see **Figure 10**). First, for Co/garnet heterostructure, we observe the reduced θ_F value compared to the bare garnet film, i.e., the contribution of the hard axis from the Co/garnet interface to hysteresis loop is found. Second, the value of the reversal magnetic collapse field is noticeably increasing from 40 to 55 Oe. In **Figure 9(b)**, the presence of Co/garnet domains on a monodomain background garnet area is well visible. In this case, the extra energy is required to switch the in-plane interfacial magnetic moment in the garnet film. For these reasons, the strong in-plane magnetic anisotropy of the ultrathin Co layer induces significant stray field on the garnet surface. Therefore, for the Co/garnet heterostructure, reduction of the domain period occurs as a consequence of decreasing the magnetostatic energy.

4. Ultrafast magnetization dynamics induced by femtosecond laser pulses in a Co/garnet heterostructure

We present the results of a study of ultrafast photoinduced magnetization dynamics in Co/YIG:Co heterostructures via the excitation of photomagnetic anisotropy [19, 20]. This anisotropy is related to an optically induced charge transfer between the anisotropic Co^{2+} and Co^{3+} ions on tetrahedral sites in the garnet lattice. The deposition of ultrathin Co layer on garnet film can result in a new type of magnetization dynamics due to the influence of the effective magnetic field of the Co layer and/or the magnetic coupling between the metallic layer and garnet film.

4.1. Time-resolved magneto-optical tools

To investigate the ultrafast magnetization dynamics in both bare YIG:Co film and Co/YIG:Co heterostructure induced by femtosecond laser pulses, we carried out time-resolved measurements at room temperature using a conventional magneto-optical pump-probe method. Pump pulses with a duration of 35 fs from an amplifier (Spitfire Ace, Spectra-Physics) at a 500 Hz repetition rate were directed at an angle of incidence about 10° from the sample normal parallel to the [001] crystallographic axis of the sample, while the probe pulses at a 1 kHz repetition rate of the pump were incident along the sample normal, see **Figure 11**. A pump beam with a wavelength of 800 nm and energy of 2 μJ was focused onto a spot about 100 μm in diameter on the sample. The pump energy was relatively small in order to not heat significantly the metallic layers of Au and Co. The sample was excited by the pump through the Co side of the bilayer. A probe beam with a wavelength of 800 nm was about two times smaller in size and the energy than the pump. The parameter of delay time Δt (see **Figure 1**) between the pump and the probe pulses could be adjusted up to 1.3 ns. The linear polarization of the pump beam was defined by angle φ to the [100] axis. The amplitude of the magnetization precession was maximal when the polarization plane of the pump was along [100] or [010] axes. On the contrary, the polarization of the probe beam was along the [1-10] axis.

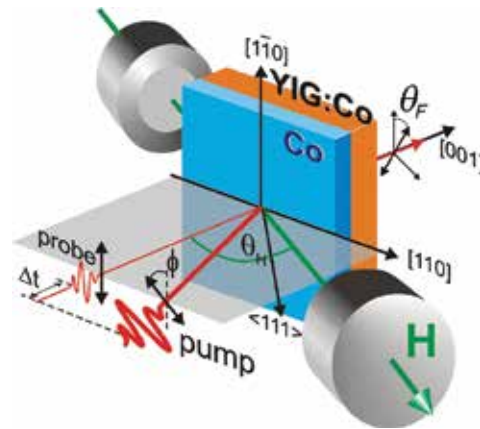


Figure 11. Sample configuration and the experimental geometry with the external magnetic field H applied with angle $\theta_H = 65^\circ$.

In this experimental geometry, we measured the Faraday rotation angle θ_F of the probe as a function of the delay time Δt between the pump and probe pulses. The rotation $\theta_F(\Delta t)$ is proportional to the out-of-plane component of the magnetization M_z . An external magnetic field H up to 5 kOe was applied along the (1-10) plane at $\theta_H = 65^\circ$ with respect to the sample normal. At the same time, H was above domain collapse field, so that a coherent spin dynamics without domain structure was investigated.

4.2. Spin precession modulation

The experimental results presented below were obtained on 2-nm Co/YIG:Co heterostructure, in which strong magnetostatic interlayer coupling has been found. **Figure 12** shows the magnetization precession (angle of Faraday rotation) as a function of the delay time Δt for different values of the amplitude of the external magnetic field with angle $\theta_H = 65^\circ$. We expect that the magnetization dynamics corresponds to a precession of the Co and garnet moments around the effective field. For a relatively small external magnetic field, one can find a slow oscillation with a main single frequency of 4.2 GHz, see **Figure 12(a)**, corresponding to the garnet film [41]. We observe periodic oscillation modulated by a higher-frequency oscillation in **Figure 12(b)**. Fast Fourier transforms (FFTs) were taken for these dependences, and the resulting power spectra confirm the presence of two different oscillation frequencies f_1 and f_2 (see **Figure 12(b)**). Both of these frequencies increase with increasing amplitude of the external magnetic field. However, we observed a main single higher oscillation frequency for the external magnetic field above 4 kOe (see **Figure 12(c)**). The Faraday rotation transients for varying external magnetic field H were fitted (**Figure 12**) with two damped sine contributions:

$$\theta_F(\Delta t) = A_1 \exp\left(\frac{-\Delta t}{\tau_1}\right) \sin(2\pi f_1 \Delta t + \phi_1) + A_2 \exp\left(\frac{-\Delta t}{\tau_2}\right) \sin(2\pi f_2 \Delta t + \phi_2) \quad (3)$$

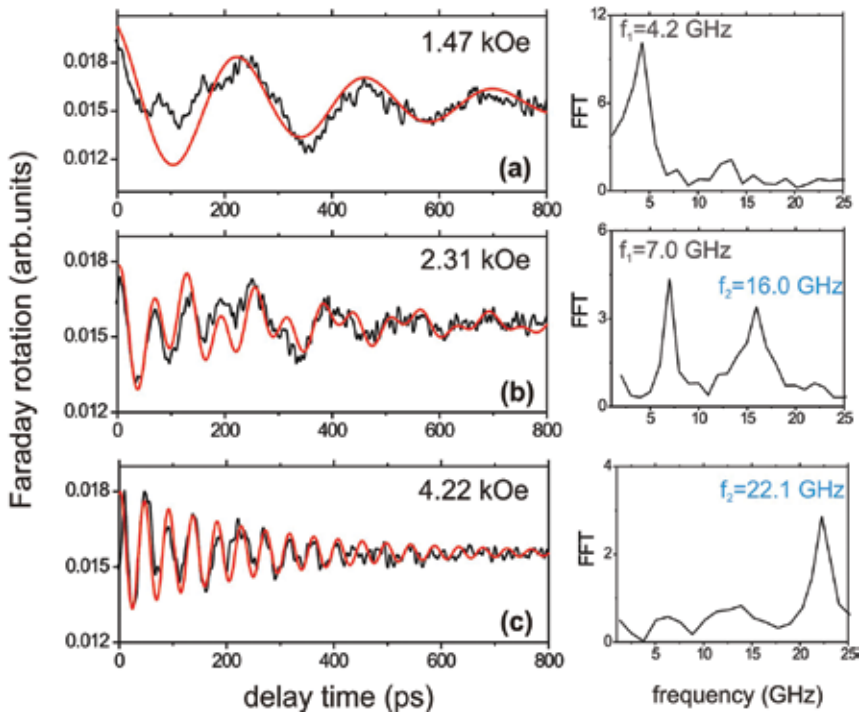


Figure 12. Time-resolved Faraday rotation as a function of the delay time Δt for (a) $H = 1.47$ kOe, (b) 2.31 kOe, and (c) 4.22 kOe. The red solid lines were fitted using FFT analysis and Eq. (3). The right panel—the FFT spectra.

where τ_i is the time decay, A_i the amplitude, and φ_i the phase. The fitted curves using FFT analysis and Eq. (3) are in good agreement with the experimental data (see **Figure 12**).

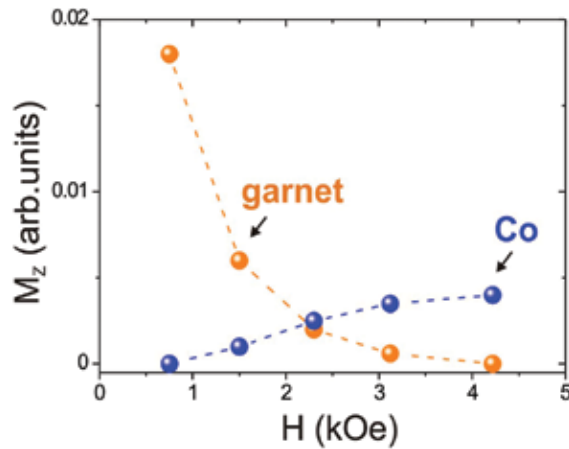


Figure 13. Dependence of the magnetization component M_z on the amplitude of external field H for the garnet and Co layer.

From the experimental curves, we deduced amplitudes of the oscillations using fitting by Eq. (3). It is clearly seen that upon increasing H , the contribution from the garnet vanishes so that at the field above 4 kOe, the contribution from the Co layer dominates (see **Figure 13**). The dependence of perpendicular component of the magnetization M_z is proportional to the Faraday rotation θ_F .

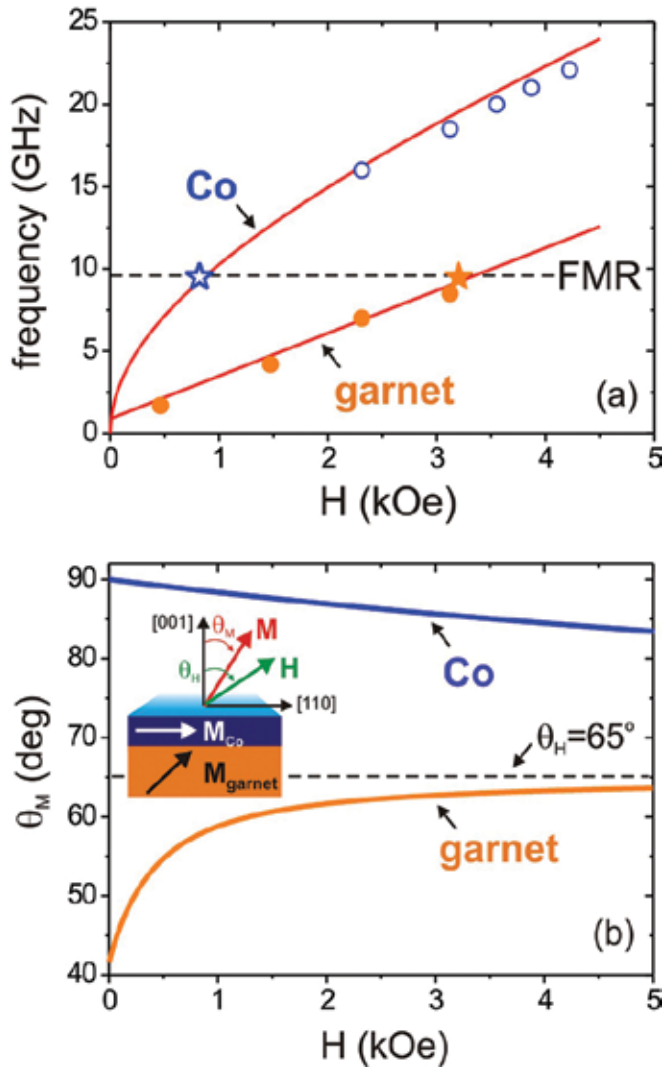


Figure 14. (a) Dependence of the frequency of magnetization precession on a function of magnetic field amplitude H for garnet (full points) and Co (open points) films of a heterostructure. The calculated FMR frequency dependences are shown using both Eqs. (1) and (2) with magnetic anisotropy constants (solid lines). The measured FMR data are shown as stars. (b) Calculation of magnetization orientation θ_M as a function of the amplitude of H for YIG:Co film and 2-nm Co layer.

Figure 14(a) plots the frequencies f_1 and f_2 obtained from experimental data for different values of the H . The dashed line is determined by the FMR frequency where the resonance field values for Co and garnet films are located (stars). To compare obtained frequencies, we calculated the FMR frequency as a function of the external magnetic field with angle $\theta_H = 65^\circ$ in both the cobalt and garnet films using a typical FMR equation [35], considering constants of the magnetic anisotropy of the 2-nm Co and 1.8 μm garnet film. The frequencies f_1 and f_2 differing by about a factor of two correspond to the precession of the magnetization excited in garnet and Co films, respectively. We see from **Figure 14(a)** that the experimental magneto-optical response data (points) agree well with the measured FMR results with single 9.5 GHz frequency (stars) and calculated FMR frequency (solid lines) for both contributions in the bilayer using Eq. (2).

Such a layer selective probing of the magnetization dynamics can be understood by a simple phenomenological model. The equilibrium state of magnetization vector at the Co/YIG:Co heterostructure could be found using the phenomenological model of magnetic anisotropy (Eq. (1)) after minimizing the total energy including energies of the magnetic anisotropies, the Zeeman at external magnetic field, and the demagnetization. **Figure 14(b)** shows the dependence of magnetization angle θ_M on an external magnetic field H for both Co and garnet films. According the Faraday configuration, the polarization rotation of the probe beam was proportional to the perpendicular magnetization component along [001] axis at the garnet (see **Figure 11**). Thus, θ_F is proportional to the amplitude of the magnetization precession. During increasing θ_M , we observed increasing the amplitude of the magnetization precession. A quantitative analysis of dependences of the angle on the external magnetic field shows the possibility of the excitation of magnetization precession at two regimes: first, at low magnetic field below 1 kOe, the amplitude of magnetization precession dominates at the garnet film due to the large angle between magnetic field H and magnetization of garnet M_{garnet} and small perpendicular magnetization component of cobalt M_{Co} ; second, at high magnetic field above 4 kOe, the amplitude of magnetization precession is dominated at the Co film with the significant perpendicular component M_{Co} when the magnetization vector M_{garnet} is close to H .

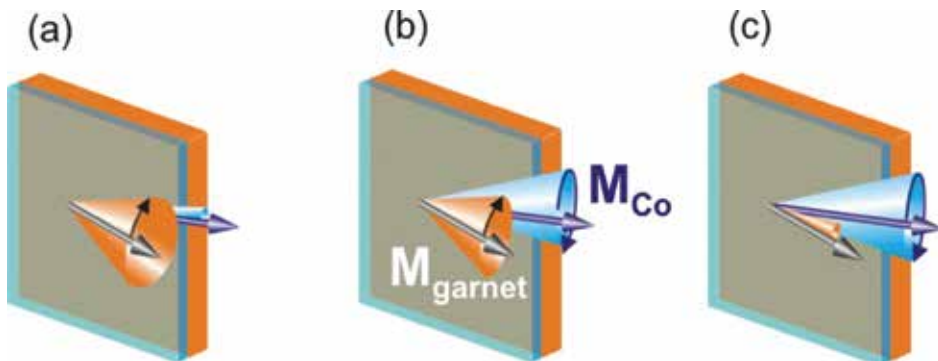


Figure 15. Graphical illustration of the precessional dynamics for: (a) $H < 1.5$ kOe, (b) $1.5 < H < 4.3$ kOe, and (c) $H > 4.3$ kOe.

We can conclude that we observe three types of magnetization precession in the bilayer: (i) mainly single-frequency precession (1–5 GHz) from the garnet for $H < 1.5$ kOe, (ii) a double frequency to modulated signal for $1.5 < H < 4.3$ kOe, and (iii) mainly single-frequency precession (>20 GHz) from the cobalt film for $H > 4.3$ kOe (see the graphical illustration of the precessional dynamics in **Figure 15**).

4.3. Laser-induced phase-sensitive magnetization precession

In this part, we compare magnetization dynamics in the Co and bare garnet films separately via selective probing and show that magnetization precession in the garnet can be manipulated by magnetostatic interlayer coupling.

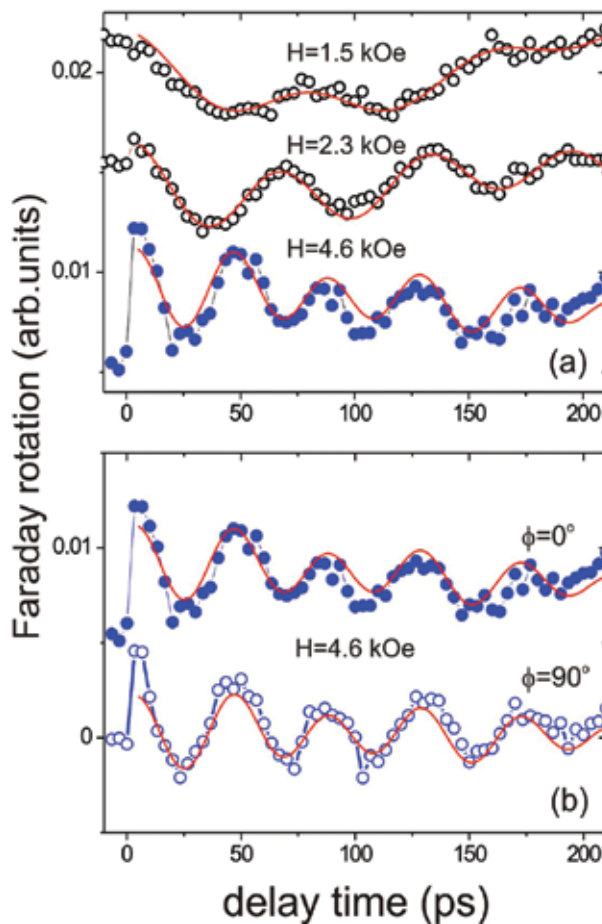


Figure 16. Time-resolved Faraday rotation of the Co/garnet heterostructure as a function of the delay time Δt for different (a) magnetic field amplitude and (b) pump polarization. Solid line was fitted using the classical oscillation function including damping for a 2-nm Co layer on a garnet film.

A rather unique combination of magnetic properties of the layers allows us to realize different regimes of the laser-induced dynamics. Changing the strength of the out-of-plane H , we were able to obtain conditions when the magnetization dynamics was dominated either by the Co or the garnet layer. As discussed in the previous part, for $H < 1$ kOe photoinduced dynamics of Co/garnet, the heterostructure is dominated by the magnetization precession of the garnet film, while at $H > 4$ kOe, the magnetization precession results from the Co layer. Time dependence of the z -component of the magnetization precession was on the function of the external magnetic field H and the angle of polarization plane of the pump beam. **Figure 16(a)** shows the magnetization precession curves measured at $H = 1.5$ kOe, 2.3 kOe, and 4.6 kOe for $\varphi = 0^\circ$. The laser-excited precessions of the magnetizations at two different frequencies are deduced from **Figure 14** as FMR frequencies in both the Co and the garnet films.

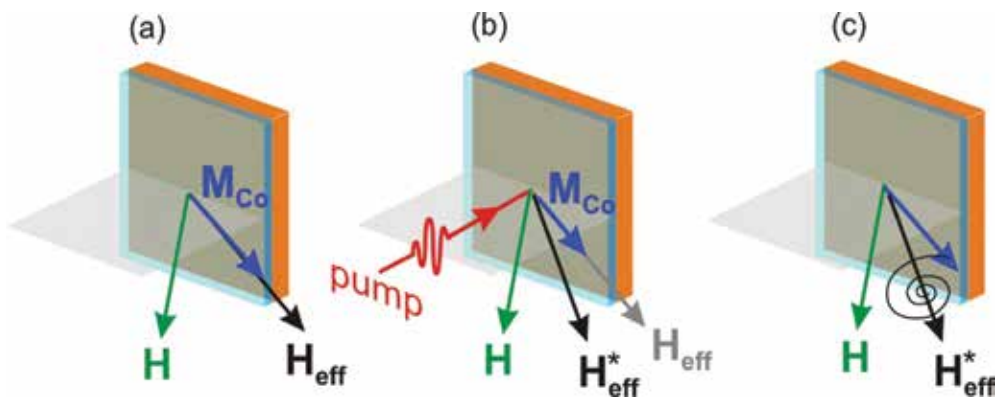


Figure 17. Graphical illustration of an ultrafast demagnetization dynamics in a 2-nm Co layer for (a) $\Delta t < 0$, (b) $0 < \Delta t < t_w$ (pulse duration), and (c) $\Delta t > t_w$.

The photoinduced magnetization precession for different pump beam polarizations at an external magnetic field with 4.6 kOe is shown in **Figure 16(b)**. These curves demonstrate no polarization dependence of the magnetization precession [42]. For such metallic ferromagnets, the ultrafast light-induced demagnetization is typical [43, 44]. The thermal demagnetization is seen as a sub-picosecond change of the magneto-optical signal measured at $H = 4.6$ kOe. The observed light-induced magnetization dynamics is a result of temperature increase of electron system on femtosecond timescale and a subsequent ultrafast reduction of M_{Co} [45], which effectively change the equilibrium orientation of the magnetization in this layer and thus triggers spin oscillations (see the graphical illustration in **Figure 17**).

To study the influence of the Co film on the ultrafast magnetization dynamics at the garnet film, the time-resolved Faraday measurements at low-field regime below 1 kOe were performed [42]. In this case, the amplitude of magnetization precession at YIG:Co film always dominates that of the Co film (see **Figure 13**). First, we measured the laser-induced magnetization dynamics in a bare garnet film. **Figure 18(a)** shows that changing the polarization of the pump induces a shift of the phase of the precession $\Delta\psi = 120^\circ$ in the bare garnet film. In this case, the decay coefficient of photoinduced anisotropy is $\tau_g \sim 20$ ps. In case of the deposition

of the 2-nm Co film on this garnet film, the polarization sensitivity of the magnetization precession disappears. The polarization angles of pump beam with $\varphi = 0$ and 90° trigger magnetization precession in YIG:Co with the same phase ($\Delta\psi \approx 0$), see **Figure 18(b)**. The time of relaxation of magnetization precession after pump pulse is $\tau_c \sim 60$ ps. This value is enlarged due to the influence of light-induced demagnetization at Co layer. The magnetization dynamics triggered in YIG:Co film and the Co/YIG:Co heterostructure with the same polarization of the pump light are clearly different. However, the frequencies of these precessions are similar.

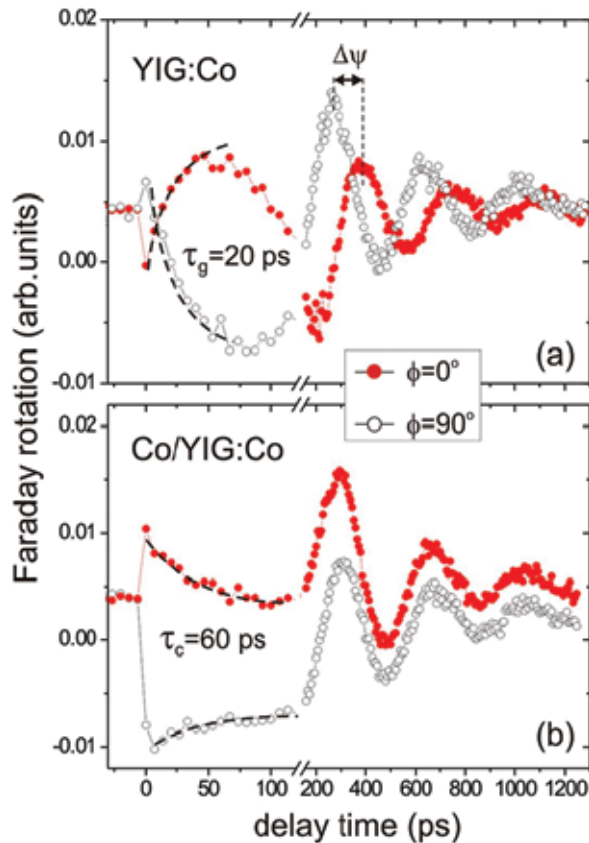


Figure 18. Time-resolved Faraday rotation of (a) bare garnet and (b) Co/garnet films as a function of the delay time Δt for $H(\theta_H = 65^\circ) = 0.75$ kOe and different pump polarization φ . Dashed lines were fitted using the exponential function with decay coefficients τ_L .

The laser excitation of Co/YIG:Co heterostructure leads to both an thermal demagnetization at Co film and a photomagnetic effect at the garnet [20]. These effects induced changing the magnetization orientation given by the effective field H_{eff} in the heterostructure (see **Figure 17**). In this case, ultrafast change triggers the precession of the magnetization vector around the new orientation H_{eff}^* (see **Figure 17(c)**). In YIG:Co, the polarization-dependent excitation with different initial phase of magnetization precession leads to a photoinduced magnetic

anisotropy [19]. However, in our heterostructure, the phase of magnetization precession is defined by both the effective anisotropy (magnetocrystalline, uniaxial, and photoinduced) field and the stray field from 2-nm Co film (the magnetization of cobalt is significant larger than the magnetization of garnet). The magnetostatic coupling between Co and YIG:Co films leads to a change in the phase of magnetization precession in YIG:Co film. Thus in heterostructure, the magnetization is precessed around the effective magnetic field with the isotropic in-plane component due to the "easy plane" of magnetic anisotropy of Co film.

5. Conclusion

In this chapter, we have presented the experimental investigation of ultrathin Co/garnet heterostructure by using time-resolved pump-probe magneto-optical spectroscopy in combination with linear magneto-optical Faraday and Kerr effects and ferromagnetic resonance. Ion beam processing procedure for preparation of Au/Co/garnet heterostructure with a sub-nanometer roughness parameter at the interface has been proposed. It was found that Gilbert damping of the ultrathin Co layers on the garnet surfaces is comparable to the damping of high-quality single and polycrystalline Co layers grown on metallic underlayers. We showed that the magnetic and magneto-optical properties of Co/garnet heterostructures can be engineered by covering the ultrathin Co layer. In particular, a strong magnetostatic interlayer coupling between the 2-nm Co layer and YIG:Co film has been found. In addition, the modification of the domain structure due to the magnetostatic coupling has been demonstrated. In principle, depositing ultrathin ferromagnetic layers on a garnet film can also lead to new effects in magnetization dynamics, due to the influence of the effective magnetic field of the ferromagnetic layer and/or the coupling between ferromagnetic layer and garnet.

The growth of a 2-nm Co layer on top of the garnet significantly changes the mechanism of the laser-induced precession in the heterostructure. We observed the modulation of spin precession in a Co/garnet heterostructure with distinct frequencies. The excitation efficiency of these precessions strongly depends on the amplitude and orientation of external magnetic field. In addition, we demonstrate that the laser pulse triggers polarization-independent precession in both the Co and garnet layers via the magnetostatic coupling between these layers.

These results demonstrate that magnetic metal/dielectric heterostructures are interesting and promising objects for further investigations of all-optical ultrafast light-induced phenomena and their potential applications.

Acknowledgements

This work was supported by the National Science Centre Poland for OPUS project DEC-2013/09/B/ST3/02669. The author would like to acknowledge the contributions of M. Pashkevich for measurements and A. Stognij for heterostructures preparation. The author is

grateful to M. Tekielak, R. Gieniusz, A. Maziewski, A. Kirilyuk, A. Kimel, and T. Rasing for fruitful discussions and research support.

Author details

Andrzej Stupakiewicz

Address all correspondence to: and@uwb.edu.pl

Laboratory of Magnetism, Faculty of Physics, University of Bialystok, Bialystok, Poland

References

- [1] A. Kirilyuk, A. V. Kimel and Th. Rasing. Ultrafast optical manipulation of magnetic order. *Rev. Mod. Phys.*. 2010;82:2731.
- [2] E. Beaurepaire, J.-C. Merle, A. Daunois, and J.-Y. Bigot. Ultrafast Spin Dynamics in Ferromagnetic Nickel. *Phys. Rev. Lett.*. 1996;76:4250.
- [3] U. Bovensiepen. Femtomagnetism: Magnetism in step with light. *Nature Physics*. 2009;5:461.
- [4] I. Radu, K. Vahaplar, C. Stamm, T. Kachel, N. Pontius, H. Dürr, T. Ostler, J. Barker, R. Evans, R. Chantrell, A. Tsukamoto, A. Itoh, A. Kirilyuk, Th. Rasing, A. Kimel. Transient ferromagnetic-like state mediating ultrafast reversal of antiferromagnetically coupled spins. *Nature*. 2011;472:205.
- [5] B. Koopmans, G. Malinowski, F. Dalla Longa, D. Steiauf, M. Fähnle, T. Roth, M. Cinchetti and M. Aeschlimann. Explaining the paradoxical diversity of ultrafast laser-induced demagnetization. *Nature Mat.*. 2010;9:259.
- [6] W. A. Challener, C. Peng, A. V. Itagi, D. Karns, W. Peng, Y. Peng, X.-M. Yang, X. Zhu, N. J. Gokemeijer, Y.-T. Hsia, G. Ju, R. E. Rottmayer, M. A. Seigler and E. C. Gage. Heat-assisted magnetic recording by a near-field transducer with efficient optical energy transfer. *Nature Photon.*. 2009;3:220.
- [7] V.I. Belotelov, I.A. Akimov, M. Pohl, V.A. Kotov, S. Kasture, A.S. Vengurlekar, Achanta Venu Gopal, D.R. Yakovlev, A.K. Zvezdin, M. Bayer. Enhanced magneto-optical effects in magnetoplasmonic crystals. *Nature Nanotech.*. 2011;1:370.
- [8] T. Satoh, Y. Terui, R. Moriya, B. A. Ivanov, K. Ando, E. Saitoh, T. Shimura, and K. Kuroda. Directional control of spin-wave emission by spatially shaped light. *Nature Photon.*. 2012;6:662.

- [9] S. Parchenko, A. Stupakiewicz, I. Yoshimine, T. Satoh, and A. Maziewski. Wide frequencies range of spin excitations in a rare-earth Bi-doped iron garnet with a giant Faraday rotation. *Appl. Phys. Lett.*. 2013;103:172402.
- [10] S.O. Demokritov, V.E. Demidov, O. Dzyapko, G.A. Melkov, A.A. Serga, B. Hillebrands, A.N. Slavin. Bose–Einstein condensation of quasi-equilibrium magnons at room temperature under pumping. *Nature*. 2006;443:430.
- [11] A.B. Chizhik, I.I. Davidenko, A. Maziewski, A. Stupakiewicz. High-temperature photomagnetism in Co-doped yttrium iron garnet films. *Phys. Rev. B*. 1998;57:14366.
- [12] F. Hansteen, A. V. Kimel, A. Kirilyuk, and Th. Rasing. Femtosecond Photomagnetic Switching of Spins in Ferrimagnetic Garnet Films. *Phys. Rev. Lett.*. 2005;95:047402.
- [13] A. V. Kimel, A. Kirilyuk, P. A. Usachev, R. V. Pisarev, A. M. Balbashov and Th. Rasing. Ultrafast non-thermal control of magnetization by instantaneous photomagnetic pulses. *Nature*. 2005;435:655.
- [14] S. Parchenko, T. Satoh, I. Yoshimine, F. Stobiecki, A. Maziewski, and A. Stupakiewicz. Non-thermal optical excitation of terahertz-spin precession in a magneto-optical insulator. *Appl. Phys. Lett.*. 2016;108:032404.
- [15] Y. S. Chun and Kannan M. Krishnan. Interlayer perpendicular domain coupling between thin Fe films and garnet single-crystal underlayers. *J. Appl. Phys.*. 2004;95:6858.
- [16] N. Vukadinovic, J. Ben Youssef, V. Castel, M. Labrune. Magnetization dynamics in interlayer exchange-coupled in-plane/out-of-plane anisotropy bilayers. *Phys. Rev. B*. 2009;79:184405.
- [17] A. Maziewski. Unexpected magnetization processes in YIG+Co films. *J. Magn. Magn. Mater.*. 1990;88:325.
- [18] M. Tekielak, A. Stupakiewicz, A. Maziewski and J. M. Desvignes. Temperature induced phase transitions in Co-doped YIG films. *J. Magn. Magn. Mater.* 2003;254–255:562.
- [19] A. Stupakiewicz, A. Maziewski, I. Davidenko, and V. Zablotskii. Light-induced magnetic anisotropy in Co-doped garnet films. *Phys. Rev. B*. 2001;64:064405.
- [20] F. Atoneche, A.M. Kalashnikova, A.V. Kimel, A. Stupakiewicz, A. Maziewski, A. Kirilyuk, and Th. Rasing. Large ultrafast photoinduced magnetic anisotropy in a cobalt-substituted yttrium iron garnet. *Phys. Rev. B*. 2010;81:214440.
- [21] G. Woltersdorf, O. Mosendz, B. Heinrich and C.H. Back. Magnetization Dynamics due to Pure Spin Currents in Magnetic Double Layers. *Phys. Rev. Lett.*. 2007;99:246603.
- [22] L. Le Guyader, A. Kleibert, F. Nolting, L. Joly, P. M. Derlet, R. V. Pisarev, A. Kirilyuk, Th. Rasing and A. V. Kimel. Dynamics of laser-induced spin reorientation in Co/SmFeO₃ heterostructure. *Phys. Rev. B*. 2013;87:054437.

- [23] I. G. Brown. *The Physics and Technology of Ion Sources*. New York: Wiley; 2004.
- [24] M. Pashkevich, R. Gieniusz, A. Stognij, N. Novitskii, A. Maziewski, and A. Stupakiewicz. Formation of cobalt/garnet heterostructures and their magnetic properties. *Thin Solid Films*. 2014;556:464.
- [25] A. Keller, S. Facsko and W. Möller. The morphology of amorphous SiO₂ surfaces during low energy ion sputtering. *J. Phys.: Condens. Matter.* 2009;21:495305.
- [26] A. I. Stognij, N. N. Novitskii, S. D. Tushina, S. V. Kalinnikov. Preparation of ultrathin gold films by oxygen-ion sputtering and their optical properties. *Technical Physics*. 2003;48:745.
- [27] Z. Šimša. Optical and magneto-optical properties of Co-doped YIG films. *Czech. J. Phys. B*. 1984;34:78.
- [28] D.L. Wood and J.P. Remeika. Effect of Impurities on the Optical Properties of Yttrium Iron Garnet. *J. Appl. Phys.* 1967;38:1038.
- [29] Landolt-Börnstein, *Numerical Data and Functional Relationships in Science and Technology*. New Series, Group III, 27/e. Berlin: Springer-Verlag; 1991.
- [30] L. G. Van Uitert, E. M. Gyorgy, W. A. Bonner, W. H. Grodkiewicz, E. J. Heilner and G. J. Zydzik. Control of bubble domain properties in garnets. *Mat. Res. Bull.* 1971;6:1185.
- [31] M. Pashkevich, A. Stupakiewicz, A. Kirilyuk, A. Stognij, A. Maziewski, Th. Rasing. Magneto-optical spectroscopy of surface/interfaces in Co/garnet heterostructures. *Appl. Surf. Sci.* 2014;305:117.
- [32] S. Pal, B. Rana, O. Hellwig, T. Thomson and A. Barman. Tunable magnonic frequency and damping in [Co/Pd]₈ multilayers with variable Co layer thickness. *Appl. Phys. Lett.* 2011;98:082501.
- [33] S. Mizukami, E. P. Sajitha, D. Watanabe, F. Wu, T. Miyazaki, H. Naganuma, M. Oogane and Y. Ando. Gilbert damping in perpendicularly magnetized Pt/Co/Pt films investigated by all-optical pump-probe technique. *Appl. Phys. Lett.* 2010;96:152502.
- [34] J-M. L. Beaujour, J. H. Lee, A. D. Kent, K. Krycka and C-C. Kao. Magnetization damping in ultrathin polycrystalline Co films: Evidence for nonlocal effects. *Phys. Rev. B*. 2006;74:214405.
- [35] M. Farle. Ferromagnetic resonance of ultrathin metallic layers. *Rep. Prog. Phys.* 1998;61:755.
- [36] H. Suhl. Ferromagnetic Resonance in Nickel Ferrite Between One and Two Kilomegacycles. *Phys. Rev.* 1955;97:555.
- [37] M. Maryško, J. Šimšová. Ferromagnetic resonance study of $Y_{3-z}Ca_zFe_{5-x-y}Co_xGe_yO_{12}$ films. *Czech. J. Phys. B*. 1984;34:1125.

- [38] M. Maryško, P. Grnert and J. Pačes. Magnetic Properties of Cobalt-Doped YIG Films Compensated by Ge^{4+} and Ti^{4+} . *Phys. Stat. Sol. A.* 1991;123:303.
- [39] G. Winkler. *Magnetic Garnets*. Braunschweig: Friedr. Vieweg & Sohn; 1981.
- [40] M. Pashkevich, A. Stupakiewicz, A. Kirilyuk, A. Maziewski, A. Stognij, N. Novitskii, A. Kimel, Th. Rasing. Tunable magnetic properties in ultrathin Co/garnet heterostructures. *J. Appl. Phys.* 2012;111:023913.
- [41] A. Stupakiewicz, M. Pashkevich, A. Maziewski, A. Stognij, N. Novitskii. Spin precession modulation in a magnetic bilayer. *Appl. Phys. Lett.* 2012;101:262406.
- [42] M. Pashkevich, A. Stupakiewicz, A. Kimel, A. Kirilyuk, A. Stognij, N. Novitskii, A. Maziewski and Th. Rasing. Laser-induced magnetization dynamics in a cobalt/garnet heterostructure. *Europhys. Lett.* 2014;105:27006.
- [43] J.-Y. Bigot, M. Vomir, L. H. F. Andrade, E. Beaurepaire. Ultrafast magnetization dynamics in ferromagnetic cobalt: The role of the anisotropy. *Chem. Phys.* 2005;318:137.
- [44] M. Vomir, L. H. F. Andrade, L. Guidoni, E. Beaurepaire, and J.-Y. Bigot. Real Space Trajectory of the Ultrafast Magnetization Dynamics in Ferromagnetic Metals. *Phys. Rev. Lett.* 2005;94:237601.
- [45] J. Kisielewski, A. Kirilyuk, A. Stupakiewicz, A. Maziewski, A. Kimel, Th. Rasing, L.T. Baczewski, and A. Wawro. Laser-induced manipulation of magnetic anisotropy and magnetization precession in an ultrathin cobalt wedge. *Phys. Rev. B.* 2012;85:184429.

Magnetic Micro-Origami

Leszek Malkinski and Rahmatollah Eskandari

Additional information is available at the end of the chapter

<http://dx.doi.org/10.5772/64293>

Abstract

Microscopic origami figures can be created from thin film patterns using surface tension of liquids or residual stresses in thin films. The curvature of the structures, direction of bending, twisting, and folding of the patterns can be controlled by their shape, thickness, and elastic properties and by the strength of the residual stresses. Magnetic materials used for micro- and nano-origami structures play an essential role in many applications. Magnetic force due to applied magnetic field can be used for remote actuation of microrobots. It can also be used in targeted drug delivery to direct cages loaded with drugs or microswimmers to transport drugs to specific organs. Magnetoelastic properties of free-standing micro-origami patterns can serve for stress or magnetic field sensing. Also, the stress-induced anisotropy and magnetic shape anisotropy provide a convenient method of tuning magnetic properties by designing a shape of the micro-origami figures instead of varying the composition of the films. Micro-origami figures can also serve as building blocks for two- and three-dimensional meta-materials with unique properties such as negative index of refraction. Micro-origami techniques provide a powerful method of self-assembly of magnetic circuits and integrating them with microelectro-mechanical systems or other functional devices.

Keywords: micro-origami, nano-origami, self-assembly, self-rolling, magnetic micro-tubes, thin film patterns, magnetic thin films, magnetic anisotropy, residual stresses, magnetoelastic effects, magnetoelectric effects, multiferroic composites

1. Introduction to origami and micro-origami

The meaning of the Japanese name “origami” is paper folding. Although the techniques of paper folding were developed in Europe and China in seventeenth and eighteenth centuries, they became the most popular in Japan. There is a vast literature on the history and practical instructions for assembly of three-dimensional objects from pieces of paper by folding [1, 2].

Origami is primarily an art but it has also an impact on technology. The origami techniques were implemented in satellite solar cells, airbag design, and stent implants [3]. Currently, mathematical [4] and computer models such as TreeMaker [5] allow designing complex three-dimensional structures for decorative arts, as well as technological applications. Some examples of origami figures are presented in **Figure 1** [6].



Figure 1. Various origami figures (reproduced from Ref. [6]).

The traditional origami methods rely on folding a single rectangular piece of paper by hand. More advanced techniques take advantage of using tools, such as bone folder, clips, or tweezers. More complex designs require cutting the paper into various patterns (different from rectangle), coloring them, combining with other materials (e.g., aluminum foil), and using multiple pieces of paper, which is called a modular origami. In contrast to static designs, some origami patterns can possess movable parts, which can be activated by kinetic energy of human's hand or inflation [7]. Another interesting trend in origami is tessellation of the figures, which is in fact a method of assembly of larger figures from building origami blocks [8].

The smallest origami figures were made from the paper pieces as small as 1 mm^2 , using a needle and optical microscope. At this point a question arises whether we can do even smaller micro-origami figures and use them to advance technology? The answer is "yes." It is possible to fabricate origami figures with features as small as 2 nm , actuate them, and assemble them into meta-materials. The submillimeter or submicrometer figures made from different materials using origami techniques are called micro- or nano-origami, respectively. A list of examples of applications of origami and micro-origami include bendable microelectronics, cell origami, origami nanorobot, pollen origami, origami lens, origami DNA, self-deployable origami stent, etc.

The materials used for micro- and nano-origami must be much thinner and tougher than conventional paper. Good candidates are thin foils and thin films. Although, in principle, it is

possible to use nanomanipulators and nanotweezers to bend and fold these materials, to make individual figures in microscale, this does not seem to be a practical approach for a mass production of various devices. Instead, other forces can be used which emerge at micro- and nanoscale. Adhesion forces, surface tension, or interfacial stresses start playing important roles when the size of the figures decreases below several micrometers [9].

Different materials and phenomena can be used for self-assembly and animation or actuation of origami figures. For example, shape memory alloys or polymers undergo significant deformations when heated by contact or radiation [10–13], capillary forces can deform paper structures [14], photosensitive polymers deform when exposed to laser light [15], and internal stresses produce deformations when the structure is released from the substrate.

Some of these forces can be used to create the micro-origami figures, while others can be used to produce motion of already formed structures. The microrobots made from stimuli-responsive materials can move, walk, or swim. These functions are especially useful in biomedical applications [16–22]. Magnetostrictive and multiferroic materials take a special place among the stimuli-responsive materials, because they couple magnetic, elastic, and electronic properties of the materials.

Currently demonstrated functional robots [21] have size of the order of centimeters, but biomedical applications require devices with dimensions smaller by at least two orders of magnitude. They should be made from thin films with submicrometer or nanometer thickness. Even the thinnest magnetic thin films preserve their magnetic and magnetostrictive properties in contrast to some shape memory alloys, which require certain thickness to undergo phase transition to produce their conformation. Therefore, magnetic films are good candidates for the micro- and nano-origami devices. In this chapter, we will discuss methods of fabrication of magnetic micro-origami structures, present experimental results on their physical properties, and indicate potential applications of magnetic micro-origami techniques.

2. Fabrication of micro-origami structures

2.1. Forces responsible for conformations

A large variety of forces is available to form or actuate thin film patterns into micro-origami figures. The magnitude of the force, elastic moduli, and the thickness of the film ultimately determine the curvature of the three-dimensional shapes. In addition, anisotropic stresses, shape of the pattern, and direction of etching decide about the direction of rolling or folding of the patterns.

2.1.1. Surface tension

Capillary forces or surface tension are negligible in macroscale; however, they are of primary importance in micro- and nanoscales. Gagler [21] and Gracias et al. [23–31] showed that the surface tension of evaporating drop of liquid is sufficient to pull the walls of the photolithographically defined thin film patterns together and form various figures, such as boxes or pyramids with the size of several micrometers. These patterns typically consist of more rigid

areas connected by thinner areas, which serve as hinges, when the thicker walls fold. This approach is versatile and can be applied to magnetic films or magnetic/nonmagnetic composites. Self-assembled structures can serve as building blocks for designing mesoscopic metamaterials with interesting responses to electromagnetic radiation in microwave, millimeter wave, and optical ranges [27, 28]. In some cases, the capillary forces can produce reversible conformations due to swelling and dehydrating of porous structures. Examples of micro-origami figures are presented in **Figure 2**.

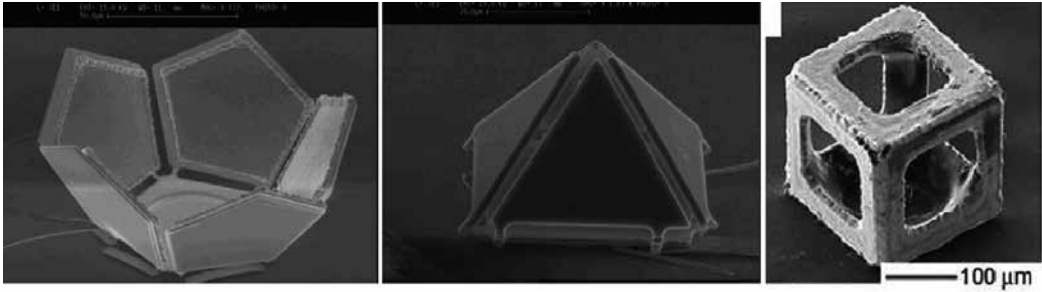


Figure 2. Examples of self-folding micro-origami structures (left and middle picture reproduced with permission from Ref. [21] and the right picture from [23]).

At this point, it is worth noting that in some cases the surface tension may cause undesirable effects. For instance, it may oppose or prevent deformation of patterns which would otherwise deform due to internal stresses or thermal stresses.

2.1.2. Residual and interfacial stresses

Different types of growth of the polycrystalline materials may result in significant residual stresses in thin film materials [32, 33]. Island growth (Volmer-Weber) or Stanski-Krastanov growth of polycrystalline films may lead to significant residual stresses due to coalescence of grains. Also, growth of bilayered or multilayered films of different materials can produce interfacial stresses due to lattice mismatch between constituent phases. When the films with residual stresses are released from the substrate on which they were grown they undergo deformation.

The curvature of the films depends on the internal stress level and the thickness of the film. For the simple bilayered beam, the continuum elasticity theory predicts that the curvature κ (inverse of radius r) is [32].

$$\kappa = \frac{6E_1E_2(h_1 + h_2)h_1h_2\varepsilon}{E_1^2h_1^4 + E_2^2h_2^4 + 4E_1E_2h_1^3h_2 + 4E_1E_2h_2^3h_1 + 6E_1E_2h_1^2h_2^2} \quad (1)$$

where E_1 and E_2 are Young's moduli, h_1 and h_2 are thicknesses of the layers, and ε denotes the interfacial strain between the two layers. Based on this equation, it is easy to demonstrate the

general rule, which states that for the layers with similar thicknesses and Young's moduli the radius of the structures is proportional to the film thickness. Thus, the smaller origami figures we wish to design the thinner films we must use. Multilayered patterns or complex shapes require numerical solutions by the means of computer simulations to predict their conformations at certain level of residual stresses. The microstructure of thin films can vary with their thickness, which results in variation of residual stresses across the film thickness. Thus, even the single polycrystalline magnetic films can form magnetic microtubes [34] or other micro-origami figures.

If the tensile stresses in the bilayers are smaller near the substrate than on the film surface, the film released from the substrate tends to bend under and may form wrinkles rather than regular micro-origami patterns. An example of wrinkled squares of magnetic films is presented in **Figure 3**. This indicates that the sequence of the deposition of the films matters. For instance, depositing metal A on top of B will not result in the same structure as depositing B on A.

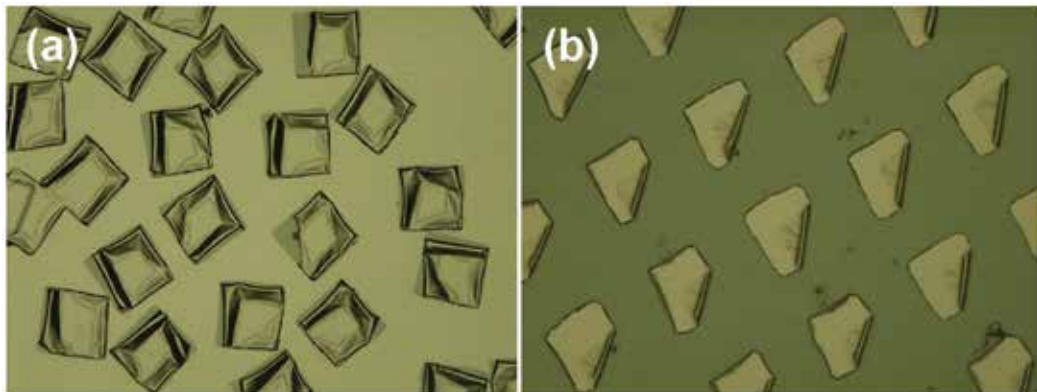


Figure 3. (a) Wrinkling of permalloy-Ti films and (b) correct rolling of the edges of Ti-permalloy squares.

The residual stresses due to grain coalescence depend on the deposition conditions, such as deposition method (sputtering, evaporation, or laser ablation), base pressure in the chamber, pressure of Ar during sputtering, and deposition rate or temperature of the substrate [33]. For this reason, it is difficult to control them and reproduce in different deposition systems.

Much better control of stresses can be achieved in heteroepitaxial structures. An excellent example of use of interfacial stresses is the technology developed by Prinz et al. [35–39].

They used misfit between single crystalline semiconductor films grown epitaxially on top of each other, as shown in **Figure 4**. Indium arsenide atoms arriving on the AlAs surface must reduce their interatomic distances to match the lattice of AlAs. Therefore, the InAs film on AlAs is in compressed state. On the other hand, GaAs atoms experience tensile stresses when they form single crystal film on the top of InAs with larger lattice constant. When AlAs sacrificial layer is selectively etched (with selectivity better than 1:1000), the initially compressed InAs expands and the strained GaAs shrinks resulting in bending and rolling of the

pattern of the bilayered film of InAs/GaAs which eventually forms a multiwall tube. For very thin films (a few atomic layers), the 7.5% mismatch strain between InAs and GaAs lattices results in a very small diameter of the tubes (down to 2 nm). Depending on the size of the rectangular pattern the number of turns can change between 1 and 40. The diameter of the tubes can be designed using formula (1). Here, it is important to note that ferromagnetic films such as single crystalline Fe or antiferromagnetic films such as Cr, KCoF_3 , or KFeF_3 can be grown epitaxially on top of GaAs [40]. In fact, a similar semiconductor template was used by the group of Mendach to prepare three-layered scrolls of InGaAs/GaAs/Au films with tunable plasma frequency in the optical range [41] and magnonic InGaAs/GaAs/NiFe films [42].

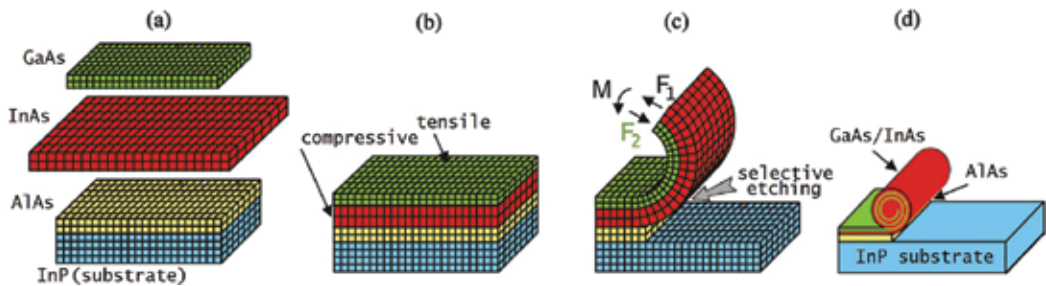


Figure 4. Heteroepitaxial semiconductor structures which result in formation of nanotubes of GaAs/InAs when sacrificial layer of AlAs on InP substrate is selectively etched releasing the film pattern from the substrate (reproduced with permission from Ref. [38]).

Thermal stresses in thin films provide another way to deform flat patterns after release from the substrate. Deposition of bilayers consisting of materials with markedly different expansion coefficients can be used to introduce internal strains when the bilayers are deposited at low or high temperatures and the films are released from the substrate at room temperature. This technique was used by Moiseeva et al. [43] to fabricate sophisticated cages from the patterns of magnetic films on top of thermal oxide with large compressive stresses. Some magnetic alloys called INVARs ($\text{Fe}_{64}\text{Ni}_{36}$) take advantage of magnetostrictive properties to reduce their linear coefficient of thermal expansion by more than one order of magnitude as compared to other metals. On the other hand, some metals such as Zn or polymers have exceptionally large thermal expansion coefficients. Combination of these dissimilar materials can result in large strains associated with relatively small temperature range during deposition or in applications.

2.1.3. Other useful forces

There are more forces which have potential for interesting applications in micro-origami. External forces were used by Jackman et al. [44] to assemble millimeter-sized cubes. Deposition of magnetic films on strained substrates has advantage over other methods: uniaxial or biaxial stresses can be applied along different directions with respect to a pattern and the direction can be varied during deposition of subsequent layers. Application of external stresses can be realized by deposition of the films on bent or strained substrates. The stress level and distribution in the films can be predicted and highly reproducible (like in the heteroepitaxial

structures) and can be easily controlled in a broad range by adjusting the curvature of the substrate or external forces. A combination of polymers with relatively small Young's modulus, which can be easily stretched, and rigid inorganic magnetic films deposited on them seems to be suitable for this kind of micro-origami applications.

Finally, significant stresses in thin films can occur when the films undergo change of crystal structure or are chemically altered. Shape memory alloys, which deform due to reversible transition from the austenitic to the martensitic phase, fall into this category. A special place among memory alloys take magnetic memory alloys such as Ni-Mn-Ga [45], which can produce strain as large as 9% when subjected to the action of a magnetic field. Strains in giant magnetostrictive alloys are almost two orders of magnitude smaller (a small fraction of %) and are considered to be insufficient to efficiently form the micro-origami figures. However, magnetostrictive materials with even smaller magnetostriction coefficients, but large magneto-mechanical coupling, are expected to be effective in stimulating already formed structures to perform certain functions, such as vibrations.

Large changes of volume of the order of 30% occur in some materials during their oxidation [46]. This effect is analogous to swelling of polymers or other porous materials. The change of the volume is associated with the increase of the linear dimensions. To exemplify this method we demonstrate the effect of the Ti oxide formation on the diameter of self-rolled microtubes of Ti/FeGa/Au and Ti/FeNi/Au. It has been suggested by Nastaushev et al. [47] that oxidation of titanium in the process of removal of the sacrificial layer may produce stresses, which affect formation of the micro-origami patterns.

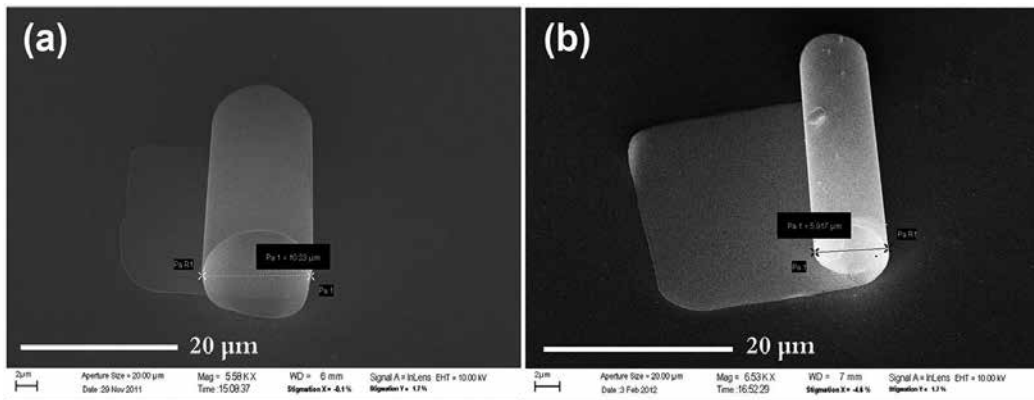


Figure 5. Effect of anodization of the Ti layer on the radius of the Ti/FeGa/Au film. (a) Original microtube, (b) anodized microtube. [48].

In our experiments, we used anodizing to completely oxidize Ti layer in already formed microtubes. A thin layer of Au was used to protect magnetic films from oxidation. The results of the experiment, displayed in **Figure 5**, show that the stresses from Ti layer, converted into TiO₂, reduced the diameter of the tubes to about a half of its original value. It was estimated that the strain associated with the oxidation was about 1% [48]. An interesting approach would

be to design processes in which magnetic metals such as Ni or Fe are chemically altered into magnetic compounds such as antiferromagnetic NiO or magnetite (Fe_3O_4). This would allow engineering stresses in the structures simultaneously with their magnetic properties.

2.2. Controlling direction of self-assembly

As demonstrated by the origami, the same flat shape, such as rectangle, can be used to create hundreds of the origami figures. What differentiates these shapes is the sequence and direction in which the original shapes were folded. The fundamental question arises how we can control direction of bending or twisting of the flat patterns in micro- and nanoscale?

First of all, the shape itself may define the direction in which deformation occurs. In our early experiments with rectangular patterns of magnetic films grown on top of PMMA photoresist, we observed that only the longer edges of the AuCo film patterns rolled and formed long double tubes as shown in **Figure 6(a)**. This tendency can be interpreted in terms of the bending moment which for the films with uniform in-plane stresses is proportional to the length of the edge. Thus, when the etching progresses uniformly from all sides, the bending of longer edges prevails. The self-rolling of the same pattern will progress differently if a part of the pattern is attached to the substrate at the short edge, which prohibits rolling of the shorter edge. However, the constraint may not be effective for the rectangles with very large aspect ratio of the sides. Also, rigid parts of the patterns, such as thicker walls of origami figures from **Figure 2**, can act as constraints on bending the patterns. A theory of deformations of thin bilayered films has been developed by Cendula et al. [49]. They predicted that for certain stress gradient level a regular wrinkling is expected rather than bending. Computer modeling can be used for predicting formation of origami figures from more complex film patterns.

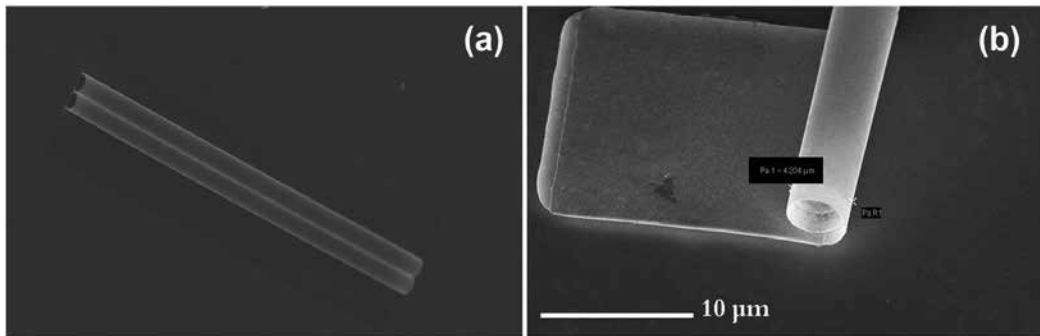


Figure 6. (a) Free-standing double tube of Cu/Co bilayer and (b) self-rolling of Ti/Ni bilayer which is attached at one end to the substrate and forms a single microtube.

Control of rolling direction is easier to achieve in heteroepitaxial structures. Prinz et al. [37] took advantage of different etching rates of Si in different crystallographic directions to fabricate microtubes or helical springs from GeSi/Si film patterns, which were deposited at different angles with respect to the crystallographic directions. Elegant experimental results by Li [50] illustrate different stages of the process of formation of an $\text{In}_{0.3}\text{Ga}_{0.7}\text{As}/\text{GaAs}$ microtube

as the etching of the sacrificial layer progresses. They also demonstrate that anisotropic elastic properties in combination with selective anisotropic etching can be used to fabricate variety of three-dimensional structures by depositing film patterns at different angles with respect to (001) direction of the GaAs substrate.

It is also possible to achieve anisotropic lateral elastic properties of polycrystalline films by engineering their microstructure. This goal can be achieved by depositing films on tilted substrates. The angular deposition results in anisotropic magnetic properties [51]. Another option is to take advantage of nanocomposites. For instance, aligned carbon nanotubes embedded in polymer or magnetic film can control the pitch of the helical structures depending on the angle between the pattern and the direction of the enforcing elements (see **Figure 7**).

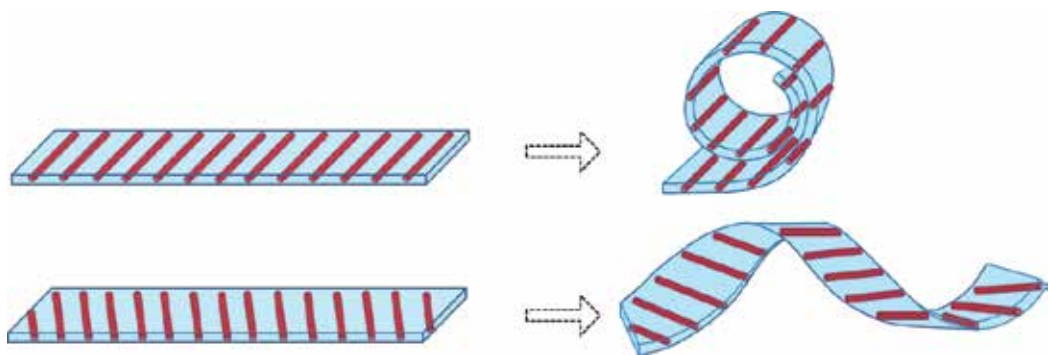


Figure 7. A concept of using anisotropic properties of composite materials to control rolling direction.

Finally, the external stresses applied to the substrates during the deposition are capable of providing a control over anisotropic film strains. The only inconvenience of this approach is the necessity of varying the stress level or direction inside a vacuum chamber, or preventing film contamination if the stresses are varied outside the chamber.

2.3. A sacrificial layer

Although it has been demonstrated that it is possible to assemble micro-origami structures on the air/water interface [52], vast majority of techniques uses solid sacrificial underlayers to build patterns on top of them.

In the case of the amorphous and polycrystalline sacrificial micro-origami structures, there are two fundamental requirements:

(a) The sacrificial layer must form a smooth surface, promote proper growth of the film, and enable patterning. It is worth mentioning that the microstructure of the polycrystalline films may strongly depend on the type of a substrate. Metals usually form smooth films when grown on top of a metal or semiconductor surface; however, when deposited on some dielectrics or organic materials they may exhibit enhanced roughness or columnar growth. An example is shown in **Figure 8**. The growth of the films can usually be improved by increasing the

temperature of the substrate with the sacrificial layer, but it can create a problem with some organic sacrificial layers which melt at relatively low temperatures.

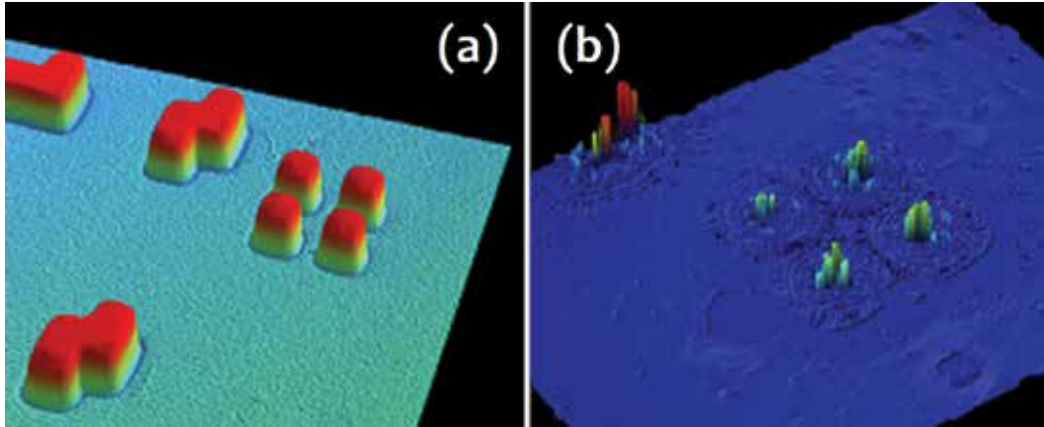


Figure 8. (a) Al/Pt film pattern deposited on top of photoresist and (b) the same bilayered film deposited on top of glucose film (images obtained by optical profiler).

The sacrificial layer should also be insensitive to the agents used in the patterning process, so that the film can be released only after the pattern is defined. Depending on the patterning technique, the agents used for dry etching (reactive or corrosive gasses) or wet etching (water, acetone, and acids) should not attack the sacrificial layer.

(b) The sacrificial layer must be from the material which has markedly different etching properties than the film pattern. An excellent example is the ratio of HF solution etching rate of GaAs to AlAs exceeding 10,000. This sacrificial layer was used by Prinz et al. [35] and Li [50] to fabricate free standing semiconductor nanostructures. Even much smaller selectivity of 1:80 for Si/SiGe system etched by the 3.7 wt% of NH_4OH allowed fabrication of high-quality micro-origami patterns. Reactive gases, such as xenon difluoride (XeF_2) vapor and CHF_3/O_2 , were used to etch Si substrate [43] and to remove Ge layer [36], respectively. Polycrystalline magnetic films can be grown on a photoresist layer which can be dissolved by acetone [52]. Aluminum sacrificial surface layer was used to grow Au/Ti bilayers and was etched with KOH-based solution [47]. Our group used 50 nm thick Cu film on Si as a sacrificial layer to deposit magnetic films [53, 54].

A disadvantage of wet etching method is that the surface tension or capillary forces of liquids used for the etching can interfere with the residual stresses and can prevent deformations of the pattern or even crack the pattern. The test for the strength of the surface tension forces in microscale is the fact that the capillary forces inside the tubes are able to collapse already formed tubes when water trapped inside the tube dries [36]. Potential solution to this problem can be the usage of supercritical conditions by elevating the temperature of water to a boiling point. Another option is to use organic solvents with much lower surface tension. Using gases

instead of liquids removes this problem. However, the gasses used for etching are highly corrosive and toxic.

Finding a proper sacrificial layer for the heteroepitaxial systems is even a greater challenge. In addition to the requirement of high selectivity, the sacrificial layer must also be a part of the heteroepitaxial system. This means that it must match both the structure of the substrate and the films which are grown on top of it. Satisfying all these three requirements simultaneously is a tough task.

This indicates a need for a search for new sacrificial layers for heteroepitaxial structures which promote single crystal growth and yet can be selectively etched. Ideally, such layers would be eco- and biofriendly.

Here, we would like to point at two prospective sacrificial layers. Single crystal NaCl (salt) sacrificial layer is a good candidate to grow magnetic films with cubic crystal structure. NaCl was a popular substrate for deposition of transition metal films in the 1960s [55], but it was not implemented in industrial processes because of its hygroscopic properties. Ironically, the same property predisposes NaCl films for the micro-origami applications. Reflection high-energy electron diffraction (RHEED) images of the MgO substrate, NaCl layer, and Cr film are presented in **Figure 9**.

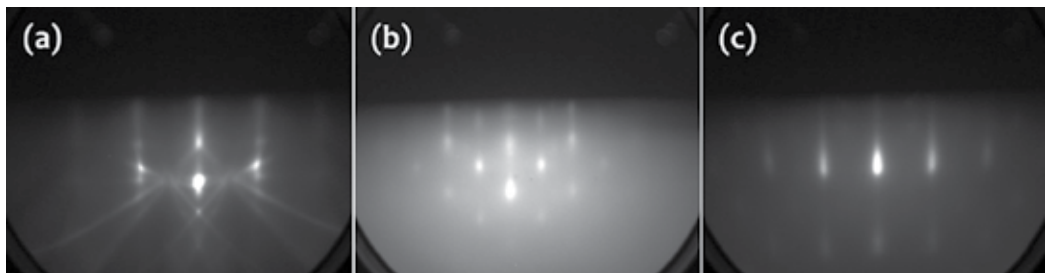


Figure 9. RHEED images of (a) the MgO substrate with 5 nm MgO film, (b) 170 nm NaCl film, and (c) 15 nm Cr film on top of NaCl sacrificial layer.

The following procedure for the electron beam evaporation was used to grow heteroepitaxial structures with NaCl sacrificial layer:

- A thin layer of MgO (typically 5 nm) was deposited on MgO substrate to improve the quality of the surface.
- NaCl was evaporated at the rate of 0.05 nm/s at 350°C.
- Various magnetic and nonmagnetic transition metal films, such as Fe, Cr, V, and Ag, were grown epitaxially on top of NaCl.

Other substrates, such as GaAs and deposition methods can also be used to grow heteroepitaxial structures with NaCl layer. This layer is biofriendly and dissolves in water; therefore, it has a great potential for biomedical applications of micro-origami structures. Glucose films which can be made by spin coating of water solutions on different substrates are also an

interesting option for biomedical applications. However, the growth of some films may lead to unexpected results, as shown in **Figure 8**.

Zn and Mg are interesting materials for the sacrificial layers because they sublime in vacuum at relatively low temperatures. Therefore, they can be removed in vacuum chamber by increasing the substrate temperature. This approach does not require corrosive gasses or liquids which affect the release of the micro-origami structures because of the surface tension. We carried out initial studies on growth and sublimation of Zn films. Zn films have hexagonal structure and a reasonably good match to lattice constants of Ru, Ti, graphene, and, most importantly, magnetic films of Co. Although literature data [56] indicate that the temperature of sublimation of Zn is 250°C, the actual sublimation temperature was found to be substantially lower (below 200°C) in ultra-high vacuum conditions. Our RHEED studies revealed that single crystal or highly textured Zn films can be grown on Ru and Ti films deposited on sapphire substrates. It was also found that the thin film growth is strongly affected by the deposition conditions. Different morphologies of the Zn film due to different growth conditions, such as deposition rate and the temperature of the substrate are shown in **Figure 10**. The best results were achieved for the deposition of Zn on Ti film at deposition rate of 0.02 nm/s and at temperatures above 100°C.

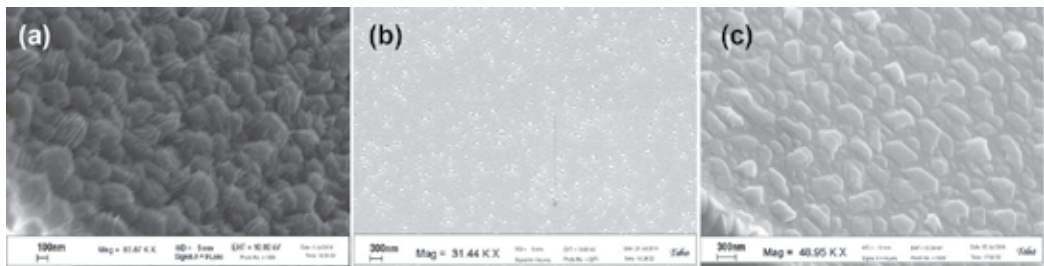


Figure 10. Zn film on Ru deposited (a) at room temperature and rate of 0.02 nm/s, (b) room temperature and 0.1 nm/s, and (c) at 100°C at 0.05 nm/s.

3. Link between the shape and magnetic properties

A discussion on static magnetic properties of magnetic scrolls has been initiated in the articles by Müller et al. [51, 57]. Angular deposition of Au/Co/Au films resulted in the in-plane magnetic anisotropy of rectangular thin film patterns. They ascribed it to stress-induced anisotropy in the as-deposited films. They also observed changes in the shape of the hysteresis loop and evolution of magnetic domain structure when the film patterns rolled and formed microtubes.

The films fabricated in our group [48, 53, 54] were isotropic in the film plane. Therefore, the effect of the self-rolling on the static magnetic properties was easier to interpret than for the

anisotropic films. Two kinds of magnetic microtubes were fabricated using the same technology described below.

First, the $50\ \mu\text{m} \times 50\ \mu\text{m}$ holes were defined in a PMMA photoresist using exposure of the photoresist to deep UV light through as mask. Thin film of Cu was deposited by sputtering on the Si wafer with (001) orientation. During a lift-off process the Cu film pieces on top of photoresist were removed by ultrasonication of the wafer immersed in acetone. The remaining $50\ \text{nm}$ thick Cu squares served as sacrificial layer. Another mask with $20\ \mu\text{m} \times 50\ \mu\text{m}$ rectangles was used to deposit the trilayered Ti/GaFe/Au and Ti/Ni/Au films. This mask was aligned in such a way that the majority of the area of the rectangular holes in photoresist was on top of the Cu squares and a smaller part on exposed Si. After deposition of the trilayer and the second lift-off process the rectangles remained on top of Cu patches, which were partially attached to Si, as presented in **Figure 11(a)**. During selective etching of the sacrificial Cu underlayer, the films with residual stresses, caused by the grain coalescence, self-rolled, and formed magnetic microtubes with 3–4 turns, diameter of 5–10 μm , and the length of 20 μm (**Figure 11b**).

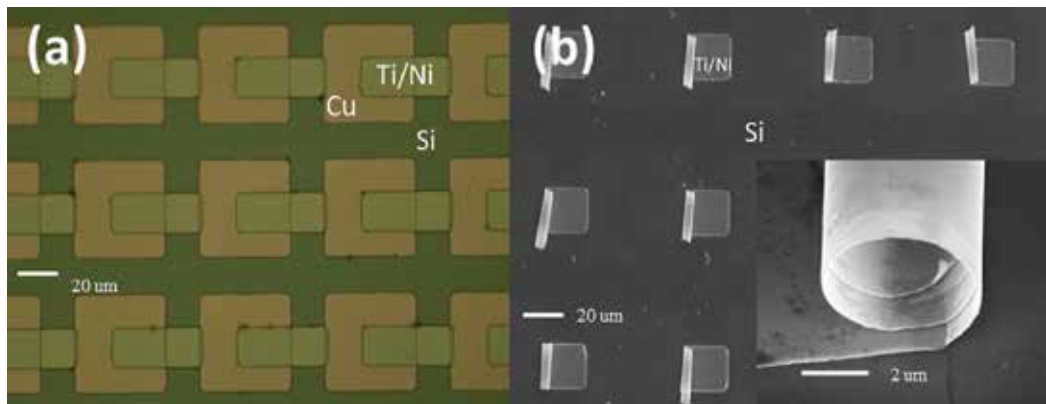


Figure 11. (a) Optical microscope image of an array of flat rectangular film patches of Ti (20 nm)/Ni (30 nm)/Au (2 nm) on top of Si wafer and partially overlapping with sacrificial Cu films squares. (b) Scanning microscope image of the array of magnetic scrolls and a magnified image of a single scroll (in the inset) formed after selective etching of Cu.

The same masks were used to deposit Ti/FeGa/Au films. A thin layer of gold was used to protect magnetic layer against oxidation. The static magnetic properties were characterized by means of vibrating sample magnetometry. The hysteresis loops of the microtubes with Ni are presented in **Figure 12**. The magnetic field was applied in two transverse directions in the substrate plane. The direction marked as 0° is the direction of the axis of the tubes formed from the patterns and the 90° is transverse to the tubes. Hysteresis loops (black lines) representing magnetization of flat patterns in these two directions are almost identical. Slight differences between the curves can be attributed to the shape anisotropy of the rectangular shapes of the patterns. Similar statement refers to the hysteresis loops of the flat patterns of the Ti (20 nm)/(GaFe 40 nm)/(Au 15 nm) film. The coercive field of the patterns with Ni was 13.4 Oe, whereas it was 60 Oe for the GaFe films.

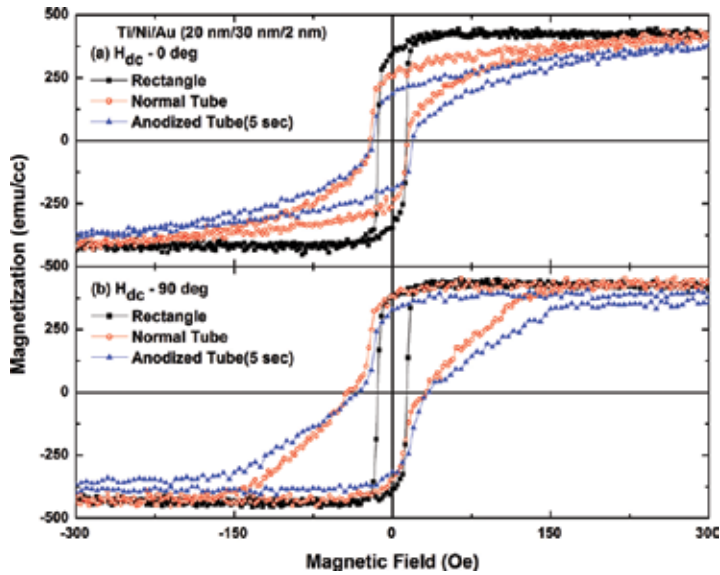


Figure 12. Magnetization hysteresis loops of rectangular film patterns $20\ \mu\text{m} \times 50\ \mu\text{m}$ with Ni layer (black line), microtubes (red line), and anodized microtubes (blue line). Top part refers to the 0° angle and the bottom to 90° angle of the applied magnetic field. (Reproduced with permission from Ref. [48].)

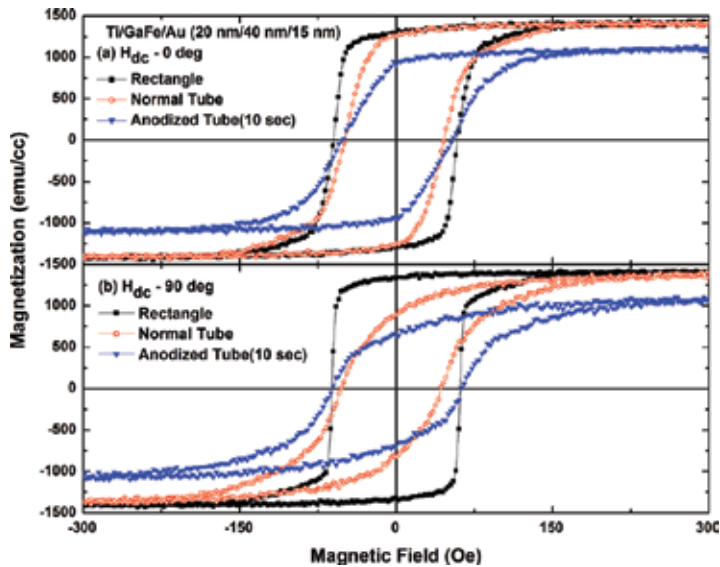


Figure 13. Magnetization hysteresis loops of rectangular film patterns $20\ \mu\text{m} \times 50\ \mu\text{m}$ with GaFe layer (black line), microtubes (red line), and anodized microtubes (blue line). Top part refers to the 0° angle and the bottom to 90° angle of the applied magnetic field. (Reproduced with permission from Ref. [48].)

Marked differences between the magnetization loops for the two directions of magnetizing field were observed for both types of magnetic materials (red symbols curves in **Figures 12** and **13**). This is the result of the change of the shape and evolution of strains of the patterns undergoing deformation after release from the substrate.

As discussed in Ref. [48], the behavior of the GaFe films could be interpreted in terms of the shape anisotropy of the microtubes for which the technical magnetization saturation is achieved at lower fields for the field applied along the easy magnetization axis (along the tubes), whereas the loops for the hard direction (perpendicular to the tubes) are tilted and approach saturation magnetization at higher fields. However, the behavior of Ni tubes opposes that of GaFe, in spite of similar contribution from the shape anisotropy. In addition, both types of materials exhibit opposite trends in the change of the coercive field. The coercivity of Ni tubes almost triples for the field applied at 90° while it decreases by about 30% for GaFe films as compared to the rectangular patterns measured in the same direction. These facts prove that the change of shape and associated shape anisotropy alone is unable to explain the changes of magnetic properties.

An important distinction between these two magnetic materials is their magnetostriction. Ni has negative linear magnetostriction coefficient of -38×10^{-6} , whereas GaFe has positive coefficient of magnetostriction of about $+70 \times 10^{-6}$. For this reason, the magnetization responds in different ways when strains in the applied magnetic field vary by about 1% during self-rolling process.

Additional evidence of the importance of the magnetoelastic contribution to the magnetization change is that the differences between the materials continue to diversify when Ti layer undergoes anodization. Expanding TiO, formed from Ti layer, exerts additional stress on the magnetic layers and reduces the diameter of the tubes by about 50%, which is also reflected in magnetic properties. The time of the anodizing was adjusted in the range from 10 to 25 s so that the entire layer of Ti could be converted into Ti oxide. The reduced saturation magnetization for the anodized samples (see **Figures 12** and **13**) indicates that the oxidation partially affected GaFe and Ni. The saturation magnetization was unaffected by the fabrication processes (coating with PMMA, using a water solution of a developer, and washing with acetone) because of the presence of a protective layer of gold.

Another magnetic method, which gives even more insight into residual stresses, is based on high-frequency measurements of spin dynamics. Spin precession at Ferromagnetic resonance (FMR) is affected by local magnetic field H_{eff} , where demagnetizing field H_D and stress-induced anisotropy field H_σ , associated with stress σ , contribute. The relation derived from Landau-Lifshitz-Gilbert equation for magnetically isotropic material with magnetostriction λ_s , gives the relation between the stress-induced anisotropy field $H_\sigma = 2\sigma\lambda_s/M_s$ due to stress σ , saturation magnetization M_s of the material, applied bias field H_A and a frequency f_r of microwave absorption at resonant conditions:

$$f_r = \frac{\gamma}{2\pi} \sqrt{(H_A + H_D + H_\sigma)(M_s + H_A + H_D + H_\sigma)} \quad (2)$$

where γ is a gyromagnetic ratio of the magnetic material. The distribution of internal stresses in magnetostrictive materials determines the linewidth of the resonant curve. Examples of FMR spectra for rectangular patterns of Ni films with thickness of 30 nm and for corresponding microtubes are presented in **Figure 14**. The resonant fields are approximately the same for the two orientations of the in-plane applied field. Larger resonant field for the out-of-plane direction of the applied field results from large demagnetization factor for this orientation. The FMR absorption spectra become more complex for rolled-up patterns. The resonance peak along the tube axis remains unaffected, except of some broadening. However, the curves measured with the field applied transverse to the microtubes are markedly different. In particular, the intensity of the absorption measured normal to the substrate decreases and additional peak forms at lower fields. This peak can be attributed to the microtubes. The high field peak may result from the part of the flat patterns which did not roll—they attach the tubes to the substrate. In the Ni tubes, the “unrolled” area was about 40% of the rectangles, but we were able to reduce it to 10% for GaFe films by adjusting technological parameters.

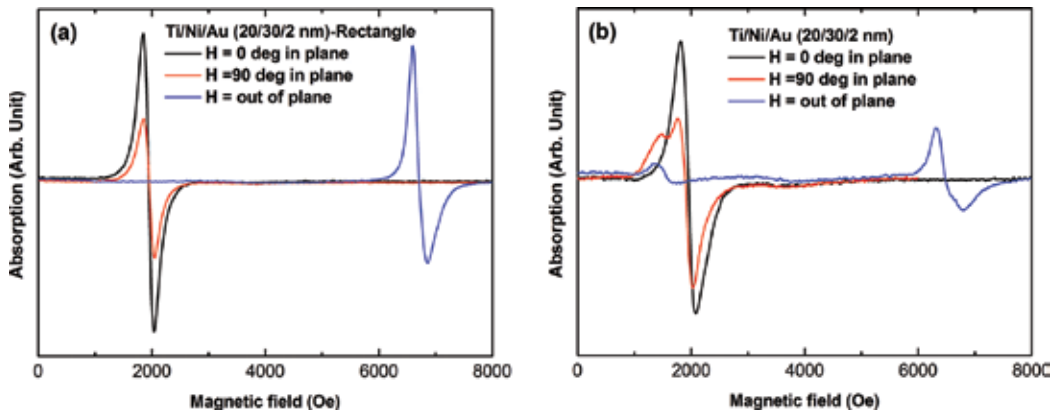


Figure 14. Ferromagnetic resonance spectra of the rectangular patterns of Ni films (a) as compared to the spectra of the microtubes (b) measured with the field out of the substrate plane (blue curves) and two directions in the film plane (field at 0° along the tubes and at 90°). (Reproduced with permission from Ref. [54].)

More detailed studies of spin dynamics in magnetic microtubes made by Balhorn et al. [42] involve spin wave properties in multiwall magnetic microtubes prepared by micro-origami techniques. They observed a series of four resonant peaks which corresponded to the constructive interference of Damon-Eshbach-type spin waves traveling along the circumference of the multiwall tubes of 20 nm permalloy film. The resonances could be tuned by the diameter and the number of turns of the tubes.

Magnetic layers can also be a part of multiferroic or magnetoelectric composites. These materials exhibit coupling between polarization and magnetization through the interfacial stresses between piezoelectric and magnetostrictive layer. Changes of external magnetic field produce magnetostrictive strains in the magnetic material which are transferred to the mechanically coupled piezoelectric and result in changes of polarization. On the other hand,

electric field applied to the piezoelectric layer produces piezoelectric strains which are transferred to the magnetic material and change its magnetization [58]. A common problem in the multilayered films is that the magnetoelectric functions are greatly reduced because either piezoelectric or magnetostrictive layer is attached to a massive substrate which prevents straining of the materials adhering to Origami technology. This is called a clamping effect. An advantage of free-standing micro-origami structures is that they do not restrict the exchange of stresses between the piezoelectric and magnetic phases and make the stress-mediated mechanism of electric and magnetic energies highly effective. In addition, magnetic scrolls occupy much smaller area than the cantilevers with the same mass. Piezoelectric/ferromagnetic composite Au (5 nm)/AlN (20 nm)/CoFe (40 nm)/Au (5 nm) form microtubes when released from the substrate [54].

4. Functions and applications

4.1. Functionality of the micro-origami structures

Converting flat pattern into micro-origami figures increases their functionality and potential for applications. For example, when magnetostrictive films are attached to the rigid substrate, the only response of the magnetic material to the applied field is a change of its magnetization. For a free-standing micro-origami structure, in addition to the change of magnetization, magnetic force can actuate the structure; it can give rise to a change of shape due to magnetostrictive strains and external strains can vary magnetization, as well.

As already mentioned in the previous section, there is a mutual link between the magnetism and shape of the micro-origami figures. This feature can be used for tuning magnetic properties or resonant microwave absorption of the micro-origami patterns. The shape of the hysteresis loops, magnetic anisotropy, and coercivity can be controlled by fabricating materials with different shapes rather than changing the composition of the magnetic material. Magnetic shape anisotropy can control anisotropic behavior of nonmagnetostrictive materials, whereas residual stresses in the magnetic layers play primary role in magnetostrictive structures. Frequency of ferromagnetic resonance and frequency of spin wave modes can be controlled by the number of turns and the diameter of the microtubes. Because the micro-origami shapes can be fabricated in the form of arrays of identical complex objects, they may exhibit interesting responses to the electromagnetic radiation.

Helicity of magnetic scrolls has been utilized to make meta-materials with negative index of refraction [59]. Similar arrays of free-standing helical structures were envisioned as the way of enhancing magnetic field for magnetic resonance imaging [60].

Micro-origami techniques provide an efficient method of self-assembly of micro- and nano-structures. Just to exemplify this statement, we propose in **Figure 15** the sequence of processes of assembly of a microscopic electromagnet consisting of a coil with a hollow magnetic core.

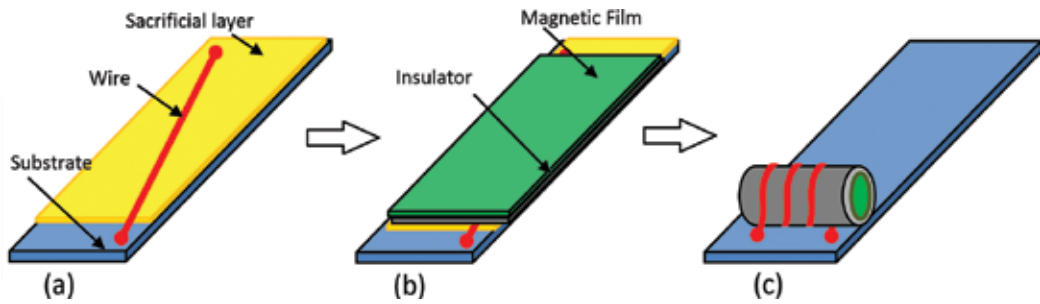


Figure 15. Three stages of fabrication of three-dimensional inductor: (a) Deposition of a wire on top of a sacrificial layer, (b) deposition of insulating and magnetic layers, and (c) self-assembly.

Multiple turns can be fabricated by adding more wires or using diagonal direction of self-rolling to produce helical springs like in Refs. [50] and [61].

It greatly simplifies fabrication of three-dimensional patterns, which usually would require many more masking and deposition processes, angular deposition, and deep etching. In addition to self-assembly of structures attached to the substrate, micro-origami figures disconnected from the substrate can serve as building blocks for meta-materials, where magnetic elements of the figures or surface tension at hydrophilic parts can be used to put these blocks together in two- or three-dimensional networks [26]. Here, tessellation methods of origami patterns can be used.

4.2. Prospective applications

Micro-origami techniques have a great potential for numerous applications, although they have not been implemented in large-scale production, yet.

Magnetic and magnetoelastic properties of the micro-origami patterns can be used in various magneto-electro-mechanical systems (MEMS) such as stress or strain sensors, microscopic actuators, magnetic field sensors, and optical shutters [62]. As described in the previous section, enhanced performance of magnetoelectric functions is expected in the free-standing micro-origami patterns as compared to the planar structures on thick substrates. This gives a promise for increased sensitivity of the multiferroic composites for magnetic field sensors [63], which have potential to reach the sensitivity of SQUID magnetometer. Another potential microelectronic application is in microwave devices based on laminated multiferroic composites such as filters where the frequency of microwave absorption peak at ferromagnetic resonance can be tuned by the means of voltage applied to the piezoelectric layer [64]. Micro-origami design can reduce size and increase tunability of laminated multiferroic composites in such devices.

Because of excellent mechanical performance of microtubes [57], the self-assembly of micro-origami structures can be used to build parts of microfluidic systems. They can serve as ducts and microchambers for chemical reactions. Magnetic and magnetostrictive properties of the tubes can be advantageous for the liquid pressure sensing or measuring flow of liquids or

gases [65]. Micro-origami techniques can also be used to assemble parts of micropumps and valves in microfluidic systems, where either magnetoelastic or magnetostatic energies can be used to actuate micromotor or control shutters.

The most recent publications on micro-origami structures emphasize prospective applications in the biomedical field and biotechnology. First of all, the micro-origami methods are capable of fabricating biomimetic materials. Magnetic materials are envisioned as candidates for targeted drug delivery [23]. Different magnetic cages [21, 23] can be loaded with drugs, dragged with the help of magnetic force to the infected organs, and released in the location where they are the most effective. The targeted delivery of drugs can be achieved with the assistance of microswimmers [16, 66], which are able to move against blood stream. Helical magnetic structures made by micro-origami techniques can function as microdrillers to remove blood clots in the veins when remotely activated by a rotating magnetic field [67]. Microgrippers and magnetic tweezers take advantage of self-folding of micro-origami patterns, as mentioned in the introduction [29].

More advanced devices which combine microtubes with giant magnetoresistive sensors or semiconducting chemical sensors are available [68, 69]. Magnetoresistive sensors prepared by micro-origami method were capable of detecting single magnetic nanoparticle passing through a microtube. This will allow a precise control of functionalized magnetic nanoparticles for drug delivery or hyperthermia.

5. Conclusions

Micro-origami techniques are very versatile and can be applied to various materials including magnetic materials. They are envisioned as a very powerful self-assembly method. Unlike traditional origami, where folding of a paper is done by hands, micro- and nano-origami methods take advantage of forces in the microscale, such as surface tension or residual stresses, to shape materials by bending, twisting, and folding thin film patterns. The curvature of the structures and direction of deformation can be controlled in wide range by the magnitude of the residual or interfacial stress, elastic properties of the patterns, the shape, and thickness of the film patterns. This makes possible fabrication of complex three-dimensional architectures from flat patterns, which are released from the substrate by selective wet etching, reactive gas etching, dissolving, or sublimation of the sacrificial layer.

Magnetic micro-origami has a special place among various micro-origami designs. Magneto-static interactions between magnetic parts of the structures and/or external magnetic field can be used to assemble building blocks into meta-materials or actuate parts of microrobots. The external field gradient can be used to direct various micromagnetic cages loaded with drugs to infected organs, where the drugs will be released. Microswimmers take advantage of alternating fields to move in liquids in controlled way and rotating magnetic field can be used to rotate microdrills to open blood clots in veins.

The magnetic properties of the micro-origami structures can be affected by their shape in three ways:

– Shape magnetic anisotropy varies when the flat patterns form three-dimensional structures. An example was provided where flat patterns possessed isotropic magnetic properties when measured with the field along different directions in the film plane, but magnetic hysteresis loops and ferromagnetic resonance curves showed marked differences for the transverse configuration of the applied fields when magnetic patterns scrolled and formed microtubes.

– Magnetoelastic properties affect magnetization of magnetostrictive films when the stress level and/or direction in the films change. This refers to the relaxation of residual stresses in the magnetic material, as well as external stresses from the adhering nonmagnetic layers exerted on magnetic layer when the multilayered film patterns bend after release from substrate. The stress-induced anisotropy affects domain structure and magnetization processes. For example, self-rolling of magnetic films with positive (FeGa) and negative magnetostriction (Ni) lead to different trends in magnetization changes as evidenced by **Figures 12 and 13**.

– The change of chemical composition of magnetic films can alter magnetic properties. For example, the ferromagnetic Ni subjected to oxidation changes into antiferromagnetic NiO, and soft magnetic Fe may evolve into magnetite (Fe_3O_4) with larger magnetocrystalline anisotropy, coercivity, and saturation field, but reduced saturation magnetization. The changes of magnetic properties of chemically altered films can be associated with enhancement of residual stresses which are responsible for the formation of the micro-origami patterns. Thus, in certain cases the changes of magnetic properties can promote change of the shape if the chemical changes are followed by the phase or composition change which produces deformation.

The changes of magnetic shape anisotropy and stress-induced anisotropy, associated with the deformation of the film patterns, provide a convenient method of tuning magnetic properties by shape design.

The coupling between elastic and magnetic properties is mutual, i.e., the magnetization changes produce magnetostrictive strains but external stresses can change magnetization. Free-standing micro-origami patterns have increased functionality. Bending of magnetostrictive layers can be used for stress, strain, or pressure sensing. Straining magnetostrictive layers in magnetoelectric composites is useful for tuning ferromagnetic resonance frequency in microwave filters by voltage applied to the piezoelectric layer. On the other hand, magnetostrictive strains generated in multiferroic composites by external fields can be converted into voltage and serve for the magnetic field sensing. Magnetoelectric performance of micro-origami structures is expected to be superior to that of flat patterns on substrates because of lack of the clamping effect. Giant magnetoresistive structures integrated with the microfluidic ducts in a single micro-origami assembly process are capable of detecting a single nanoparticle flowing through a duct.

The micro- and especially nano-origami architectures have great potential for biomedical applications. Majority of publications on magnetic origami concern objects with the radius of a few micrometers. Future applications of the micro-origami in biotechnology may require reduction of the size of magnetic structures to sub-micrometers or nanometers and combining them with organic materials. Also, the preference for these applications is for biocompatible

magnetic materials such as magnetite and biofriendly sacrificial layers. Initial results presented here look promising. More information about nano-origami techniques is available in the recent publication by Cavallo and Lagally [70].

Acknowledgements

The authors acknowledge contributions from Dr. Seonggi Min and summer interns Adam Wang and Brandon Buchanan who carried out research on NaCl and Zn sacrificial layers. We also acknowledge support through grants LEQSF-EPS(2012)-Pfund-302, NSF EPSCoR LA-SiGMA project under award #EPS-1003897 with additional support from the Louisiana Board of Regents through contract NSF (2010-15)-RII-UNO.

Author details

Leszek Malkinski* and Rahmatollah Eskandari

*Address all correspondence to: lmalkins@uno.edu

Department of Physics and Advanced Materials Research Institute, University of New Orleans, New Orleans, Louisiana, USA

References

- [1] Hatori, K. History of Origami in the East and the West before Interfusion. In: Wang-Iverson P, Lang RJ, Yim M, editors. *Origami 5: Fifth International Meeting of Origami Science, Mathematics, and Education*. CRC Press, Boca Raton, FL, USA; 2011: 3–11. DOI: 10.1201/b10971.
- [2] Beech, R. *The Practical Illustrated Encyclopedia of Origami: The Complete Guide to the Art of Paperfolding*. 1st Ed. Lorenz Books, London, UK; 2009.
- [3] Min CC, Suzuki H. Geometrical properties of paper spring. In: Mitsuishi M, Ueda K, Kimura F, editors. *Manufacturing Systems and Technologies for the New Frontier. The 41st CIRP Conference on Manufacturing Systems May 26–28, Tokyo: 2008: 159–162*. DOI: 10.1007/978-1-84800-267-8
- [4] Wang-Iverson P, Lang RJ, Yim M, editors. *Origami 5: Fifth International Meeting of Origami Science, Mathematics, and Education*. United States: CRC Press; 2011: 335–370.
- [5] Lang RJ. Robert J. Lang Origami [Internet]. 2016. Available from: <http://www.langorigami.com/article/treemaker>.

- [6] Origami History [Internet]. Available from: <http://japanese-old-customs.weebly.com/origami.html>
- [7] Lang RJ. *Origami in Action: Paper Toys That Fly, Flap, Gobble, and Inflate*. 1st ed. St. Martin's Griffin Press, New York: 1997.
- [8] Origami Resource Center, Origami Science [Internet]. 2016. Available from: <http://www.origami-resource-center.com/origami-science.html>.
- [9] Paul KB, Malkinski L. Friction on the microscale. *Review of Scientific Instruments*, 2009; 80:085110–1. DOI: 10.1063/1.3212672.
- [10] Tolley MT, Felton SM, Miyashita S, Aukes D, Rus D, Wood RJ. Self-folding origami: Shape memory composites activated by uniform heating. *Smart Materials and Structures*. 2014; 23(9):094006. DOI:10.1088/0964-1726/23/9/094006
- [11] Felton S, Tolley M, Demaine E, Rus D, Wood R. A method for building self-folding machines. *Science*. 2014;345(6197):644–646. DOI: 10.1126/science.1252610
- [12] Hubert A, Calchand N, Le Gorrec Y, Gauthier JY. Magnetic shape memory alloys as smart materials for micro-positioning devices. *Advanced Electromagnetics*. 2012;1(2): 75–84. DOI:10.7716/aem.v1i2.10
- [13] Yasu K, Inami M. POPAPY: Instant paper craft made up in a microwave oven. *Advances in Computer Entertainment*. Berlin Heidelberg: Springer; 2012: pp. 406–420. DOI: 10.1007/978-3-642-34292-9_29
- [14] Guberan C., Hydro-Fold by ECAL [Internet]. 2012. Available from: <http://www.christopheguberan.ch/Hydro-Fold>.
- [15] Fusco S, Sakar MS, Kennedy S, Peters C, Bottani R, Starsich F, Mao A, Sotiriou GA, Pané S, Pratsinis SE, Mooney D. An integrated microrobotic platform for on-demand, targeted therapeutic interventions. *Advanced Materials*. 2014;26(6):952–957. DOI: 10.1002/adma.201304098
- [16] Honda T, Arai KI, Ishiyama K. Micro swimming mechanisms propelled by external magnetic fields. *IEEE Transactions on Magnetics*. 1996;32(5):5085–5087. DOI: 10.1109/20.539498
- [17] Ishiyama K, Sendoh M, Arai KI. Magnetic micromachines for medical applications. *Journal of Magnetism and Magnetic Materials*. 2002;242:41–46. DOI:10.1016/S0304-8853(01)01181-7
- [18] Pawashe C, Floyd S, Sitti M. Modeling and experimental characterization of an untethered magnetic micro-robot. *The International Journal of Robotics Research*. 2009;28(8):1077–1094. DOI: 10.1177/0278364909341413
- [19] Vollmers K, Frutiger DR, Kratochvil BE, Nelson BJ. Wireless resonant magnetic microactuator for untethered mobile microrobots. *Applied Physics Letters*. 2008;92(14): 144103. DOI: 10.1063/1.2907697

- [20] Diller E, Giltinan J, Lum GZ, Ye Z, Sitti M. Six-degrees-of-freedom remote actuation of magnetic microrobots. In: Proceedings of Robotics Science and Systems Conference X. Berkeley, USA, July 12–16, 2014, DOI: 10.15607/RSS.2014.X.013.
- [21] Gagler R, Bugacov A, Koel BE, Will PM. Voxels: Volume-enclosing microstructures. *Journal of Micromechanics and Microengineering*. 2008;18(5):055025. DOI: 10.1088/0960-1317/18/5/055025
- [22] Miyashita S, Guitron S, Ludersdorfer M, Sung CR, Rus D. An untethered miniature origami robot that self-folds, walks, swims, and degrades. In: 2015 IEEE International Conference on Robotics and Automation (ICRA), Seattle, USA, May26–30, IEEE; 2015: pp. 1490–1496. DOI: 10.1109/ICRA.2015.7139386.
- [23] Gimi B, Leong T, Gu Z, Yang M, Artemov D, Bhujwala ZM, Gracias DH, Self-assembly three-dimensional radio frequency (RF) shielded containers for cell encapsulation. *Biomedical Microdevices*. 2005;7(4):341–345. DOI: 10.1007/s10544-005-6076-9
- [24] Fernandes R, Gracias DH. Self-folding polymeric containers for encapsulation and delivery of drugs. *Advanced Drug Delivery Reviews*. 2012;64(14):1579–1589. DOI: 10.1016/j.addr.2012.02.012
- [25] Leong TG, Lester PA, Koh TL, Call EK, Gracias DH. Surface tension-driven self-folding polyhedra. *Langmuir*. 2007;23(17):8747–8751. DOI: 10.1021/la700913m
- [26] Cho JH, Azam A, Gracias DH. Three dimensional nanofabrication using surface forces. *Langmuir*. 2010;26(21):16534–16539. DOI: 10.1021/la1013889
- [27] Randhawa JS, Gurbani SS, Keung MD, Demers DP, Leahy-Hoppa MR, Gracias DH. Three-dimensional surface current loops in terahertz responsive microarrays. *Applied Physics Letters*. 2010;96(19):191108. DOI: 10.1063/1.3428657
- [28] Cho JH, Keung MD, Verellen N, Lagae L, Moshchalkov VV, Van Dorpe P, Gracias DH. Nanoscale origami for 3D optics. *Small*. 2011;7(14):1943–1948. DOI: 10.1002/smll.201100568
- [29] Breger JC, Yoon C, Xiao R, Kwag HR, Wang MO, Fisher JP, Nguyen TD, Gracias DH. Self-folding thermo-magnetically responsive soft microgrippers. *ACS Applied Materials & Interfaces*. 2015;7(5):3398–3405. DOI: 10.1021/am508621s
- [30] Shenoy VB, Gracias DH. Self-folding thin-film materials: From nanopolyhedra to graphene origami. *MRS Bulletin*. 2012;37(09):847–854. DOI: 10.1557/mrs.2012.184
- [31] Malachowski K, Jamal M, Jin Q, Polat B, Morris CJ, Gracias DH. Self-folding single cell grippers. *Nano Letters*. 2014;14(7):4164–4170. DOI: 10.1021/nl500136a
- [32] Freund LB, Suresh S. *Thin Film Materials: Stress, Defect Formation and Surface Evolution*. Cambridge University Press, Cambridge, UK; 2004. DOI: 10.1017/CBO9780511754715.

- [33] Koch R. The intrinsic stress of polycrystalline and epitaxial thin metal films. *Journal of Physics: Condensed Matter*. 1994;6(45):9519. DOI: 10.1088/0953-8984/6/45/005
- [34] Songmuang R, Deneke C, Schmidt OG. Rolled-up micro-and nanotubes from single-material thin films. *Applied Physics Letters*. 2006;89(22):223109. DOI: 10.1063/1.2390647
- [35] Prinz VY, Vorob'ev AB, Seleznev VA. Three-dimensional structuring using self-rolling of strained InGaAs/GaAs films. 28th International Symposium of Compound Semiconductors, Tokyo, Japan, 1–4 October 2001, Institute of Physics Conference Series, 2002; 170:319–323.
- [36] Prinz VY. Precise semiconductor, metal and hybrid nanotubes and nanofibers. *Nano-engineered Nanofibrous Materials*. 2004;169:47. DOI: 10.1007/978-1-4020-2550-1_1
- [37] Golod SV, Prinz VY, Mashanov VI, Gutakovsky AK. Fabrication of conducting GeSi/Si micro-and nanotubes and helical microcoils. *Semiconductor Science and Technology*. 2001;16(3):181–185. DOI: 10.1088/0268-1242/16/3/311
- [38] Prinz VY. A new concept in fabricating building blocks for nanoelectronic and nanomechanic devices. *Microelectronic Engineering*. 2003;69(2):466–475. DOI: 10.1016/S0167-9317(03)00336-8
- [39] Seleznev VA, Prinz VY, Aniskin VM, Maslov AA. Generation and registration of disturbances in a gas flow. 1. Formation of arrays of tubular microheaters and micro-sensors. *Journal of Applied Mechanics and Technical Physics*. 2009;50(2):291–296. DOI: 10.1007/s10808-009-0039-5
- [40] Malkinski L, O'Keevan T, Camley RE, Celinski Z, Wee L, Stamps RL, Skrzypek D. Exchange bias in the Fe/KCoF₃ system: A comprehensive magnetometry study. *Journal of Applied Physics*. 2003;93(10):6835–6837. DOI: 10.1063/1.1558653
- [41] Schwaiger S, Bröll M, Krohn A, Stemmann A, Heyn C, Stark Y, Stickler D, Heitmann D, Mendach S. Rolled-up three-dimensional metamaterials with a tunable plasma frequency in the visible regime. *Physical Review Letters*. 2009;102(16):163903. DOI: 10.1103/PhysRevLett.102.163903
- [42] Balhorn F, Mansfeld S, Krohn A, Topp J, Hansen W, Heitmann D, Mendach S. Spin-wave interference in three-dimensional rolled-up ferromagnetic microtubes. *Physical Review Letters*. 2010;104(3):037205. DOI: 10.1103/PhysRevLett.104.037205
- [43] Moiseeva E, Senousy YM, McNamara S, Harnett CK. Single-mask microfabrication of three-dimensional objects from strained biphases. *Journal of Micromechanics and Microengineering*. 2007;17(9):N63. DOI: 10.1088/0960-1317/17/9/N01
- [44] Jackman RJ, Brittain ST, Adams A, Prentiss MG, Whitesides GM. Design and fabrication of topologically complex, three-dimensional microstructures. *Science*. 1998;280(5372):2089–2091. DOI: 10.1126/science.280.5372.2089

- [45] Heczko O, Scheerbaum N, Gutfleisch O. Magnetic shape memory phenomena. In: *Nanoscale Magnetic Materials and Applications*. Springer, USA. 2009; pp. 399–439. DOI: 10.1007/978-0-387-85600-1
- [46] Ventrice, CA, Jr, Geisler H. The growth and structure of epitaxial metal-oxide/metal interfaces. *Thin Films: Heteroepitaxial Systems*. 1999;15:167–210. DOI: 10.1142/9789812816511_0004
- [47] Nastaushev YV, Prinz VY, Svitashva SN. A technique for fabricating Au/Ti micro-and nanotubes. *Nanotechnology*. 2005;16(6):908. DOI: 10.1088/0957-4484/16/6/047
- [48] Min S, Gaffney J, Eskandari R, Tripathy J, Lim JH, Wiley JB, Malkinski L. Novel approach to control diameter of self-rolled magnetic microtubes by anodizing Ti layer. *IEEE Magnetics Letters*. 2012;3. DOI:10.1109/LMAG.2012.2213074
- [49] Cendula P, Kiravittaya S, Mei YF, Deneke C, Schmidt OG. Bending and wrinkling as competing relaxation pathways for strained free-hanging films. *Physical Review B*. 2009;79(8):085429. DOI:10.1103/PhysRevB.79.085429
- [50] Li X. Strain induced semiconductor nanotubes: From formation process to device applications. *Journal of Physics D: Applied Physics*. 2008;41(19):193001. DOI: 10.1088/0022-3727/41/19/193001
- [51] Müller C, Khatri MS, Deneke C, Fähler S, Mei YF, Ureña EB, Schmidt OG. Tuning magnetic properties by roll-up of Au/Co/Au films into microtubes. *Applied Physics Letters*. 2009; 94(10):102510. DOI:10.1063/1.3095831.
- [52] Yao P, Wang H, Chen P, Zhan X, Kuang X, Zhu D, Liu M. Hierarchical assembly of an achiral π -conjugated molecule into a chiral nanotube through the air/water interface. *Langmuir*. 2009;25(12):6633–6636. DOI:10.1021/la901435s
- [53] Min S, Lim JH, Gaffney J, Kinttle K, Wiley JB, Malkinski L. Fabrication of scrolled magnetic thin film patterns. *Journal of Applied Physics*. 2012;111(7):07E518. DOI: 10.1063/1.3679555
- [54] Malkinski L. “Magnetics with a twist”, *Magnetics Technology International magazine*, 2013: 8–12. ISSN 2047-0509.
- [55] Ohring M. *Materials Science of Thin Films*. Academic Press, USA; 2001.
- [56] Yamaguti T, Watanabe Y. Sublimation of cleaved surfaces of zinc and galena single crystals I: Experimental. *Thin solid films*. 1987;147(1):57–64. DOI: 10.1016/0040-6090(87)90040-X
- [57] Müller C, de Souza GB, Mikowski A, Schmidt OG, Lepienski CM, Mosca DH. Magnetic and mechanical properties of rolled-up Au/Co/Au nanomembranes with multiple windings. *Journal of Applied Physics*. 2011;110(4):044326. DOI:10.1063/1.3625256

- [58] Nan CW, Bichurin MI, Dong S, Viehland D, Srinivasan G. Multiferroic magnetoelectric composites: Historical perspective, status, and future directions. *Journal of Applied Physics*. 2008;103(3):031101. DOI:10.1063/1.2836410
- [59] Schurig D, Mock JJ, Justice BJ, Cummer SA, Pendry JB, Starr AF, Smith DR. Metamaterial electromagnetic cloak at microwave frequencies. *Science*. 2006;314(5801):977–980. DOI: 10.1126/science.1133628
- [60] Wiltshire MC, Pendry JB, Young IR, Larkman DJ, Gilderdale DJ, Hajnal JV. Microstructured magnetic materials for RF flux guides in magnetic resonance imaging. *Science*. 2001;291(5505):849–851. DOI: 10.1126/science.291/5505/849
- [61] Smith EJ, Makarov D, Sanchez S, Fomin VM, Schmidt OG. Magnetic microhelix coil structures. *Physical Review Letters*. 2011;107(9):097204. DOI:10.1103/PhysRevLett.107.097204
- [62] Lobontiu N, Garcia E. *Mechanics of microelectromechanical systems*. Kluwer Academic Publishers, Springer, USA; 2005. DOI: 10.1007/b100026.
- [63] Hu JM, Nan T, Sun NX, Chen LQ. Multiferroic magnetoelectric nanostructures for novel device applications. *MRS Bulletin*. 2015;40(09):728–735. DOI:10.1557/mrs.2015.195
- [64] Yang X, Liu M, Peng B, Zhou ZY, Nan TX, Sun HJ, Sun NX. A wide-band magnetic tunable bandstop filter prototype with FeGaB/Al₂O₃ multilayer films. *Applied Physics Letters*. 2015;107(12):122408. DOI:10.1063/1.4931757
- [65] Ureña EB, Mei Y, Coric E, Makarov D, Albrecht M, Schmidt OG. Fabrication of ferromagnetic rolled-up microtubes for magnetic sensors on fluids. *Journal of Physics D: Applied Physics*. 2009;42(5):055001. DOI:10.1088/0022-3727/42/5/055001
- [66] Qiu F, Fujita S, Mhanna R, Zhang L, Simona BR, Nelson BJ. Magnetic helical microswimmers functionalized with lipoplexes for targeted gene delivery. *Advanced Functional Materials*. 2015; 25(11):1666–1671. DOI:10.1002/adfm.201403891
- [67] Xi W, Solovev AA, Ananth AN, Gracias DH, Sanchez S, Schmidt OG. Rolled-up magnetic microdrillers: Towards remotely controlled minimally invasive surgery. *Nanoscale*. 2013; 5(4):1294–1297. DOI:10.1039/C2NR32798H
- [68] Mönch I, Makarov D, Koseva R, Baraban L, Karnaushenko D, Kaiser C, Arndt KF, Schmidt OG. Rolled-up magnetic sensor: Nanomembrane architecture for in-flow detection of magnetic objects. *ACS Nano*. 2011;5(9):7436–7442. DOI:10.1021/nn202351j
- [69] Grimm D, Bof Bufon CC, Deneke C, Atkinson P, Thurmer DJ, Schäffel F, Gorantla S, Bachmatiuk A, Schmidt OG. Rolled-up nanomembranes as compact 3D architectures for field effect transistors and fluidic sensing applications. *Nano Letters*. 2012;13(1): 213–218. DOI:10.1021/nl303887b
- [70] Cavallo F, Lagally MG. Nano-origami: Art and function. *Nano Today*. 2015;10(5):538–541. DOI: 10.1016/j.nantod.2015.07.001

Magnetic Properties of Gadolinium-Doped ZnO Films and Nanostructures

Iman S. Roqan, S. Assa Aravindh and
Singaravelu Venkatesh

Additional information is available at the end of the chapter

<http://dx.doi.org/10.5772/63320>

Abstract

The magnetic properties of Gd-doped ZnO films and nanostructures are important to the development of next-generation spintronic devices. Here, we elucidate the significant role played by Gd-oxygen-deficiency defects in mediating/inducing ferromagnetic coupling in in situ Gd-doped ZnO thin films deposited at low oxygen pressure by pulsed laser deposition (PLD). Samples deposited at higher oxygen pressures exhibited diamagnetic responses. Vacuum annealing was used on these diamagnetic samples (grown at a relatively high oxygen pressures) to create oxygen-deficiency defects with the aim of demonstrating reproducibility of room-temperature ferromagnetism (RTFM). Samples annealed at oxygen environment exhibited superparamagnetism and blocking-temperature effects. The samples possessed secondary phases; Gd segregation led to superparamagnetism. Theoretical studies showed a shift of the $4f$ level of Gd to the conduction band minimum (CBM) in Gd-doped ZnO nanowires, which led to an overlap with the Fermi level, resulting in strong exchange coupling and consequently RTFM.

Keywords: ZnO, DMS, ferromagnetism, Gd, rare earth

1. Introduction

New generations of electronic devices will likely be developed using spintronics technologies [1]. However, generating reproducible long-range ferromagnetism in wide bandgap (WBG)-diluted magnetic semiconductor (DMS) materials remains a major obstacle to the

fabrication of spintronic devices operating above room temperature [2]. This obstacle has prompted significant research efforts on WBG-DMSs, particularly doped ZnO [3]. Rare earth (RE) dopants have emerged as promising candidates in the search for room-temperature ferromagnetism (RTFM) in ZnO and have been the subject of intense investigations. Doping ZnO with gadolinium (Gd) should produce stronger ferromagnetism compared with doping ZnO with transition metals due to partially filled $4f$ sublevel [4, 5]. Gd is a RE atom that possesses seven spin-up electrons in partially filled $4f$ sublevel and one electron in $5d$ sublevel that are buried deep below fully filled $6s$ and $5p$ sublevels. The interesting magnetic properties of RE elements arise from the $4f$ electrons, which can strongly couple with host s electrons, yielding the possibility of ferromagnetism mediated by carrier electrons. Irrespective of the strong localization of $4f$ sublevels in RE elements, f - s and f - d magnetic coupling (when f sublevel of Gd^{3+} ion overlaps with s or d band of the host, respectively, allowing exchange coupling) is expected to give rise to strong defect-mediated ferromagnetism in such systems. However, the ferromagnetism of RE dopants remains controversial, owing to the interaction between localized $4f$ electrons and host electrons [4, 5]. Presently, there is no consensus on the exact exchange mechanism in such WBG-DMSs [6]. The ferromagnetism in ZnO has been attributed to defect-induced [7] or defect-mediated magnetism [8–12]. Furthermore, a density functional theory (DFT) study of Eu-doped ZnO reported ferromagnetic coupling when the RE atoms were in nearest neighbor positions [13]. On the other hand, research on Gd-doped ZnO revealed that ferromagnetic coupling depends on the crystal structure and positions of the dopant atoms in the host matrix, as well as the distance between the RE dopants [14].

Ferromagnetism was observed in Gd-doped ZnO films and nanostructures prepared by different methods [15–20], which can be further improved by annealing [17, 18]. ZnO single crystals implanted with Gd atoms exhibited saturation moments of up to $1.8\mu_B/\text{Gd}$ [15]. Ferromagnetism has also been observed in nanocrystalline ZnO doped with 3.5% Gd [16]. In addition, Dakhel et al. [20] found that Gd^{3+} ions produce oxygen vacancies in ZnO, which in turn decreases the lattice parameter and increases the tensile stress. Even though magnetic behavior is generally reported in Gd-doped ZnO thin films, these studies failed to obtain long-range FM in Gd-doped ZnO, perhaps due to severe distortion in the crystal as a result of ion implantation damage, to the high Gd dopant concentration (>2 at%), or to the use of lattice-mismatched substrates [15–21]. Paramagnetism has also been observed at high concentrations of Gd [21]. This is associated with the precipitation of Gd atoms at higher concentrations, leading to structural degradation. As a consequence, paramagnetism prevails in the sample. On the contrary, Murmu et al. [17, 18] found that at higher concentrations, Gd leads to precipitation in ZnO single crystals, which may also suppress the long-range ferromagnetic order in the material. The structure, doping method, and dopant concentration are therefore crucial factors in determining the magnetic and electronic properties of Gd-doped ZnO. To clarify how Gd-doped ZnO behaves, we report here on experimental and theoretical studies of the magnetic properties of Gd-doped ZnO films and nanostructures.

2. Experimental studies on Gd-doped ZnO thin films

In this section, we describe the ferromagnetic behavior of Gd-doped ZnO thin films as observed experimentally and posited theoretically. We then determine the origin of the ferromagnetism in these materials.

2.1. Sample preparation

All in situ Gd-doped wurtzite ZnO thin films were grown by pulsed laser deposition (PLD) on lattice-matched *a*-sapphire (Al_2O_3) substrate (0.08% lattice mismatch between [11–21] *a*- Al_2O_3 and (0001) *c*-ZnO). When the lattice mismatch was minimized, good quality films could be produced as structural defects in which line defects were substantially reduced. The Gd-doped ZnO and Gd targets were synthesized using 99.99% pure ZnO powder mixed with 0.1–2 wt% Gd_2O_3 powder. The films were deposited at different oxygen deposition pressures (P_d) (5–500 mTorr) and at a substrate temperature of 650°C, using a Lambda Physik KrF laser with a wavelength of 248 nm. The details of the target synthesis and PLD conditions are reported in Refs. [22, 23].

2.2. Structural properties

Understanding the structural properties of the materials is crucial to identifying the origin of their magnetic properties. In this respect, in DMS materials, the film orientation, dopant concentrations, crystal quality, defects, and secondary phase inclusions should be identified clearly. The growth direction, the crystal quality, and the lattice parameters can be studied by X-ray diffraction measurements. A long-range scan (shown in **Figure 1**) of Gd-doped ZnO thin films reveals that they are single crystal and were grown along the *c*-axis. In the scan shown in **Figure 1**, no secondary or impurity phase could be observed within the resolution limit of the instrument [22]. The lattice parameters were measured using the extended bond method [24] with the (004) and (104) planes. The concentration of Gd increases with oxygen pressure (P_d) [25]. The *a*-parameter increased while the *c*-parameter decreased with incorporation of Gd

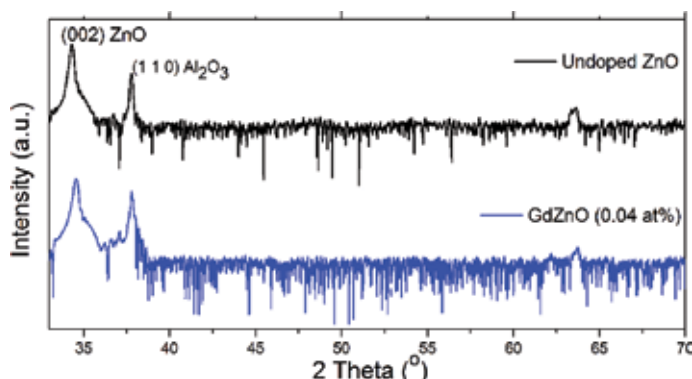


Figure 1. XRD 2 θ scans of undoped and Gd-doped ZnO samples showing ZnO growth oriented along the [0 0 0 1] direction (log scale) [22].

compared to without incorporation of Gd. DFT calculations confirmed that Gd-oxygen vacancy (V_O) complexes cause c -parameter contraction [25].

We used high-resolution transmission electron microscopy (HR-TEM) to study crystal distortion and to investigate structural defects. The samples did not exhibit any line defects, as shown in **Figure 2**. In addition, no secondary phases were observed near the interface, indicating that the diluted Gd concentration was sufficiently low to prevent the formation of clusters and secondary phases [22].

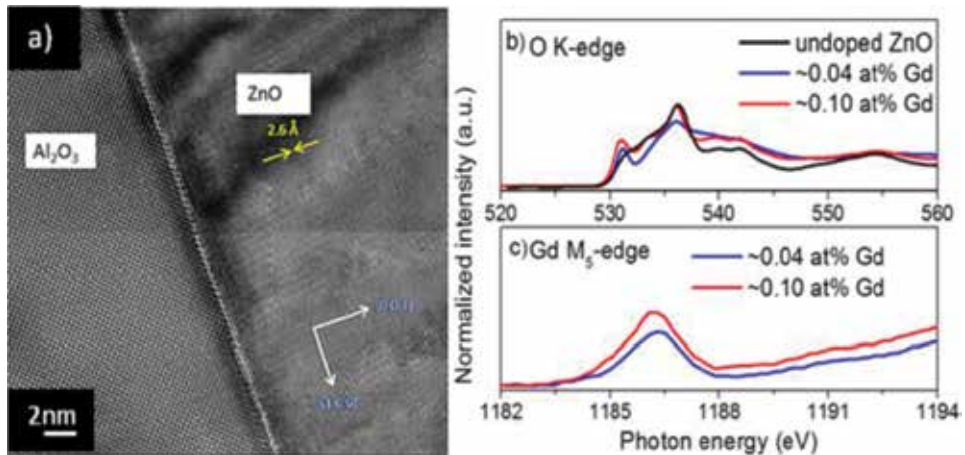


Figure 2. (a) HR-TEM image of a Gd-doped ZnO sample with 0.87 at.% Gd. The image contrast is due to the thickness variation. (b) XAS spectra at the O K-edge. (c) NEXAFS spectra at the Gd $M_{5,4}$ -edge after subtracting the background [22].

Materials with secondary phases and segregations are not suitable for practical spintronic applications. Near-edge X-ray absorption fine structure (NEXAFS) spectra can be used to investigate the existence of secondary phases. Because a ZnO matrix cannot be fully polarized and because ferromagnetic signals coming from phase segregation do not contribute to long-range reproducible ferromagnetism, we ran NEXAFS scans to confirm that no secondary phases and segregations were present in the DMS samples. NEXAFS spectra at the O K-edge and Gd $M_{5,4}$ -edge revealed the hybridization between Gd and O in Gd-ZnO samples (**Figure 2(b, c)**). The O K-edge spectra shown in **Figure 2(b)** indicate that the two peaks at ~531 eV and ~535 eV are stronger for Gd-doped ZnO compared with those for undoped samples, due to strong O $2p$ state hybridization with the Gd $4f$ and Zn $3d$ states [26, 27]. The intensity of these peaks increases as the Gd concentration increases, due to the higher electronegativity of Gd relative to Zn [28, 29]. The Gd valence state measured at the Gd $M_{5,4}$ -edge shown in **Figure 2(c)** indicates the $3+$ oxidation state of Gd [30, 31]. The intensity variation at 1190 eV increases with increased Gd concentration, which is in good agreement with the OK spectra. The absence of secondary phases and Gd segregation in these films are therefore confirmed by NEXAFS measurements, which is important for elucidating the origin of the magnetic properties of the materials [22].

2.3. Optical properties

The study of optical properties allows the investigation of defects that may affect the magnetic properties of materials. We performed low-temperature photoluminescence (PL) measurements to study the role of defects. In **Figure 3(a)**, the peak at ~ 369.1 nm represents the ZnO band edge emission. Moreover, the undoped ZnO spectrum shows an orange-red defect band at 587 nm, which we attributed to oxygen interstitials (O_i) using deep-level transient spectroscopy (DLTS) [32]. The spectra pertaining to the Gd-doped ZnO films grown at low P_d (oxygen-deficiency conditions) show a dominant green PL band at 495 nm (2.50 eV), attributed to V_O [33–36]. Previous research has suggested that this green band in ZnO comes from complex defects, such as defects related to pairs of V_O –Zn vacancies (V_{Zn}) [37] or associated with zinc interstitials (Zn_i) [38] or antisites (O_{Zn}) [39]. A sample grown under rich oxygen conditions ($P_d > 25$ mTorr) shows a dominant red band emission centered at 690 nm as shown in **Figure 3(b)**. We attributed this red band to O_i and V_{Zn} [32, 33]. After a sample was annealed under vacuum conditions to create oxygen vacancies, a significant reduction in the red band was observed, while the spectrum of the vacuum-annealed sample became dominated by the green band (**Figure 3(b)**) [22, 25].

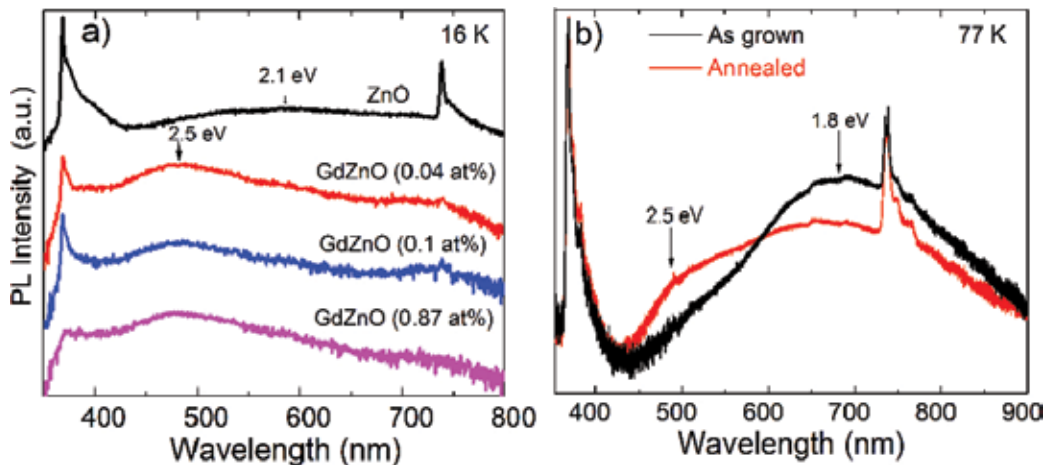


Figure 3. (a) The PL spectra of the samples grown at low P_d and (b) the PL spectra of the sample grown at high P_d before and after vacuum annealing [22].

2.4. Magnetic properties

2.4.1. The effect of oxygen deficiency

We measured the magnetization using a superconducting quantum interference device (SQUID) magnetometer (MPMS, Quantum Design, USA) and a SQUID vibrating sample magnetometer (SVSM, Quantum Design, USA). The samples were initially cooled from room temperature to 5 K without application of any magnetic field (zero-field-cooled, ZFC). A field

of 100 Oe was then applied and the magnetic data were recorded as a function of temperature as the sample was heated to 300 K and then cooled to 5 K under the same applied field (field-cooled, FC). All undoped ZnO thin films prepared under high or low P_d did not exhibit ferromagnetism before or after vacuum annealing as shown in **Figure 4** and **Figure 5**. All Gd-doped ZnO films deposited at low P_d (≤ 25 mTorr) exhibited RTFM, as shown in the field strength (H) vs magnetization (M) (H - M) measurements (**Figure 6** and **Figure 7**), whereas samples deposited at higher P_d (with the same concentration of Gd) did not exhibit RTFM (**Figure 8(a)**). **Figure 7** shows H - M loops for samples grown at low P_d (5 mTorr), albeit at different Gd concentrations. All samples investigated produced RTFM responses. Furthermore, nonmagnetic Gd-doped ZnO thin films (deposited at high P_d) became ferromagnetic after vacuum annealing under oxygen-deficiency conditions (**Figure 8(a)**). **Figure 8(b)** shows that the PL defect band related to oxygen deficiency becomes dominant after vacuum annealing. This finding suggests that the introduction of Gd^{3+} ions, together with the presence of certain defects related to oxygen deficiency (such as oxygen vacancies), causes a reproducible long-range ferromagnetic exchange in Gd-doped ZnO thin films. In addition, ferromagnetism is still observed at higher temperatures (380 K), as shown in **Figure 6(a)**, indicating that the Curie temperature (T_C) is above room temperature.

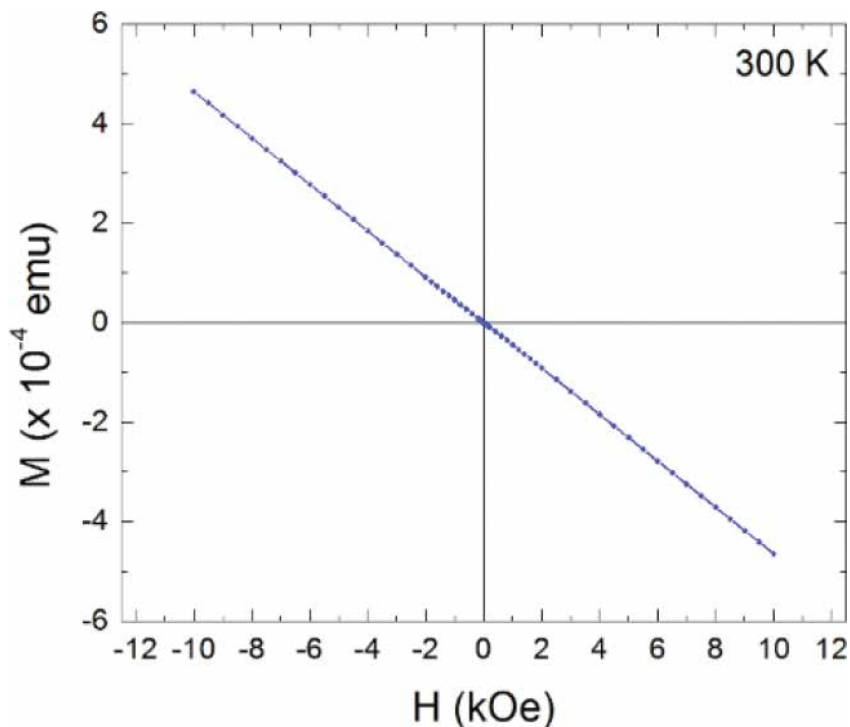


Figure 4. The diamagnetic response of undoped ZnO on a-sapphire prepared by PLD at low oxygen pressure (5 mTorr). The diamagnetic response is shown at 5 K as well.

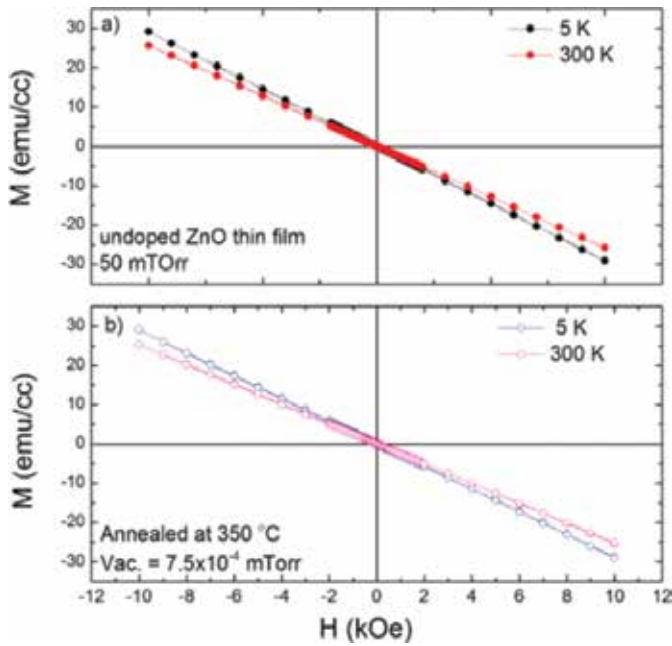


Figure 5. Magnetization measurements of undoped ZnO films deposited at high oxygen pressure (50 mTorr) (a) before and (b) after vacuum annealing under similar conditions of that of Gd-doped ZnO samples.

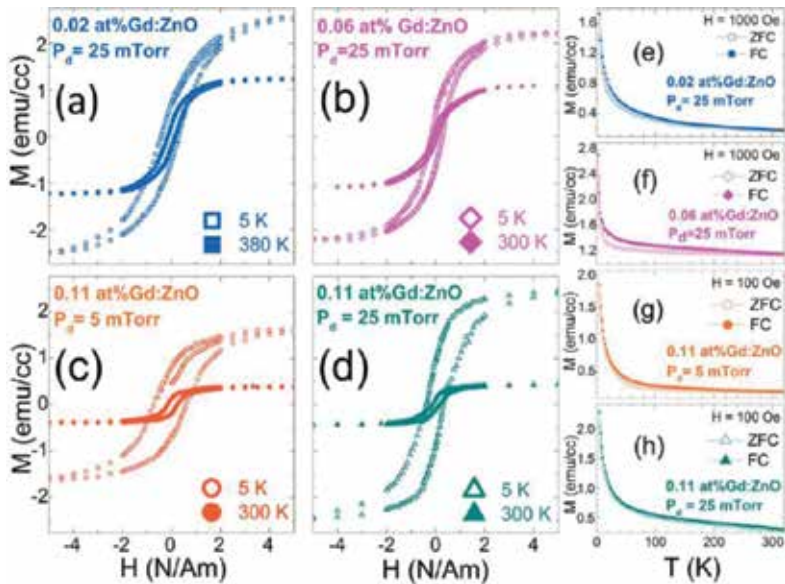


Figure 6. (a)–(d) Typical H-M loops of Gd:ZnO films prepared at $P_d \leq 25$ mTorr. (e)–(f) ZFC and FC for samples shown in (a)–(d), respectively. All measurements were done with H normal to the thin-film plane [23].

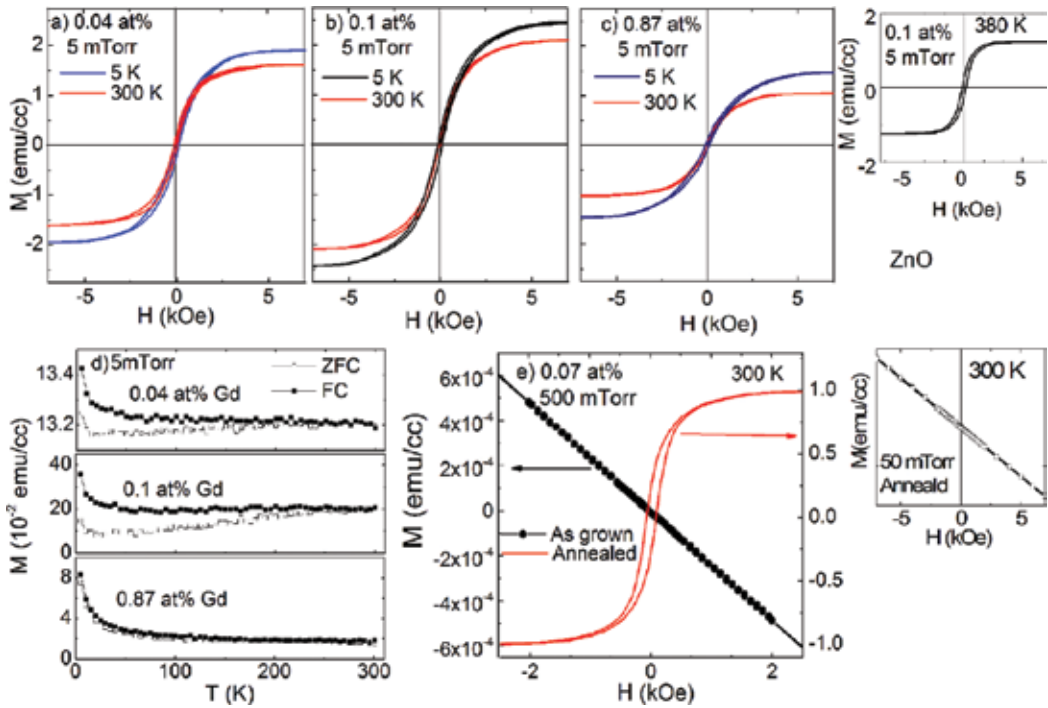


Figure 7. (a)–(c) M-H loops and (d) ZFC-FC magnetization for Gd-doped ZnO samples deposited at 5 mTorr (top inset: M-H loops at high temperature (380 K)) and (e) M-H loops of Gd-doped ZnO samples grown at high P_a and after vacuum annealing (bottom inset: magnetization measurements of undoped ZnO films deposited at high oxygen pressure (50 mTorr) after vacuum annealing) [22].

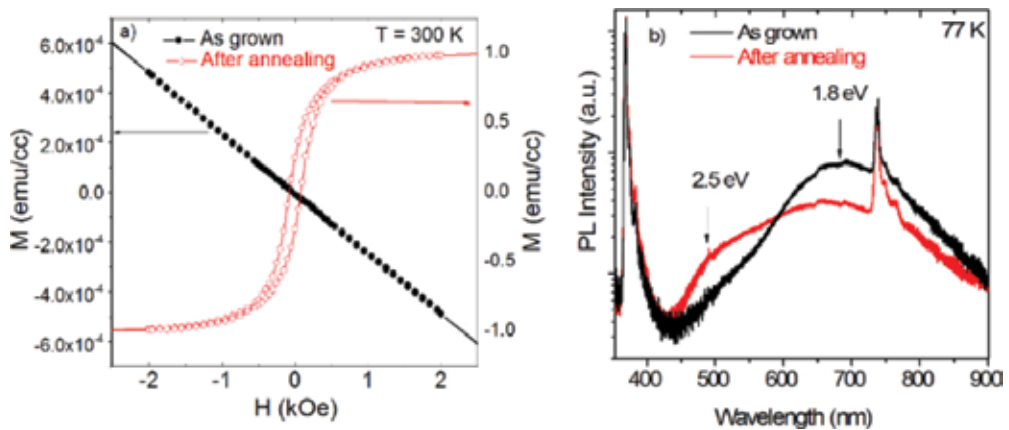


Figure 8. (a) H-M loops of as-grown Gd-doped ZnO (deposited at high P_a) and after vacuum annealing and (b) their PL spectra. The samples were annealed inside a small glass capsule to avoid any contamination [22].

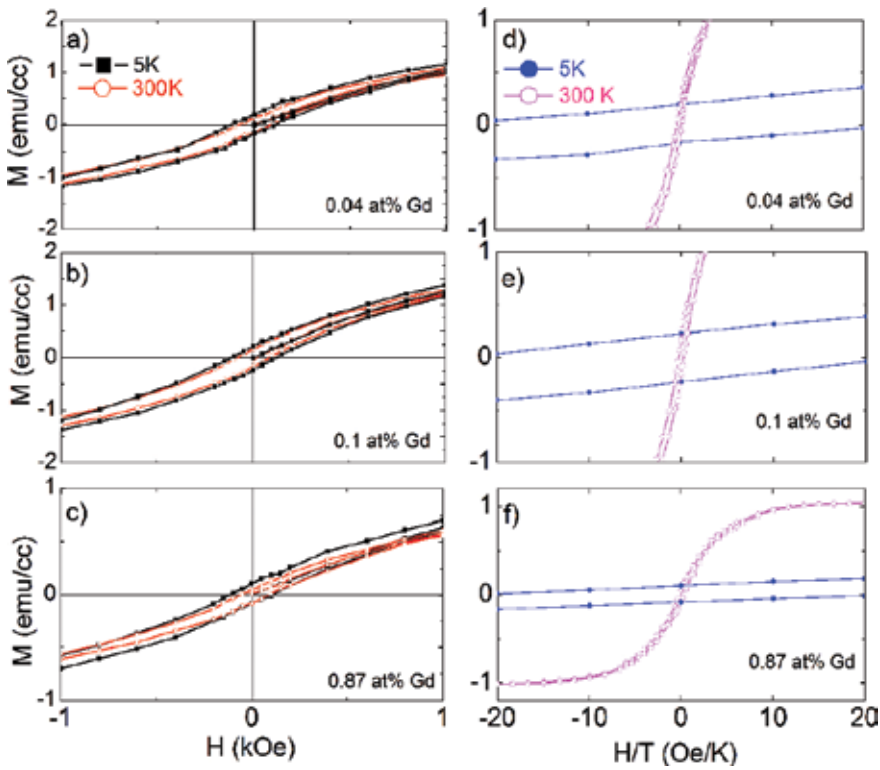


Figure 9. (a)–(c) Nonzero coercivity of H-M loops for Gd-doped ZnO samples deposited at 5 mTorr and (d)–(f) M as a function of H/T for the same Gd-doped ZnO samples, exhibiting ferromagnetic behavior without any superparamagnetic phases [22].

Measurements of the dependence of magnetism on temperature were also conducted. Results are shown in the ZFC and FC curves in **Figure 6** and **Figure 7**. **Figure 6(e–h)** and **Figure 7(d)** show the ZFC-FC curves without magnetic phase transitions or blocking temperatures. Furthermore, nonzero coercivity was observed in both sets of samples at room temperature, as shown in **Figure 6** and **Figure 7**. The magnetism as a function of the field strength/temperature (H/T) in the samples is shown in **Figure 9**, indicating that there is no superimposing universality at 5 K and 300 K, excluding the possibility of superparamagnetism [40]. In addition, the Gd-doped ZnO sample (**Figure 7(a)**) grown with 0.04 at% Gd concentration shows the maximum coercivity (H_C) and the highest magnetic moment of $12.35\mu_B$ per Gd^{3+} ion at 5 K, whereas the sample grown with 0.11 and 0.85 at% Gd concentration shows a magnetic moment of 5.8 (**Figure 7(b)**) and $0.44\mu_B$ per Gd^{3+} ion at 5 K (**Figure 7(c)**). This evidence indicates that no superparamagnetic or spin-glass-like transitions were observed within the temperature range measured in any of the ferromagnetic samples and that RTFM is intrinsic (i.e., it is from the ferromagnetism originating from the polarized ZnO matrix).

To confirm the effect of oxygen defects, a ferromagnetic sample of Gd-doped ZnO (0.08 at% Gd) grown at low P_a (5 mTorr) was annealed at 300°C under flowing oxygen to reduce the

density of the oxygen-deficiency defects in the film. The ferromagnetic signal became very weak and was accompanied by a superparamagnetic signal after annealing as shown in **Figure 10**. The superparamagnetic loop at 5 K suggests a significant reduction in the defect-mediated magnetization. In addition, the blocking temperature ($T_B = 37.5$ K) is observed in **Figure 10**, indicating the formation of either ferromagnetic and/or antiferromagnetic nanoclusters (cluster size smaller than a magnetic domain) during annealing, which results in the superparamagnetic behavior of the materials [41, 42]. Murmu et al. [17, 18] reported that annealing Gd-implanted ZnO under a vacuum introduced ferromagnetic and superparamagnetic phases below the blocking temperature, suggesting that this phenomenon is due to ferromagnetic nanoclusters resulting from the nonhomogeneous distribution of Gd in the film. A similar transition was observed in antiferromagnetic nanoparticles [43]. In contrast to an antiferromagnetic bulk material, antiferromagnetic nanoclusters introduced a nonzero magnetic moment because the antiparallel sublattices were characterized by a small angle with respect to the easy magnetic axes. In this case, the spins of the two sublattices were not fully antiparallel with respect to each other, resulting in a net magnetic moment due to the different precession angles [44].

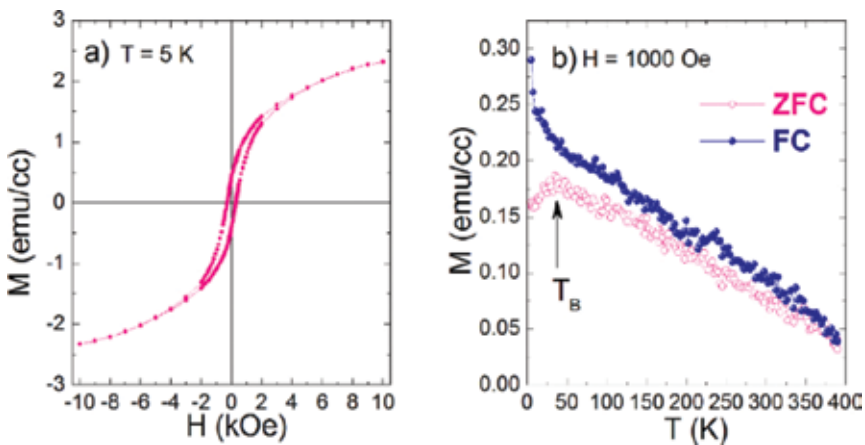


Figure 10. (a) Superparamagnetic behavior after annealing (at 300°C for 5 h in O_2 flow) a ferromagnetic Gd (0.08 at%)-doped ZnO sample. (b) ZFC-FC curves for the sample after annealing.

Extant studies have confirmed that Gd^{3+} ions exhibit magneto-crystalline anisotropy due to the $4f$ electron cloud experiencing a tetrahedral crystalline electric field in the lattice and the associated spin splitting [45, 46]. To establish if RTFM is mediated/induced by the Gd-defect complexes, the ferromagnetism would have show magnetic anisotropy. Anisotropic magnetization loops were observed in Gd-doped ZnO grown at 25 torr and Gd 0.05 wt% (0.02 at%), indicating a higher magnetic situation when the field (H) was applied parallel to c -axis relative to that observed when the field is perpendicular to it. This magnetic anisotropic behavior suggests that the ferromagnetism was due to the Gd-defect complex as RE dopants have strong anisotropy [47]. The exchange interaction is therefore dependent on the Gd concentration. Subramanian et al. [16] observed anisotropy in polycrystalline Gd-doped ZnO [23].

2.4.2. The effect of secondary phases

Finding ferromagnetism in samples annealed at high temperatures (380 K) (described in Sections 2.4.1. and 2.4.2.) suggests that the ferromagnetism does not originate from separation or secondary phases. **Figure 11(a)** shows FC-ZFC curve for a Gd-doped ZnO sample with secondary phases as well as the Curie temperature (T_C) of the Gd clusters. $GdZn_2$ segregation is clearly shown in the curve (T_C at ~ 70 K as shown in **Figure 11**), whereas the T_C of Gd is very close to room temperature, as shown in **Figure 11(a)**. In addition, paramagnetic signals are observed from Gd metals above room temperature, as shown in **Figure 11(b)**. The other expected phase is Gd_2O_3 , which is an antiferromagnetic material.

In highly Gd-doped samples (~ 2.5 at%) grown at 50 mTorr on c-sapphire substrates, segregation of the secondary phase was observed near the film-substrate interface, as indicated by the HR-TEM results (**Figure 12(a)**). The M-H loop (**Figure 12(b)**) at 5 K is dominated by superparamagnetic behavior, as there is no magnetic saturation. Such behavior was reported by Murmu et al. [19] for (2.5 at%) Gd-implanted ZnO films.

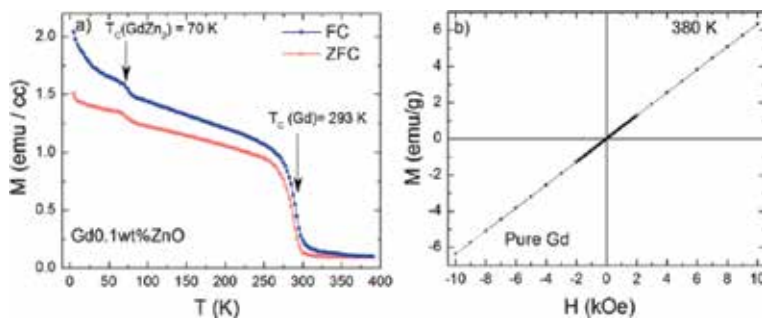


Figure 11. (a) The Curie temperature of other Gd phases. Gd-doped ZnO with a secondary phase and Gd clusters. (b) The pure Gd metal has a paramagnetic response at high temperature (380 K).

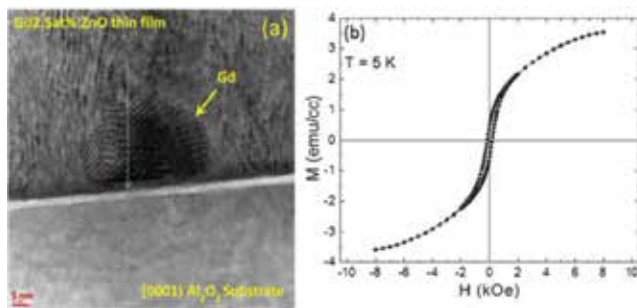


Figure 12. (a) HR-TEM micrograph of Gd (2.5 at%)-doped ZnO deposited on c-sapphire, showing clusters of Gd near the interface. The arrow indicates the line profile from the energy dispersive X-ray (EDX) spectrum showing scanning across the cluster confirming the presence of Gd. (b) M-H loop of the same sample showing a superparamagnetic response.

3. Theoretical studies on Gd-doped ZnO

3.1. The origin of the ferromagnetism in Gd-doped ZnO films

All Gd-doped ZnO samples showed n-type conductivity with about 10^{18} cm^{-3} carrier concentration. RTFM was observed in all samples grown at low P_{O_2} . This ferromagnetism can potentially be attributed to Gd-oxygen-deficiency (donor) defects. Theoretical analyses are necessary for in-depth understanding of magnetic interactions.

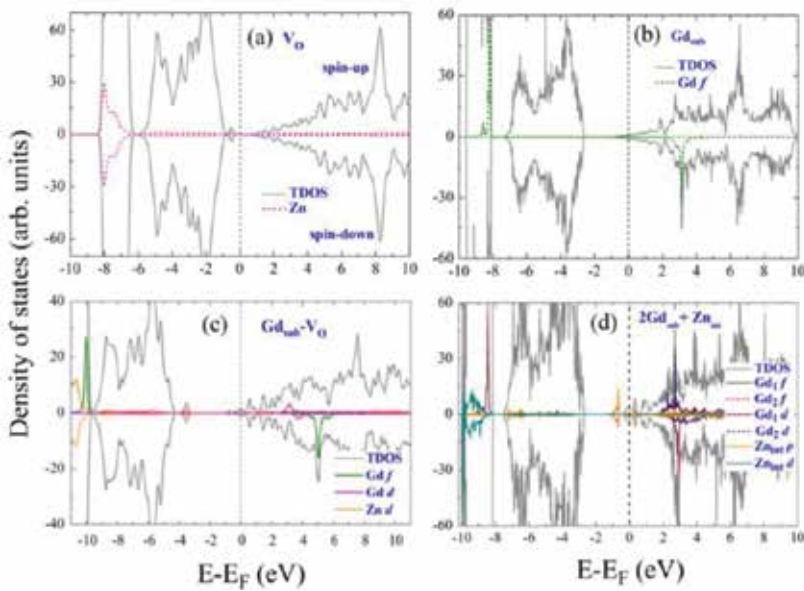


Figure 13. The DOS of (a) a V_{O} defect, calculated using the PBE + U; (b) a substitutional Gd (Gd_{sub}); (c) Gd + V_{O} , calculated using hybrid functional HSE06 ($\alpha = 0.25$ for the Hartree-Fock exchange); and (d) $2\text{Gd}_{\text{sub}} + \text{Zn}_{\text{v}}$, calculated using PBE + U [22].

The theoretical analysis performed in this work focuses on the effect of the Gd complexes with intrinsic defects that introduce donor electrons [22]. First-principles simulations were performed using the Vienna Ab-initio Simulation Package (VASP) [48, 49] with projector-augmented wave potentials (PAW) and a plane-wave expansion of 400 eV on $2 \times 2 \times 2$ k-meshes for structural relaxation. The exchange and correlations were treated in the Perdew-Burke-Ernzerhof generalized gradient approximation (GGA) and a little higher accuracy for the energy calculation. All configurations were fully relaxed until the forces per atom were less than $0.02 \text{ eV}/\text{\AA}$. For the localized Zn $3d$ and Gd $4f$ states, Hubbard U correction was taken into account with $U_{\text{eff}} = 5 \text{ eV}$ for Zn $3d$ and 6 eV for Gd $4f$ states. The energy convergence was set to $5 \times 10^{-5} \text{ eV}$ [22].

Ferromagnetism occurs when the Fermi level (E_{F}) is located near the band edge and overlaps with the impurity level. As a result, it can be partially occupied by the donor electrons and

magnetic exchange coupling can take place [50]. **Figure 13** shows that introducing V_O does not shift the Fermi level to the band edge, which, however, moves above the conduction band minimum (CBM) with the introduction of Gd impurities. However, the presence of Gd dopants in defect-free ZnO is not sufficient to induce exchange coupling, as the magnetic results pertaining to Gd:ZnO reveal predominantly paramagnetic behavior [14]. **Figure 13** shows a 2-Gd complex with V_O and Zn_i , respectively, suggesting three possibilities of magnetic coupling that lead to the observed RTFM in Gd-doped ZnO deposited at different oxygen-deficiency conditions. First, Gd induces FM through s - f or s - d coupling, which is not possible because the f state is far the CBM and does not overlap with the Fermi level, an observation that is in line with our earlier DFT calculations [51]. Second, defect-induced RTFM can be possible in this case if the defect band and the CBM are located near the Fermi level. A shallow donor band located near the Fermi level is created due to the presence of Gd- Zn_i complexes, as shown in **Figure 13**. Therefore, this band may allow ferromagnetic coupling between the s state of the host and donor levels, resulting in RTFM. Third, Gd can mediate RTFM, in which case the RTFM will be due to the exchange coupling between the defect states and the host [52]. In this case, the band broadening formed by intrinsic defects is resonant with Gd f states producing RTFM [52], as shown in **Figure 13**. Venkatesh et al. [23] showed that the formation of a Gd-oxygen-deficiency defect band located near the Fermi level mediated the ferromagnetism through spin splitting of the defect band [22].

3.2. The origin of the ferromagnetism in Gd-doped ZnO nanowires

First-principles DFT calculations were carried out within the GGA to elucidate the magnetic phenomena in the Gd-doped ZnO nanowires. A wurtzite ZnO nanowire grown along the [0001] direction doped with Gd was considered. The presence of point defects in the nanowire along with the Gd dopant is discussed in the context of magnetic and electronic properties. The possibility of carrier-mediated ferromagnetism originating from the f - s coupling was demonstrated using electronic structure analysis [53].

The $Zn_{48}O_{48}$ nanowire was modeled by employing super cell approximation in which a vacuum of 15 Å is created along the X and Y directions and infinite periodicity is maintained along the Z direction. Since a comparison of the results obtained with and without the Hubbard U parameter did not alter the qualitative picture, we adopted the GGA approximation as implemented in the plane-wave-based code VASP [48, 49]. Projected augmented wave (PAW) pseudopotentials were considered with a plane-wave cutoff of 400 eV. A Monkhorst-Pack K grid of $1 \times 1 \times 8$ was used for the Brillouin zone integration. With the abovementioned input settings, we were able to achieve energy and force tolerances of 0.0001 eV and 0.004 eV/Å, respectively.

The formation energy was calculated by incorporating the Gd atoms in all possible non-equivalent sites in the ZnO nanowire encompassing the surface, subsurface, and bulk-like regions (**Figure 14**) using the following equation:

$$E_f = E(Zn_{48-m}O_{48Gdm}) - E(Zn_{48}O_{48}) + n\mu(Zn) - m\mu(Gd), \quad (1)$$

where E and μ denote the total energy and chemical potential (total energy of metallic Zn and Gd), respectively. Here, n represents the number of Zn atoms removed from the supercell and m is the number of Gd atoms replaced by the Zn atoms.

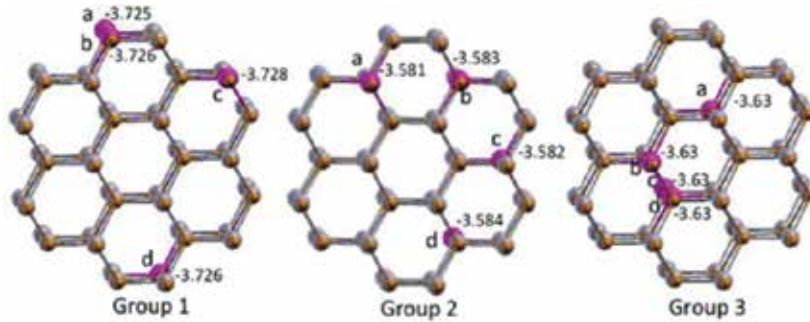


Figure 14. $\text{Zn}_{47}\text{O}_{48}\text{Gd}$ nanowires with all 12 non-equivalent doping sites grouped in to three classes including the surface, subsurface, and bulk-like sites. The formation energy of Gd atoms in each site is also shown (in eV) [53].

The optimization of a pristine nanowire resulted in a reduction of bond length along the c-axis (1.89 Å), while the ab-plane underwent extension, compared to bulk ZnO (1.99 Å). Substitution of a Gd atom resulted in slight elongation along c-axis, to 2.08 Å, whereas the change within the a-b plane was almost negligible, indicating that the $\text{Zn}_{47}\text{O}_{48}\text{Gd}$ nanowires reached structural stability with minimal lattice distortion. The Gd atoms preferred to occupy the surface sites in agreement with the in situ deposition experiments.

Configuration	ΔE (meV)	$\Delta E(e)$ (meV)	$\Delta E(V_O)$ (meV)
a	4	20	31
b	11	35	96
c	21	57	134
d	9	23	108
e	17	86	200
f	13	21	60
g	9	14	46

Table 1. The difference in total energy (ΔE ; meV) between the FM and AFM configurations for the $\text{Zn}_{46}\text{O}_{48}\text{Gd}_2$ nanowires, without vacancies (second column), with electron injection (third column) and with V_O (fourth column).

The energetic preference of the clustering of Gd atoms was analyzed by putting a pair of Gd atoms in the host ZnO matrix and the lowest formation energies for widely separated Gd atoms were obtained. This is an important result indicating that segregation of Gd atoms in ZnO nanowires is unlikely to occur and that the magnetism does not originate from the Gd clusters. Our findings support the homogeneous distribution of RE atoms during implantation in ZnO.

The Gd atoms, when placed in near vicinity, exhibited ferromagnetic exchange coupling in the neutral state with exchange energies (ΔE) as large as 21 meV. The introduction of additional charge to the nanowire by the injection of an electron further enhanced ΔE , indicating that the presence of O vacancies may stabilize ferromagnetic coupling in the nanowire, given that a single O vacancy can release two electrons into the system. The ΔE increased to 200 meV in the presence of O vacancies, supporting the possibility of an increased f - s coupling (**Table 1** [53]).

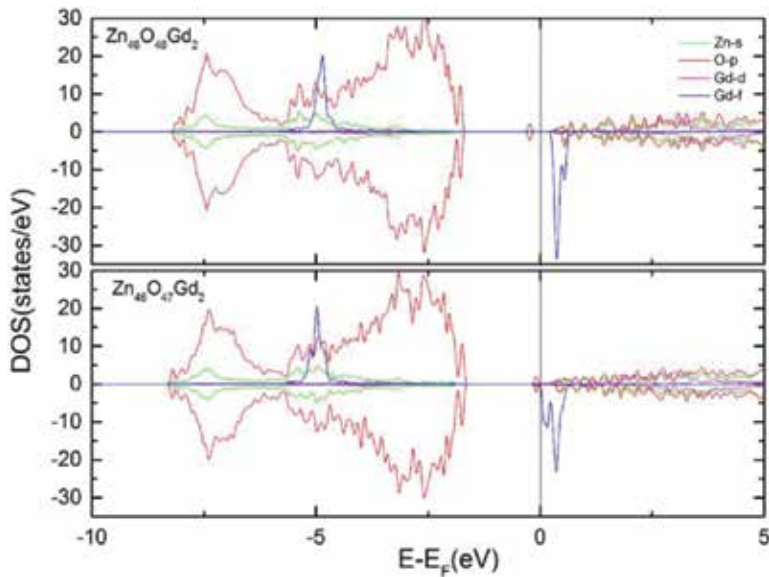


Figure 15. The density of states of Gd-doped ZnO nanowires with and without O vacancies [53].

The density of states (DOS) of Gd-doped ZnO nanowires with and without O vacancies provided further insight into the exchange mechanism. A pristine ZnO nanowire is semiconducting with nonmagnetic characteristics (**Figure 15**) [53]. Doping with Gd atom causes a significant shift of the Fermi level to the conduction band close to the Gd f states. The predominant feature observed from DOS is that the majority Gd f levels are buried deep inside the valence band and the unoccupied minority states are localized in the vicinity of the Fermi level. With the introduction of V_O , hybridization increases in the vicinity of the Fermi level, mediating the interaction between s (from Zn) and the f states. In the present context, the ferromagnetic exchange interaction is mediated by the valence electrons provided by the V_O , unlike Zener's p - d exchange mechanism in which valence hole states are involved [54]. The double-exchange mechanism is also less likely, as it is based on a physical picture of the d electron hopping between atoms with strong on-site exchange [55]. The shift of the Fermi level towards the conduction band eliminates the possibility of change " pnf " to " p - f " exchange mediated by the hole states. These findings establish that O vacancies play a key role in stabilizing ferromagnetic exchange in Gd-doped ZnO nanowires.

4. Conclusion

The origin of RTFM in Gd-doped ZnO is intrinsic due to exchange coupling mediated or introduced by a defect band related to the Gd-defect complex. Quantum confinement of the nanowire structure can strengthen the RTFM, as O vacancies play a key role in stabilizing ferromagnetic exchange in Gd-doped ZnO nanowires.

Acknowledgements

The authors would like to thank the team involved in this study. In particular, we thank Zhenkui Zhank, Shamima Hussain, Tahani H. Flembar, and Ioannis Bantounas from our group at KAUST. We thank J.B. Franklin, B. Zou, P.K. Petrov, M.P. Ryan, and N.M. Alford from Imperial College London and J-S. Lee from the Stanford Synchrotron Radiation Light-source, SLAC National Accelerator Laboratory. We thank P. Edwards, K.P. O'Donnell, and R.W. Martin for providing access to the EPMA for WDX measurements at the University of Strathclyde. We thank Ratnamal Chatterjees's group at IIT Delhi, India, for conducting the SQUID experiments.

Author details

Iman S. Roqan*, S. Assa Aravindh and Singaravelu Venkatesh

*Address all correspondence to: iman.roqan@kaust.edu.sa

King Abdullah University of Science and Technology (KAUST), Physical Science and Engineering Division, Thuwal, Saudi Arabia

References

- [1] G. A. Prinz. Magnetolectronics. *Science*. 1998;282:1660–1663.
- [2] S. Chambers. Is it really intrinsic ferromagnetism? *Nat. Mater.* 2010;9:956–957.
- [3] P. Sharma, A. Gupta, K. V. Rao, F. J. Owens, R. Sharma, R. Ahuja, J. M. O. Guillen, B. Johansson, G. A. Gehring. Ferromagnetism above room temperature in bulk and transparent thin films of Mn-doped ZnO. *Nat. Mater.* 2003;2:673–677.
- [4] H. Shi, P. Zhang, S. S. Li, J. B. Xia. Magnetic coupling properties of rare-earth metals (Gd, Nd) doped ZnO: first-principles calculations. *J. Appl. Phys.* 2009;106:023910.

- [5] G. M. Dalpian, S.-H. Wei. Electron-induced stabilization of ferromagnetism in $\text{Ga}_{1-x}\text{Gd}_x\text{N}$. *Phys. Rev. B*. 2005;72:115201.
- [6] P. Dev, P. Zhang. Unconventional magnetism in semiconductors: role of localized acceptor states. *Phys. Rev. B*. 2010;81:085207.
- [7] X.-L. Li, J.-F. Guo, Z.-Y. Quan, X.-H. Xu, G. A. Gehring. Defects inducing ferromagnetism in carbon-doped ZnO films. *IEEE Trans. Magn.* 2010;46:1382–1384.
- [8] J. B. Yi, C. C. Lim, G. Z. Xing, H. M. Fan, L. H. Van, S. L. Huang, K. S. Yang, X. L. Huang, X. B. Qin, B. Y. Wang, T. Wu, L. Wang, H. T. Zhang, X. Y. Gao, T. Liu, A. T. S. Wee, Y. P. Feng, J. Ding. Ferromagnetism in dilute magnetic semiconductors through defect engineering: Li-doped ZnO. *Phys. Rev. Lett.* 2010;104:137201.
- [9] C. D. Pemmaraju, R. Hanafin, T. Archer, H. B. Braun, S. Sanvito. Impurity-ion pair induced high-temperature ferromagnetism in Co-doped ZnO. *Phys. Rev. B*. 2008;78:054428.
- [10] H. Gu, Y. Jiang, Y. Xu, M. Yan. Evidence of the defect-induced ferromagnetism in Na and Co codoped ZnO. *Appl. Phys. Lett.* 2011;98:012502.
- [11] A. Khodorov, A. G. Rolo, E. K. Hlil, J. Ayres de Campos, O. Karzazi, S. Levichev, M. R. Correia, A. Chahboun, M. J. M. Gomes. Effect of oxygen pressure on the structural and magnetic properties of thin $\text{Zn}_{0.98}\text{Mn}_{0.02}\text{O}$ films. *Eur. Phys. J. Appl. Phys.* 2012;57:10301.
- [12] Y. Belghazi, G. Schmerber, S. Colis, J. L. Rehspringer, A. Dinia, A. Berrada. Extrinsic origin of ferromagnetism in ZnO and $\text{Zn}_{0.9}\text{Co}_{0.1}\text{O}$ magnetic semiconductor films prepared by sol-gel technique. *Appl. Phys. Lett.* 2006;89:122504.
- [13] M. H. N. Assadi, Y. Zhang, R. Zheng, S. P. Ringer, S. Li. Structural and electronic properties of Eu- and Pd-doped ZnO. *Nanoscale Res. Lett.* 2011;6:357.
- [14] I. Bantounas, S. Goumri-Said, M. B. Kanoun, A. Manchon, I. Roqan, U. Schwingenschlogl. Ab initio investigation on the magnetic ordering in Gd doped ZnO. *J. Appl. Phys.* 2011;109:083929.
- [15] K. Potzger, S. Zhou, F. Eichhorn, M. Helm, W. Skorupa, A. Mücklich, J. Fassbender, T. Herrmannsdörfer, A. Bianchi. Ferromagnetic Gd-implanted ZnO single crystals. *J. Appl. Phys.* 2006;99:063906.
- [16] M. Subramanian, P. Thakur, M. Tanemura, T. Hihara, V. Ganesan, T. Soga, K. H. Chae, R. Jayavel, T. Jimbo. Intrinsic ferromagnetism and magnetic anisotropy in Gd-doped ZnO thin films synthesized by pulsed spray pyrolysis method. *J. Appl. Phys.* 2010;108:053904.
- [17] P. P. Murmu, J. Kennedy, B. J. Ruck, G. V. M. Williams, A. Markwitz, S. Rubanov, A. A. Suvorova. Effect of annealing on the structural, electrical and magnetic properties of Gd-implanted ZnO thin films. *J. Mater. Sci.* 2012;47:1119.

- [18] P. P. Murmu, R. J. Mendelsberg, J. Kennedy, D. A. Carder, B. J. Ruck, A. Markwitz, R. J. Reeves, P. Malar, T. Osipowicz. Structural and photoluminescence properties of Gd implanted ZnO single crystal. *J. Appl. Phys.* 2011;110:033534.
- [19] P. P. Murmu, J. Kennedy, G. V. M. Williams, B. J. Ruck, S. Granville, S. V. Chong. Observation of magnetism, low resistivity and magnetoresistance in the near-surface region of Gd implanted ZnO. *Appl. Phys. Lett.* 2012;101:082408.
- [20] A. A. Dakhel, M. El-Hilo. Ferromagnetic nanocrystalline Gd-doped ZnO powder synthesized by coprecipitation. *J. Appl. Phys.* 2010;107:123905.
- [21] V. Ney, S. Ye, T. Kammermeier, K. Ollefs, F. Wilhelm, A. Rogalev, S. Lebègue, A. L. da Rosa, A. Ney. Structural and magnetic analysis of epitaxial films of Gd-doped ZnO. *Phys. Rev. B.* 2012;85:235203.
- [22] I. S. Roqan, S. Venkatesh, Z. Zhang, S. Hussain, I. Bantounas, J. B. Franklin, T. H. Flemban, B. Zou, J.-S. Lee, U. Schwingenschlogl, P. K. Petrov, M. P. Ryan, N. M. Alford. Obtaining strong ferromagnetism in diluted Gd-doped ZnO thin films through controlled Gd-defect complexes. *J. Appl. Phys.* 2015;117:073904.
- [23] S. Venkatesh, J. B. Franklin, M. P. Ryan, J.-S. Lee, H. Ohldag, M. A. McLachlan, N. M. Alford, I. S. Roqan. Defect-band mediated ferromagnetism in Gd-doped ZnO thin films. *J. Appl. Phys.* 2015;117:013913.
- [24] N. Herres, L. Kirste, H. Obloh, K. Kohler, J. Wagner, P. Koidl. X-ray determination of the composition of partially strained group-III nitride layers using the Extended Bond Method. *Mater. Sci. Eng. B.* 2002;91–92:425–432.
- [25] T. H. Flemban, M. C. Sequeira, Z. Zhang, S. Venkatesh, E. Alves, K. Lorenz, I. S. Roqan. Identifying the influence of the intrinsic defects in Gd-doped ZnO thin-films. *J. Appl. Phys.* 2016;119:065301.
- [26] L. Armelao, F. Heigl, A. Jurgensen, R. I. R. Blyth, T. Regier, X.-T. Zhou, T. K. Sham. X-ray excited optical luminescence studies of ZnO and Eu-doped ZnO nanostructures. *J. Phys. Chem. C.* 2007;111:10194.
- [27] R. A. Rosenberg, G. K. Shenoy, L. C. Tien, D. Norton, S. Pearton, X. H. Sun, T. K. Sham. Anisotropic X-ray absorption effects in the optical luminescence yield of ZnO nanostructures. *Appl. Phys. Lett.* 2006;89:093118.
- [28] L. A. Grunes, R. D. Leapman, C. N. Wilker, R. Hoffmann, A. B. Kunz. Oxygen K near-edge fine structure: an electron-energy-loss investigation with comparisons to new theory for selected 3d transition-metal oxides. *Phys. Rev. B.* 1982;25:7157–7173.
- [29] J. G. Chen, B. Frühberger, M. L. Colaianni. Near edge X-ray absorption fine structure characterization of compositions and reactivities of transition metal oxides. *J. Vac. Sci. Technol. A.* 1996;14:1668–1673.

- [30] G. Kaindl, G. Kalkowski, W. D. Brewer, B. Perscheid. M-edge X-ray absorption spectroscopy of 4f instabilities in rare earth systems. *J. Appl. Phys.*. 1984;55:1910–1915.
- [31] B. T. Thole, G. van der Laan, J. C. Fuggle, G. A. Sawatzky, R. C. Karnatak, J.-M. Esteve. 3d X-ray-absorption lines and the $3d^9 4f^n + 1$ multiplets of the lanthanides. *Phys. Rev. B.* 1985;32:5107–5118.
- [32] C. H. Ahn, Y. K. Young, C. K. Dong, S. K. Mohanta, H. K. Cho. A comparative analysis of deep level emission in ZnO layers deposited by various methods. *J. Appl. Phys.* 2009;105:013502.
- [33] D. M. Hofmann, D. Pfisterer, J. Sann, B.K. Meyer, R. Tena-Zaera, V. Munoz-Sanjose, T. Frank, G. Pensl. Properties of the oxygen vacancy in ZnO. *Appl. Phys. A.* 2007;88:147–151.
- [34] L. S. Vlasenko, G. D. Watkins. Optical detection of electron paramagnetic resonance in room-temperature electron-irradiated ZnO. *Phys. Rev. B.* 2005;71:125210.
- [35] K. Vanheusden, W. L. Warren, C. H. Seager, D. R. Tallant, J. A. Voigt, B. E. Gnade. Mechanisms behind green photoluminescence in ZnO phosphor powders. *J. Appl. Phys.* 1996;79:7983–7990.
- [36] X. J. Wang, L. S. Vlasenko, S. J. Pearton, W. M. Chen, I. A. Buyanova. Oxygen and zinc vacancies in as-grown ZnO single crystals. *J. Phys. D: Appl. Phys.*. 2009;42:175411.
- [37] J. Ji, L. A. Boatner, F. A. Selim. Donor characterization in ZnO by thermally stimulated luminescence. *Appl. Phys. Lett.* 2014;105:041102.
- [38] N. O. Korsunskaya, L. V. Borkovskaya, B. M. Bulakh, L. Y. Khomenkova, V. I. Kushnirenko, I. V. Markevich. The influence of defect drift in external electric field on green luminescence of ZnO single crystals. *J. Lumin.* 2003;102:733–736.
- [39] B. X. Lin, Z. X. Fu, Y. B. Jia. Green luminescent center in undoped zinc oxide films deposited on silicon substrates. *Appl. Phys. Lett.* 2001;79 :943.
- [40] S. Bedanta, W. Kleemann. Supermagnetism. *J. Phys. D: Appl. Phys.* 2009;42:013001.
- [41] J. P. Bucher, D. C. Douglass, L. A. Bloomfield. Magnetic properties of free cobalt clusters. *Phys. Rev. Lett.* 1991;66:3052–3055.
- [42] R. H. Kodama, Salah A. Makhlof, A. E. Berkowitz. Finite size effects in antiferromagnetic NiO nanoparticles. *Phys. Rev. Lett.* 1997;79:1393–1396.
- [43] S. Mørup, B. R. Hansen. Uniform magnetic excitations in nanoparticles. *Phys. Rev. B.* 2005;72:024418.
- [44] D. C. Douglass, J. P. Bucher, L. A. Bloomfield. Magnetic properties of free cobalt and gadolinium clusters. *Phys. Rev. B.* 1993;47:12874–12889.
- [45] Y. E. Kitaev, P. Tronc. Ferromagnetic and antiferromagnetic ordering in the wurtzite-type diluted magnetic semiconductors. *Phys. Sol. State.* 2012;54:520–530.

- [46] A. Łusakowski. Ground state splitting of S 8 rare earth ions in semiconductors. *Phys. Rev. B.* 2005;72:094429.
- [47] R. Skomski, D. J. Sellmyer. Anisotropy of rare earth magnets. *J. Rare Earths.* 2009;27:675.
- [48] G. Kresse, D. Joubert. Ab initio molecular dynamics for liquid metals. *Phys. Rev. B.* 1993;47:558
- [49] G. Kresse, J. Furthmuller. Efficient iterative schemes for ab initio total-energy calculations using a plane-wave basis set. *Phys. Rev. B.* 1996;54:11169.
- [50] L. Liu, P. Y. Yu, Z. Ma, S. S. Mao. Ferromagnetism in GaN:Gd: a density functional theory study. *Phys. Rev. Lett.* 2008;100:127203.
- [51] I. Bantounas, V. Singaravelu, I. S. Roqan, U. Schwingenschlogl. Structural and magnetic properties of Gd-doped ZnO. *J. Mater. Chem. C.* 2014;2:10331.
- [52] Y. Gohda, A. Oshiyama. Intrinsic ferromagnetism due to cation vacancies in Gd-doped GaN: first-principles calculations. *Phys. Rev. B.* 2008;78:161201(R).
- [53] S. Assa Aravindh, U. Schwingenschoel, I. S. Roqan. Ferromagnetism in Gd doped ZnO nanowires: a first principles study. *J. Appl. Phys.* 2014;116:233906.
- [54] T. Dietl, H. Ohno, F. Matsukura, J. Cibert, D. Ferrand. Zener model description of ferromagnetism in zinc-blende magnetic semiconductors. *Science.* 2000;287:1091.
- [55] P. M. Krstajic, F.M. Peters, A. Ivanov, V. Fleurov, K. Kikoin. Double-exchange mechanisms for Mn-doped III–V ferromagnetic semiconductors. *Phys. Rev. B.* 2004;70:195215.

Edited by Khan Maaz

This book reports on the recent progresses in theory, application, and characterization of magnetic materials. It covers a broad spectrum of topics on magnetic materials with different shapes and morphologies such as transition metals, cylindrical and 2D ferromagnetic nanowires, core-shell nanowires, monoatomic-layered nanostructures, and nanocrystals. This book addresses diverse groups of readers with general background in physics and material science and also covers topics for the specialists in the field of magnetism. It is believed that this book will be interesting for the readers and will provide a solid foundation about the topic for the students, scientists, and engineers working in the field of material science and condensed matter physics.

Photo by LiborF / CanStock

IntechOpen

